An Investigation of Fluid Transport in Porous Solids Using Nuclear Magnetic Resonance

William Matthew Holmes, B.Sc (Hons.).

Thesis submitted to the University of Nottingham for the degree of Doctor of Philosophy, March 2001.

Declaration.

I declare that the work contained in this thesis submitted by me for the degree of Doctor of Philosophy is my own work, except where due reference is made to other authors, and has not previously been submitted by me for a degree at this or any other university.

Abstract

A commercially available NMR spectrometer has been used to investigate fluid transport within porous solids. Two water-wet porous solids were investigated. The first was a sample of Fontainebleau sandstone, and the second was an idealised porous solid made from a random packing of glass beads. The samples were saturated with two immiscible phases, i.e an oil and water phase. Pulsed field gradient (PFG) NMR measurements of one- and two-dimensional displacement probability distributions are reported, for steady-state flow and diffusion, within two phase saturated porous solids. Measurements were made with the porous solids prepare in different steady-state saturations. NMR relaxation measurements are also reported.

Using the NMR data it was possible to evaluate the physical importance of parameters such as wettability and phase saturation on transport phenomena in two phase saturated porous solids. Various computer simulations were developed to model the experimental data.

Acknowledgements

" It was the best of times, it was the worst of times...."

Charles Dickens

On writing these acknowledgements I have been a student at the Chemistry Department of the University of Nottingham for 9 years and 7 months. In that time I have received the kind help and friendship of many people, only a few of whom I can acknowledge here.

Firstly, I want to thank my family for helping me through more than 3 years of suffering from M.E.. During this time they believed in me when nobody else did, and it is only because of them that I was able to return to University. I particularly want to thank my Dad, who slowly and wisely walked me back to health, something I will truly never forget.

This PhD was special for me because it became both a challenge and a passion. For this I have to thank my supervisor, Ken Packer, who gave me great freedom in my research, which I thrived on. I especially enjoyed discussing results and ideas with someone so enthusiastic and knowledgeable.

To get through a PhD you need good friends, people to turn to for help (usually steve), advice, sympathy when nothing works, half-hour coffee breaks, relieving the boredom, chocolate brownies and, of course, to go drinking with (usually at the Wheat sheaves). This mainly included Physical Chemistry, but especially Kat, Steve and Ross (excellent people).

I also had a great time with the 'Running Club', i.e. Graham, Deano, John etc etc, with whom I ran hundreds of miles and trained for my first marathon. The Physical Chemistry Cricket team was another passion, what we lacked in technique, tactics, ability, fitness and sportsmanship was not compensated for by our enthusiasm and team spirit(?). Though I was proud to be hailed as their "leading wicket-taker for 3 years running".

Contents

Chapter 1 Introduction

1.1 INTRODUCTION....3

1.2 AIMS AND OBJECTIVES....4

1.3 OVERVIEW....5

Chapter 2 Nuclear Magnetic Resonance

2.1 INTRODUCTION....9

2.2 BASIC NMR THEORY....9

2.3 PULSES AND SPIN ECHOES....14

2.4 NUCLEAR SPIN INTERACTIONS....18

2.5 RELAXATION....20

2.6 RELAXATION IN POROUS SOLIDS....25

2.7 MEASUREMENT OF MOTION USING NMR....27

2.8 PULSED NMR INTRUMENTATION....36

2.9 REFERENCES....41

Chapter 3 Porous Solids

3.1 INTRODUCTION....45

3.2 MACROSCOPIC PARAMETERS....45

3.3 MICROSCOPIC PARAMETERS....48

3.4 WETTABILITY....52

3.5 DISPLACEMENT PROCESSES....53

3.6 MEASURING WETTABILITY....55

3.7 GEOLOGICAL POROUS SOLIDS....57

3.8 REFERENCES....60

Chapter 4 Review

4.1 INTRODUCTION.. 63

4.2 RELAXATION 63

4.3 PULSED FIELD GRADIENT NMR.. 67

4.4 IMAGING.. 69

4.5 REFERENCES.. 71

Chapter 5 Experimental

5.1 INTRODUCTION..78

5.2 THE SPECTROMETER.. 78

5.3 FONTAINEBLEAU SANDSTONE.. 78

5.4 GLASS BEAD PACKS.. 87

5.5 RELAXATION MEASUREMENTS.. 88

5.6 PULSED FIELD GRADIENT EXPERIMENTS.. 91

5.7 REFERENCES

Chapter 6 Relaxation Study of Fontainebleau Sandstone

6.1 INTRODUCTION.. 98

6.2 LONGITUDINAL RELAXATION.. 98

6.3 TRANSVERSE RELAXATION.. 104

6.4 REFERENCES 109

Chapter 7 Stagnant Oil Produced by Secondary Imbibition

7.1 INTRODUCTION.. 112

7.2 PRELIMINARY INVESTIGATION.. 112

7.3 INVESTIGATION OF STAGNANT OIL FRACTION.. 119

7.4 PRELIMARY SIMULATION RESULTS..124

7.5 CONCLUSIONS.. 126

7.6 REFERENCES 127

Chapter 8 Diffusion in Thin Films

8.1 INTRODUCTION 130

8.2 EXPERIMENTAL 130

8.3 ISOTROPIC INFINITE PLANES MODEL FOR DIFFUSION IN SURFACE WETTING FILMS 135

8.4 CONCLUSIONS 143

8.5 REFERENCES. 144

Chapter 9 Diffusion in Thin Films 2

9.1 INTRODUCTION 147

9.2 EXPERIMENTAL 147

9.3 COMPUTER SIMULATION 154

9.4 FINAL SIMULATION 159

9.5 RESULTS AND DISCUSSION 169

9.6 CONCLUSION 179

9.7 REFERENCES 180

Chapter 10 Two-Dimensional Propagators

10.1 INTRODUCTION 184

10.2 THE TWO-DIMENSIONAL APGSTE SEQUENCE 184

10.3 HANKEL TENASFORM 189

10.4 CORRELATION BETWEEN DISLACEMENTS IN X AND Z 193

10.5 THEORETICALLY DERIVED $C_\Delta(X,Z)$ 194

10.6 EXPERIMENTALLY DERIVED $C_\Delta(X,Z)$ 197

10.7 CONCLUSION 206

10.8 REFERENCES 207

APPENDIX 208

Chapter 1

Introduction

Contents

1.1 INTRODUCTION......3

1.2 AIMS AND OBJECTIVES......4

1.3 OVERVIEW......5

1.1 Introduction

The study of multi-phase flow and fluid distributions in porous solids are topics of fundamental importance for several fields of scientific endeavour. Chemical engineers are interested in the effectiveness of porous catalysts and the transport of fluids through packed columns. Biologists are interested in the flow of blood through organ tissues. The study of porous solids is also directly relevant to such diverse disciplines as food science, environmental science (e.g. waste water treatment) and separation technologies (e.g. liquid chromatography).

The origins of this thesis lie in the petroleum industry. Petroleum (Gr. *Petra*, rock, L. *oleum*, oil) is the general term used to describe all natural hydrocarbons. As its etymology suggests, petroleum is usually found trapped within the interstices of a rock, into which it migrated from source rocks over a period of millions of years. Petroleum has been used for many centuries, primarily for heating and lighting, but it is only in the last century that its influence upon global economics has become so profound. In search of this 'liquid gold' petroleum engineers have explored some of the most inaccessible places on earth.

The main concern of the petroleum industry is the economic extraction of hydrocarbons from porous reservoirs rocks. This usually involves the displacement of the hydrocarbons by aqueous phases and/or gas. It is a painful fact that during such displacement processes a large fraction of the hydrocarbon is not recovered. The recognition that petroleum is a finite resource has led to a growing interest in understanding the fundamental physics of flow, diffusion and displacement processes within porous solids. Many experimental techniques are used in the study of porous solids, although NMR has the advantage over other techniques of being non-invasive and non-destructive. A wide range of NMR methods are available to study the structure of porous solids, the transport of fluids through porous solids and the distribution of fluids within porous solids.

1.2 Aims and Objectives

At the beginning of this research project only very general aims and objectives were set. The broad aim was to use NMR techniques to investigate fluid saturated porous solids. During the course of the project a number of interesting research topics were identified and pursued.

An investigation was undertaken into porous solids saturated with two immiscible phases (i.e. oil and water). The phase distribution within a porous solid is determined by the wettability of the sample. The two samples used in this project (Fontainebleau sandstone and packs of glass beads) were both strongly water-wet. In this case the water phase (the wetting phase) is always in contact with the surface of the sample, whereas the oil phase (the non-wetting phase) never comes in contact with the surface. An important parameter when a porous solid is saturated with two immiscible phases is the saturation state. The saturation of each phase is defined as the fraction of the total pore volume occupied by that phase. One of the aims of this research project was to investigate how the saturation state of a water-wet porous solid affects the diffusive transport of the wetting phase, and also how it affects the longitudinal relaxation properties of both phases.

A universal method of oil recovery from oil reservoirs is to pump water and/or gas into the reservoir at strategic points, in an attempt to displace the oil. Understanding such displacement processes is of considerable interest to the petroleum industry. Another of the aims of this research project was to investigate the effects of such displacement processes on fluid transport through a sample of Fontainebleau sandstone.

There are many situations, not related to the petroleum industry, in which the diffusion of a fluid is hindered or restricted by a confining structure. For example in emulsions, biological samples, foods, rocks and various industrial materials. The final objective of this research project was to explore the possibility of using NMR to quantify the eccentricities and symmetries of these confining structures.

1.3 Overview

This section gives details about the structure of this thesis and about where various concepts and data are presented.

Chapter 2 describes the theoretical background of this thesis. An outline is given of the theory of NMR, its sources, the concept of relaxation and nuclear spin interactions. A detailed description is given of the Pulsed Gradient Spin Echo NMR (PGSE NMR) technique, with particular attention paid to the application of this technique to the study of porous solids. Finally, an elementary description is given of modern NMR instrumentation, with reference made to the NMR spectrometer used in this study.

Chapter 3 provides a general introduction to porous solids. Some important macroscopic parameters are defined, such as porosity, permeability, saturation and surface-to-volume ratio. Some important microscopic parameters are also discussed, such as pore size distribution, surface tension and wettability. Finally, an overview is given of geological porous solids.

Chapter 4 reviews the application of NMR to the study of porous solids, with particular emphasis placed on work of a petrophysical nature. The broad topics of NMR relaxation, pulsed field gradient (PFG) NMR and magnetic resonance imaging are reviewed.

Chapter 5 outlines the experimental methods used in this research project. Information is given about the spectrometer, the multi-phase flow system and the porous solids used. A description is also given of the NMR pulse sequences used, along with typical experimental parameters.

In experiments where the porous solid is saturated with two immiscible phases, an important parameter is the saturation state of the sample. The saturation of each phase is defined as the fraction of the total pore volume occupied by that phase. Details are given in this chapter about how different saturation states were produced within the porous solids, and how these saturation states were measured.

Chapter 6 presents the results of NMR relaxation measurements made on the Fontainebleau sample, with the sample saturated with two immiscible phases (oil and water). These results provided background information for later studies.

An interesting result was the variation in the longitudinal relaxation times of the water phase measured at different saturation states. This result is discussed in more detail in chapter 9, where it is compared with similar measurements performed on glass bead packs.

Chapter 7. In this chapter pulsed field gradient (PFG) NMR is used to investigate two phase (oil and water) flow through a sample of Fontainebleau sandstone, with the sample in a steady-state saturation. The effect on fluid transport of changing the steady-state saturation was investigated. The steady-state saturation of the Fontainebleau sandstone was changed using a primary drainage/secondary imbibition cycle (described in detail in chapter 6).

Chapter 8. The Fontainebleau sample used in this research is strongly water-wet. This means that when the Fontainebleau sample is saturated with both water and oil, the water phase (wetting phase) is always in contact with the rock's surface. At low water saturations the water phase forms a thin continuous surface-wetting film that covers all the grain surfaces of the rock. In this chapter pulsed field gradient (PFG) NMR is used to investigate the diffusion of the water phase contained within these thin surface-wetting films. A simple theoretical model is proposed to help explain the experimental results.

Chapter 9. In chapter 8 measurements were made for the diffusion of water within the surface-wetting films of Fontainebleau sandstone, at low water saturations. The complex nature of Fontainebleau sandstone makes a detailed interpretation of these results difficult. Therefore, similar measurements were performed on a less complex porous solid i.e. a random packing of mono-disperse, water-wet, glass beads.

Water-wet glass beads were saturated with oil and water, in varying proportions. At low water saturations, the water phase is present in the form of pendular rings, which form where two sphere touch, and as a thin continuous film covering the remaining surface of each sphere. Pulsed field gradient (PFG) NMR is used to investigate the diffusion of the water phase within such a system. A random walk simulation is presented, which models the diffusive transport of the water phase, at low water saturations. The simulation helps to explain the crucial role played by surface-wetting films in the diffusive transport of the wetting phase. Using this simulation estimates are made of the thickness of the surface wetting films.

This chapter also presents the results of an investigation into the effects of saturation on longitudinal relaxation times. These results are compared with similar measurements performed on the Fontainebleau sandstone. The crucial role played by the thin surface-wetting films on longitudinal relaxation measurements is discussed.

Chapter 10. In this chapter PFG NMR is used to measure the two-dimensional displacement probability distribution, $P_\Delta(X,Z)$. This describes the probability of a spin-bearing particles simultaneously having displacements X and Z in a time Δ. Measurements of $P_\Delta(X,Z)$ were made for the diffusion of a liquid phase within various confining structures. From these measurements a correlation distribution $C_\Delta(X,Z)$ is derived, which describes the correlations between X and Z displacements. These results are compared to theoretically derived correlation distributions. It is suggested that these correlation distributions will allow detailed characterisation of the confining structure.

Chapter 2

Nuclear Magnetic Resonance

Contents

2.1 INTRODUCTION....9

2.2 BASIC NMR THEORY....9

- 2.2.1 NUCLEAR MAGNETIC MOMENTS....9
- 2.2.2 THE ZEEMAN INTERACTION....9
- 2.2.3 BULK MAGNETISATION....11
- 2.2.4 A SEMI-CLASSICAL DESCRIPTION....11
- 2.2.5 THE EFFECT OF RF RADIATION....13

2.3 PULSES AND SPIN ECHOES....14

- 2.3.1 90° PULSE....14
- 2.3.2 SLICE SELECTIVE 90° PULSE....15
- 2.3.3 180° PULSE....16
- 2.3.4 SPIN ECHOES....16
- 2.3.5 STIMULATED ECHO....16

2.4 NUCLEAR SPIN INTERACTIONS....18

- 2.4.1 DIPOLE-DIPOLE INTERACTION....18
- 2.4.2 CHEMICAL SHIFT....19
- 2.4.3 SCALAR COUPLING....20

2.5 RELAXATION....20

- 2.5.1 SPIN-LATTICE RELAXATION $-T_1$....20
- 2.5.2 TRANSVERSE RELAXATION $-T_2$....21
- 2.5.3 MEASURING NUCLEAR RELAXATION....21
- 2.5.4 RELAXATION VIA DIPOLAR INTERACTIONS....22

2.6 RELAXATION IN POROUS SOLIDS....25

- 2.6.1 SURFACE RELAXATION....25
- 2.6.2 DIFFUSION THROUGH MAGNETIC FIELD GRADIENTS....26

2.7 MEASUREMENT OF MOTION USING NMR....27

- 2.7.1 PULSED FIELD GRADIENT SPIN ECHO....27
- 2.7.2 UNRESTRICTED SELF DIFFUSION....30
- 2.7.3 HINDERED DIFFUSION....32
- 2.7.4 RESTRICTED DIFFUSION....33
- 2.7.5 FLOW....35

2.8 PULSED NMR INSTRUMENTATION....36

- 2.8.1 STATIC MAGNETIC FIELD....36
- 2.8.2 PULSE PROGRAMMER....36
- 2.8.3 TRANSMITTER AMPLIFIER....36
- 2.8.4 PROBE....36
- 2.8.5 PRE-AMPLIFIER AND PHASE SENSITIVE DETECTOR....37
- 2.8.6 FILTERS....37
- 2.8.7 ANALOGUE TO DIGITAL CONVERTER....39
- 2.8.8 SHIM COILS....39
- 2.8.9 GRADIENT COILS....39
- 2.8.10 SIGNAL-TO-NOISE....39
- 2.8.11 PHASE CYCLING....40

2.9 REFERENCES....41

2.1 Introduction

This chapter contains a summary of the essential principles of NMR relevant to this thesis. A full description of the theory of NMR can be found in greater detail in the extensive literature that is available. The reader is referred especially to comprehensive sources such as Abragam [1] and Slichter [2]. The reader is also referred to an excellent book on NMR microscopy by Callaghan[3].

2.2 Basic NMR Theory

2.2.1 Nuclear Magnetic Moments

Stable atomic nuclei may have a spin angular momentum **P**, which is governed by the constituent protons and neutrons. Quantum mechanics states that angular momentum is quantised in both magnitude and direction. The spin angular momentum operator is given by:

$$\hat{\mathbf{P}} = \hbar\hat{\mathbf{I}} \tag{2.1}$$

where $\hat{\mathbf{I}}$ is the nuclear spin angular momentum operator. The operator $\hat{\mathbf{I}}^2$ has eigenvalues of $I(I+1)$ where I is the nuclear spin angular momentum quantum number, which takes values $0, 1/2, 1 \ldots$. The magnitude of the angular momentum is given by:

$$|P| = \hbar\sqrt{I(I+1)} \tag{2.2}$$

The operator $\hat{\mathbf{I}}_z$ gives the z-component of the nuclear spin angular momentum. It has eigenvalues m_I, which can take values $I, I-1 \ldots, -I$. There are $(2I+1)$ possible orientations given by the magnetic quantum number m_I. A nucleus with a non-zero angular momentum will possess a magnetic moment μ:

$$\mu = \gamma \mathbf{P} \tag{2.3}$$

where the constant of proportionality is known as the magnetogyric ratio γ. The magnetogyric ratio and the nuclear spin quantum number are characteristic of an individual isotope, meaning that different nuclei possess different magnetic moments. The possible z-components of the nuclear magnetic moment being:

$$\mu_z = \gamma\hbar m_I \tag{2.4}$$

2.2.2 The Zeeman Interaction

The interaction energy of a magnetic dipole moment μ in an externally applied static magnetic field $\mathbf{B}_0$ is written classically and quantum mechanically as $-\mu\cdot\mathbf{B}_0$ so that the Hamiltonian operator for the case of $\mathbf{B}_0$ oriented along the z axis is:

$$\hat{\mathbf{H}} = -\gamma\hbar B_0 \hat{\mathbf{I}}_z \tag{2.5}$$

The Hamiltonian gives rises to energy eigenvalues $E(m_I)$:

$$E(m_I) = -\gamma\hbar B_0 m_I \tag{2.6}$$

The coupling of an isolated spin with an external magnetic field thus produces (2I+1) energy levels, an effect known as the Zeeman interaction. For the case of hydrogen, which has $I = \frac{1}{2}$, two spin energy states are formed, corresponding to $m_I = \pm \frac{1}{2}$. The energy difference between the two spin states, see figure 2.1, is given by:

$$\Delta E = \gamma\hbar B_0 \tag{2.7}$$

Transitions between these energy levels can be induced by the stimulated absorption or emission of a photon of frequency ω_0:

$$\omega_0 = -\gamma \mathbf{B}_0 \tag{2.8}$$

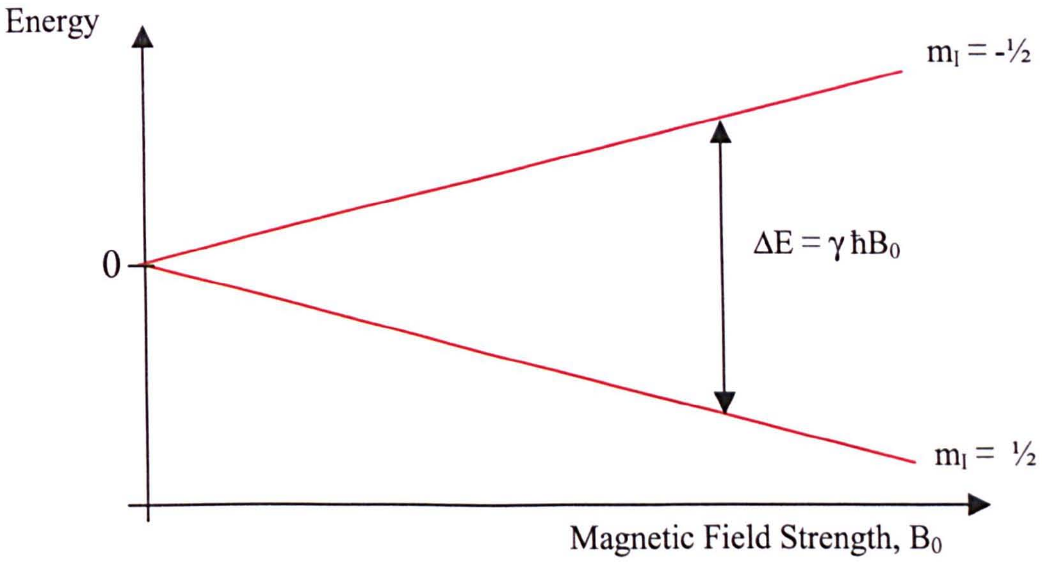

Figure 2.1 Energy level splitting for different field strengths.

The values of γ are such that, for currently achievable field strengths, ω_0 lies in the radio frequency (RF) range of the electromagnetic spectrum. Note that Planck's constant has disappeared from the resonance equation. This fact suggests that the result is closely related to a classical picture [2].

2.2.3 Bulk Magnetisation.

An assembly of non-interacting spins in thermal equilibrium with the surrounding lattice, will populate the two energy states according to a Boltzmann distribution. If the population of the higher energy level is $N_{-1/2}$ and the population of the lower energy level is $N_{1/2}$, then:

$$\frac{N_{-1/2}}{N_{+1/2}} = \exp\left(\frac{-\hbar\omega_0}{k_B T}\right) \cong 1 - \frac{\hbar\omega_0}{k_B T} \tag{2.9}$$

where T is the temperature of the lattice with which the spins are in thermal contact. The second equality in equation 2.9 is known as the high temperature approximation. It assumes that the mean thermal energy of the lattice is considerably greater than the energy needed for transitions, ie $k_BT >> \Delta E$. Under such conditions there is a very small excess of spins in the lower energy state, $n = N_{1/2} - N_{-1/2}$:

$$n \cong \frac{N\hbar\omega_0}{2k_B T} \tag{2.10}$$

This small excess is sufficient to create a total bulk magnetisation M_0 in the sample. This bulk magnetisation is given by:

$$\begin{aligned} M_0 = n\mu_{m=1/2} &\cong \left(\frac{N\hbar\gamma B_0}{2k_B T}\right)\left(\frac{\gamma\hbar}{2}\right) \\ &\cong \frac{CB_0}{k_B T} \end{aligned} \tag{2.11}$$

This is the Curie law of temperature-dependent paramagnetism, where C is the Curie constant. It states that the bulk magnetisation M_0 is proportional to the number of spins N and the applied magnetic field B_0 and is inversely proportional to the lattice temperature T. The energy difference between the two spin states for hydrogen ($\gamma = 2.675221 \times 10^8$ rad $s^{-1}T^{-1}$) in a 2.0T magnet is 5.64×10^{-26} J. This gives a population difference of around 7 nuclei per million at 20 °C. It is this small excess which gives rises to the measured signal, hence the low sensitivity of NMR spectroscopy in comparison with spectroscopy involving higher frequencies.

2.2.4 A Semi-Classical Description

While a full description of the properties of a spin system is best carried out using the density operator method [2], a simpler semi-classical model provides a valuable insight. Consider the classical motion of a magnetic moment $\boldsymbol{\mu}$, which has an associated spin angular momentum **P** in a uniform magnetic field $\mathbf{B}_0$. The associated equation of motion is:

$$\frac{d\mathbf{P}}{dt} = \boldsymbol{\mu} \times \mathbf{B}_0 \tag{2.12}$$

And since, $\boldsymbol{\mu} = \gamma\,\mathbf{P}$:

$$\frac{d\boldsymbol{\mu}}{dt} = \gamma\boldsymbol{\mu}\times\mathbf{B}_0 \tag{2.13}$$

Equation 2.13 describes the precession of the magnetic moment about the B_0 axis. Such motion being analogous to the precession of a gyroscope. The solution of equation 2.13 gives the frequency of the precession as ω_L:

$$\boldsymbol{\omega}_L = -\gamma\mathbf{B}_0 \tag{2.14}$$

This is called the Larmor frequency. It is significant that this precessional frequency is precisely the frequency a photon needs to produce a transition between the energy levels in figure 2.1. In the classical case, the half-angle of the cone of precession θ can take any value. To incorporate the quantisation of the Zeeman energy, the half angle of the cone is determined by the magnetic quantum number m_I, which, for a $I = \frac{1}{2}$ nucleus, has only two states $m_I = \pm\frac{1}{2}$, hence two precessional cones. An ensemble of non-interacting spins maybe represented as in figure 2.2. At thermal equilibrium the magnetic moments are evenly distributed in the x-y plane, giving a net magnetisation of zero in the xy plane. There is only a component of the bulk magnetisation along the z-axis.

$$M_z^{eq} = M_0 \;;\; M_x^{eq} = M_y^{eq} = 0 \tag{2.15}$$

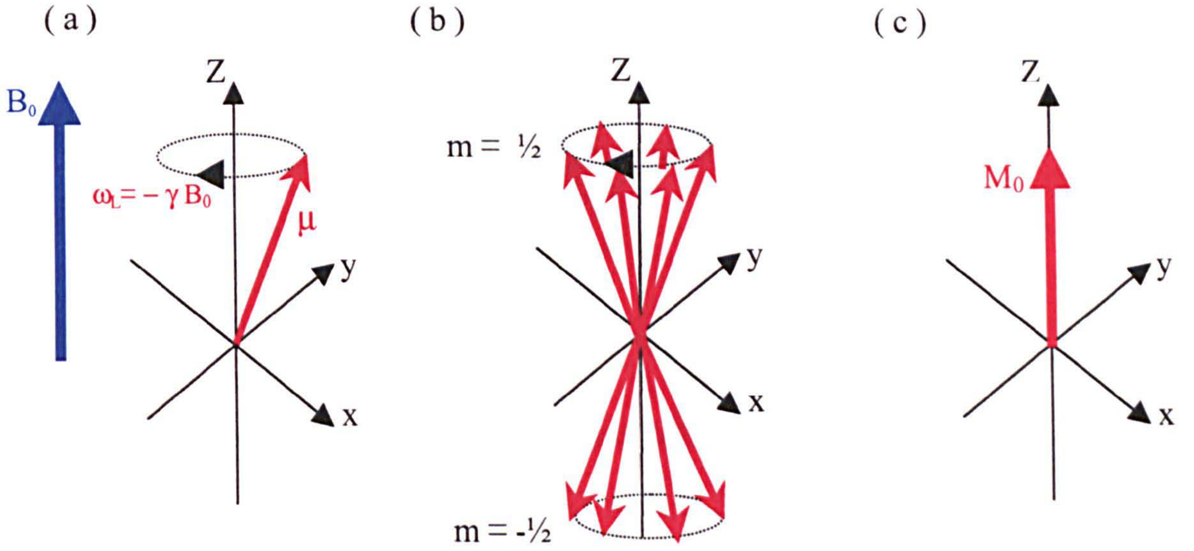

Figure 2.2 Precession model of spins. a) Precession of isolated spin about B_0. b) Ensemble of spins at equilibrium precessing about B_0. c) Slight excess of spins in m= ½ state produces a net magnetisation M_0.

2.2.5 The Effect of RF Radiation

The important component of RF radiation for NMR is the magnetic component. A linearly polarized source has a sinusoidally oscillating magnetic field which can be considered as the superposition of two magnetic vectors rotating in opposite directions. Only the component which rotates in the same sense as the precessional motion of the spins, called $B_1(\omega)$, can induce transitions between energy levels. In order to induce transitions its frequency must match the Larmor frequency i.e. $\omega = \omega_0$. It is convenient to consider the spins and RF field in a reference frame rotating about the z-axis at the frequency of the applied radiation,ω. In this rotating frame, there is an effective magnetic field B_{eff}:

$$\mathbf{B}_{\text{eff}} = B_0\mathbf{k}' + \frac{\omega}{\gamma}\mathbf{k}' + B_1\mathbf{i}' \tag{2.16}$$

where $\mathbf{i}'$ and $\mathbf{k}'$ are unit vectors along the x' and z' axis of the rotating frame. The bulk magnetisation, which is the vector sum of the individual magnetic moments, then precesses about this effective field. This is illustrated in figure 2.3. The equation of motion being:

$$\frac{d\mathbf{M}}{dt} = \gamma\mathbf{M} \times \mathbf{B}_{\text{eff}} \tag{2.17}$$

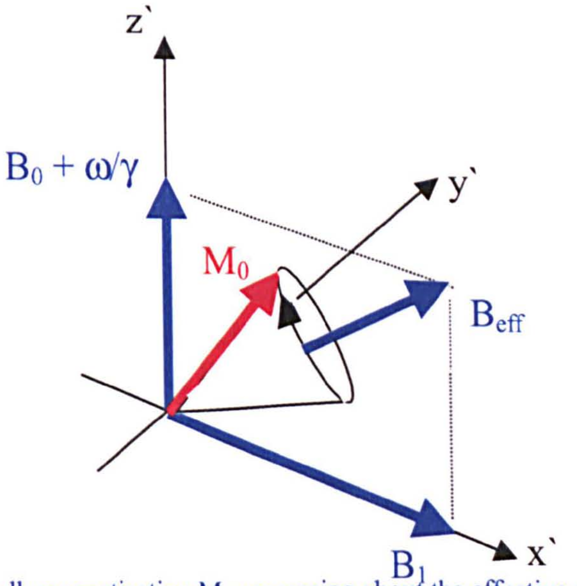

Figure 2.3 The bulk magnetisation M_0 precessing about the effective magnetic field B_{eff}.

In the rotating frame, at resonance ($\omega = \omega_0$), all the individual magnetic moments of the total spin system appear static, because the common high frequency ω_0 has been removed. The only field the spins experience in this frame of reference is the $\mathbf{B}_1$ field, which is arbitrarily chosen to lie along the x` axis of the rotating frame. Thus the bulk magnetisation rotates about the x` axis at a frequency $\omega_1 = -\gamma\mathbf{B}_1$. If the $\mathbf{B}_1$ field is applied for a duration t_p, the angle of nutation (see figure 2.4) is given by:

$$\theta = \gamma B_1 t_p \tag{2.18}$$

The application of an RF pulse or pulses may produce a non-zero transverse magnetisation. After the RF pulses any transverse magnetisation will precess about the B_0 field, this then induces a signal in the receiver coil.

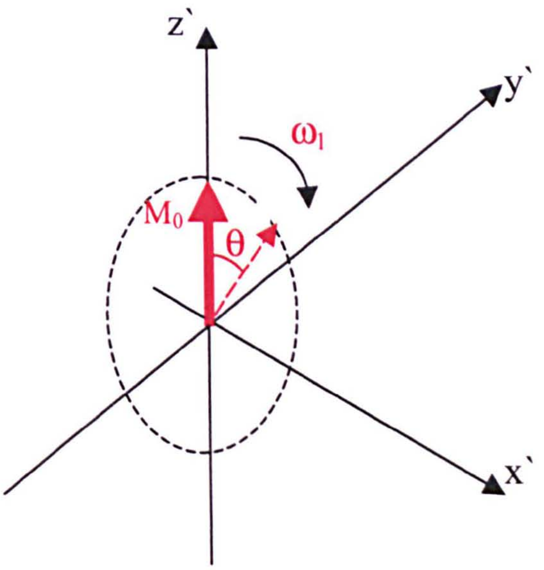

Figure 2.4 Nutation of the magnetisation M_0 through an angle θ after a time t_p.

2.3 Pulses and Spin Echoes

2.3.1 90° Pulse

The largest signal is detected when the bulk magnetisation has been rotated by 90° and is aligned along the y` axis. A pulse of RF radiation with a duration that produces this condition is called a $90°_x$ pulse. Following a $90°_x$ pulse the components of the bulk magnetisation are:

$$M_{z'} = M_{x'} = 0 \quad ; \quad M_{y'} = M_0 \tag{2.19}$$

In terms of the semi-classical model, the two spin states have the same population. On its own this would lead to a zero net magnetisation. However, the spins have also gained a phase coherence, which manifests itself as a net magnetization in the x`y` plane. The decay of the signal following a 90° pulse is called the Free Induction Decay (FID) and this is the Fourier transform of the frequency spectrum of the spins. It should also be noted that a B_1 pulse of frequency ω_0 and duration t_p will excite a range of frequencies about ω_0. The frequency and time domain of the RF pulse has the Fourier relationship given by equation 2.20. The Fourier transform of a rectangular pulse in the time domain is a sinc function in the frequency domain, and is illustrated in figure 2.5. To excite a large bandwidth of frequencies a short pulse is required.

$$F(\omega) = \int_{-\infty}^{\infty} f(t)\exp(-i\omega t)\,dt$$
$$f(t) = \frac{1}{2\pi}\int_{-\infty}^{\infty} F(\omega)\exp(i\omega t)\,d\omega \qquad (2.20)$$

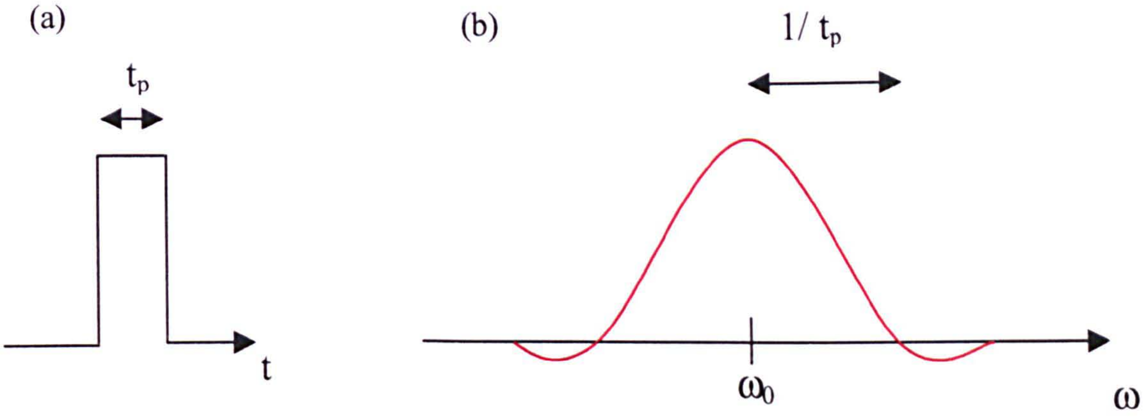

Figure 2.5 a) A rectangular pulse of RF radiation of frequency ω_0. b) The corresponding frequency domain.

2.3.2 Slice Selective 90° pulse

The 90° pulse described above excites a bandwidth of frequencies inversely proportional to the pulse duration. In NMR spectroscopy the pulse duration is made sufficiently short so that the associated bandwidth covers the chemical shifts of all the spins of a given nuclear species. It is also possible to selectively excite a specific region of the NMR spectrum by using pulses of longer duration.

This is particularly useful when the RF pulse is applied in the presence of a linear magnetic field gradient, then the Larmor frequency of individual spins depends upon their position along the gradient direction. From equation 2.20 it is clear that a rectangular slice in space can be excited by modulating the RF pulse with a sinc function. However, the pulse has to have finite duration in the time domain and therefore the sinc function has to be truncated, this leads to artefacts in the frequency domain.

After applying a sinc modulated RF pulse of finite duration (-T to T) in the presence of a linear gradient along the z direction G_z, the magnetisation is in a dephased state. The magnetization of a spin plane normal to z has a net phase shift $\gamma z G_z T$. This can be removed by applying a gradient of the opposite sense for a time T [3].

2.3.3 180° Pulse

If a 180° pulse is applied to a spin system that is in equilibrium with its surroundings it inverts the population of the two spin states. The components of the bulk magnetisation following a $180°_x$ pulse are:

$$M_{z'} = -M_0 \; ; M_{x'} = 0 \, , M_{y'} = 0 \tag{2.21}$$

2.3.4 Spin Echoes

Inhomogeneities in the applied magnetic field cause nuclear spins to precess at slightly different Larmor frequencies depending on their position in the sample. Following a 90° pulse, this spread of Larmor frequencies results in a dephasing of the transverse magnetisation. Hahn [4] recognised that this loss of phase coherence was inherently reversible. He found that applying a 180° pulse a time τ after the 90° pulse, causes some degree of refocusing of the transverse magnetisation at a time 2τ. This is illustrated in figure 2.6. The incomplete refocusing causes attenuation of the spin echo with respect to the initial FID, this is a consequence of transverse relaxation {see section 2.5.2}.

2.3.5 Stimulated Echo

Another form of echo which is used in this thesis is the stimulated echo. The stimulated echo pulse sequence is shown in figure 2.7. The first $90°_x$ pulse tips the bulk magnetisation M_0 along the y` axis, hence giving the spin system a phase coherence. Inhomogeneities in the applied magnetic field results in a dephasing of the transverse magnetisation. The second $90_x$ pulse at time $\tau$ has the effect of rotating the y` component of the magnetisation along the z-axis, the components of the stored magnetisation have amplitude proportional to their phase at time τ . Any x` component of the magnetisation is unaffected. Application of a third $90°_x$ pulse returns the magnetisation stored along the z-axis to the transverse plane. A stimulated echo forms at a time $T+\tau$. This sequence of RF pulses also generates additional spin echoes. An effective method to remove these unwanted echoes is to use a homogeneity spoiling (homospoil) magnetic field gradient pulse, during the interval between the second and third RF pulses, as shown below:

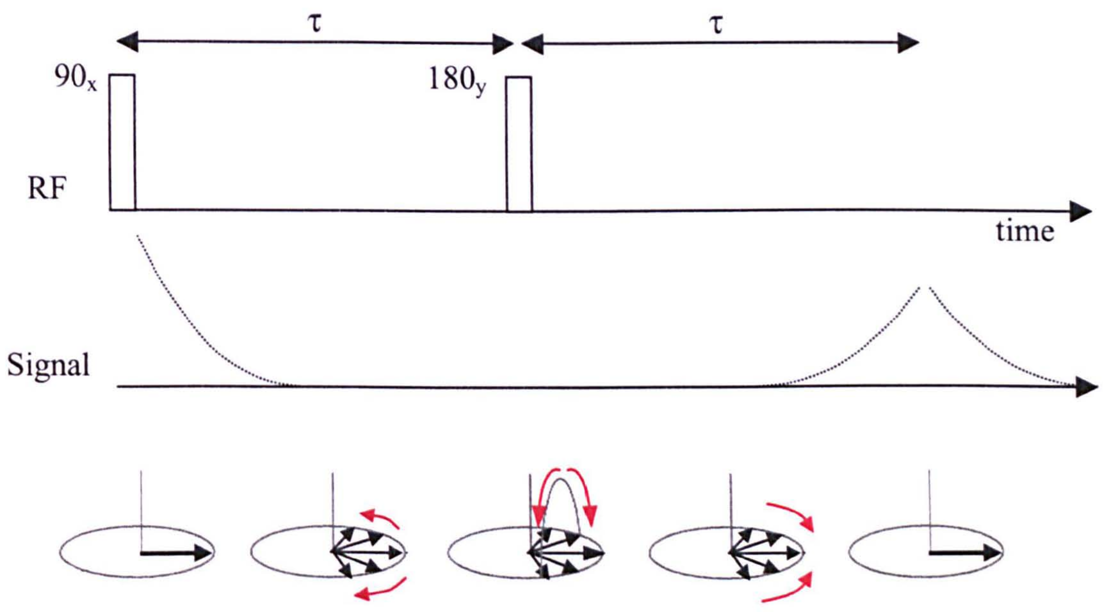

Figure 2.6 The spin-echo experiment.

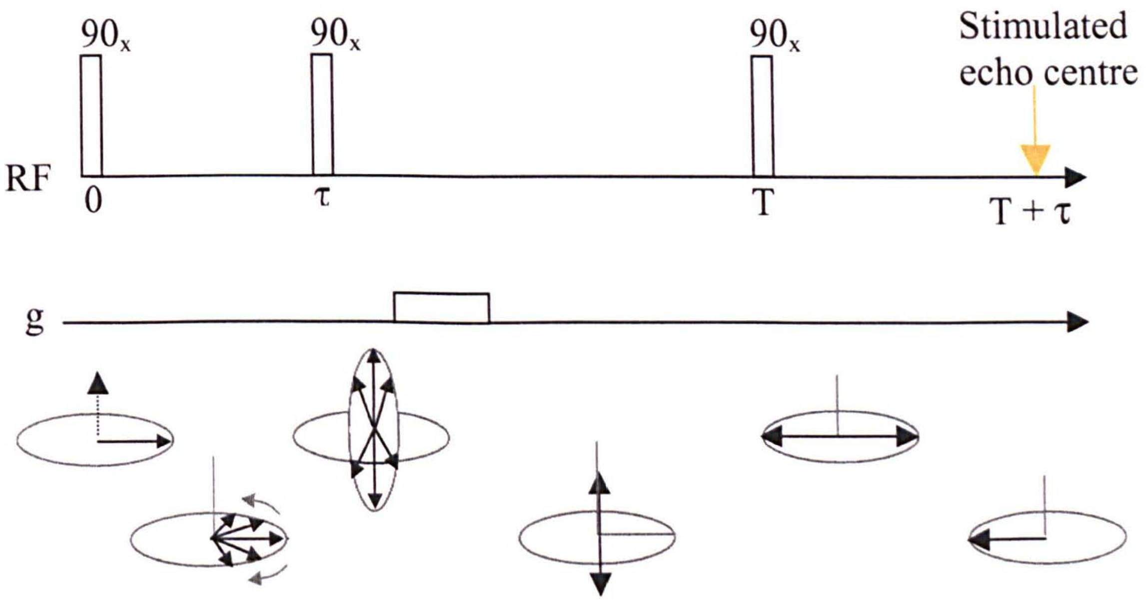

Figure 2.7 Stimulated echo pulse sequence using a homospoil pulse during the 'z-storage' period.

2.4 Nuclear Spin Interactions

The interaction of nuclear spins with externally applied magnetic fields have already been discussed. An important feature of nuclear magnetic resonance is that many other, often much weaker, internal interactions produce effects on the observed properties of the nuclear magnetisation. This means that very fine features in the Hamiltonian may be detected, and these contain valuable information regarding the dynamics and structure of the sample. The Hamiltonian H for the interactions of nuclear spins can be expressed as the combination of the more common couplings:

$$H = H_z + H_{RF} + H_{DD} + H_J + H_{CSA} + H_Q + H_{SR} \tag{2.22}$$

where:

H_z	Zeeman term. The interaction of nuclear spins with the external static field, B_0, including spatial gradients of the field.
H_{RF}	The interaction of nuclear spins with externally applied RF fields, $B_1(\omega)$.
H_{DD}	Dipole-Dipole term. Interaction of nuclear spins via direct, through-space, interaction of the nuclear magnetic dipole moments.
H_J	J coupling term. Indirect interaction of nuclear spins via coupling through molecular electronic structure.
H_{CSA}	Chemical shift anisotropy term. Modification of Zeeman coupling arising from the shielding effect of the electronic/molecular structure.
H_Q	Quadrupolar coupling term. Interaction of quadrupolar nuclei ($I > \frac{1}{2}$) with local electric field gradients, arising from the electronic distribution
H_{SR}	Spin-Rotation interaction. Coupling between nuclear and molecular angular momentum.

2.4.1 Dipole-Dipole Interaction

The intrinsic magnetic moment of a nucleus exerts a significant influence on its neighbours. The local dipolar field of each nuclei, is experienced by all other nuclei via a direct through space interaction. The interaction between two magnetic dipoles, separated by **r**, can be expressed by the Hamiltonian:

$$H_{DD} = \gamma^2 \hbar^2 \frac{\mu_0}{4\pi} \left\{ \frac{\hat{\mathbf{I}}_1 . \hat{\mathbf{I}}_2}{r^3} - 3\frac{(\hat{\mathbf{I}}_1 . \mathbf{r})(\hat{\mathbf{I}}_2 . \mathbf{r})}{r^5} \right\} \tag{2.23}$$

By expanding the scalar products, converting to spherical polar coordinates and expressing in terms of the raising and lowering operators, the hamiltonian becomes:

$$H_{DD} = r^{-3}\gamma^2\hbar^2 \frac{\mu_0}{4\pi}\{A+B+C+D+E+F\} \tag{2.24}$$

where:

$$\begin{aligned}
A &= \hat{I}_{1z}\hat{I}_{2z}(3\cos^2\theta-1)\\
B &= \frac{1}{4}\left[\hat{I}_{1+}\hat{I}_{2-}+\hat{I}_{1-}\hat{I}_{2+}\right](3\cos^2\theta-1)\\
C &= -\frac{3}{2}\left[\hat{I}_{1z}\hat{I}_{2+}+\hat{I}_{1+}\hat{I}_{2z}\right]\sin\theta\cos\theta\exp(-i\varphi)\\
D &= -\frac{3}{2}\left[\hat{I}_{1z}\hat{I}_{2-}+\hat{I}_{1-}\hat{I}_{2z}\right]\sin\theta\cos\theta\exp(i\varphi)\\
E &= -\frac{3}{4}\hat{I}_{1+}\hat{I}_{2+}\sin^2\theta\exp(-2i\varphi)\\
F &= -\frac{3}{4}\hat{I}_{1-}\hat{I}_{2-}\sin^2\theta\exp(2i\varphi)
\end{aligned} \tag{2.25}$$

The common factor is referred to as the dipolar coupling constant R:

$$R = r^{-3}\gamma^2\hbar^2\frac{\mu_0}{4\pi} \tag{2.26}$$

In liquids molecular motion causes (θ,ϕ,r), and hence H_{DD}, to fluctuate. In all but the most viscous or ordered liquids, isotropic molecular tumbling causes the averaging of the geometrical factor in equation 2.24, therefore the dipolar Hamiltonian is averaged to zero. In these circumstances it does not produce splitting in the NMR spectrum. It must be noted that this only holds true if there is no preferred orientation during molecular tumbling. This is not the case, for example, with liquid crystals.

The rapidly fluctuating non-secular (non-adiabatic) terms in H_{DD} can induce transitions between energy levels and hence contribute to both spin-lattice and transverse relaxation and this is discussed in section 2.5. Also, the secular (adiabatic) fluctuations contribute to the transverse relaxation.

2.4.2 Chemical Shift

The electrons present in a molecule are induced to circulate around the nuclei by the applied magnetic field. This induces a magnetic moment opposing the applied external field. The interaction of this field with the nuclear spins is called the chemical shift, as its presence shifts the resonance frequency of the nucleus. These interactions are characteristic of the local electronic environment of a nucleus. For this reason NMR spectroscopy has become an essential tool in structural organic chemistry, biochemistry, materials science and many other areas. The Hamiltonian associated with the chemical shift is:

$$H_{CS} = \gamma \hbar \hat{I} \cdot \sigma \cdot B_0 \tag{2.27}$$

Where σ is the chemical shielding tensor (a 3×3 matrix). In the case of the chemical shift, rapid isotropic tumbling as in normal solutions or liquids leaves a residual Hamiltonian:

$$H_{CS} = \gamma \hbar I_z \sigma_{iso} B_0 \tag{2.28}$$

Where σ_{iso} is the isotropic chemical shift. Chemical shifts are usually described in terms of a parts per million (ppm) scale, corresponding to the shift in hertz divided by the frequency of the spectrometer, relative to a standard reference molecule.

2.4.3 Scalar Coupling

The finest structural detail in the liquid state NMR Hamiltonian arises from the scalar spin-spin coupling. This is an indirect interaction between nuclei which arises through the mediation of electrons in the molecular orbitals. Therefore, it acts only through the medium of covalent bonds. This spin-spin interaction imparts a characteristic signature on high-resolution spectra, enabling detailed structural determination. The Hamiltonian of scalar spin-spin coupling takes the form:

$$H_J = \hbar J \hat{I}_1 \hat{I}_2 \tag{2.29}$$

2.5 Relaxation

After one or more pulses of RF radiation, the spin system will return to equilibrium. This process is called relaxation. Detailed discussions of relaxation mechanisms and their mathematical formulation may be found in a number of standard texts [1,2,5,6]. A general overview of relaxation processes is given below, with particular attention given to relaxation processes of fluids contained within porous solids.

2.5.1 Spin-Lattice Relaxation –T_1

The return of magnetisation in the direction of the static field B_0 towards its equilibrium value M_0, is known as longitudinal or spin-lattice relaxation. Spin-lattice relaxation describes the return of the system from a non-equilibrium population of energy states, to a Boltzmann distribution. As the name implies this process involves a radiationless exchange of energy between the spin system and the surrounding thermal reservoir known as the lattice, with which it is in contact. In the simplest case, the return of the bulk magnetisation to its equilibrium condition can be described by:

$$\frac{dM_Z}{dt} = \frac{M_Z - M_0}{T_1} \tag{2.30}$$

giving:

$$M_z(t) = M_z(0)\exp\left(-\frac{t}{T_1}\right) + M_0\left(1 - \exp\left(-\frac{t}{T_1}\right)\right) \tag{2.31}$$

where T_1 is the spin-lattice relaxation time. In more complex cases the relaxation maybe described by a sum of exponential terms.

2.5.2 Transverse Relaxation $-T_2$

Transverse relaxation describes the irreversible loss of phase coherence by the spin system and the return of the transverse magnetisation to its equilibrium condition, $M_x, M_y \rightarrow 0$. It is clear that the non-adiabatic process described for spin-lattice relaxation will also apply to transverse relaxation. There are additional adiabatic (secular) contributions to transverse relaxation. In the simplest case, the return to equilibrium of the transverse magnetisation can be described by:

$$\frac{dM_{x'}}{dt} = -\frac{M_{x'}}{T_2} \tag{2.32}$$

giving:

$$M_{x',y'}(t) = M_{x',y'}(0)\exp\left(-\frac{t}{T_2}\right) \tag{2.33}$$

The loss of phase coherence can be attributed to many possible mechanisms, for example inhomogeneities in the B_0 field. Observed decays of transverse magnetisation may be faster than that determined solely by T_2 relaxation. Spatial variations in the magnetic field B_0 and the presence of internal field gradients in heterogeneous samples, lead to differences in precessional frequencies, producing an additional loss of phase coherence. The timescale for this contribution is usually represented by T_2^* which is the relaxation time measured directly from the FID when $T_2^* \ll T_2$.

2.5.3 Measuring Nuclear Relaxation

Initially, Hahn [4] suggested using spin-echo measurements at increasing τ values to measure transverse relaxation. Inhomgeneities in the B_0 field cause Larmor frequencies to differ slightly over the sample. For precise refocusing of a spin echo the nuclei must each experience a constant magnetic field during the experiment. Diffusion causes nuclei to move and experience different parts of the inhomogeneous field. This results in reduced echo amplitudes and an under estimate of T_2.

Carr and Purcell drastically reduced the contribution to T_2 of diffusion through inhomogeneous B_0 fields by using a $90°_x$, τ, $180°_x$, 2τ, $180°_x$, 2τ, $180°_x$ ..... sequence. This produces a series of echoes at 2τ, 4τ, 6τ, 8τ .... the composite decay of the signal magnitude being given to calculate T_2.

In practice, the Carr-Purcell sequence usually results in T_2 values which are too short because of the cumulative error of each pulse not being exactly 180°. A modification of the Carr-Purcell sequence was proposed by Meiboom and Gill [7]. By applying the 180° pulses along the positive y' axis the error in the 180° pulse is cancelled with each cycle. This sequence is known as the Carr-Purcell-Meiboom-Gill (CPMG) sequence. This is illustrated schematically in figure 2.8.

Spin-lattice relaxation is most commonly measured using the inversion recovery method [8]. The pulse sequence and vector diagram for this experiment are shown in figure 2.9. The 180° pulse inverts the bulk magnetisation, which then begins to relax back towards its equilibrium value M_0. At a time τ after the 180° pulse, a 90° pulse is used to inspect the remaining longitudinal magnetisation. This is then recorded as $M_z(\tau)$. This is repeated for another value of τ after waiting a time τ_D. The time τ_D must be long enough compared with T_1 to allowed the magnetisation to return to its equilibrium value M_0, before another measurement is made. Usually $\tau_D = 5T_1$ is used.

2.5.4 Relaxation via Dipolar Interactions

Dipolar relaxation is the dominant relaxation mechanism for the ^1H spins in bulk liquid samples of small mobile molecules, such as those used in this thesis e.g. water at room temperature. The molecular motions of molecules, which contain nuclear magnetic moments, produce fluctuating local magnetic fields. These fluctuating local fields, **b**(t), may be characterised by a time correlation function, G(t):

$$G(t) = \langle \mathbf{b}(t) \cdot \mathbf{b}(t+\tau) \rangle \tag{2.34}$$

This function describes, on average, how the local field at time t correlates with the local field at a time τ later. For systems at equilibrium it is only a function of τ and it is assumed to be exponential:

$$G(\tau) = \langle \mathbf{b}(t) \cdot \mathbf{b}(t+\tau) \rangle_{eq} = \langle b^2 \rangle_{eq} \exp(-t / \tau_c) \tag{2.35}$$

where $\langle b^2 \rangle_{eq}$ is the mean squared value of the local field and τ_c is known as the correlation time of the fluctuating local field. The correlation time is the memory or persistence of the local field before it is changed substantially by molecular motion. The power of the fluctuating field is described by the spectral density function $J(\omega)$, which is given by the Fourier transformation of the correlation function $G(\tau)$:

$$\begin{aligned} J(\omega) &= \int G(\tau) \exp(-i\omega t)\, d\tau \\ G(\tau) &= \frac{1}{2\pi} \int J(\omega) \exp(i\omega t)\, d\omega \end{aligned} \tag{2.36}$$

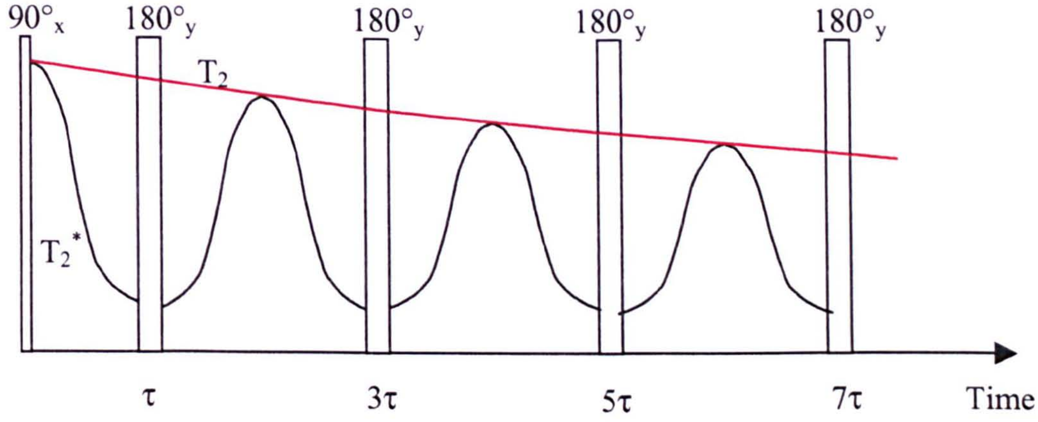

Figure 2.8 The Carr-Purcell-Meiboom-Gill (CPMG) sequence.The magnitude of the echoes produces a decay that is equivalent to T_2.

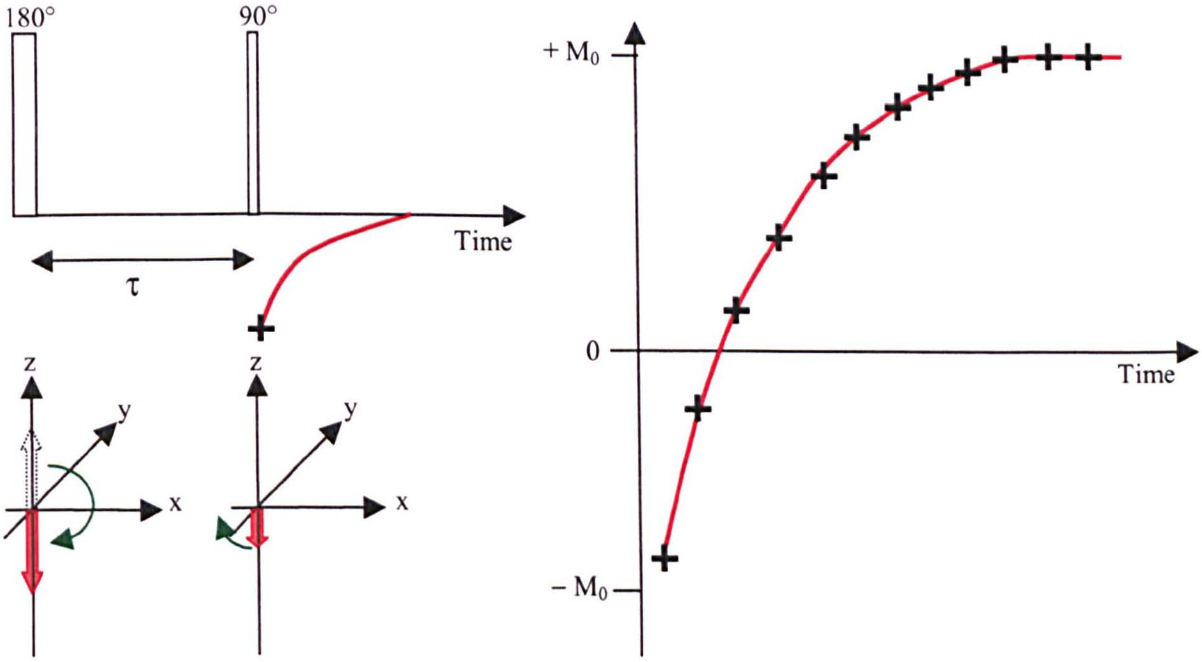

Figure 2.9 Inversion recovery sequence.

1. 180° pulse inverts the bulk magnetisation.
2. Magnetisation experiences spin-lattice relaxation during time τ.
3. 90° pulse rotates magnetization into xy plane, where the signal amplitude is measured.
4. During τ_D the magnetisation returns to equilibrium, ie $M_z = M_0$.
5. The measurement is repeated for another τ value.

The exponential form of G(τ) leads to J(ω) being Lorentzian:

$$J(\omega) = < b^2 >_{eq} \frac{2\tau_c}{(1+\omega^2\tau^2)} \tag{2.37}$$

Figure 2.10 contains typical spectral density functions for slow, intermediate and fast molecular motions, represented by large, intermediate and small values of τ_c respectively. The total dipolar coupling power available to produce relaxation is fixed i.e. the area under the different curves is constant (neglecting changes in spin-spin distances which would be produced by temperature or pressure changes). The frequency distribution depends upon the correlation time τ_c , this is illustrated in figure 2.10.

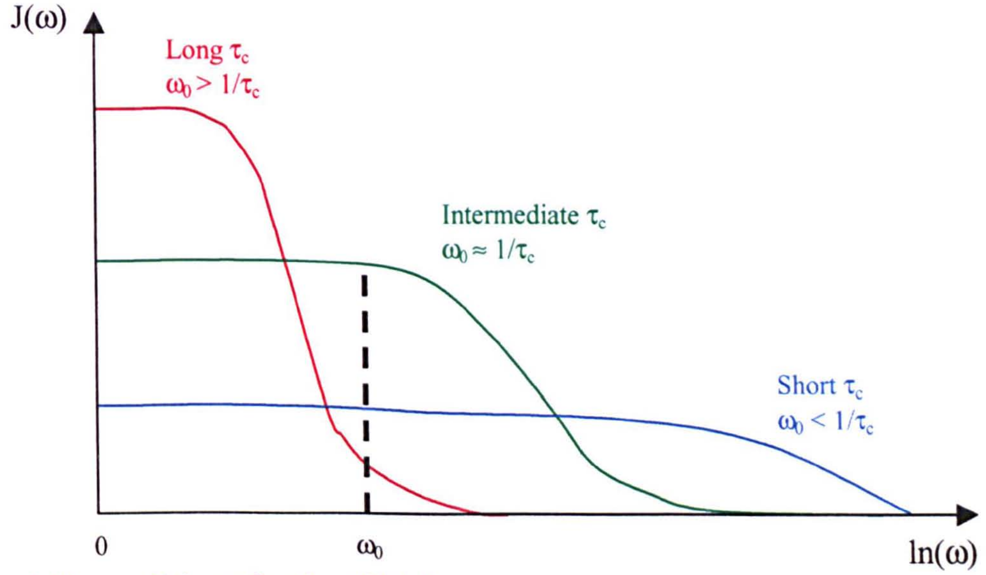

Figure 2.10 J(ω) as a function of ln(ω)

$J(\omega_0)$ is the power available from the fluctuating field at the Larmor frequency at a particular correlation time. This determines the rate of spin-lattice relaxation. The case when $\omega_0\tau_c \ll 1$ is known as the extreme narrowing condition and is valid for mobile liquids for which τ_c is of the order of picoseconds. The liquids used in this investigation all correspond to the extreme narrowing condition. Under these conditions equation 2.37 reduces to:

$$J(\omega) = < b >_{eq} 2\tau_c \tag{2.38}$$

and it can be shown that the rate of spin-lattice relaxation for this simple model is given by:

$$R_1 = \frac{1}{T_1} = \gamma^2 < b^2 >_{eq} 2\tau_c \tag{2.39}$$

This implies that in the extreme narrowing limit the rate of spin-lattice relaxation decreases as τ_c decreases (mobility increases) and that the spin-lattice relaxation rate is independent of the spectrometer frequency. Because the correlation time τ_c depends on molecular motion, then such parameters as viscosity, temperature, diffusion coefficient, size and structure will influence spin lattice relaxation.

The same factors affecting spin-lattice relaxation will also cause transverse relaxation. However, whereas the non-secular contributions require a fluctuating magnetic field, and thus depend on $J(\omega_0)$, the secular contributions involve no energy change, and are determined by $J(0)$. In the extreme narrowing limit it can be shown that spin-lattice and transvere relaxation are equal for an isotropic molecular system.

The concepts regarding relaxation given above were first proposed by Bloembergen, Purcell and Pound [9] and are commonly referred to as BPP theory. It should be noted that this theory is only valid in the 'weak collision limit', when $\tau_c < T_2$, which is true for mobile liquids.

2.6 Relaxation in Porous Solids

It has long been observed that the relaxation times of a fluid are reduced when the fluid is confined within a porous solid [10,11]. This behaviour is directly attributable to the structure of the porous solid and not any contamination of the saturating fluid by the solid.

In addition to dipolar relaxation a fluid contained in a porous solid will experience additional relaxation mechanisms. These include surface relaxation and diffusion through magnetic field gradients set up by susceptibility differences between the fluid and the solid matrix. Indeed, there has been considerable interest in extracting structural information from relaxation data. The petroleum industry is particularly interested in using relaxation measurements to estimate pore-size distributions, permeability, porosity etc of rock samples [12].

2.6.1 Surface Relaxation

Fluid molecules close to a solid/liquid interface may experience an enhanced relaxation rate. It has been suggested that physisorption and the presence of paramagnetic impurities, such as iron and manganese, in the porous solid [13] are possible mechanisms of enhanced surface relaxation. In many applications, knowledge of the specific nature of the enhanced interaction is not required. It is normally assumed that interactions are averaged over the whole surface of the porous solid and expressed as a mean surface relaxivity.

A simple physical model of surface relaxation called the "two-fraction fast exchange model" was proposed by Korringa [14]. This assumes that the fluid is present in two distinct phases within a pore: a bulk phase with relaxation characteristic of the bulk fluid; and a surface phase with a much faster relaxation. Assuming that diffusion is much faster than the surface relaxation, the observed relaxation is a single average value:

$$\frac{1}{T}=\frac{a}{T_{bulk}}+\frac{b}{T_{surface}} \tag{2.40}$$

where *a* and *b* are the proportions of fluid in each phase.

In 1979 Brownstein and Tarr [15] solved the relevant diffusion equations to accurately predict the relaxation behaviour of water in biological cells and estimate their size. In their model the initial magnetisation is considered uniform across the cell. The evolution of the system is then governed by enhanced relaxation at the cell's surface and by diffusion of the water. Solutions were obtained for planar, cylindrical and spherical geometries, the general solution being a multi-modal exponential decay. There are three qualitatively different regions of behaviour, determined by a dimensionless parameter $\rho l/D$, where l is the characteristic length scale of the structure, D is the bulk self-diffusion coefficient and ρ is the surface relaxivity.

- Fast Diffusion Regime ($\rho l/D < 1$). The time needed to diffuse a distance l is short compared with the inverse of the rate of relaxation at the surface. Therefore the lowest relaxation mode is completely dominant, ie a single exponential decay with relaxation rate $R_0 = (T_0)^{-1} \approx \rho(S/V)$, where S/V is the surface-to-volume ratio.

- Intermediate Regime ($1 < \rho l/D < 10$). In the intermediate regime the contribution of higher modes causes a significant deviation from single-exponential relaxation behaviour.

- Slow Diffusion Regime ($\rho l/D >> 10$). The time needed to diffuse a distance l is long compared with the inverse of the rate of relaxation at the surface. Consequently, there is significant multi-modal relaxation. Those spins which are close to the surface, give rise to short relaxation times and those spins located in the centre of pores give relaxation times approaching that of the bulk fluid. The limiting, slowest relaxing mode has a contribution determined by l^2/D, the time taken on average for spins to get to the surface.

2.6.2 Diffusion Through Magnetic Field Gradients

The influence upon spin echo amplitudes of diffusion through inhomogeneities in the applied field was apparent to Hahn in his original paper [4]. Carr and Purcell [16] calculated the effect of diffusion through a linear magnetic field gradient on the Carr Purcell sequence, which gives an additional term to the transverse relaxation equation:

$$M(t)=M(0)\exp\left(-\frac{t}{T_2}-\frac{2}{3}\gamma^2 g^2 D\tau^2 t\right) \tag{2.41}$$

where g is the linear magnetic field gradient, τ is the inter pulse spacing and D is the self diffusion coefficient of the fluid. For the Carr Purcell sequence the effect of diffusion through magnetic gradients can be minimized by using small τ values.

When a fluid-saturated porous solid is placed in a homogeneous magnetic field, susceptibility differences between the solid matrix and the saturating fluid, lead to substantial spatial variations in the internal magnetic field on the scale of the local pore space. These susceptibility-induced magnetic field gradients are called internal gradients. The diffusion of spins through internal gradients, causes the spins to experience a fluctuating magnetic field. This leads to enhanced transverse relaxation, as described in section 2.62. These fluctuations are of low frequency and hence have no effect on longitudinal relaxation, only upon transverse relaxation measurements.

The exact form of the internal gradients produced within individual pores by susceptibility differences, will have a complex dependence upon the size and geometry of the pores. The usual practice has been to approximate the internal gradients by a uniform field gradient. There is much evidence that this approach is not satisfactory in explaining the transverse relaxation data of rocks. Le Doussal and Sen [17] have proposed the use of a parabolic gradient as an improved approximation.

2.7 Measurement of Motion Using NMR

Apart from the usually indirect investigation of molecular motions via spin-relaxation behaviour, there have developed methods for characterising translational motion which are more direct. These are based on the use of spatial gradients in the B_0 field. The suggestion that nuclear magnetic resonance could be used to measure molecular motion in this way dates back to the beginning of research in this field. In 1950 Hahn [4] realised that magnetic field gradients impart a spatial signature to nuclear spins. In his original paper on spin echoes he pointed out that the echo amplitude would be influenced by molecular diffusion arising from Brownian motion through magnetic field inhomogeneities. In 1954 Carr and Purcell [16] derived an expression for the effect of diffusion on spin echo formation in the presence of a constant linear gradient, equation 2.41. Later work has concentrated on the use of time-dependent or pulsed gradients. The classic experiment used to measure molecular motion is the Pulsed Field Gradient Spin Echo (PGSE) technique.

2.7.1 Pulsed Field Gradient Spin Echo

In 1963 McCall et al [18] first proposed using the PGSE experiment to measure molecular motions. It was later demonstrated experimentally by Stejkal and Tanner [19]. The PGSE experiment comprises two essential elements for the measurement of molecular motion. Firstly, the use of pulsed magnetic field gradients to impose spatial labels on spins. Secondly, the use of spin echoes to measure phase shifts induced by the motion of spins in between gradient pulses. The theory outlined here is essentially that of Stejskal and Tanner but is formulated using the terminology of Caprihan and Fukushima [20] and Callaghan [3].

The simple PGSE sequence comprises a $90°_x{-}\tau{-}180°_y{-}\tau$ echo sequence with two identical field gradient pulses applied. This sequence is shown in figure 2.11. The field gradient pulses have a magnitude of $g=|\mathbf{g}|$, a duration δ and are separated by an observation time Δ. In the following analysis of the PGSE sequence two assumptions are made. The first assumption is that the two gradient pulses are of negligible duration (narrow pulse approximation). This implies that there is no motion of the spins along the gradient direction during the gradient pulses. Secondly, the effect of relaxation processes are neglected.

The $90°_x$ pulse tips the bulk magnetisation M_0 along the y`-axis, giving the spin system a phase coherence. The origin of time, $\Delta = 0$, is taken as the start of the first gradient pulse. The applied gradients are linear, ie $g_x = dB/dx$. In a linear gradient g_x the resonance frequency of the i^{th} spin depends upon its x position :

$$\omega_i(x) = \omega_0 + \gamma x_i g_x \tag{2.42}$$

The first field gradient pulse gives phase shifts to spins proportional to their initial position in the gradient, e.g. for the i^{th} spin with position $x_i(0)$ at $\Delta = 0$:

$$\phi_i(0) = \gamma\delta g_x\, x_i(0) \tag{2.43}$$

This produces a helical phase twist in the transverse magnetisation along the gradient axis, see figure 2.12. The second field gradient pulse together with the $180°_y$ pulse, imparts a phase shift to the spins proportional to their final position, but in the opposite sense, unwinding the helical phase twist. This gives resultant phases proportional to the displacement X_i of the i^{th} spin during the observation time Δ. The resultant phase shift of the i^{th} spin being:

$$\phi_i(\Delta) = \gamma\delta g_x\, [x_i(\Delta) - x_i(0)] = \gamma\delta g_x X_i(\Delta) \tag{2.44}$$

What is clear from equation 2.44 is that if all the spins have not changed their x coordinates in the time Δ, they all have no net phase shift, the coherence destroyed by the first gradient pulse is recovered by the second. In general, however, the molecules carrying the spins experience a distribution of displacements $P[X_i(\Delta)]$ during the observation time Δ, and hence experience a distribution of phase shifts $P[\phi(\Delta)]$. The contribution to the total NMR signal E of an individual spin is proportional to $\exp[i\phi(\Delta)]$. The total NMR signal is a superposition of the transverse magnetisations, an ensemble average, where the phase term $\exp[i\phi(\Delta)]$ is weighted by the probability of that phase shift $P[\phi(\Delta)]$:

$$E(g,\delta,\Delta) = \int P[\phi(\Delta)] \exp[i\phi(\Delta)]\, d\phi \tag{2.45}$$

This can be expressed in terms of the spin displacements:

$$E(g,\delta,\Delta) = \iint P(x_0) P(x_0 \mid x,\Delta) \exp(i\gamma\delta g[x(\Delta) - x_0])\, dx dx_0 \tag{2.46}$$

or more generally:

$$E(\mathbf{q},\Delta) = \iint P(\mathbf{r}_0) P_s(\mathbf{r}_0 \mid \mathbf{r},\Delta) \exp(i2\pi\mathbf{q}[\mathbf{r} - \mathbf{r}_0])\, d\mathbf{r} d\mathbf{r}_0 \tag{2.47}$$

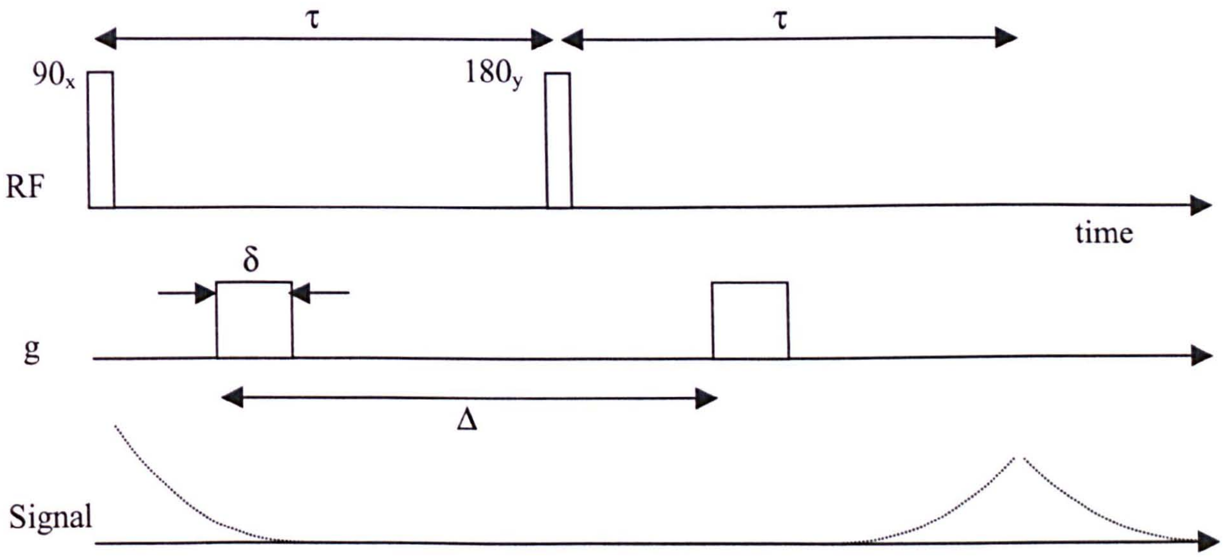

Figure 2.11 The Pulsed Field Gradient Spin Echo (PGSE) pulse sequence.

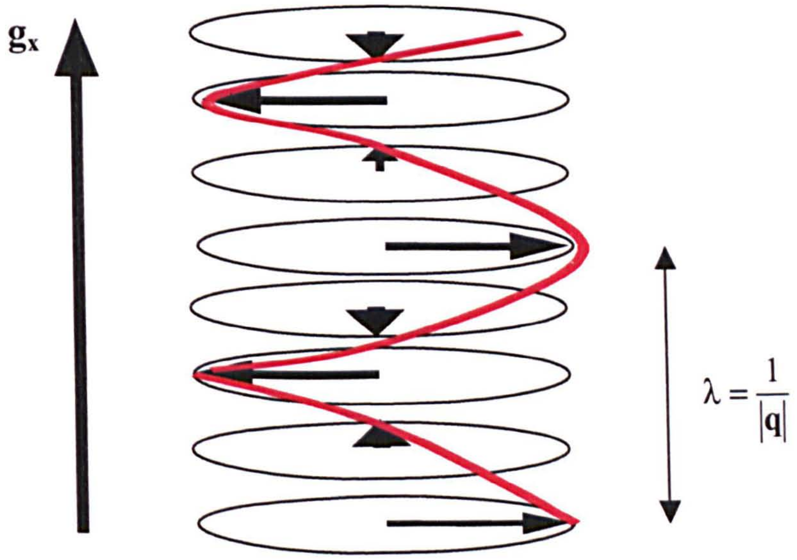

Figure 2.12 Diagram representing the helical phase twist given to the transverse magnetisation along the gradient direction. The wavelength of the helix is q^{-1}.

where $\mathbf{q}=(2\pi)^{-1}\gamma\delta\mathbf{g}$, $\mathbf{r}_0$ is the initial position and $\mathbf{r}$ is the position after a time Δ. $P(x_0|x,\Delta)$ and $P(\mathbf{r}_0|\mathbf{r},\Delta)$ are the conditional probabilities for displacements $(x-x_0)$ and $(\mathbf{r}-\mathbf{r}_0)$, respectively, in time Δ, and $P(\mathbf{r}_0)$ is the density function of initial positions. The echo attenuation function is labelled E instead of the conventional S because it is obtained by dividing the echo amplitude at $\mathbf{q}$ by the echo amplitude at $\mathbf{q}=0$.

Equation 2.47 may also be written in terms of what Kärger and Heink [21] called the 'average propagator', $\overline{P}_s(R,\Delta)$:

$$E(\mathbf{q},\Delta)=\int\overline{P}_s(\mathbf{R},\Delta)\exp(i2\pi\mathbf{q}\cdot\mathbf{R})\,d\mathbf{R} \tag{2.48}$$

where $\mathbf{R}=\mathbf{r}-\mathbf{r}_0$ and the average propagator is given by:

$$\overline{P}_s(\mathbf{R},\Delta)=\int\rho(\mathbf{r}_0)(P_s(\mathbf{r}_0\,|\,\mathbf{r},\Delta)\,d\mathbf{r}_0 \tag{2.49}$$

Equation 2.48 shows there is a simple Fourier relationship between the NMR signal and the displacement distribution. This expression is similar to the scattering function, which applies in neutron scattering where $\mathbf{q}$ is the scattering wave vector [3]. A visualization of q is given in figure 2.12.

The measurement of displacements by PGSE may often be limited by the loss of phase coherence due to transverse relaxation. To overcome this the pulsed field gradient stimulated echo (PGSTE) sequence was suggested by Tanner [22]. The stimulated echo allows longer observation times to be used in systems where the $T_1 >> T_2$. This condition is found most often in heterogeneous systems with structural features on the scale of typical diffusion lengths. The stimulated echo sequence, figure 2.7, stores the spatially encoded magnetisation along the z-axis, which can be recalled later. Over the storage period the spins experience T_1 relaxation rather than T_2 relaxation.

2.7.2 Unrestricted Self Diffusion

The random motion of molecules of the same species caused by thermal energy is called diffusion. From the classical description of diffusion [23], the distribution $\overline{P}_s(\mathbf{R},\Delta)$ is the solution of Fick's second law:

$$\frac{\partial\overline{P}_s}{\partial t}=D\nabla^2\overline{P}_s \tag{2.50}$$

where:

$$\nabla^2=\frac{\partial^2}{\partial x^2}+\frac{\partial^2}{\partial y^2}+\frac{\partial^2}{\partial z^2} \tag{2.51}$$

is the Laplace operator expressed in orthogonal Cartesian coordinates and D is the diffusion coefficient. For isotropic unrestricted diffusion D is constant. With the initial condition $\overline{P}_s(\mathbf{R},0) = \delta(\mathbf{R})$ and the boundary condition $\overline{P}_s(\mathbf{R},\Delta) \rightarrow 0$ for $\mathbf{R} \rightarrow \infty$, the solution of Equation 2.50 is the normalised Gaussian function:

$$\overline{P}_s(\mathbf{R},\Delta) = \frac{1}{(4\pi D\Delta)^{\varsigma/2}} \exp\left\{-\frac{\mathbf{R}^2}{4D\Delta}\right\} \qquad (2.52)$$

where $\zeta = 1,2,3$ is the dimensionality of the diffusion process. The average propagator of diffusion depends on the displacement of particles, but not the initial position of particles. This is because the statistics of Brownian motion are Markovian [3]. For diffusion in three dimensions the width of the displacement distribution is suitably characterised by its second moment, ie the mean squared displacement:

$$\left\langle \mathbf{R}^2(\Delta) \right\rangle = \int_{-\infty}^{\infty} \mathbf{R}^2 \overline{P}_s(\mathbf{R},\Delta) d\mathbf{R} = 6Dt \qquad (2.53)$$

If the direction of the applied gradient g is along the x-axis , the displacement distribution is one dimensional and given by:

$$\overline{P}_s(X,\Delta) = \frac{1}{(4\pi D\Delta)^{\varsigma/2}} \exp\left\{-\frac{X^2}{4D\Delta}\right\} \qquad (2.54)$$

The mean squared displacement for such a one-dimensional displacement distribution is 2Dt.

$E_\Delta(q)$ is particularly simple to evaluate for the case of self-diffusion. Substituting equation 2.54 into the expression of the echo attenuation function in equation 2.48 gives:

$$E_\Delta(q_x) = \int_{-\infty}^{+\infty} (4\pi D\Delta)^{-1/2} \exp(-X^2/4D\Delta) \exp(i2\pi q_x X)\, dX \qquad (2.55)$$

The Fourier transform of a Gaussian function is simply another Gaussian, and is given by:

$$E_\Delta(q_x) = \exp\left(-4\pi^2 q_x^2 D\Delta\right) = \exp\left(-2\pi^2 q_x^2 \overline{X^2}\right) \qquad (2.56)$$

where $\overline{Z^2} = \langle Z^2 \rangle = 2D\Delta$ is the one-dimensional mean squared displacement. Equation 2.56 is derived assuming that there are no movements during the gradient pulse duration δ. If this is not the case, i.e. δ is finite, a general treatment by Stejskal and Tanner [19] shows the exact result is:

$$E_\Delta(q_x) = \exp\left(-4\pi^2 q_x^2 D(\Delta - \delta/3)\right) \qquad (2.57)$$

2.7.3 Hindered Diffusion

In the case of free self-diffusion {see section 2.72} the average propagator is Gaussian, equation 2.54, and the mean squared displacement increases linearly with observation time. Hindered diffusion is taken as describing any situation in which the average propagator evolves in a non-Gaussian fashion but the mean squared displacements are not bounded. There are many examples of hindered diffusion [3], the most important in the context of this thesis, is the diffusion of fluids contained in porous solids.

In this section two examples for hindered diffusion are going to be considered. The first example is the diffusion of a fluid within a thin planar layer. When the thickness of the layer is small compared to the rms displacement of the diffusing molecules, the diffusion can be considered as quasi two-dimensional. The second example is the diffusion of a fluid contained within a fine capillary. When the diameter of the capillary is small compared to the rms displacement of the diffusing molecules, the diffusion can be considered as quasi one-dimensional. The echo attenuation of the PGSE sequence produced by such quasi one and two-dimensional diffusion processes is going to be derived as proposed by Callaghan et al [3].

For diffusion which is anisotropic, the diffusion equation takes the form:

$$\frac{\partial \overline{P}_s}{\partial t} = \nabla \cdot \mathbf{D} \cdot \nabla \overline{P}_s \qquad (2.58)$$

where **D** is now the Diffusion Cartesian tensor, $D_{\alpha\beta}$, where α and β may take any of the Cartesian directions x,y,z. Structures of certain symmetry can be represented by a diagonal Diffusion tensor where only the diagonal elements D_{xx}, D_{yy} and D_{zz} are non-zero. For cylindrical symmetry, in the reference frame (x′,y′,z′) with axis of symmetry along z′, then the diagonal terms of the Diffusion tensor are $D_{x'x'} = D_{y'y'} = D_{\perp}$ and $D_{//} = D_{z'z'}$, where $D_{//}$ and $D_{\perp}$ are the diffusion coefficients for diffusion parallel and perpendicular to the axis of the cylinder.

The echo attenuation of the PGSE sequence is given by equation 2.56, and depends only on the mean squared displacement along the gradient axis. If the gradient axis is taken as the laboratory z-axis, and the axis of cylindrical symmetry is aligned along the z′, at an angle θ to the laboratory z-axis, then the mean squared displacement of particles along the z-axis is given by:

$$\begin{aligned} \overline{Z^2} &= \overline{Z'^2}\cos^2\theta + \overline{X'^2}\sin^2\theta \\ \overline{Z^2} &= 2D_{//}\Delta\cos^2\theta + 2D_{\perp}\Delta\sin^2\theta \end{aligned} \qquad (2.59)$$

Therefore, from equation 2.56 the echo attenuation for a system of cylindrical symmetry is given by:

$$E_{\Delta}(q) = \exp\left(-4\pi^2 q^2 \Delta \left(D_{//}\cos^2\theta + D_{\perp}\sin^2\theta\right)\right) \tag{2.60}$$

For a randomly orientated array of elements each with an axis of cylindrical symmetry, $E_{\Delta}(q)$ is obtained by averaging over all angles of θ, each orientation weighted by the sphere area element sinθ dθ, giving:

$$E_{\Delta}(q) = \exp\left(-4\pi^2 q^2 \Delta D_{\perp}\right)\int_0^1 \exp\left(-4\pi^2 q^2 \Delta [D_{//} - D_{\perp}]x^2\right)dx \tag{2.61}$$

For diffusion confined within an isotropic array of narrow capillaries, i.e. quasi one-dimensional diffusion, then $D_{//} >> D_{\perp}$ and equation 2.61 reduces to:

$$E_{1D} = \int_0^1 \exp\left(-4\pi^2 q^2 \Delta D_{//} x^2\right)dx \tag{2.62}$$

For diffusion in a randomly orientated array of thin layers, i.e quasi two-dimensional diffusion, then $D_{//} << D_{\perp}$ and equation 2.61 reduces to:

$$E_{2D} = \exp\left(-4\pi^2 q^2 \Delta D_{\perp}\right)\int_0^1 \exp\left(4\pi^2 q^2 \Delta D_{\perp} x^2\right)dx \tag{2.63}$$

For the case of isotropic diffusion, i.e. three-dimensional diffusion, then $D_{//}$ and $D_{\perp}$ are equal and equation 2.61 reduces to the familiar Stejskal Tanner equation, equation 2.57. The echo attenuation functions for one and two-dimensional diffusion are compared with isotropic three-dimensional diffusion in figure 2.13.

2.7.4 Restricted Diffusion

Restricted diffusion describes molecular translational displacements that are constrained by impermeable barriers to remain trapped within a finite region of space. For restricted diffusion the echo attenuation of the PGSE sequence depends on the observation time Δ.

For PGSE pulse spacing $\Delta << L^2/D$, where L is a characteristic length scale, the echo attenuation will be characteristic of unrestricted isotropic diffusion, except for a small fraction of molecules in close proximity to the wall.

For $\Delta >> L^2/D$ all molecules, irrespective of starting position, maybe found with equal probability anywhere within the region of space. This is called the long-time limit. In this limit the probability $P_s(\mathbf{r}_0 | \mathbf{r},\infty)$ in equation 2.49 simply becomes the molecular density $\rho(\mathbf{r})$. Therefore, from equation the average propagator is given by:

$$\overline{P}_s(\mathbf{R},\infty) = \int \rho(\mathbf{r}_0)\rho(\mathbf{r}_0 + \mathbf{R})\, d\mathbf{r}_0 \tag{2.64}$$

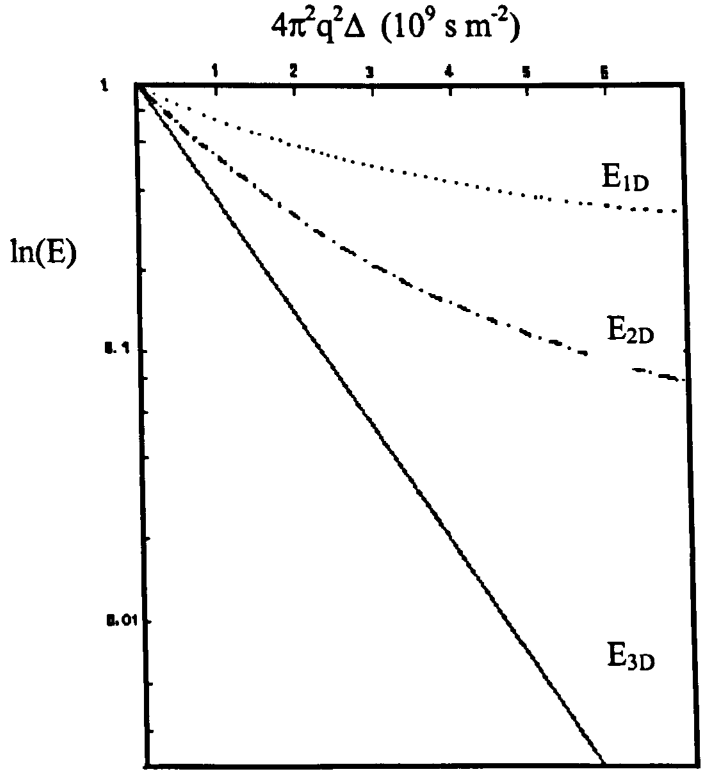

Figure 2.13 Theoretical echo attenuations for one, two and three-dimensional diffusion in a randomly oriented array of elements.

Equation 2.64 states that in the long time limit for restricted diffusion the average propagator $\overline{P}_s(\mathbf{R},\infty)$ is the autocorrelation function of the molecular density $\rho(\mathbf{r}_0)$. This implies, by the Wiener-Kintchine theorem [24], that E(**q**,∞) will be the power spectrum of $\rho(\mathbf{r}_0)$. This can be shown by utilizing equation 2.48, giving:

$$\begin{aligned} E(\mathbf{q},\Delta) &= \iint \rho(\mathbf{r}_0)\rho(\mathbf{r})\exp(i2\pi\mathbf{q}[\mathbf{r}-\mathbf{r}_0])\,d\mathbf{r}d\mathbf{r}_0 \\ &= |S(\mathbf{q})|^2 \end{aligned} \tag{2.65}$$

Where S(**q**) is the Fourier spectrum of ρ(**r**), namely:

$$S(\mathbf{q}) = \int \rho(\mathbf{r})\,\exp(i2\pi\mathbf{q}\cdot\mathbf{r})\,dr \tag{2.66}$$

It is interesting to note that the spatial spectrum S(**q**) is analogous to the quantity measured in conventional NMR imaging.

2.7.5 Flow

The flow of a fluid can be described as laminar or turbulent. Laminar flow can be characterised by a constant flow field, whereas in the case of turbulent flow, the flow field changes randomly with time. Here only laminar flow will be considered.

The general principles governing the PGSE NMR response to flow are the same as those discussed in the previous section for diffusion. The response is particularly simple in the case of 'plug flow', in which all the spins move at the same time-independent velocity v. After an observation time Δ all the spins have experienced the same phase shift $\phi(\Delta) = \gamma\delta g_x \Delta \cdot$ v. The echo attenuation function in the narrow pulse approximation is simply:

$$E(q_x) = \exp(i\gamma\delta g_x \Delta \cdot v) = \exp(i2\pi q_x \Delta \cdot v) \tag{2.67}$$

For the case of diffusion superimposed on 'plug flow' the three-dimensional convection-diffusion equation is given by:

$$\frac{\partial \bar{P}_s}{\partial t} = D\nabla^2 \bar{P}_s + \nabla \cdot v\bar{P}_s \tag{2.68}$$

where v is the constant velocity and D is the diffusion coefficient. If the flow direction is parallel to the gradient direction g_x, then the solution of equation 2.68 is:

$$\bar{P}_s(X,t) = (4\pi Dt)^{-\frac{1}{2}} \exp\left[-(X - vt)^2 / 4Dt\right] \tag{2.69}$$

It can be seen from equation 2.69, for the case of diffusion superimposed on 'plug flow' the average propagator is the convolution of the diffusion Gaussian with the delta function $\delta(X - vt)$. Therefore, the echo attenuation function $E_\Delta(q)$, which is the Fourier transform of equation 2.69, is the product of the Fourier transform of the Gaussian and the Fourier transform of the delta function:

$$E(q_x) = \exp(-4\pi^2 q_x^2 D\Delta + i2\pi q_x \Delta \cdot v) \tag{2.70}$$

where the generic time t has been substituted with the experimental observation time Δ.

2.8 Pulsed NMR Instrumentation

In this section an elementary description of the workings of a modern NMR spectrometer is given, with particular reference made to the GE Omega CSI spectrometer used in this study. The basic NMR instrumentation consists of a strong magnetic field, a means of applying RF and field gradient pulses and a method for detecting and recording the RF signal. These functions are all computor controlled. A block diagram illustrating the essential features of a modern NMR spectrometer is shown in figure 2.14.

2.8.1 Static Magnetic Field

Virtually all modern high resolution spectrometers use superconducting magnets. Superconducting magnets provide high magnetic fields (up to ≈ 19T) that are stable and homogeneous. The homogeneity of the field over a large sample volume can be improved by use of correction (shim) coils {see section 2.8.8}. The GE Omega is based around an Oxford instruments 31cm horizontal cylindrical bore, 2T superconducting magnet.

In some situations superconducting magnets are not appropriate. For example, strong electromagnets are very convenient for variable field experiments. In low-field analytical spectrometers it is common to use low cost permanent magnets. Permanent magnets are also employed in NMR well-logging tools {see section 4.2.4} because of size and weight considerations.

2.8.2 Pulse Programmer

Outputs from the pulse programmer are used to 'gate' the signal from the frequency synthesizer, to produce a pulse of the correct phase and length. The modulator unit can, if necessary, generate more complicated waveforms. The pulse programmer needs a stable time base for the accurate timing of multiple pulse experiments.

2.8.3 Transmitter Amplifier

The transmitter amplifier amplifies pulses before they are sent to the probe. The transmitter amplifier within the GEΩ-CSI spectrometer gives a maximum RF power output of 1.3 KW.

2.8.4 Probe

The probe contains an RF coil and is positioned in the centre of the magnet. It generates the RF pulses and acts as the receiver for the NMR signal. The probe is exposed to several kV's during a pulse, it is then required to measure a signal of a few μV. The geometry of the RF transmitter/receiver coil depends on the geometry of the magnet. For superconducting magnets easy entry of the sample down the main field axis, requires that the RF coil has either a Helmhotz saddle or bird-cage design.

To protect the sensitive receiver from high voltages and to reduce the dead-time, crossed diodes are used. These diodes have negligible resistance at high voltages and high resistance at low voltages. A pair of crossed diodes is placed before the probe to prevent leakage from the transmitter. A second pair is placed on an earth loop between the probe and the pre-amplifier. When a pulse is applied this has low resistance and protects the receiver from high voltages. In the absence of a pulse it has high resistance and the weak signal is routed to the receiver. After the application of a RF pulse the receiver becomes saturated as a result of the diodes letting through a small voltage. The time needed for the receiver to recover is called the dead-time.

Two probes were used in this thesis to produce the transverse RF field within the cylindrical volume of the superconducting magnet. The first is a 32 element 'bird cage' coil [25] designed and constructed by GE, which produces a cylindrical homogeneous region of diameter 100mm and length 150mm. At maximum power of B_1, this RF coil produces a 90° pulse length of 67µs. The second coil is also a bird cage design with a cylindrical homogeneous region of diameter 26mm and length 26mm. At maximum power of B_1, this RF coil produces a 90° pulse length of 37µs.

2.8.5 Pre-amplifier and Phase Sensitive Detector

A low noise, high gain amplifier, known as the pre-amplifier, is used to initially amplify the small NMR signal. Because of the weak signal this is placed as close to the probe as possible to reduce loss of signal and thermal noise. At this stage the signal is around the Larmor frequency, which for this spectrometer is 85Mhz. This high frequency is difficult to handle, therefore the signal is mixed with the reference output from the Frequency Synthesiser, a process known as heterodyning. This process is inherently phase sensitive. By separately mixing the NMR RF signal with two heterodyne references, 90° out of phase, separate in-phase (real) and quadrature (imaginary) phase output signals are obtained, in effect detecting M_x M_y in the frame of reference rotating at the heterodyne reference frequency. This process called quadrature detection and as already indicated, is tantamount to observing the NMR signal in the rotating reference frame.

2.8.6 Filters

Following detection, the NMR signal is audiofrequency in character. In order to remove noise from the signal, which has a frequency either above or below the range of interest, the signal is passed through a series of audio filters, the bandwidth of which is selectable.

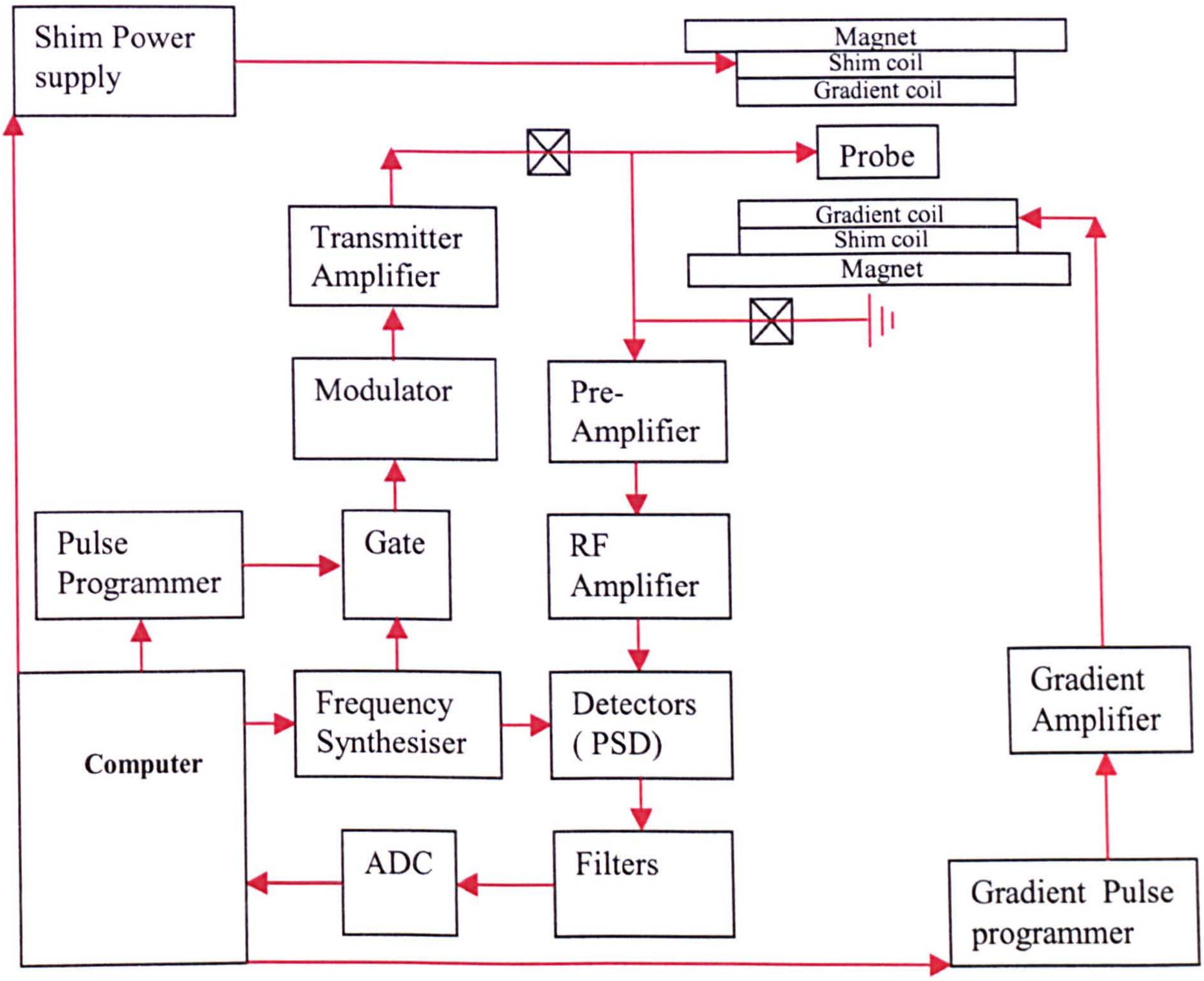

Figure 2.14 Schematic of Modern NMR spectrometer

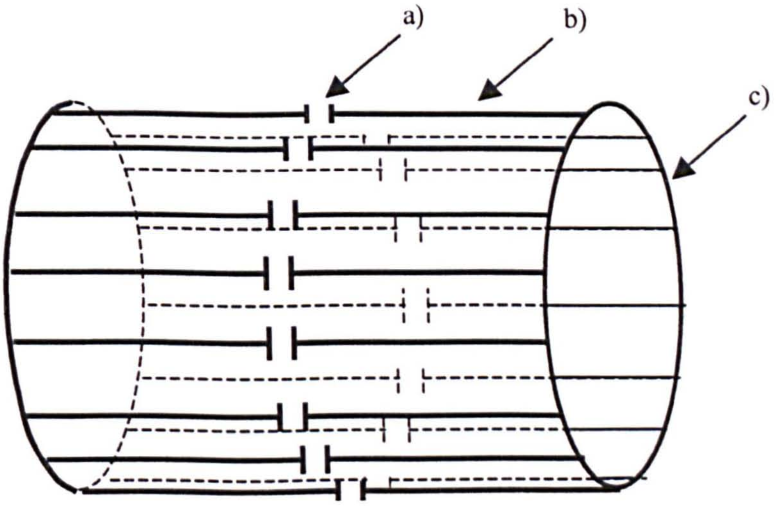

Figure 2.15 Schematic diagram of 'bird cage' RF coil design (Low Pass version). a) Capacitor. b) Straight segment. c) Circular end ring.

2.8.7 Analogue to Digital Converter

In order to be able to perform signal averaging or data processing, it is necessary to digitise the NMR signal. In liquid state the resonance lines are narrow due to motional narrowing, corresponding to a long-lived FID. Hence, digitiser speed is not as important as it is in solid state NMR. The GE Omega can record signals with a 200KHz sweep width from two channels (real and imaginary) with 32-bit precision.

2.8.8 Shim Coils

All superconducting magnets possess inhomogeneities in their magnetic field. These intrinsic inhomogeneities are further degraded by the magnetic susceptibilities of the probe, the sample container and the sample itself. The homogeneity of the B_0 field over the sample volume can be improved by the use of correction (shim) coils [26]. The GE Omega has a 15-term set of room temperature shim coils. Shimming is performed by monitoring the FID, while manually adjusting the current through each shim coil. A long and exponential FID indicates good homogeneity in the B_0 field over the sample volume.

2.8.9 Gradient Coils

NMR imaging and PGSE experiments require pulses of magnetic field gradient to spatially encode the position and displacement of spins. The gradient pulse programmer sets the shape and the amplitude of the gradient pulses. The high power gradient amplifies increase the power of the gradient pulses to a level sufficient to drive the gradient coils.

The GE-Omega spectrometer has an interchangeable gradient system, two sets of gradient coils are used in this thesis. The first set is an Acustar S150 with active shielding and a 150mm bore. The gradient set is capable of delivering gradients of up to 0.2T/m in three orthogonal directions. The second set of gradient coils, is also actively shielded and can generate gradients up to 2.5T/m in three orthogonal directions. Both gradient and shim coils are water cooled, using a CFT re-circulating cooler.

The concept of actively shielding gradient coils was first suggested by Mansfield and Chapman [27] to overcome the problem of eddy currents. Rapidly changing magnetic fields arising from the gradient pulses can interact with the surrounding metal of a supercoducting magnet inducing eddy currents. The eddy currents have associated magnetic fields, which distort the gradient profile around the sample. Actively shielded gradient sets are designed to have zero field outside the coil boundaries. This is achieved by a second layer of current density outside the primary gradient coil, which nullifies the field produced by the primary coil outside the screen.

2.8.10 Signal-to-Noise

In section 2.2.3 the Curie law of temperature-dependent paramagnetism and the consequent low sensitivity of NMR were discussed. The e.m.f. induced by the transverse magnetisation in the receiver coils is of the order of microvolts. This weak NMR signal is superposed on experimental noise that arises from many sources e.g. thermal noise in RF receiver coil. The signal-to-noise ratio can be improved by working at lower temperatures, at higher magnetic fields or using larger numbers of spins in the sample. These options are not always experimentally practical. Another way of improving the signal-to-noise ratio is to co-add signals from N successive measurements. The genuine NMR signal adds coherently while the noise adds in random phase. As a result the signal-to-noise improves by a factor of $N_{½}$. However, the time between two successive measurements has to be sufficient to allow the spin system to return to equilibrium, this is generally taken as 5 T_1.

2.8.11 Phase Cycling

The phase of the signal following a 90° RF pulse depends on the phase of the pulse. For example incrementing the RF phase by 180° will invert the signal. Thus a successive phase alternation of the pulse in 180° steps, linked to successive addition and subtraction of the signal, leads to a coherent superposition of the signal and cancellation of noise. The process of addition and subtraction can be substituted by an alternation of the receiver phase by 180°. The phase cycle can be written as (0°,0°)–(180°,180°), where RF receiver and transmitter phases are given inside the brackets. This is called coherent noise cancellation and is the simplest form of phase cycling.

Anomalies in the phase and amplitude of quadrature detection, can be corrected to the first order, by swapping the channels used to acquire the in-phase (real) and quadrature-phase (imaginary) signal. This is equivalent to successively incrementing the transmitter and receiver phase by 90°, i.e. (0°,0°)–(90°,90°)–(180°,180°)–(270°-270°). This is called the CYCLOPS sequence [28] and is generally incorporated as a sub-cycle in most phase cycles.

2.9 References

1. Abragam A. "The Principle of Nuclear Magnetism". 1961. Oxford University Press.
2. Slichter C.P. "Principles of Magnetic Resonance". 1963. Harper and Row. New York.
3. Callaghan P.T. "Principles of Nuclear Magnetic Resonance". 1991. Oxford University Press.
4. Hahn E.L. "Spin Echoes". 1954. Physical Review. 15. 580-594
5. Farach A., Poole P. "Relaxation in Magnetic Resonance". 1971. Academic Press. London.
6. Cowan B. "Nuclear Magnetic Resonance and Relaxation". 1997.Cambridge University Press. Cambridge.
7. Meiboom S., Gill D. 1558. Rev. Sci. Inst. 29. 688.
8. Vold R.L., Waugh J.S., Klein M.P., Phelps D.E. Journal of Chemical Physics. 1968. 48. 383.
9. Bloemberger N., Purcell E.M., Pound R.V. 1948. Physical Review. 73. 639.
10. Bloch F. 1951. Physical Review .83. 1062.
11. Brown R.J.S, Fatt I. "Measurements of Fractional Wettability of Oilfield Rocks by the Nuclear Magnetic Relaxation Method". 1956. AIME. 207. 262-264.
12. Kleinberg R.L. "Well Logging". Encyclopaedia of NMR.
13. Foley I., Farqooqui S.A., Kleinburg R.L. "Effect of Paramagnetic ions on the NMR Relaxation of Fluids at the Solid Surface". 1996. Journal of magnetic Resonance. 123. 95-104.
14. Korringa J., Seevers D.O., Torrey H.C. "Theory of Spin Pumping and Relaxation in Systems with a Low Concentration of Electron Spin Resonance Centres". 1962. Physical Review. 127. 1143-1150.
15. Brownstein K.R., Tarr C.E. "Importance of Classical Diffusion in NMR Studies of Water in Biological Cells". 1978. Physical Review A. 19. 2446-2453.
16. Carr H.Y., Purcell E.M. "Effects of Diffusion on Free Precession in Nuclear Magnetic Resonance Experiments". 1954. Physical Review. 94. 630-638.
17. Le Doussal P., Sen P.N. "Decay of Nuclear Magnetization by Diffusion in a Parabolic Magnetic Field". 1992. Physical Review B.46. 3465-3485.
18. McCall D.W., Douglass D.C., Anderson E.W. 1963. Ber. Bunsenges. Physik. Chem. 67. 366.
19. Stejskal E.O., Tanner J.E. 1965. Journal of Chemical Physics. 42. 288.
20. Caprihan A., Fukushima E. "Flow Measurements by NMR". 1990. Physics Reports. 198. 195-235.
21. Karger J., Heink W. "The Propagator Representation of Molecular Transport in Microporous Crystallites". 1983. Journal of Magnetic Resonance.51. 1-7.
22. Tanner J.E. "Use of the Stimulated Echo in NMR Diffusion Studies". 1970. Journal of Chemical Physics. 52. 2523-2526.
23. Crank J. "Mathematics of Diffusion". 1956. Oxford University Press. Oxford.

24. Marshall A.G., Verdun F.R., "Fourier Transforms in NMR, Optical and Mass Spectrometry". 1990. Elsevier. New York.

25. Hayes C.E., Edelstein W.A., Schenck J.F., Mueller O.M., Eash M. "An Efficient, Highly Homogeneous Radio Frequency Coil for Whole-Body NMR Imaging at 1.5T". 1985. Journal of Magnetic Resonance. 63. 622-628.

26. Miner V.W., Conover W.W. "Shimming of Superconducting Magnets". Encyclopaedia of NMR.

27. Mansfield P., Chapman B. L. W. 1986. Journal of Magnetic Resonance. 66. 573.

28. Hoult D.I., Richards R.E. 1975. Proceedings of the Royal Society. A344, 311.

Chapter 3

Porous Solids

Contents

3.1 INTRODUCTION 45

3.2 MACROSCOPIC PARAMETERS 45

3.2.1 POROSITY 45
3.2.2 PERMEABILITY 46
3.2.3 SATURATION 47
3.2.4 SURFACE-TO-VOLUME RATIO 47
3.2.5 FORMATION RESISTIVITY FACTOR 48

3.3 MICROSCOPIC PARAMETERS 48

3.3.1 SURFACE TENSION 50
3.3.2 ADHESION AND COHESION 50
3.3.3 CAPILLARITY 51
3.3.4 CAPILLARY PRESSURE 52

3.4 WETTABILITY 52

3.4.1 WATER-WET 52
3.4.2 OIL-WET 52
3.4.3 FRACTIONAL WETTABILITY. 53
3.4.4 MIXED WETTABILITY 53

3.5 DISPLACEMENTS PROCESSES 53

3.5.1 DRAINAGE 53
3.5.2 IMBIBITION 54

3.6 MEASURING WETTABILITY 55

3.6.1 CONTACT ANGLE METHOD 55
3.6.2 THE AMOTT TEST 56
3.6.3 IMBIBITION METHOD 56

3.7 GEOLOGICAL POROUS SOLIDS 57

3.7.1 DENSE ROCKS 57
3.7.2 IGNEOUS ROCKS 58
3.7.3 NON-INDURATED SEDIMENTS 58
3.7.4 INDURATED SEDIMENTARY ROCKS 58
3.7.5 SHALES 58
3.7.6 SANDSTONES 58
3.7.7 CARBONATE ROCKS 59

3.8 REFERENCES 60

3.1 Introduction

Porous materials are ubiquitous in everyday life, indeed most solids are porous to varying degrees. A solid would generally be considered porous if

- The solid contains small void spaces (pores).
- The solid is permeable, i.e. it is possible to flow a fluid through the solid. This means the void spaces (pores) are connected.

A solid that merely contains void spaces would not be considered porous. A few common examples of porous solids would include wood, bricks, textiles, paper, soil, food products, rocks etc, etc, etc. It is therefore not surprising that the study of porous solids is of fundamental importance in several disciplines. For example food science, biological sciences, chemical engineering, hydrology and petroleum engineering. Each of these disciplines has its own literature and terminology. As mentioned earlier, the origins of this thesis lie in the petroleum industry, therefore the terminology used will be related to this.

3.2 Macroscopic Parameters

Macroscopic parameters represent the average behaviour of a sample. Therefore, the sample must contain a statistically significant number of pores. All macroscopic properties will be influenced to some degree by the pore structure. The most important macroscopic parameters, as regards the petroleum industry, are porosity, permeability, water saturation, surface-to-volume ratio and the formation resistivity factor.

3.2.1 Porosity

There are two definitions of porosity ϕ. First, the absolute porosity is defined as the fraction of the bulk volume of the sample that is void space. In metals the absolute porosity is close to zero, whereas thermal insulators often have a very high absolute porosity:

$$\phi_{abs} = \frac{V_{void}}{V_{bulk}} \tag{3.1}$$

where V_{void} and V_{bulk} are the volumes of the void space and bulk volume of the sample respectively. The void space inside a sample can be described as being interconnected or isolated. The isolated void space cannot contribute to fluid transport across the porous solid, hence is of little interest in the context of petroleum recovery. The term effective porosity has consequently been introduced. This describes the fraction of the bulk volume of the sample that is interconnected void space:

$$\phi_{eff} = \frac{V_{eff}}{V_{bulk}} \tag{3.2}$$

where V_{eff} is the volume of the interconnected space.

There are many experimental methods used to measure the porosity of a sample [1], the most common of which are described below.

- **Direct method.** The sample is compacted and the void volume destroyed. From the initial and final volumes, the void volume and hence the absolute porosity, can be determined.

- **Imbibition method.** The sample is immersed in a wetting fluid under vacuum. Given enough time the wetting phase imbibes into the sample. The initial and final weight of the sample, coupled with the density of the wetting fluid, allows the determination of the effective void volume and hence the effective porosity.

- **Mercury injection method.** The effective void volume is determined by the injection of mercury into the sample under high pressure. Comparison with the bulk volume of the sample gives the effective porosity.

- **Gas expansion method.** The basic principle is to determine the volume of air contained in the pore volume. To achieve this the sample is enclosed in a container of known volume and pressure and connected to a second evacuated chamber of known volume. When the connecting valve is opened, the ideal gas law can be used to derive the effective porosity.

The characteristics of the material dictate which is the most suitable method for porosity measurements. The Mercury injection method and gas expansion method are the petroleum industry standard.

3.2.2 Permeability

Experiments performed in 1856 by Henri Darcy found the relationship between the flow rate Q of a fluid through a porous solid and the pressure drop across it ΔP:

$$Q = K\frac{A\,\Delta P}{l} \tag{3.3}$$

Where l is the length and A the cross section area of the sample. The constant of proportionality K is the 'permeability constant' and depends upon the properties of the porous solid and the saturating fluid. It was later proposed by Nutting [2] that the effect of the fluid could be removed by defining the permeability constant K as:

$$K = \frac{k}{\mu} \tag{3.4}$$

Where μ is the fluid viscosity and k is the 'specific permeability' of the material. The standard version of Darcy's law is now:

$$Q = k\frac{A\Delta P}{\mu l} \tag{3.5}$$

A convenient unit of the specific permeability is the Darcy. A porous solid has a permeability of 1 Darcy if a pressure drop of 1atm, forces a fluid of viscosity 1cP, to flow at $1\text{cm}^3/\text{s}$, through a cube of material of dimensions 1cm x1cm x 1cm.

Laboratory measurements of permeability are normally performed on cylindrical core samples. Both liquids and gases have been used for these measurements, though both have their experimental difficulties. Indeed specific permeabilities can be anisotropic and show tensor properties. To give the reader a feel for the specific permeabilities found in reservoir rocks, below is listed a classification of permeability ranges given by Timmerman [3] for the ease of oil production from reservoir rocks.

Specific permeability (mD)	**classification**
1 -15	Poor to fair
15 – 50	Moderate
50 – 250	Good
250 – 1000	Very good
>1000	Excellent

3.2.3 Saturation

When a porous solid is saturated with more than one phase the saturation of each phase is defined as the fraction of the pore volume occupied by that phase. The NMR methods used to measure saturation in this thesis are outlined later. When a rock sample is saturated with two immiscible phases, i.e. an aqueous phase and an hydrocarbon phase, then the saturation state is expressed as the water or oil saturations S_w, S_o. This is the fraction of the pore volume occupied by the respective phase.

3.2.4 Surface-to-Volume Ratio

The specific surface-to-volume ratio is defined as the surface area of interconnected voids per unit volume of effective void space. The surface-to-volume ratio plays an important role in determining the effectiveness of catalysts, ion exchange columns and filters. It is also of central importance in the theory of NMR relaxation in porous solids, which is used to determine pore size distributions {see section 4.2}.

3.2.5 Formation Resistivity Factor

Electrical conductivity measurements of a porous solid saturated with an ionic solution can be made on porous solids of negligible electrical conductivity [1]. The Formation Resistivity factor F is defined as:

$$F = \frac{R}{R_0} \tag{3.6}$$

where R is the electrical resistivity of the saturated sample and R_0 is the electrical resistivity of the same volume of bulk ionic solution. The influence of the pore structure on electrical resistivity measurements can be divided into two contributions; the orientation and topography of the conducting pores and the reduction of the cross area available for conduction.

3.3 Microscopic Parameters

The study of microscopic pore structure is extremely difficult because of the irregularity in pore geometries and sizes. This is strikingly apparent from figure 3.1 and serves to underline the great difficulties involved in quantification. A widely used description of a porous solid is the pore size distribution. Many methods for measuring pore size distributions have been suggested [1].

The pore structure of a porous solid can be viewed using optical or electron microscopes. By taking thin sections of a porous solid and making some assumptions a three-dimensional reconstructions of the pore structure can be made. This is called Stereology [4]. Such three-dimensional reconstruction can then be used in computer simulations of flow and diffusion [5,6].

Complex pore structures can be abstractly represented in terms of geometrically shaped pores (spherical, rectangular and cylindrical pores) with a distribution of pore sizes. Narrower pore throats then connect these pores. The number of connections of each pores being determined by a distribution of co-ordination numbers. Many computer models of porous solids use this approach [7].

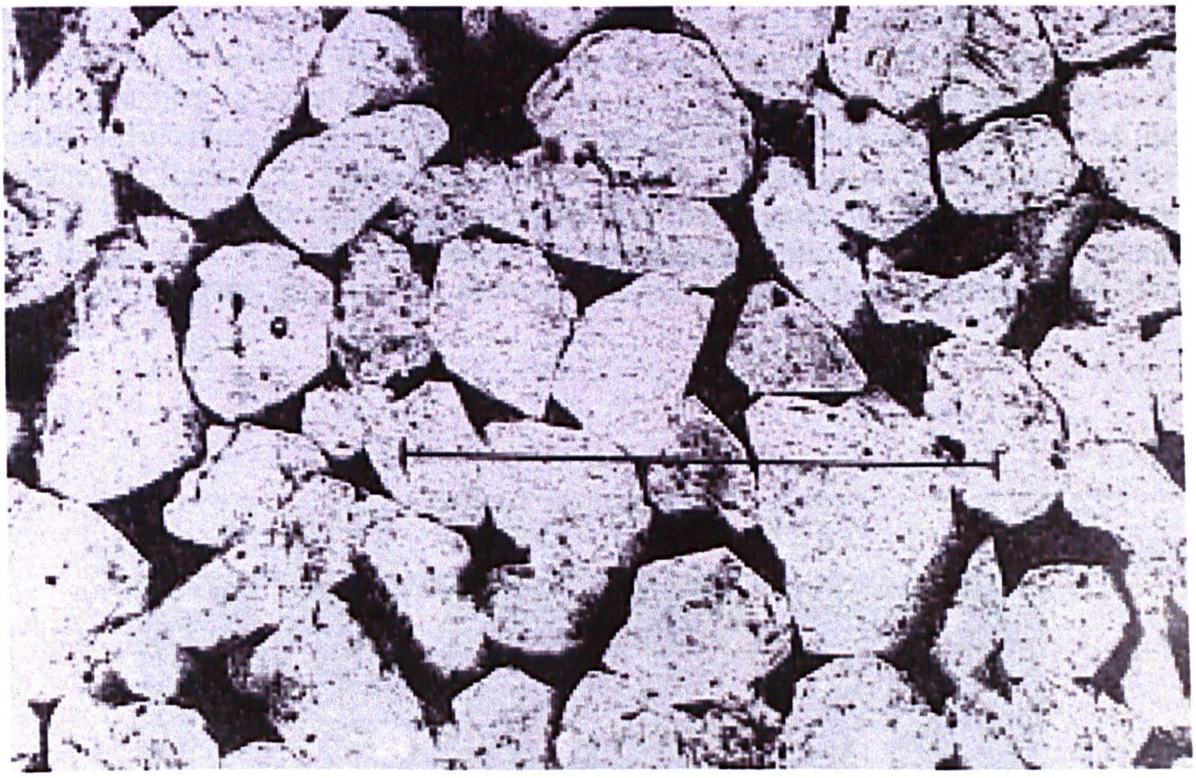

Figure 3.1 Optical micrograph of thin section of Fontainebleau Sandstone, porosity 25%. The bar scale is 500μm.

3.3.1 Surface Tension

Short range intermolecular forces, called Van der Waals forces, are responsible for the existence of the liquid state [8]. The phenomenon of surface tension can readily be explained in terms of these forces. Molecules located in the bulk of a liquid are, on average, subject to equal forces of attraction in all directions, whereas molecules at a liquid- air interface experience a net inward pull, which leads to the contraction of the surface, see figure 3.2. Surface tension is defined as the energy required to increase the area of a surface isothermally and reversibly by a unit amount. At the interface between two liquids there is again an imbalance of intermolecular forces but of a lesser extent. Interfacial tensions generally lie between the individual surface tensions of the two liquids.

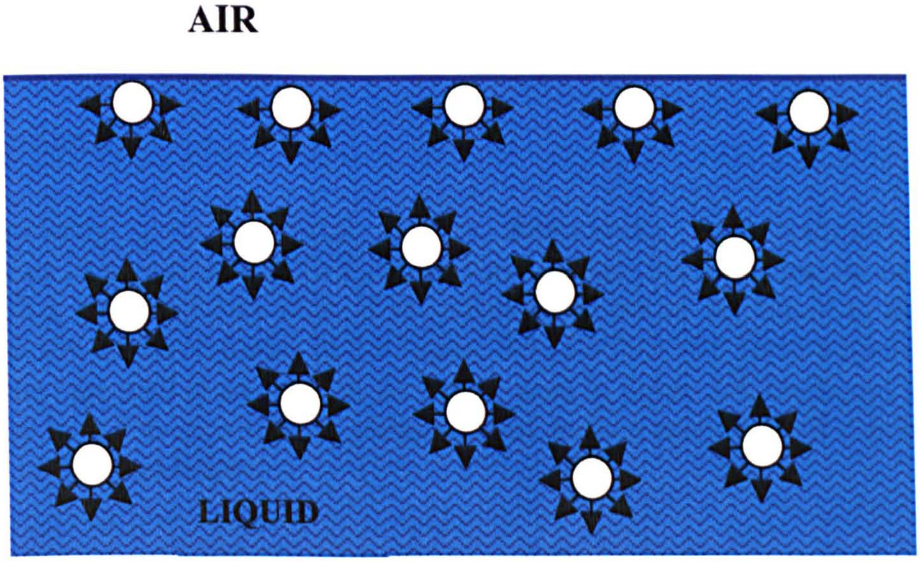

Figure 3.2 Attractive forces between molecules at the surface and interior of a liquid.

3.3.2 Adhesion and Cohesion

For two immiscible liquids which form a liquid-liquid interface, the *work of adhesion* is defined as the work required to separate a unit area of the liquid-liquid interface and form two separate liquid-air interfaces [9]. This is described by the Dupre equation:

$$W_{add} = \gamma_A + \gamma_B - \gamma_{AB} \tag{3.7}$$

where γ_A and γ_B are the surface tensions, and γ_{AB} the interfacial tension. For a single liquid, the *work of cohesion* is defined as the work per unit area required for separation, is given by:

$$W_{coh} = 2\gamma_A \tag{3.8}$$

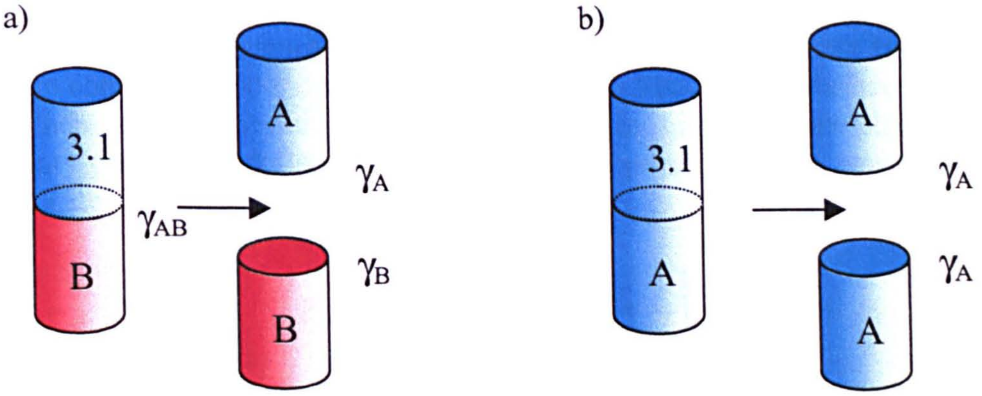

Figure 3.3 a) The work of adhesion between two immiscible liquids equals the work required to separate a unit area of liquid –liquid interface. b) the work of cohesion for a single liquid is the work required to separate a unit area of liquid.

3.3.3 Capillarity

Capillarity plays a crucial role in determining fluid transport and fluid displacements in porous solids. To illustrate this consider the phenomenon of a liquid in contact with a glass capillary tube. If the adhesive forces of the liquid to the glass are greater than the cohesive forces in the liquid, the interface will form a meniscus which intersects the tube wall at an angle θ. As can be seen in figure 3.4, the liquid is pulled up the capillary by a non-zero vertical component of surface tension, until it is balanced by the weight of the fluid below.

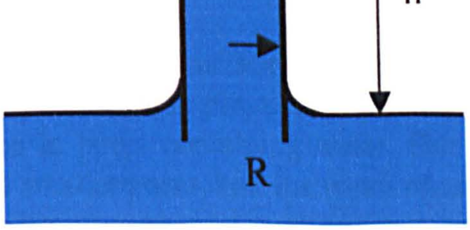

$$\pi R^2 h\rho g = 2\pi R\gamma\cos\theta$$

$$h = \frac{2\gamma\cos\theta}{\rho g R}$$

Figure 3.4 Capillary rise. Water wets the bottom of the capillary, creating an upward component of interfacial tension which acts to draw the liquid up the capillary.

3.3.4 Capillary pressure

A more general example was considered by Laplace [1], where two immiscible fluids are in contact in a bounded system, e.g. water and oil. Due to surface tension at the interface, there is a discontinuity in the pressure field moving from one phase to another. The capillary pressure is defined as the difference in pressure of the two phases, and is given by Lapace's equation:

$$P_c = P_{oil} - P_{water} = \gamma_{ow}\left[\frac{1}{r_1} + \frac{1}{r_2}\right] \tag{3.9}$$

Where γ_{ow} is the surface tension of the oil/water interface, r_1 and r_2 are the principal radii of curvature of the interface. The importance of capillary pressure in two-phase saturated porous systems is illustrated in section 3.5.

3.4 Wettability

Wettability is defined as the tendency of one fluid to spread on or adhere to a solid surface in the presence of other immiscible fluids. In a rock/oil/brine system it is a measure of the preference that the rock has for either the oil or the water phase. Wettability has a very strong influence on the flow properties of a multi-phase system [10]. It is a major factor controlling the location, flow and distribution of fluids in a porous solid. For this reason, the wettability of reservoir rocks has long been the study of petroleum engineers [11].

3.4.1 Water-Wet

A sample whose surface is preferential wetted by water is called water-wet. The Fontainebleau sandstone used in this study is strongly water-wet, the water phase forms a continuous film over the entire rock surface, even in pores containing oil. Due to capillary pressure the water preferentially occupies the smaller pores, and the oil phase the centre of larger pores.

3.4.2 Oil-wet

A sample whose surface is preferential wetted by the oil phase is called oil-wet. For a strongly oil-wet sample, the oil phase forms a continuous film over the entire rock surface, even in pores containing water. Due to capillary pressure the oil preferentially occupies the smaller pores, and the water phase the centre of larger pores.

Historically, all petroleum reservoirs were believed to be strongly water-wet, there were two reasons for this. First, almost all 'clean' sedimentary rocks are strongly water-wet. Secondly, most sedimentary rocks were deposited in aqueous environments into which the oil later migrated. The existence of oil-wet reservoirs was demonstrated by Nutting in 1934 [12], and later studies have shown [13,14] that the majority of reservoir rocks are indeed oil-wet. Measurements of oil/water contact angles have demonstrated that strongly water-wet mineral surfaces can become oil-wet with prolonged exposure to crude oil [11]. Some crude oils make a rock oil-wet by depositing a thick organic film on the mineral surfaces, other crude oils contain polar compounds that are absorbed by the rock surface.

3.4.3 Fractional wettability.

Some rocks display heterogeneous wettability, with variations in the wetting preference at the pore scale. The adsorption of crude oil components depends on the surface chemistry and adsorption properties of the rock surface. Heterogeneous mineralogy can lead to local variations in wettability, with a fraction of the total pore surface being preferentially oil-wet, the remainder water-wet [11].

3.4.4 Mixed Wettability

This term was introduced by Salathiel [15] to describe a special type of fractional wettability, where the oil-wet surfaces form continuous paths through the largest pores. Oil continuity is maintained as the oil saturation is decreased, permitting the drainage of oil to very low residual saturations. Salathiel proposed that mixed wettability arises when oil migrates into a water-wet reservoir, preferentially filling the larger pores {see section 3.5}, the smaller pores are left containing water. The wettability of the larger pores is then altered by the presence of the crude oil.

3.5 Displacements Processes

The saturation state of a rock depends on its history of exposure to incoming water and oil floods. The common history of most reservoir rocks is as follows. When formed, reservoir rocks were initially fully saturated with water. Later in the rock's history, the water was displaced by invading oil. Today a standard technique in oil recovery is to pump water into the reservoir and force out the oil. On a microscopic scale a number of factors affect these displacement processes. These include the pore structure of the rock, capillary pressure and wettability [1,7].

3.5.1 Drainage

A drainage displacement process is defined as an increase in the non-wetting phase saturation. For example, consider flowing oil through a strongly water-wet rock saturated with water $S_w=1$, displacing the water phase. For capillary dominated displacements the non-wetting phase will preferentially fill the larger pores first. To demonstrate consider three water-wet capillaries of different radii containing water, connected to a oil reservoir at pressure P_{oil}. For the oil to displace the water from the capillaries in has to overcome the capillary pressure P_c. Equation 3.9 shows that P_c is inversely proportional to the radius of the capillary. As the pressure of the oil phase P_{oil}

is increased, the water is first displaced from the largest capillary first. The pressure has to be increased further to displace the water from the smaller capillaries.

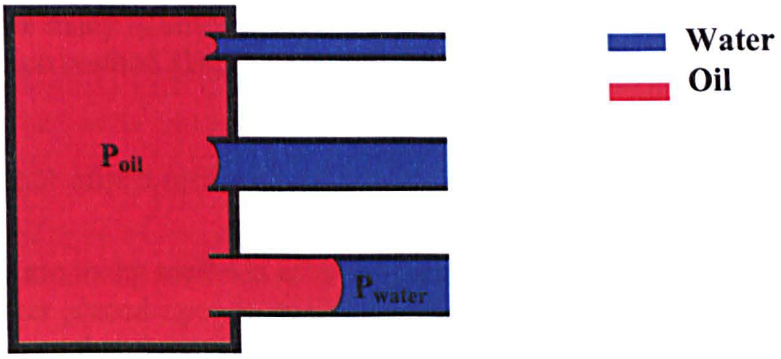

Figure 3.5 Water-wet capillaries connected to a oil reservoir at pressure P_{oil}. The oil is displaced first from the capillary with the largest radius.

In strongly water-wet rocks the water phase is continuously connected by a thin surface wetting film {see section 3.4.1 }. Therefore, during drainage the water phase cannot become trapped and very low water saturations can be achieved. Although, all the water phase is never displaced from the rock. For a particular pressure, an equilibrium water saturation is reached, comprising the water in the continuous film and water in grooves, edges and wedges. This saturation is called the irreducible water saturation S_{wi}, increasing the pressure displaces more water resulting in a slightly lower S_{wi}.

3.5.2 Imbibition

An imbibition displacement process is defined as an increase in the wetting phase saturation. Imbibition can be spontaneous or forced. An example of imbibition is flowing water through a strongly water-wet rock saturated with oil ($S_{wi}=0$), displacing the oil phase. Because of capillary pressure the invading water phase preferentially fills the smaller pores first (opposite of drainage). After a time no more oil is displaced by the water, this saturation state is called the residual oil saturation state S_{or}. Because there is no continuous surface film connecting the oil phase, it is possible for the oil phase to become trapped. This leads to high residual oil saturations.

3.6 Measuring Wettability

There are currently three techniques being used for quantitative measurement of rock wettability, they are – contact angles, Amott test and USBM wettability index [1]. The contact angle method is used to measure the wettability of a specific mineral surfaces, while the Amott and USBM methods measure the average wettability of a rock core. There are many qualitative methods of measuring wettability, the most widely used is the imbibition method [16]. These technique will be briefly outlined below.

3.6.1 Contact angle method

There are many methods of measuring contact angles [9]. For simplicity consider a drop of water placed upon a mineral surface that is immersed in oil, figure 3.6. The three different surface tensions are related by the Young-Dupre equation:

$$\gamma_{os} + \gamma_{ws} = \gamma_{ow} \cos\theta \tag{3.10}$$

The wettability of the surface can be quantified by inspecting the contact angle θ. The system is considered water-wet if $\theta < 75°$ and oil-wet if $\theta > 105°$. If $75 < \theta < 105°$, the system is considered to be intermediately-wet, i.e. has no strong preference for either of the two fluids.

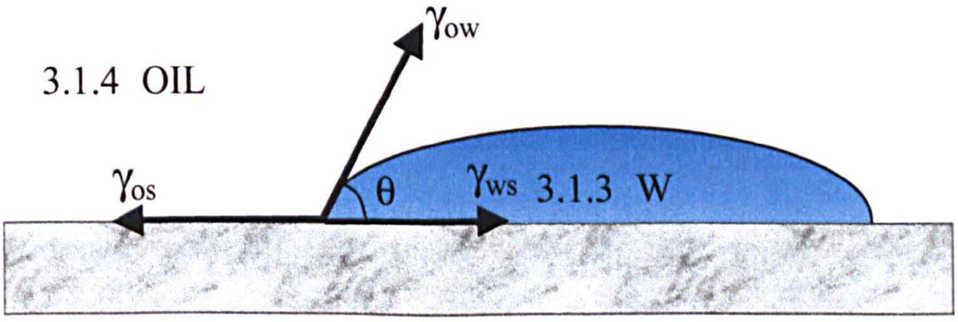

Figure 3.6 Force balance acting on a liquid drop in equilibrium.

Contact angle measurements are affected by surface roughness, trace contaminants and surface heterogeneities. Such measurements are therefore confined to the idealized case of pure fluids on single flat, polished mineral crystal surfaces. A special case of the Young-Dupre equation, equation 3.10, is when the contact angle approaches zero. Then the drop begins to spontaneously spread and cover the surface.

3.6.2 The Amott Test

The Amott test [17] correlates the average wettability of a sample, with the ratio of spontaneous to forced imbibition. It relies on the fact that water will spontaneously imbibe along water-wet pathways in a porous solid, but will require over pressure to enter oil-wet regions. The opposite being true for the oil phase. The Amott test consists of the following five steps:

1. The sample is centrifuged under brine until the residual oil saturation is achieved.
2. The sample is then immersed in oil and the volume of water displaced by spontaneous imbibition is measured, $V_{w\,sp}$.
3. The sample is then centrifuged under oil until the irreducible water saturation is reached, and the volume of water displaced is measured, $V_{w\,cent}$.
4. The sample is then immersed in water and the volume of oil displaced by spontaneous imbibition is measured, $V_{o\,sp}$.
5. The sample is then centrifuged under water until the residual oil saturation is reached, and the volume of oil displaced is measured, $V_{o\,cent}$

These measurements are expressed as two ratios, the 'displacement by oil ratio, δ_0' and the 'displacement by water ratio, δ_w', where

$$\delta_o = \frac{V_{w\,sp}}{V_{w\,sp} + V_{w\,cent}} \qquad \delta_w = \frac{V_{osp}}{V_{osp} + V_{o\,cent}} \tag{3.11}$$

The wettability of the sample is given by the 'Amott-Harvey displacement index, I'

$$I = \delta_w - \delta_o \tag{3.12}$$

This combines the two ratios into a single wettability index, that varies from +1 for strongly water-wet samples to –1 for strongly oil-wet samples. The main problem with the Amott test is its lack of sensitivity near neutral wettability. This is because at intermediate wettabilities neither phase will spontaneously imbibe.

3.6.3 Imbibition Method

The Imbibition Method is a commonly used qualitative measure of wettability. It gives a rough measure of wettability, quickly and without the need of specialised laboratory equipment. The sample is first reduced to its irreducible water saturation and then submerged in water in a graduated cylinder. The rate at which the water is imbibed indicates how water-wet the sample is. The sample is then driven to its residual oil saturation and then submerged in oil. The rate at which the oil is imbibed indicates how oil-wet the sample is. If the sample imbibes neither oil or water it is intermediately wet, in some cases both water and oil are imbibed suggesting the sample has fractional or mixed wettability.

3.7 Geological Porous Solids

The types of porous solids of interest to the petroleum industry are geological in nature. Geology is an integrative science, it encompasses many fields of study including mineralogy (the constituents of rocks), petrology (the distribution and structure of rock formations), geochemistry (the chemistry of rocks), geophysics (the study of physical processes within the earth), stratigraphy (the history of rock layers) and the more applied fields of mining, petroleum and engineering geology. A detailed coverage of these fields is not possible here, for a useful introduction to petroleum geology the reader is referred to F.K North [18]. It will be sufficient here to give a brief overview of the four main geological materials, as outlined by Dullien [1] and Davies [19].

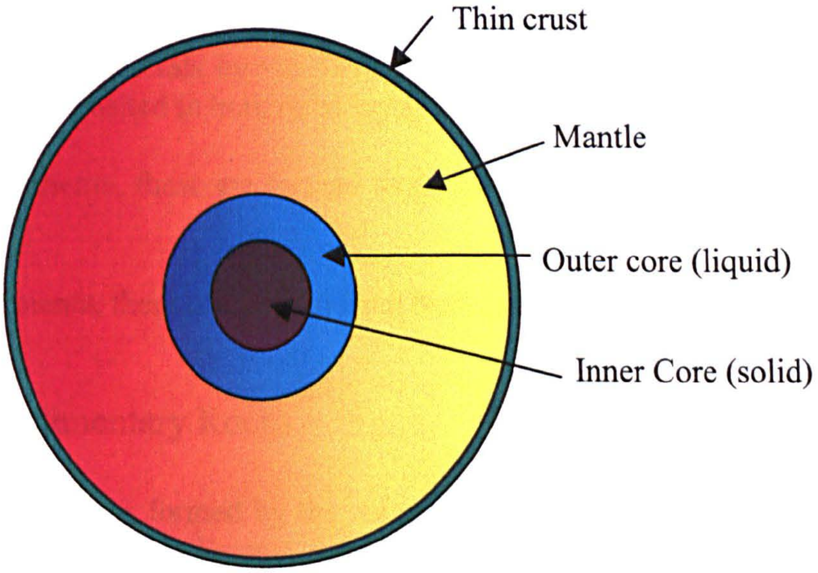

Figure 3.7 Shells of the Earth's interior.

3.7.1 Dense Rocks

The earth has an inner core (radius 1500km) of solid iron and a outer core (radius 3400km) of liquid iron. Around the central core is a wide shell called the Mantle (radius 6400km), figure 3.7. The earth's crust is a very thin outer shell with an average continental thickness of 35km and an average oceanic thickness of 7km [20,21]. The Mantle is composed of dense rock, of low permeability (<0.01D) and low porosity (<2%). Examples of dense rocks found near the surface include granite, dolerite, quartzite and gabbro. These rocks are of little interest to the oil industry, as they have no inherent reservoir potential.

3.7.2 Igneous Rocks

Volcanic or igneous rocks are the product of molten material, called magna, which rises up through the Earth's crust. Igneous rocks are of two major types –intrusive and extrusive. Intrusive igneous rocks are formed when magma cools hundreds of feet below the surface, generally resulting in dense and almost non-permeable rocks. Conversely, extrusive igneous rocks are formed from magma which reaches the surface, and can form some of the most permeable aquifers known.

3.7.3 Non-Indurated sediments

These are sediments that have not yet been consolidated, for example gravel, sand and soil. There are three main sources of sediments,

1. **Clastic sediments**, these are formed from the mechanical breakdown of pre-existing rocks and minerals by weathering and erosion. The fragments are then transported and deposited in horizontal layers.
2. **Chemical sediments**, these are formed from the precipitation of salts dissolved in water.
3. **Organic sediments**, these are formed from biotic activity.

3.7.4 Indurated Sedimentary Rocks

Sedimentary rocks are formed by the compaction and cementation of soft fiable sediments. Overtime layers of sediments form and become buried, the weight of new layers acts to compress, compact and harden the sediment. Minerals present in solution precipitate to form cementing materials (e.g. ferruginous, siliceous, calcareous etc), which bind the sediment particles together. Thus the soft sediment over time becomes layers of harden rock. Most indurated sedimentary rocks can be broadly classified as shales, carbonate rocks and sandstones.

3.7.5 Shales

Shales as used in the broad sense refer to clay-rich sedimentary rocks, and make up over 50% of indurated sediments. They have porosities ranging from 2-25% (depending on depth) and low permeabilities in the 0.01 to 1.0 mD, making them ideal reservoir seals.

3.7.6 Sandstones

Sandstones are of vital importance to the petroleum industry, it has been estimated that over 60% of oil reservoirs are in sandstones [18]. Sandstones make up about 25% of indurated sediments, with quartz generally the dominant mineral. Their porosities typically range from 5-25%, and tends to diminish systematically with depth, sandstones below 10km generally have porosities below 5%. This has a profound effect on the economics of petroleum recovery. The permeability of sandstones depends on the grain size and the amount of cementation. The presence of horizontal stratification in large samples e.g. 100m^3, means permeability is anisotropic. The vertical permeability of large masses can be very low, even though the horizontal permeability is quite high.

3.7.7 Carbonate Rocks

Carbonate rocks consist mainly of calcite and dolomite, often with small amounts of quartz and clay material. Young carbonate rocks, such as coral reefs and atolls, have a high porosity (ϕ = 20-50%) and permeability (K = 1000D). Older more compacted carbonates have much lower permeabilities in the milli Darcy range. Carbonate oil reservoirs are of significant importance.

3.8 REFERENCES

1. Dullien F.A.L. "Porous Media: Fluid Transport and Pore Structure". 1992. Academic Press Ltd.
2. Nutting P.G. "Physical Analysisof Oil sands". 1930. American society of Petroleum Geology. 14. 10. 1337.
3. Timmerman A."Practical Reservoir Engineering". 1982.
4. sterology
5. Adler P.M., Jacquin C.G. Quiblier J.A. "Flow in Simulated Porous Media". 1990. International Journal of Multiphase Flow". 16. 691.
6. Tessier J.J., Packer K.J., Thovert J.F., Adler P.M. "NMR Measurements and numerical simulations of Fluid Transport in Porous Solids". 1997. AiChEJ. 43. 1653.
7. Sahimi M. "Flow and Transport in Porous Media and Fractured Rock". 1995. VCH.
8. Atkins P.W. "Physical Chemistry". Oxford University Press.
9. Shaw D.J. "Colloids and surface Chemistry".1989. Butterworth-Heinemann Ltd.
10. Blunt M.J. "Pore Level Modeling of the Effects of Wettability". 1997. Society of Petroleum Engineers. 2.
11. Anderson, W.G. "Wettability Literature survey part 1". 1986 oct. Journal of Petroleum Technology. 1125-1144.
12. Nutting P.G. "Some Physical and Chemical Properties of Reservoir Rocks Bearing on the Accumulation and Discharge of Oil". 1934. Problems of Petroleum Geology. AAPG. 825.
13. Treiber L.E.,Archer D.L., Owens W.W. "A Laboratory Evaluation of the wettability of Fifty Oil Producing Reservoirs". 1972 dec. Society of Petroleum Engineering Journal. 531-540.
14. Chilingar G.V., Yen T.F. "Wettability and Relative Permeabilies of Carbonate Reservoir Rocks". 1983. Energy Sources. 7. 67-75.
15. Salathiel R.A. "Oil Recovery by Surface Film Drainage in Mixed-Wettability Rocks". 1973 oct. Journal of Petroleum Technology. 1216-1224.
16. Anderson, W.G. "Wettability Literature survey part 2". 1986 nov. Journal of Petroleum Technology. 1246-1262.
17. Amott E. "Observations Relating to the Wettability of Porous Rock". 1959. AIME. 216. 156-162.
18. North F.K. "Petroleum Geology". 1985. Allen and Unwin Inc.
19. Davis S.N. "Flow through Porous Media". 1969. Academic Press. New York.
20. Potter A.W.R. "Geology". 1975. Macdonald and Evans Ltd.
21. Owen T.R. "Geology". 1983. Hodder and Stoughton Ltd.

Chapter 4

Review

Contents

4.1 INTRODUCTION 63

4.2 RELAXATION 63

- 4.2.1 LONGITUDINAL RELAXATION 64
- 4.2.2 MISCELLANEOUS EXPERIMENTAL OBSERVATIONS 65
- 4.2.3 WETTABILITY 66
- 4.2.4 WELL LOGGING 66

4.3 PULSED FIELD GRADIENT NMR 67

- 4.3.1 UNRESTRICTED SELF-DIFFUSION 67
- 4.3.2 RESTRICTED DIFFUSION 67
- 4.3.3 STUDIES OF FLOW THROUGH POROUS SOLIDS. 68

4.4 IMAGING 69

- 4.4.1 SPIN DENSITY IMAGES 69
- 4.4.2 RELAXATION IMAGES 69
- 4.4.3 PHASE DISCRIMINATION 69
- 4.4.4 DIFFUSION AND FLOW IMAGING 69

4.5 REFERENCES 71

- 4.5.1 RELAXATION 71
- 4.5.2 DIFFUSION 73
- 4.5.3 FLOW 74
- 4.5.4 IMAGING 74

4.1 Introduction

The study of porous solids, saturated with one or more fluids, is of importance in several fields of scientific endeavour. The petroleum industry is interested in the extraction of hydrocarbons from reservoir rocks. Chemical engineers are interested in the effectiveness of porous catalysts and the transport of fluids through packed columns. Biologists are interested in the flow of blood through organ tissues. The study of porous solids are also directly relevant to such diverse disciplines as food science, environmental science (e.g. waste water treatment) and separation technologies (e.g. liquid chromatography).

Many experimental techniques are used in the study of porous solids[1,2,3]. NMR has the advantage over other techniques of being non-invasive and non-destructive. A wide range of NMR methods are available to study the structure of porous solids, the transport of fluids through porous solids and chemical reactions within porous solids [4]. The use of NMR to characterize real porous solids is often handicapped by problems associated with magnetic susceptibility differences between the solid matrix and the saturating fluid. Many studies are therefore performed on idealized porous solids e.g. glass bead packs.

This chapter aims to review the field of porous solids studied by NMR, with particular emphasis placed on work of a petrophysical nature. The broad topics of relaxation, pulse field gradient (PFG) NMR and magnetic resonance imaging (MRI) experiments are outlined in the following sections.

4.2 Relaxation

It has long been observed that the relaxation times of a fluid are reduced when the fluid is confined within a porous solid [5]. This is directly attributable to the structure of the porous solid and not any contamination of the saturating fluid by the solid. The various NMR relaxation times can be useful in the characterisation of porous solids. Fluids confined within a porous solid experience the additional relaxation mechanisms of surface relaxation and diffusion through internal magnetic field gradients {see section 2.6.2}.

The majority of studies involving relaxation times of fluids in porous solids, have been performed on geological samples. This is because of the commercial significance of the petroleum industry. Until recently most laboratory relaxation measurements performed on rocks were of longitudinal relaxation, where the dominant relaxation mechanism is surface relaxation. Measurements of transverse relaxation were avoided, because above a Larmor frequency of 10MHz the diffusion of molecules through internal magnetic field gradients becomes the dominant relaxation mechanism. This makes the interpretation of relaxation data much more complex. With the advent of pulsed NMR well logging tools [6] working at low resonance frequencies, typically 2MHz, there has been more interest in transverse relaxation measurements.

4.2.1 Longitudinal Relaxation

Most early studies concentrated on direct correlations between spin-lattice relaxation measurements of fluid saturated rocks and their macroscopic flow properties. In 1966 Seevers [7] proposed an empirical relationship between the permeability of a sample k, its porosity ϕ and its average T_1:

$$k = C\,\phi\,(T_1)^2 \tag{4.1}$$

Where C is a constant. More recently Kenyon et al [8] used a 'stretched-exponential' representation of longitudinal relaxation and found a closer relationship given by:

$$k = C\,\phi^4\,(T_1)^2 \tag{4.2}$$

In 1968 Timur [9] created a quantity called FFI_3 (Three component Free Fluid index), extracted from T_1 relaxation measurements. It provided a good approximation of the water volume that could be removed from a saturated rock sample by centrifuging. Timur [10] also suggested a empirical relationship between FFI_3 and porosity and irreducible water saturation, based on measurements of 188 sandstone samples. These correlations were broadly successful, because of the connection between surface relaxation and pore size distribution.

The principles of NMR relaxation of fluids at solid surfaces, were established by Korringa et al [11]. Brownstein and Tarr developed a more general model, incorporating diffusion [12]. Two surface processes were identified, relaxation at all sites (non-magnetic) on the surface and relaxation at sites containing paramagnetic ions e.g. Fe, Mg, Ni and Cr. It has generally been believed that surface relaxation in rocks is dominated by the presence of paramagnetic impurities. Work by D'Orazio et al [13] on silica beads suggests the relaxation process associated with non-magnetic sites is weak. Though this conclusion is contradicted by the more recent work of Kleinberg et al [14] on synthetic calcium silicates, this compound being proposed as a good model of the oxide surface of sandstones. Experiments showed the oxide surface to be an unexpectedly good relaxer of fluid borne spins. Also, the effect of paramagnetic ion concentration on the surface relaxivity was found to be surprisingly small.

The temperature dependence of T_1 and T_2 distributions of a dozen saturated rocks were investigated by Latour et al [15]. He found relaxation distributions were almost independent of temperature between 25 and 175°C. This lack of temperature dependence shows that relaxation is independent of diffusion, because diffusion coefficients are very sensitive to temperature. This indicates the fast diffusion limit of the Brownstein Tarr model is largely applicable to these samples. When this is the case the relaxation of spins in an individual isolated pore is mono-exponential, and dependent up on the surface-to-volume ratio of the pore, but not the pore shape {section 2.6.1}:

$$\frac{1}{T_1} = \rho_1\left(\frac{S}{V}\right)_{pore} + \frac{1}{T_{1Bulk}} \tag{4.3}$$

In real porous solids, for example rocks, there is usually a complex distribution of pore shapes and sizes. The observed relaxation behaviour will be the sum over all contributing pores, generally giving multi-exponential relaxation decay. Many approaches have been used to extracted information about pore size distributions from relaxation measurements. The simplest approaches are to determine a mean T_1 value [16], to fit to the sum of 2 or 3 exponentials [17] or to fit to an alternative function such as a 'stretched exponential' function [8].

A more realistic approach is to determine a continuous distribution of T_1 values [18]. Smith et al [19] used the 'two fraction fast exchange' model to convert T_1 distributions directly into pore size distributions. A more rigorous approach was used by Davies et al [20,21] to convert T_1 distributions into pore size distributions using the Brownstein Tarr model. There are a number of limitations in using relaxation time distributions to determine pore size distributions. First, mathematical analysis to obtain a distribution of relaxation times from relaxation measurements is problematic. Second, the surface relaxivity parameter is required to obtain the pore size distribution. Finally, it is assumed there is fast diffusion within pores but negligible inter-pore coupling.

Pore size distributions derived from NMR relaxation measurements, have been compared with pore size distributions derived from other methods. Gallegos and Smith [19] found good agreement between pore size distributions derived from NMR relaxation measurements and those derived from mercury porosimetry on glass bead packs. Straley [22] also found reasonable agreement for sandstone samples. In addition, a strong correlation between pore size distributions derived from NMR and those derived from thin-section imaging has been shown [23,24]. The problem with such comparisons is that each method is sensitive to different parameters, NMR relaxation is sensitive to the surface-to-volume ratio, whereas mercury porosimetry senses the size of pore throats rather than pore size and thin-section imaging is insensitive to small micro pores. Hence, an unequivocal verification of NMR pore size distributions is difficult if not impossible.

4.2.2 Miscellaneous Experimental Observations

Straley et al [25] explored the T_1 relaxation distribution as a function of water saturation. The sandstone samples were centrifuged, at increasing speeds, progressively expelling water from the sample. There was a progressive loss of the longest T_1 components indicating that water molecules with long relaxation times resided in the larger, easier to drain pores.

Kleinberg et al [26] investigated the frequency dependence of T_1 for eight rocks, including sandstones and carbonates, at 5, 40 and 90 MHz , and found little variation for the rocks samples considered.

T_1 relaxation distributions of rocks containing mixtures of water and kerosene were measured by Straley [25]. It was discovered that when kerosene was introduced into a water saturated rock, the kerosene relaxed at its bulk liquid relaxation rate, while the water in contact with the grain surfaces experienced more rapid relaxation. It was also found that when the rock was dried at 60°C for 5 weeks and then saturated with kerosene, the kerosene experienced more rapid relaxation.

This experiment was repeated by Latour [15], who used the same drying protocol as Straley. It was found that the T_1 relaxation distributions of hydrocarbon saturated rocks, matched that of the water saturated rocks. However, the grain surface was less efficient in relaxing the hydrocarbon than the water phase. A review by Kleinberg [27] noted that sonic attenuation measurements revealed that to remove the last monolayer of water from a rock required repeated cycling to very high temperatures at very low pressures (10^{-11} Torr vacuum) [28]. He proposed that the drying procedure used by Latour was inadequate to remove the last mono-layer of water from the rock's surface. As surface relaxation effects are dictated by couplings acting over atomic distances, the presence of even a mono-layer of water would explain the lower surface relaxivity experienced by the hydrocarbon.

4.2.3 Wettability

As long ago as 1956 Brown and Fatt [29] proposed using the surface sensitive nature of longitudinal relaxation as a measure of wettability {for wettability see section 3.4}. They and Kumar et al [30], studied sand packs and bead packs made of varying fractions of oil- and water-wet particles. Devereaux (1967) [31] studied the effect on longitudinal relaxation of changes in wettability caused by the 'ageing' of sandstones using crude oil {see section 3.4.2}. These early works were contradictory and inconclusive, which is not surprising considering the complexity of wettability. More recent studies have been carried out [32,33] though NMR is still not used as a practical measure of wettability.

4.2.4 Well Logging

Oil field engineers require quick and reliable information about the rocks and fluids found down bore holes. Well logging provides continuous, in situ, measurement of physical parameters as a function of bore hole depth. A variety of electrical, acoustic and radioactive instruments are used for this purpose [34,35]. Boreholes are typically 20cm in diameter and up to 10km deep. Temperatures can rise to 175°C and pressures range up to 140MPa. The high costs involved in stopping oil production, means the time available to perform well logging measurements is severally limited.

Early NMR logging tools used the earth's magnetic field [36]. Later designs enabled pulsed NMR techniques to be used. Reviews of NMR applications in well logging are given by Kleinberg [6] and Kenyon [37]. For time efficiency NMR bore hole measurements focus on transverse rather than longitudinal relaxation. Transverse relaxation is caused not only by surface relaxation but also by the diffusion of spins through internal field gradients {see section 2.6.2}. To minimize this effect, T_2 measurements are performed at low magnetic fields and use short echo delays. In well logging, the proton resonance frequencies used are $\leq$ 2MHz and echo delays are less than 70μs. Under these conditions it has been shown that transverse relaxation is dominated by surface relaxation, even in the presence of large internal gradients [38]. Moriss et al [39] found that pore size distributions derived from mercury injection porosimetry show good agreement with T_2 distributions measured using a NMR logging tool.

4.3 Pulsed Field Gradient NMR

The translational displacements of fluid molecules can be studied by Pulse Field Gradient (PFG) NMR. Molecular translational displacements can be described as either diffusion or flow. Diffusion is driven by internal thermal energy, which produces chaotic and randomly directed molecular displacements. Flow is driven by any macroscopic constraint, usually external to the system, such as a pressure, temperature or density gradient. The classic Pulsed Field Gradient Spin Echo (PGSE) NMR technique is used to study flow and diffusion processes [4].

4.3.1 Unrestricted Self-Diffusion

The PGSE experiment has been extensively used for measuring the self-diffusion coefficients of liquids. The echo attenuation function $E_\Delta(q)$ for molecules under going unrestricted self-diffusion is given by the Stejskal Tanner equation [40] {see section 2.7.2 }:

$$E_\Delta(q) = E_0 \exp\left\{-4\pi^2 q^2 D(\Delta - \delta/3)\right\} \tag{4.4}$$

A plot of $\ln(E_\Delta(q))$ against $4\pi^2 q^2(\Delta - \delta/3)$ will be linear with gradient –D. The diffusion coefficients of different components of a mixture of liquids, can be measured using FT-PGSE. This was first demonstrated in 1973 by McDonald et al [41] on a DMSO-water system by simultaneously measuring both diffusion coefficients.

4.3.2 Restricted Diffusion

Restricted diffusion is defined as molecular translational displacements that are constrained by impermeable barriers to remain within finite regions of space. For restricted diffusion the echo attenuation as a function of q is no longer Gaussian, and is influenced by pore geometry. Analytical expressions for $E_\Delta(q)$ have only been obtained for simple geometries. In 1968 Tanner and Stejskal derived $E_\Delta(q)$ for the diffusion of particles confined within a rectangular box using the narrow pulse approximation [42]. Using the same approximation, expressions have been derived for spherical [43-45] and cylindrical [45] geometries. Expressions for these three geometries have also been derived using the Gaussian phase approximation [46] both for steady field gradients [46] and for pulsed field gradients [44,47]. The validity of the narrow pulse approximation and gaussian phase approximation has been investigated by Blees [48]and Linse et al [49]. These calculations predict minima in $E_\Delta(q)$, which is analogous to diffraction peaks in light scattering experiments. Such diffusive diffraction effects have been observed for pentane constrained between parallel plates and water in a cylinder [4].

In porous solids, the diffusion of molecules within pores and interconnecting channels is hindered by the solid structure. On the basis of pore-hopping models, diffusive diffraction maxima are predicted at q=1/b,2/b .... , where b is the distance between pore centres. This has been shown experimentally for the diffusion of water in the interstices of randomly packed polystyrene spheres [50]. More recently, similar diffraction like effects have been reported using PGSE NMR observations of molecular displacements produced by fluid flow through porous solids [51,52]. The advantage of flow over diffusion being the increased range of structural scales that become accessible.

The theory of restricted diffusion has been widely used to gain information about the size and shape of the restriction [53]. For example, in 1972 Packer and Rees [54] used restricted diffusion measurements to determine the size distribution of emulsion droplets and in 1983 Callaghan et al [55] determined the size distribution of fat globules in cheese. Cory and Garroway [56] used PFG NMR to measure displacement probabilities of restricted diffusion of water in yeast cells, this allowed a mean measurement of compartment size well below that accessible by NMR imaging techniques.

4.3.3 Studies of Flow Through Porous Solids.

Like diffusion the effects of flow upon NMR signals was apparent very early on. Carr and Purcell [57] noted the effects of convection on odd and even echoes in the CP sequence. A review of early work carried out on flow is given by Caprihan [58].

In 1983 Karger and Heink [59] showed there was a Fourier relationship between $E_\Delta(q)$ and the average propagator $P_\Delta(X)$, this was discussed in section 2.7.1. Measurements of average propagators have been used to study single phase flow through glass bead packs [60] and Fontainebleau sandstone [61]. An extensive series of experiments has also been made of multi-phase flow and diffusion in Fontainebleau sandstone [62,63]. These experiments revealed the influence of parameters such as wettability, spreading and phase saturation on transport phenomena. The resulting average propagators have proved to be a strenuous test for computer simulations of fluid flow through porous solid [64,65].

It is also possible to perform a two-dimensional version of the PFG spin echo experiment, using two orthogonal gradients {see section 5.6.3}. This yields the two-dimensional propagator $P_\Delta(X,Z)$, which corresponds to the joint probability for molecular displacements X and Y in time Δ. Such two-dimensional propagators have been measured for flow through glass beads, Fontainebleau sandstone and various fibrous systems (oriented and non oriented) [64,66].

As a fluid flows through a porous solid it experiences dispersion [1]. Dispersion can be thought of as, the 'spreading out' of an element of fluid as it travels through the medium, it is analogous to diffusion for stagnant fluids. A number of studies have used PFG NMR to investigate dispersive processes [67,68,69].

An interesting application of PFG NMR has been in the field of Chromatography. The kinetics of mass transfer between fluid percolating through the system and the stagnant fluid in the diffusional pores is important in the efficiency of Chromatographic columns. Tallarek et al [70] used displacement propagators to study mass transfer, flow and dispersion through chromatographic columns of porous glass beads. Indeed PFG NMR may prove ideally suited to chromatographic research.

4.4 Imaging

Many studies of porous solids have used NMR imaging techniques. NMR imaging of the saturating fluid phase(s) can be performed using a variety of image contrast mechanisms [53]. An outline of the use of MRI to characterise oil reservoir rocks has been given by Packer [71].

4.4.1 Spin Density Images

Basic imaging experiments can measure the spatial spin density distribution of fluid contained within porous solids. Unfortunately, magnetic susceptibility effects usually limit the image resolution. Typically the highest resolution will be a voxel of dimensions $0.2\times 0.2 \times 1$ mm^3. The pore scale of most rock samples is below this resolution, and the voxel properties are an average over many pores. In rocks it is therefore only possible to image larger scale heterogeneities, such as fractures [72].

4.4.2 Relaxation Images

Spatially resolved T_1 and T_2 images have been recorded for water saturated rocks [72-74]. These images are of interest because of the relationship between surface relaxation and pore size distribution {see section 4.2.1}. It has also been found that with flowing water there is a correlation between the T_1 and the local flow rate [75].

4.4.3 Phase Discrimination

The imaging of two or more phases within a porous solid requires a means of discriminating between the signals from each phase. The choice of method will depend upon the detailed characteristics of the system. The principal methods are based on chemical shift [76] or relaxation time differences [77]. It is also possible to image nuclei other than ^1H [78] or to use fluids that do not contain resonant spins e.g. D_2O in place of water. Such images can be used to investigate the distribution of phases within the sample.

Another use that is of interest to the petroleum industry is the monitoring of fluid distributions in rock samples during displacement processes i.e. imbibition and drainage. A number of studies of drainage and imbibition processes in rocks have been undertaken. For example, Fordham et al [79] used an aqueous phase of D_2O and an oil phase of dodecane. The oil saturation was imaged along the length of a rock sample at various times during a drainage process.

4.4.4 Diffusion and Flow Imaging

Another important contrast which can be used in NMR imaging experiments are molecular displacements caused by diffusion and flow. The theory behind using pulse field gradients to measure molecular displacements was discussed in section 2.7.1. It is possible to acquire an image in which each pixel contains imformation on molecular displacements. This technique is called Flow or Velocity Imaging. Such images have been used to probe structure-flow correlations in packed bead beds [80], to study rheology [81] and to measure vascular flow in living plants [82].

4.5 References

1. Dullien F.A.L. "Porous Media: Fluid Transport and Pore Structure". 1992. Academic Press Ltd. London.

2. Schneidegger A.E. " The Physics of Flow Through Porous Media". 1960. University of Toronto Press. Toronto.

3. Bear J. "Dynamics of Fluids in Porous Media". 1972. American Elsevier. New York.

4. Barrie P.J. "Characterization of Porous Media using NMR Methods". 2000. Annual Reports on NMR Spectroscopy. 41. 265-316.

4.5.1 Relaxation

5. Brown R.J.S, Fatt I. "Measurements of Fractional Wettability of Oilfield Rocks by the Nuclear Magnetic Relaxation Method". 1956. AIME. 207. 262-264.

6. Kleinberg R.L. "Well Logging". Encyclopaedia of NMR

7. Seevers D.O. "A Nuclear Magnetic Method for Determining the Permeability of Sandstones". 1966. Trans. SPWLA. Paper L.

8. Kenyon W.E., Day R.I., Straley C., Willemsen J.F "Relaxation Properties of water-Saturated Sandstones". 1986. 61st Annual SPE Conference.

9. Timur A. "Pulsed Nuclear Magnetic Resonance Studies of Porosity, movable fluid and permeability of sandstones". 1969. Journal of petroleum technology. 21. 775-786.

10. Timur A. "Producible porosity and permeability of sandstones investigated through Nuclear Magnetic Resonance Principles". 1969. Log anal. 10. Jan-Feb. 3-11.

11. Korriga J., Seevers D.O., Torrey H.C. "Theory of Spin Pumping and Relaxation in Systems with a Low Concentration of Electron Spin Resonance Centres". 1962. Physical Review. 127. 1143-1150.

12. Brownstein K.R., Tarr C.E. "Importance of Classical Diffusion in NMR Studies of Water in Biological Cells". 1978. Physical Review A. 19. 2446-2453.

13. D'Orazio F., Bhattacharja S., Halperin W.P. "Molecular Diffusion and Nuclear Resonance Relaxation of Water in unsaturated Porous silica". 1990. Physical Review B. 42. 9810-9818.

14. Foley I., Farooqui S.A., Kleinberg R.L. "Effect of Paramagnetic Ions on NMR Relaxation of Fluids at Solid Surfaces". 1996. Journal of Magnetic Resonance A. 123. 95-104.

15. Latour L.L., Kleinberg R.L. Sezginer A. "Nuclear Magnetic Resonance Properties of Rocks at Elevated Temperatures". 1992. Journal of Colloid and Interface Science. 150. 535-548.

16. Loren J.D., Robinson J.D. 1970. Society of Petroleum Engineering Journal. 10. 268.

17. Cogwill D.F., Pitman J.K Seevers D.O. 1981. Proc. SPE/DOE Low Permeability Symposium.

18. Brown R.J.S. "Information Available and Unavailable from Multi exponential Relaxation Data". 1989. Journal of Magnetic Resonance. 82. 539-561.

19. Gallegos D.P., Smith D.M. "A NMR Technique for the Analysis of Pore Structure: Determination of Continuous Pore Size Distributions". 1988. Journal of Colloid and Interface Science. 122. no. 1. 143-153

20. Davies S., Packer K.J. "Pore-Size Distributions from Nuclear Magnetic Resonance Spin-Lattice Relaxation Measurements of Fluid Saturated Porous Solids. Part 1". 1990. Journal of Applied Physics. 67. 3163-3170.

21. Davies S., Kalam M.Z, Packer K.J., Zelaya F.O. "Pore-Size Distributions from Nuclear Magnetic Resonance Spin-Lattice Relaxation Measurements of Fluid Saturated Porous Solids. Part 2". 1990. Journal of Applied Physics. 67. 3171-3176.

22. Straley C., Matteson A., Feng S., Schwarz L., Kenyon W. "Magnetic Resonance, Digital Analysis and Permeability of Porous Media". 1987. Applied Physics Letters. 51. 1146-1148.

23. Kenyon W.E., Howard J.J., Sezginer A., Straley C.,Matteson A., Ehrlich R. "Pore Size Distribution and NMR in Microporous Cherty Sandstones". 1989. Transactions of the SPWLA 30th Annual Logging Symposium.

24. Ehrlich R., Crabtree S.J. Jr, Kennedy S.K., Cannon R.L. " Petrographic Image Analysis. Analysis of Reservoir Pore Complexes". 1984. J. Sed. Pet. 54.1365-1378.

25. Straley C., Morriss C.E., Kenyon W.E., Howard J.J. "Transactions of the SPLWLA 32nd Annual Logging Symposium". 1991.

26. Kleinberg R.L., Farooqui S.A., Horsfield M.A. "T_1/T_2 Ratio and Frequency dependence of NMR Relaxation in Porous Sedimentary Rocks". 1993. Colloid and Interface Science. 158. 195-198.

27. Kleinberg R.L., Kenyon W.E., Mitra P.P. "Mechanism of NMR Relaxation of Fluids in Rock". 1994. Journal of Magnetic Resonance A. 108. 206-214.

28. Tittmann B.A., Clark V.A., Richardson J.M., Spencer T.W., 1980. J. Geophys. Res. 85. 5199.

29. Brown R.J.S, Fatt I. "Measurements of Fractional Wettability of Oilfield Rocks by the Nuclear Magnetic Relaxation Method". 1956. AIME. 207. 262-264.

30. Kumar J., Fatt I., Saraf D.N. "Nuclear Magnetic Relaxation Time of Water in a Porous Medium with Heterogeneous Surface Wettability". 1969. Journal of Applied Physics. 40. 4165-4171.

31. Devereaux O.F. "Effect of Crude Oil on the NMR Relaxation Time Of Water in a Porous Media". 1967. Nature. 215.No. 10. 614-615.

32. Hsu W.F., Li X., Flumerfelt R.W. " Wettability of Porous Media by NMR Relaxation Methods". 1992. 67th Annual Meeting of the Society of Petroleum Engineers. 1027.

33. Howard J.J., Spinler E.A. "Nuclear Magnetic Resonance Measurements of Wettability and Fluid Saturations in Chalk". 1993. 68th Annual Meeting of the Society of Petroleum Engineers. 565.

34. Synder D.D., Flemming D.B. "Well Logging – A 25 Year Perspective". 1985. Geophysics. 50. 2504-2529.

35. North F..K. "Petroleum Geology". 1985. Allen and Unwin Inc.

36. Brown R.J.S., GamsonB.W. 1960. Petroleum Transactions AIME. 219. 199.

37. Kenyon W.E. "Nuclear Magnetic Resonance as a Petrophysical Measurement". 1992. Nuclear Geophysics. 6. 153-171.

38. Goelman G., Prammer M.G. "The CPMG pulse Sequence in Strong Magnetic Field Gradients with Applications to Oil-Well Logging". 1995. Journal of Magnetic Resonance A. 113. 11-18.

39. Morriss C.E., MacInnis J., Freedman R., Smaardyk J., Straley C., Kenyon W.E., Vinegar H.J., Tutunjian P.N. "Field Test of Test of an Experimental Pulsed Nuclear Magnetism Tool". 1993. SPWLA 34th Annual Logging Symposium.

4.5.2 Diffusion

40. Stejskal E.O., Tanner J.E. 1965. Journal of Chemical Physics. 42. 288.

41. James T.L., McDonald G.G. 1973. Journal of Magnetic Resonance. 11. 58.

42. Tanner J.E., Stejskal E.O. 1968. Journal of Chemical Physics. 49. 1768.

43. Mitra P.P., Sen P.N. 1992. Physical Review B. 45. 143.

44. Balinov B., Jonsson B., Linse P., Soderman O. "The NMR Self Diffusion Method Applied to Restricted Diffusion. Simulation of Echo Attenuation from Molecules in Spheres and between Planes". 1993. Journal of Magnetic Resonance Series A. 104. 17-25.

45. Callaghan P.T. "Pulsed –Gradient Spin-Echo NMR for Planar, Cylindrical and Spherical Pores under Conditions of Wall Relaxation". 1994. Journal of Magnetic Resonance. 113. 53-59.

46. Neuman C.H. "Spin Echo of Spins Diffusing in a Bounded Medium". 1973. Journal of Chemical Physics. 60. no.11. 4508-4511.

47. Murday J.S., Cotts R.M. 1968. Journal of Chemical Physics.48. 4938.

48. Blees M.H. "The Effect of Finite Duration Of Gradient Pulses on the Pulsed Field Gradient NMR Method for Studying Restricted Diffusion". 1994. Journal of Magnetic Resonance series A.109. 203-209.

49. Linse P., Soderman "The Validity of the Short-Gradient-Pulse Approximation in NMR Studies of Restricted Diffusion. Simulations of Molecules Diffusing between Plane, in Cylinders and Spheres". 1995. Journal of Magnetic Resonance Series A. 116. 77-86.

50. Callaghan P.T., Coy A., MacGowan D., Packer K.J., Zelaya F.O. "Diffraction Like Effects in NMR Diffusion Studies of Fluids in Porous Solids". 1991. Nature. 351. 467.

51. Seymour J.D., Callaghan P.T. " Flow Diffraction Structural Characterization and Measurements of Hydrodynamic Dispersion in Porous Media". 1996. Journal of Magnetic Resonance A. 122. 90-93.

52. De Panfilis C., Packer K.J. "Characterization of Porous Media by NMR Imaging and Flow Diffraction". 1999. European Physical Journal Applied Physics. 8. 77-86.

53. Callaghan P.T. "Principles of Nuclear Magnetic Resonance Microscopy". 1991. Oxford University Press. Oxford.

54. Packer K.J., Rees C. "Pulsed NMR Studies of Restricted Diffusion". 1972. Journal of Colloid and Interface Science. 40. 206.

55. Callaghan P.T., Jolley K.W., Humphrey R.S. "Diffusion of Fat and Water in Cheese as Studied by Pulsed Field Gradient Nuclear Magnetic Resonance". 1982. Journal of Colloid and Interface Science. 93. no.2. 521-529.

56. Cory D.G., Garroway A.N. "Measurements of Translational Displacement Probabilities by NMR: An Indicator of Compartmentation". 1990. Magnetic Resonance in Medicine. 14. 435-444.

4.5.3 Flow

57. Carr H.Y., Purcell E.M. "Effects of Diffusion on Free Precession in Nuclear Magnetic Resonance Experiments". 1954. Physical Review. 94. no.3. 630-638.

58. Caprihan A., Fukushima E. "Flow Measurements by NMR". 1990. Physics Reports. 198. 195-235.

59. Karger J., Heink W. "The Propagator Representation of Molecular Transport in Microporous Crystallites". 1983. Journal of Magnetic Resonance.51. 1-7.

60. Lebon L., Oger L., Leblonb J., Hulin J.P., Martys N.S., Schwartz L.M. " Pulsed Gradient NMR Measurements and Numerical Simulations of Flow Velocity Distributions in Sphere Packings". 1996. Physics of Fluids. 8. 293-301.

61. Packer .K.J., Tessier J.J. "The Characterization of Fluid Transport in a porous solid by Pulsed Field Gradient Stimulated Echo NMR". 1996. Molecular Physics. 87. 267.

62. Tessier J.J., Packer K.J. "Characterization of Multiphase Fluid Transport in a Porous Solid by Pulsed Field Gradient Stimulated Echo NMR". 1998. Physios of Fluids. 10. 75-85.

63. Holmes W.M., Packer K.J. In Preparation.

64. Stapf S., Packer K.J., Graham R.G., Thovert J.F., Adler P.M. " Spatial Correlations and Dispersion for Fluid Transport Through Packed Glass Beads Studied by Pulsed Field-Gradient NMR". 1998. Physical Review E. 58. 6206-6221.

65. Damion R.A., Packer K.J., Sorbie K.S., McDougall S.R. "Pore Scale Network Modelling of Flow Propagators derived from Pulsed Field Gradient Spin Echo NMR Measurements in Porous Media". 2000. Chemical Engineering Sciences. 55. 5981-5998.

66. Stapf S., Packer K.J. "Two-Dimension Propagators and Spatio-Temporal Correlations for Flow in Porous Media". 1998. Applied Magnetic Resonance. 15. 303-322.

67. Seymour J.D., Callaghan P.T. "Generalised Approach to NMR Analysis of Flow and Dispersion in Porous Media". 1997. AIChE. 43. 2096-2111.

68. Tallarek U., Bayer E., Guiochon G. "Study of Dispersion in Packed Chromatographic Columns by Pulsed Field Gradient NMR". 1998. Journal of the American Chemical Society. 120. 1494-1505.

69. Lebon L., Leblond J., Hulin J.P. "Experimental Measurements of Dispersion Processes at Short Times Using a Pulsed Field Gradient NMR Technique". 1997. Physics of Fluids. 9. 481.

70. Tallarek U., Dusschoten D.V., Van AS H., Bayer E., Guiochon G. " Study of Transport Phenomena in Chromatographic Columns by Pulsed Field Gradient NMR". 1998. Journal of Physical Chemistry. 102. 3486-3497.

4.5.4 Imaging

71. Packer K.J. "Oil Reservoir Rocks Examined by MRI". Encyclopaedia of NMR. 3376-3378.

72. Bolam A. "The characterisation of Fluid Transport in Heterogeneous Porous Media using NMR". 1998. Thesis. University of Nottingham.

73. Roberts S.P., Mcdonald P.J., Pritchard T. "A Bulk and Spatially Resolved NMR Relaxation Study of Sandstone Rock Plugs". 1995. Journal of Magnetic Resonance A. 116. 189-195.

74. Attard J.J., Doran S.J., Herrod N.J., Carpenter T.A., Hall L.D. "Quantitative NMR Spin-Lattice-Relaxation Imaging of Brine Saturated Sandstone Reservoir Cores". 1992. Journal of Magnetic Resonance. 96. 514-525.

75. Mansfield P., Issa B., Magnetic Resonance Imaging. 1994. 12. 275.

76. Hall L.D., Rajanayagam V., Hall C. "Chemical-Shift Imaging of Water and n-Dodecane in Sedimentary Rocks". 1986. Journal of Magnetic Resonance. 68. 185-188.

77. Davies S., Hardwich A., Spowage K., Packer K.J. "Fluid Velocity Imaging of Reservoir Core Samples". 1994. Magnetic Resonance Imaging. 12. 265-268.

78. Sarkar S.N., Dechter J.J., Komoroski R.A.. 1993. Journal of Magnetic Resonance A. 102. 314.

79. Fordham E.J., Hall L.D., Ramakrishnan T.S. Roemer P.B. Mueller O.M.. 1993. AIChE J., 39. 1431.

80. Sederman A.J., Johns M.L., Alexander P., Gladden L.F. "Visualisation of Structure and Flow in Packed Beds". 1998. Magnetic Resonance Imaging. 16. 497-500.

81. Britton M.M., Callaghan P.T. "Nuclear Magnetic Resonance Visualization of Anomalous Flow in Cone-and-Plate Rheometry". 1997. Journal of Rheology. 41. 1365-1386.

82. Kockenberger W., Pope J.M., Xia Y., Jeffery K.R., Komor E., Callaghan P.T. 1997. Planta. 201. 53.

Chapter 5

Experimental

Contents

5.1 INTRODUCTION 78
5.2 THE SPECTROMETER 78
5.3 FONTAINEBLEAU SANDSTONE 78
  5.3.1 SAMPLE CHARACTERISTICS 78
  5.3.2 THE FLOW SYSTEM 79
  5.3.3 CLEANING THE FONTAINEBLEAU SANDSTONE. 80
  5.3.4 ESTABLISHING DIFFERENT SATURATION STATES 81
  5.3.5 MEASURING THE WATER SATURATION OF THE FONTAINEBLEAU SAMPLE. 84
  METHOD 1 84
  METHOD 2 86
  5.3.6 COMPARISON 87
5.4 GLASS BEAD PACKS 87
  5.4.1 SAMPLE CHARACTERISTICS 87
  5.4.2 ESTABLISHING DIFFERENT SATURATIONS 87
5.5 RELAXATION MEASUREMENTS 88
  5.5.1 MEASURING LONGITUDINAL RELAXATION 88
  5.5.2 MEASURING TRANSVERSE RELAXATION 90
5.6 PULSED FIELD GRADIENT EXPERIMENTS 91
  5.6.1 ALTERNATING PULSED FIELD GRADIENT STIMULATED ECHO (APGSTE) 91
  5.6.2 ONE-DIMENSIONAL DISPLACEMENT PROPAGATORS 91
  5.6.3 TWO-DIMENSIONAL DISPLACEMENT PROPAGATORS 93
5.7 REFERENCES 95

5.1 Introduction

In this chapter, the experimental techniques employed in this thesis are presented. This includes a description of the NMR spectrometer and flow systems utilized in this study. A description is given of the two porous solids studied, a natural sample of Fontainebleau sandstone and an idealized sample of glass beads. The procedures used to prepare the samples in different saturation states and the methods used to measure these saturation states are also outlined. Finally, the pulse sequences used in this study are presented.

5.2 The Spectrometer

NMR measurements were performed using a GE Omega CSI spectrometer operating for proton resonance at 85 MHz, the field being provided by an Oxford instruments 85/310 horizontal bore magnet (310mm inner diameter), equipped with room temperature shims. Two sets of gradient coils were used in this work, both provide gradients in three orthogonal directions. The first set is an S-150 Accustar actively shielded 150mm inner diameter gradient coil, which provides gradients up to 0.2T/m. The associated RF system consists of a bird cage coil with a cylindrical homogeneous region of length 150mm and diameter 100mm. The RF amplifier has a maximum power output of 1.3kW, which produces in this coil a 90° pulse length of 67μs. The second set of gradient coils, is also actively shielded, and can generate gradients up to 2.5T/m. The associated RF system consists of a bird cage coil with a cylindrical homogeneous region of length 26mm and diameter 26mm. This RF coil at maximum power produces a 90° pulse length of 37μs. The receiver and digitiser can record signals with a 200 kHz sweep width from two channels with 32-bit precision.

5.3 Fontainebleau Sandstone

5.3.1 Sample Characteristics

The natural porous solid used in these experiments was an extremely clean outcrop sandstone found near Fontainebleau, France. As Fontainebleau sandstone contains few paramagnetic impurities it is particularly well suited for NMR investigations. A cylindrical core of 39mm diameter and 52mm length was used, which had a mean grain size of the order of 200μm corresponding to a mean pore size of the order of 50μm [1]. An optical micrograph of the sample is shown in figure 3.1.The sample is strongly water-wet, and has a permeability of 2.05D and a porosity of 25%. The high porosity of the Fontainebleau sample is advantageous, as it provides a good signal/noise ratio.

Measurements were performed with the Fontainebleau sample saturated with two phases, an aqueous phase (wetting phase) and an oil phase (non-wetting phase). The aqueous phase used was a 3% w/v NaCl solution made with either H_2O or D_2O (99.1%

Aldrich). Either hexane (95+% Aldrich) or dodecane (98+% Aldrich) were used as the oil phase.

Both phases were degassed before use to prevent air bubbles forming in the sample. The two phases were placed in a sealed container to prevent re-absorption of gases from the atmosphere and to prevent D_2O exchanging to form DHO or H_2O. The purity of the deuterium oxide was continually monitored, by comparing the ^1H NMR signal of a 4cm^3 sample of used D_2O with the ^1H NMR signal of the same volume of fresh D_2O. There was no degradation of the deuterium oxide over several weeks of experiments. Figure 5.1 shows a schematic diagram of the apparatus.

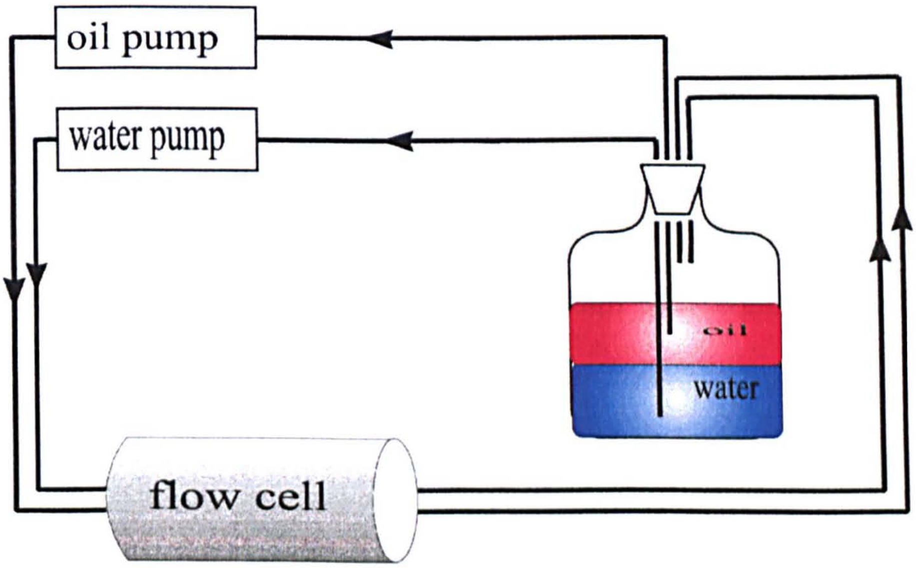

Figure 5.1 Schematic diagram of the apparatus. The oil and water phases were placed in a sealed container. High precision HPLC pumps (Pharmacia P500) were used to pump the oil and water phases at constant volume flow rates through the sample, which was contained inside the flow cell.

5.3.2 The Flow System

The flow system was designed and built by BP Exploration to perform three-phase (two liquid and one gas) flow experiments on rock core samples. The system includes four Pharmacia P500 pumps, each capable of providing the smooth delivery of up to 500ml/h in 1ml/h steps, and one Pharmacia P50 capable of delivering 50ml/min in 0.1ml/min steps. Both of these pump types incorporate a smoothing mechanism to prevent pulsating flow. The flow system has the facility to accurately measure the differential pressure of the flowing fluid across the sample, although this capability was not used.

The cylindrical rock sample was held in a specially constructed flow cell. The flow cell and sample holder were made from the engineering plastic, Delrin (polyoxymethylene,$(\text{-}CH_2O\text{-})_n$). The sample was placed in a tight fitting and impermeable neoprene rubber sleeve, and attached securely to the sample holder, shown in figure 5.2. The ends of the sample holder incorporated a 'maze-like' diffuser, which ensured the flowing fluid was evenly distributed across the face of the sample.

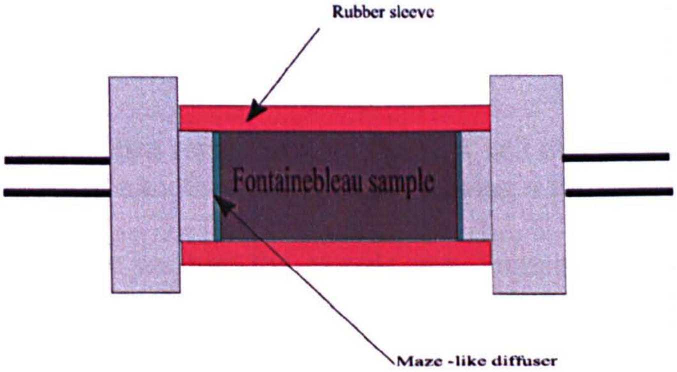

Figure 5.2 The sample holder.

The above arrangement was placed inside the flow cell, figure 5.3, the insides of which were filled with an inert liquid called 'Fluorinert' at a pressure of 28 bar. This pressurised the sleeve tightly around the sample, preventing any flow around the perimeter of the sample. As Fluorinert has no proton content, no ^{1}H NMR signal is obtained from this pressurizing liquid. The oil and water phases enter the flow cell via narrow tubes (3mm diameter), using precision pumps to determine the constant volume flow rates.

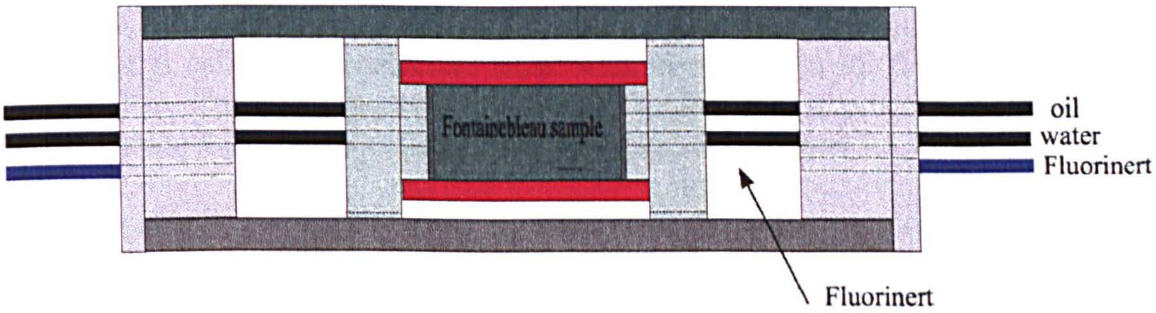

Figure 5.3 Flow cell for Fontainebleau sandstone

5.3.3 Cleaning the Fontainebleau Sandstone.

During the course of this investigation, it was sometimes necessary to achieve a single phase saturation state in the Fontainebleau sample. When the sample contained an aqueous phase and an oil phase, it was not possible to produce a $S_w = 1$ or a $S_w = 0$ state simply by flushing the sample with either the aqueous or oil phase. This was because an irreducible water saturation or a residual oil saturation would remain {see section 3.5}. Therefore, to achieve a single phase saturation state the sample had to be 'cleaned' and re-saturated. BP Exploration recommended the following procedure:

1. The sample was placed in the flow cell as previously described and flushed with 500ml of toluene. The miscibility of toluene with the oil phase allows the oil to be displaced from sample.

2. The sample was then flushed with 500ml of degassed methanol. The methanol was degassed to avoid allowing any air into the sample. The miscibility of methanol with both toluene and the aqueous phase allows for both to be displaced from the sample, producing a $S_{MeOH}=1$ state.

3. The sample was then removed from the flow cell and placed under vacuum for 24 hours. The volatile methanol evaporates leaving a fully dried sample.

4. While still under vacuum the sample was immersed under 300ml of degassed solvent. Either 3% NaCl solution, hexane or dodecane was used to produce the desired single phase saturation state.

5.3.4 Establishing Different Saturation States

A primary drainage/secondary imbibition process was used to produce different saturation states in the Fontainebeau sample [2]. The sample was first cleaned using the procedure described above and saturated with the water phase giving a $S_w = 1$ state. This was followed by,

Primary drainage. $S_w=1$ to S_{wi}

The oil phase (non-wetting phase) was flowed at a suitably high flow rate (1500ml/h) through the sample, displacing the water phase (wetting phase), for a period of 24 hours. Eventually no more water was displaced from the sample. This steady-state saturation is called the irreducible water saturation S_{wi}. An oil flow rate of 1500ml/h produced an irreducible water saturation of $S_{wi}\sim0.06$. This process of decreasing the wetting phase saturation is called primary drainage {see section 3.5.1}.

It should be noted that the irreducible water saturation produced in the sample depends on the flow rate of the oil phase (i.e. the pressure of the oil phase), higher oil flow rates produce lower irreducible water saturations. In a strongly water-wet sample like Fontainebleau sandstone the wetting phase is continuously connected via a thin surface wetting film {see section 3.4.1}, there is no possibility of the wetting phase becoming isolated. Hence, given a high oil flow rate (i.e. high oil pressure) and enough time the wetting phase saturation can be reduce to very low values.

Secondary Imbibition. Stepwise increase from S_{wi} to S_{or}

The water saturation was increased from S_{wi} by simultaneously flowing the oil and water phases through the sample. This simultaneous flow can be characterised by the fractional water flow rate, F_w ,which is defined as:

$$F_w = \frac{Q_{wat}}{Q_{oil} + Q_{wat}} \tag{5.1}$$

where Q_{oil} and Q_{wat} are the constant volume flow rates of the oil and water phases.

Starting with the sample at S_{wi}, the oil and water phases were initially flowed through the sample at a very low F_w, the water phase gradually displacing a small amount of oil from the sample. Eventually, a new steady-state water saturation was reached. Experiments were then performed at this new steady-state saturation before increasing the water saturation again.

Successive increases in the water saturation were produced by increasing F_w in small increments. After each increase in F_w time was allowed for the sample to reach a new steady-state saturation, any experiments were then performed at this new saturation. This stepwise process was repeated, until $F_w=1$, which produced the residual oil saturation S_{or} {see section 3.5.2}. This process of increasing the wetting phase saturation from S_{wi} is called Secondary Imbibition.

Table 5.1 shows typical combinations of flow rates used in the primary drainage/secondary imbibition cycles. The mean interstitial velocity of the oil phase $<v_0>$ is slightly misleading because during secondary imbibition an increasing fraction of the oil phase becomes trapped and does not contributed to flow. This is discussed in detail in chapter 7. Figure 5.4 shows the steady-state water saturations produced in the sample by stepwise increases in the fractional water flow rate F_w. The strongly water-wet character of the Fontainebleau sandstone is shown by the initial rapid increase in S_w, produced by small initial increases in F_w. Indeed, if Fontainebleau sandstone at $S_o=1$ is placed under water, the water will spontaneously imbibe displacing some of the oil phase {see section 3.6.3}. In figure 5.4 the difference in the curves measured for the two oil phases, is the result of different viscosities and interfacial tensions [2].

The average interstitial velocities of the imbibing water phase , see table 5.1, are comparable to those found in producing oil reservoirs ie 10-100μm/s [3]. The transport of fluid through the strongly water-wet Fontainebleau sandstone, at these low interstitial velocities, is capillary dominated, capillary number $\sim 10^{-6}$ [1]. In this regime the imbibing water phase preferentially occupies the relatively small pores {section 3.5.2} and the two-phases flow in separate three-dimensional networks of pore channels, where the flow of each phase can be regarded as hydrodynamically independent [2]. The two fluids are separated from each other by stable interfaces which, in steady-state, are stationary and behave like rigid partitions.

It is well known that the cycle of primary drainage and secondary imbibition exhibits an hystersis effect [4], i.e. the saturation state produced in the sample is dependent on the saturation history of the sample. Therefore, to repeat measurements at a lower water saturation the sample was first returned to its irreducible water saturation, before again following the stepwise increase in the water saturation described above.

F_w	S_w	Q_o (ml/h)	Q_w (ml/h)	$<v_o>$ (µm/s)	$<v_w>$ (µm/s)
0	0.06	1500	0	1484	0
0.004	0.17	500	2	560	11
0.027	0.25	250	7	310	26
0.057	0.34	250	15	352	41
0.211	0.45	150	40	253	82
0.474	0.53	100	90	198	158
0.818	0.61	40	180	95	274
1	0.7	0	200	0	266
0	0.06	1500	0	1484	0

Table 5.1 Typically primary drainage/secondary imbibition cycle used. Where $<v_o>$ and $<v_w>$ are the mean interstitial velocities of the oil and water phases.

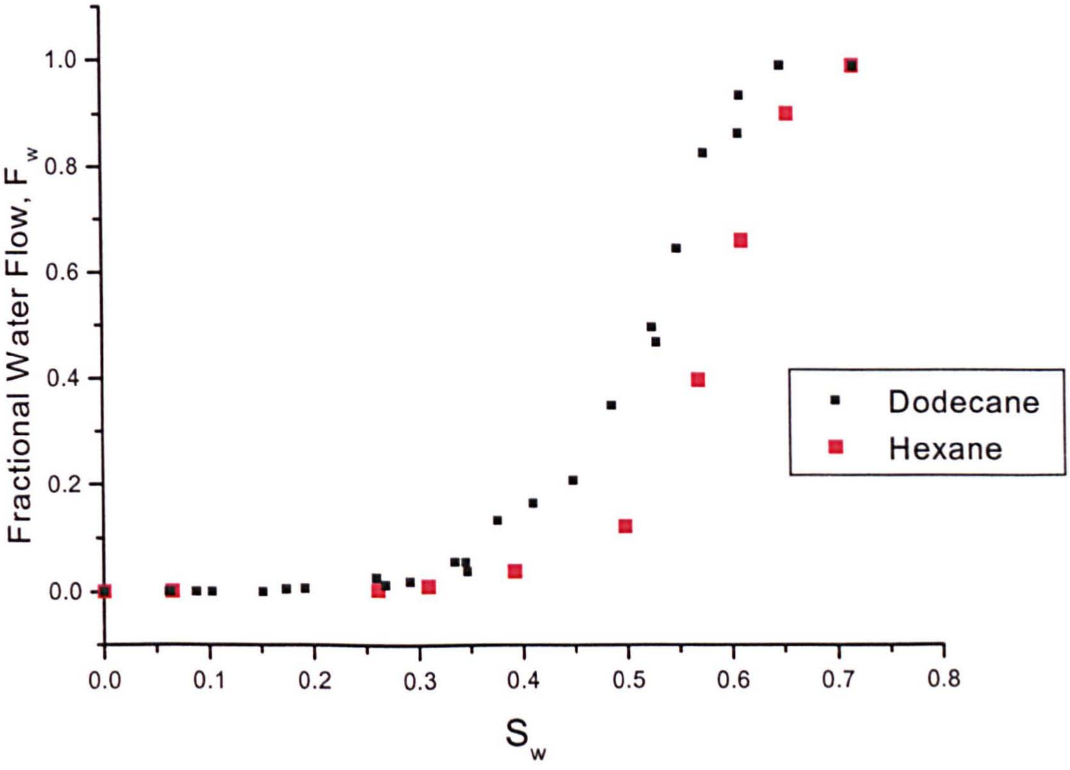

Figure 5.4 This plot shows how stepwise increases in the fractional water flow rate F_w, produce increasing steady-state water saturations in the Fontainebleau sandstone. Both hexane and dodecane were used as the oil phase.

5.3.5 Measuring the Water Saturation of the Fontainebleau Sample.

Experiments were performed with the Fontainebleau sandstone saturated with both an aqueous and an oil phase. An important parameter was therefore the water saturation S_w {see section 3.2.3}. Two different methods were required to measure the water saturation of the sample, depending on whether the aqueous phase of 3% w/v NaCl brine was made with D_2O or H_2O.

Method 1

With the aqueous phase made with H_2O the total ^1H NMR signal arises from both the aqueous and oil phases. In this case the water saturation was determined from the ^1H NMR chemical shift spectrum.

A slice selective spin-echo sequence, see figure 5.5, was used to obtain the time varying ^1H NMR signal of the central 36mm slice of the sample, with both phases stationary. This signal was Fourier transformed and the magnitude calculation performed to give the magnitude spectra. The NMR properties of Fontainebleau sandstone are such that, with the B_0 field homogenised over the sample by careful adjustment of the correction (shim) coils {see section 2.8.8}, the ^1H NMR spectrum can be resolved into contributions from the aqueous and oil phases, see figure 5.6.

The slice selection ensured that only ^1H NMR signal from inside the sample was measured and that end effects were avoided. The formation of a spin echo is important because it establishes a symmetry in the NMR signal which eliminates the contribution of the dispersion lineshape after Fourier transformation [1,5]. As a result the usual magnitude calculation can be performed without broadening the NMR spectrum, keeping the oil and water components well separated.

The fact that the area of the magnitude spectra is directly proportional to the number of protons present in the sample, was used to determine the water saturation of the sample. The chemical shift spectrum was fitted to the sum of three Gaussians, one each for the H_2O, CH_2 and CH_3 protons, figure 5.6 shows such a deconvolution. The fit was constrained by making use of the known relative chemical shifts of the H_2O, CH_2 and CH_3 protons and the ratio of CH_2 to CH_3 protons in the oil phase. The water saturation S_w was determined from the ratio of the area of the water peak to the total area of the spectrum.

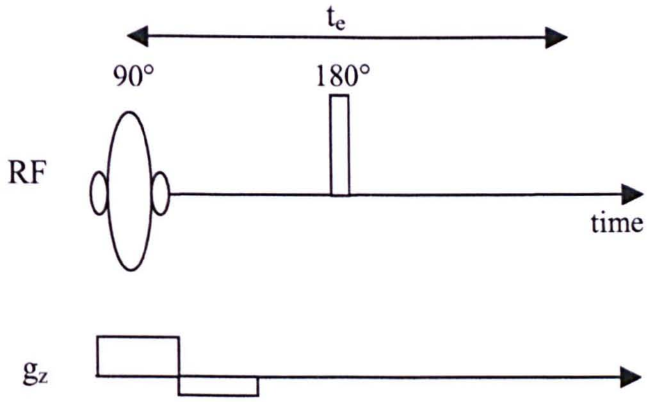

Figure 5.5 The slice selective spin echo sequence.

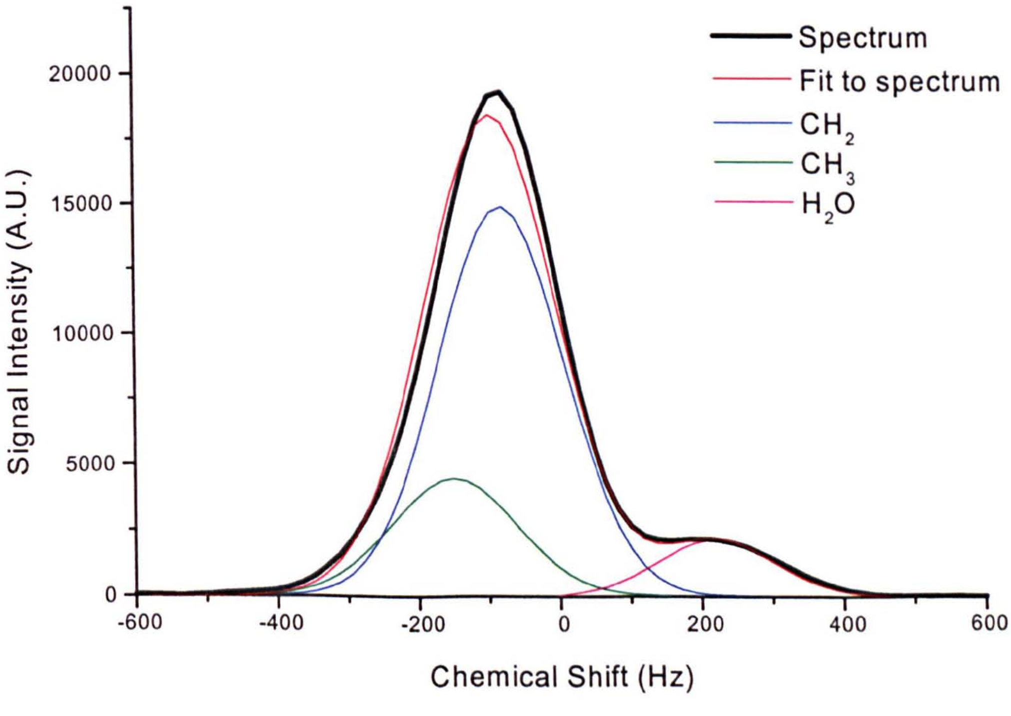

Figure 5.6 Chemical shift spectrum of dodecane and water in Fontainebleau sandstone at S_{wi}=0.06 and the deconvolution into H_2O, CH_2 and CH_3 protons.

Parameter name[*]	**Description**	**Value**
t_e	Echo time	15ms
pw	90° pulse width	67μs
sinct	Soft pulse duration	600μm
spl	Soft pulse power	21%
st	Slice thickness	36mm
cb	Number of data points	256
dw	Dwell time	53μs
na	Number of scans	32

[*] Parameter names used in GEΩ pulse programming software.

Table 5.2 Experimental parameters used in slice selective spin echo sequence.

Method 2

With the aqueous phase made with D_2O, the ^1H NMR signal only arises from the oil phase. In this case the water saturation was determined from the magnitude of the ^1H NMR signal of the oil phase.

The sample was initially cleaned and 100% saturated with the oil phase, i.e. S_w=0. A slice selective 90° pulse was used to measure the ^1H NMR signal of the central 36mm slice of the sample, using the parameters in table 5.3. The magnitude of this signal $M(S_w=0)$ was used as the reference. After a new water saturation had been produced in the sample, via the primary drainage/second imbibition process, the proton signal of the central 36mm slice was measured again, using the same parameters. Measurements were made with both phases stationary. The magnitude of this signal $M(S_w)$ was used to give the new water saturation S_w:

$$S_w = 1 - \frac{M(S_w)}{M(S_w = 0)} \tag{5.2}$$

Parameter[*]	**Description**	**Value**
sinct	Soft pulse duration	600μs
spl	Soft pulse power level	21%
st	Slice thickness	36mm
tr	Recycle time	$5\times T_1$
na	Number of scans	32
gn	gain	10

[*] Parameter names used in GEΩ pulse programming software.

Table 5.3 Experimental parameters of the slice-selective 90° pulse used to measure the water saturation in method 2.

5.3.6 Comparison

Measurements of S_w made by the two methods, can be compared when the sample is at the well defined states of S_{wi} and S_{or} , these states being produced by the primary drainage and secondary imbibition cycle. Both methods gave the irreducible water saturation as $S_{wi} \sim 0.06$, although method 1 gave the residual oil saturation as $S_{or} \sim 0.38$ (i.e. S_w=0.62) whereas method 2 gave $S_{or} \sim 0.3$ (i.e. S_w=0.7). Because method 2 is intrinsically the more accurate, saturations measured with method 1 were scaled to have a residual oil saturation of $S_{or} = 0.3$ (i.e. S_w=0.7).

5.4 Glass Bead Packs

5.4.1 Sample Characteristics

The idealized porous solids used in this thesis were packs of water-wet glass beads, which had a nominal diameter of 100μm. Measurements were performed with the beads saturated with two immiscible phases, a wetting phase of distilled water and a non-wetting phase of tetrachloroethylene (C_2Cl_4). The latter was chosen because it gives no ^{1}H NMR signal. The sample used comprised a 40.4 mm inner diameter cylindrical glass tube packed with glass beads initially saturated with distilled water. Packing was achieved by stepwise addition of the glass beads into the glass tube filled with water, the beads were allowed to settle and then gently compacted. The glass tube was fitted at both ends with sintered glass disks and caps. The sintered glass disks ensured an even distribution of flow over the face of the sample

5.4.2 Establishing Different Saturations

Starting with the sample at S_w=1, lower water saturations were produced by flowing tetrachloroethylene at a constant flow rate through the sample, until an equilibrium was reached and no more water was produced. The maximum flow rate that could be applied without damaging the sample was 600ml/h, which gave rise to S_w=0.25. In order to reach smaller values of S_w the glass bead pack was re-made. The glass beads were washed with acetone using a vacuum Buckner flask, and then dried in an oven (100°C). The appropriate amount of water was added to the clean dry beads to produce the desired water saturation, the beads were then mixed by stirring to create a uniform distribution of the water. An excess of tetrachloroethyene was then added and mixed by stirring. The sample was re-packed and left for several hours to equilibrate. This was performed for S_w = 0.05, 0.1, 0.15 and 0.2. The value of S_w was determined by the same method described in section 5.3.5 method 2, but with a slice thickness of 40mm. To verify that the water was uniformly distributed throughout the sample, one-dimensional ^{1}H NMR profiles were also acquired.

5.5 Relaxation Measurements

In this thesis relaxation measurements are reported for both the Fontainebleau sandstone and the glass bead pack samples. All relaxation curves were fitted using a discrete multiple exponential method, using a non-linear least squares regression program called XFIT. This program was written by BP Research.

5.5.1 Measuring Longitudinal Relaxation

The inversion-recovery sequence was used to measure spin-lattice relaxation. The sequence was modified to include a slice selective 90° pulse, as shown in figure 5.7. This ensured that only the ^{1}H NMR signal from fluid contained within the porous solid was acquired, and not from fluid present in the supply pipes and the maze-like diffuser at the end of the sample holder {see figure 5.2}. Typical experimental parameters are given in table 5.4. The inversion recovery sequence generates '*maxpts*' number of points, logarithmically spaced from '$T1max \times fract$' to '$5 \times T1max$' {see table 5.4}.

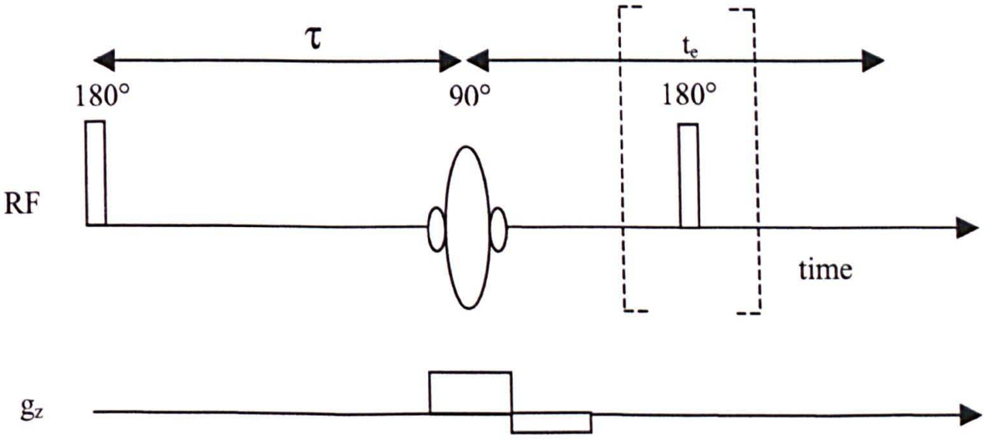

1. First 180° pulse = {0,0,0,0,90,90,90,90,180,180,180,180,270,270,270,270}
2. Soft 90° pulse = {0,90,180,270, 90,180,270,0,180,270,0,90 ,270,0,90,180}
3. Second 180° pulse = {0,0,0,0 ,90,90,90,90,180,180,180,180,270,270,270,270}
4. Receiver phase = {180,90,0,270,270,180,90,0,0,270,180,90,90,0,270,180}

Figure 5.7 The inversion recovery sequence, with slice selection. To acquire the signal as a spin echo a 180° pulse is added after the soft pulse. Phase cycling given in the inset table.

Parameter name[*]	**Description**	**Value**
maxpts	Number of data points	32,64
T1max	Maximum T_1 value	Depends on sample
fract	Fraction of T_1 for first point	0.005
t_e	Echo time	15ms
pd	Pre-delay	5×T1max
pshift	Receiver phase	Adjusted for each sample
ppl	Pulse power level	100%
pw	90° pulse width	67μs
st	Slice thickness	36mm (Fontainebleau) 40mm (glass beads)
sinct	Soft pulse duration	600μs
spl	Soft pulse power	21%
sincc	Sinc pulse cycles	2

* Parameter names used in GEΩ pulse programming software.

Table 5.4 Typical experimental parameters used in the inversion-recovery sequence.

In the case of Fontainebleau sandstone saturated with an aqueous phase made with H_2O and an oil phase, the chemical shifts of the two phases can be resolved. It was therefore possible to measure the longitudinal relaxation of both phases simultaneously. To accomplish this, the signal from the inversion recovery sequence, for each τ value, was acquired as a spin echo (t_e=15ms, see figure 5.7). Fourier transforming the spin echo and taking the absolute value, gave the chemical shift spectrum for that value of τ. The decays of the aqueous and oil peaks with τ were then fitted to give the longitudinal relaxation times of each phase. The formation of a spin echo was important in helping to resolve the chemical shift spectrum {see section 5.3.5}.

5.5.2 Measuring Transverse Relaxation

The transverse relaxation behaviour was measured using the CPMG pulse sequence {see section 2.5.2}. This pulse sequence was again modified to include a slice-selective 90° pulse, see figure 5.8. Typical experimental parameters are given in table 5.5.

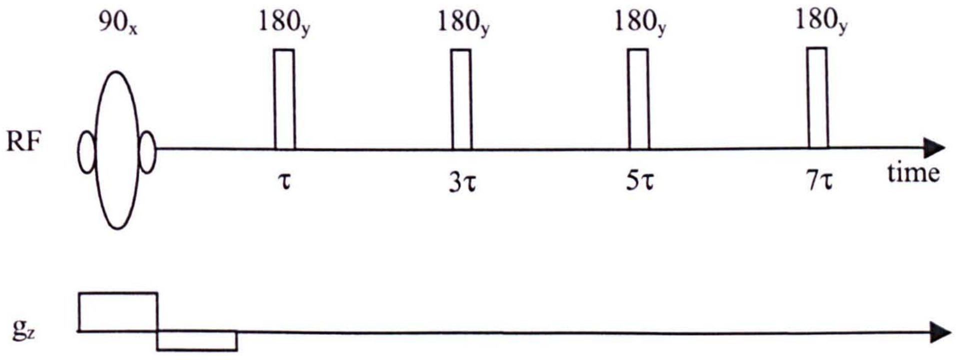

1. Soft 90° pulse = {0,180,90,270,0,180,90,270}
2. 180° pulses = {90,90,180,180,270,270,0,0}
3. Receiver = {0,180,90,270,0,180,90,270}

Figure 5.8 The CPMG pulse sequence with an initial slice selective 90° pulse. Phase cycling given in the inset table.

Parameter name*	**Description**	**Value**
nechoes	Number of echoes	1024
tau	τ	1.2, 2, 3 and 4ms
pw	90° pulse width	67μs
sinc	Soft pulse width	600μs
spl	Soft pulse power	21%
st	Slice thickness	36mm (Fontainebleau) 40mm (Glass Beads)
pd	Pre-delay	$5\times T_1$
pshift	Reciever phase shift	Adjusted for each sample

* Parameter names used in GEΩ pulse programming software.

Table 5.5 Typical experimental parameters for the CPMG sequence.

5.6 Pulsed Field Gradient Experiments

The basic pulsed field gradient experiment is the PGSE experiment, this was described in detail in section 2.7.1. However, this sequence is not the most suitable for studying porous solids. Therefore, measurements were performed using a variant sequence called the alternating pulsed field gradient stimulated echo sequence (APGSTE). This sequence was used to measure one- and two-dimensional displacement propagators.

5.6.1 Alternating Pulsed Field Gradient Stimulated Echo (APGSTE)

The basic pulsed field gradient spin echo (PGSE) experiment, and the stimulated echo modification (PGSTE) of Tanner [6] were described earlier {section 2.7.1}. In a sample like Fontainebleau sandstone, the differences between the magnetic susceptibilities of the porous solid and the saturating fluid results in non-uniform internal magnetic field distributions, i.e. background magnetic field gradients. These susceptibility effects can be as significant as that of the applied field gradients [7]. These internal effects add vectorially to the externally applied gradients and exhibit a complex influence on the observed echo attenuation. Dual or multiple alternating gradient pulse methods [8,9,10] have been proposed to decouple the effect of background gradients. The sequence used in this study is a variant of the '13-interval, Condition I' sequence of Cotts et al [11]. This sequence reduces the effect of background field gradients by having opposite polarity gradient pulse pairs symmetrically disposed about a 180° pulse, see figure 5.9. The phase encoding caused by the applied gradients then accumulates whilst that caused by any background gradients is significantly refocused, to the extent permitted by molecular translations [12]. It was shown by Lucas et al. [13] that the APGSTE sequence was less sensitive to the effect of strong background field gradients than either the PGSE or PGSTE pulse sequences. A further modification was proposed by Johnson and Gibbs [14] to avoid errors arising from eddy current fields induced by large gradient pulses. This modification involves the z-storage of the stimulated echo, for a period 'stor_z', this separates the acquisition window from any field transients produced by the final gradient pulses.

The APGSTE sequence of RF pulses can generate several signals during the acquisition period corresponding to different coherence transfer pathways. Gradient spoiler pulses and full phase cycling {see figure 5.9} ensure that the desired signal is accumulated preferentially. This phase cycling was adapted from Fordham et al [15] to discriminate the effects of positive and negative displacements on the NMR signal. This was done by offsetting the phase of the second 90° pulse ("90 z storage" in figure 5.9) by $\pi/2$, in order to measure both transverse components of the NMR stimulated echo.

5.6.2 One-dimensional Displacement Propagators

One-dimensional displacement propagators were measured in the following manner. The one-dimensional APGSTE ^1H NMR signal $E_\Delta(q_z)$ was acquired for a central slice (36mm for Fontainebleau, 40mm for glass beads). This ensured that only the ^1H

NMR signal from fluid inside the porous solid was acquired, and not from fluid present in the supply pipes and the maze-like diffuser at the end of the sample holder. $E_{\Delta}(q_z)$ was measured for 32, 64 or 128 values of q_z in the range $-q_{max}$ to q_{max}, where $q_z = (2\pi)^{-1}\gamma g_z\delta$. The q_z value was obtained by stepping the magnitude of the pulsed magnetic field gradient g_z, whilst leaving the gradient duration $\delta/2$ constant {see figure 5.9}. The Fourier transformation of $E_{\Delta}(q_z)$ with respect to q_z gives the average propagator $P_{\Delta}(Z)$ {see section 2.7.1, equation 2.48}. The average propagators were then normalised. Typical experimental parameters are given in table 5.6.

In chapter 8 measurements are made with the Fontainebleau sandstone saturated with an aqueous phase made with H_2O and an oil phase of dodecane. As described in section 5.3.5 it is possible to resolve the chemical shift spectrum of these two phases, it is therefore possible to measure the average propagators of both phases simultaneously. To do this the response of the APGSTE sequence was acquired as a full spin echo $E_{\Delta}(q_z,t)$, using an echo time t_e=15ms and collecting 256 points with a dwell time of 53μs. The magnitude of the two-dimensional Fourier transform of $E_{\Delta}(q_z,t)$, with respect to q_z and t, results in chemical shift resolved propagators. The water and oil propagators were taken from the chemical shift peaks of the water and oil phases.

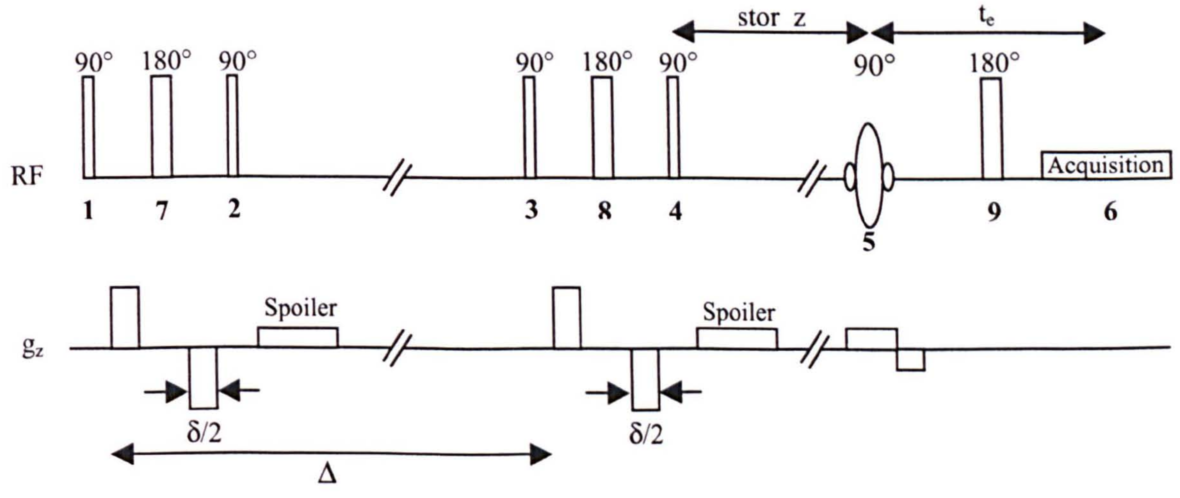

1 “first 90 pulse” = { 0,0,90,90,180,180,270,270,0,0,90,90,180,180,270,270}
2 “90 z-storage” = {0,0,0,0,0,0,0,0,90,90,90,90,90,90,90,90}
3 “90 read” = {180,180,270,270,180,180,270,270,180,180,270,270,180,180,270,270}
4 “90 z-storage” = {180,180,180,180,180,180,180,180, 180,180,180,180,180,180,180,180}
5 “90 read pulse” = {0,0,0,0,0,0,0,0,0,0,0,0,0,0,0,0}
6 “receiver” = {0,180,0,180,180,0,180,0,90,270,90,270,270,90,270,90}
7 “first 180 pulse” = {90,180,180,270,270,0,90,90,180,180,270,2700,0,90}
8 “second 180 pulse” = { 270,270,0,0,270,270,0,0,270,270,0,0,270,270,0,0}

Figure 5.9 The Alternating Pulse Field Gradient Stimulated Echo pulse sequence. The full phase cycling is given in the inset table. Each RF pulse is labelled with a number

Parameter name*	**Description**	**Value**
big_d	Observation time Δ	100ms – 2s
dfgrmaxx	Maximum x-gradient	4000 Hz/mm (maximum)
dfgrmaxz	Maximum z-gradient	4000 Hz/mm (maximum)
small_d	Duration of gradient pulses, δ/2	1 - 5 ms
flowres	Number of q values	16,32,64,128
tr	Recycle time	5×T_1
spoil1	First crusher gradient duration	4ms
spoil2	Second crusher gradient duration	5ms
spmag1	Size of first spoiler gradient	1500 Hz/mm
spmag2	Size of second spoiler gradient	-1800 Hz/mm
set_t	Time between gradient and RF pulses	750μs
stor_z	z-storage time	50ms
t_e	Echo time	15ms
sinct	Soft pulse duration	600μs
spl	Soft pulse power	21%
sincc	Sinc pulse cycles	2

* Parameter names used in GEΩ pulse programming software.

Table 5.6 Typical experimental parameters for the APGSTE sequence.

5.6.3 Two-dimensional Displacement Propagators

The one-dimensional APGSTE sequence was modified by Stapf et al [16,17] to measure two-dimensional propagators. This was achieved by applying gradient pulses simultaneously in two orthogonal directions. Figure 5.10 shows the pulse sequence used. The echo attenuation $E_\Delta(\mathbf{q})$ of this two-dimensional APGSTE sequence is given by equation 2.48, where **q** consists of two orthogonal components q_x and q_z thus:

$$\mathbf{q} = q_x\mathbf{i} + q_z\mathbf{k} \tag{5.3}$$

where **i** and **k** are unit vectors along the x- and z-axes, respectively. A 16×16 matrix of $E_\Delta(\mathbf{q})$ was acquired by stepwise variation of q_x and q_z, using 14 positive and 2 negative evenly spaced values of q_x and q_z. The two negative q values serve to determine the zero-q phase shift, which enables the reconstruction of the full 28×28 matrix of $E_\Delta(\mathbf{q})$. The maximum gradient value used is q_{max}, which determines the resolution in displacement space. The two-dimensional average propagator $P_\Delta(X,Z)$, for displacements X and Z, is calculated by successively Fourier transforming the matrix in both directions. The two-dimensional displacement propagator $P_\Delta(X,Z)$ describes the probability density of a spin bearing particle simultaneously having displacements X and Z in the time interval Δ.

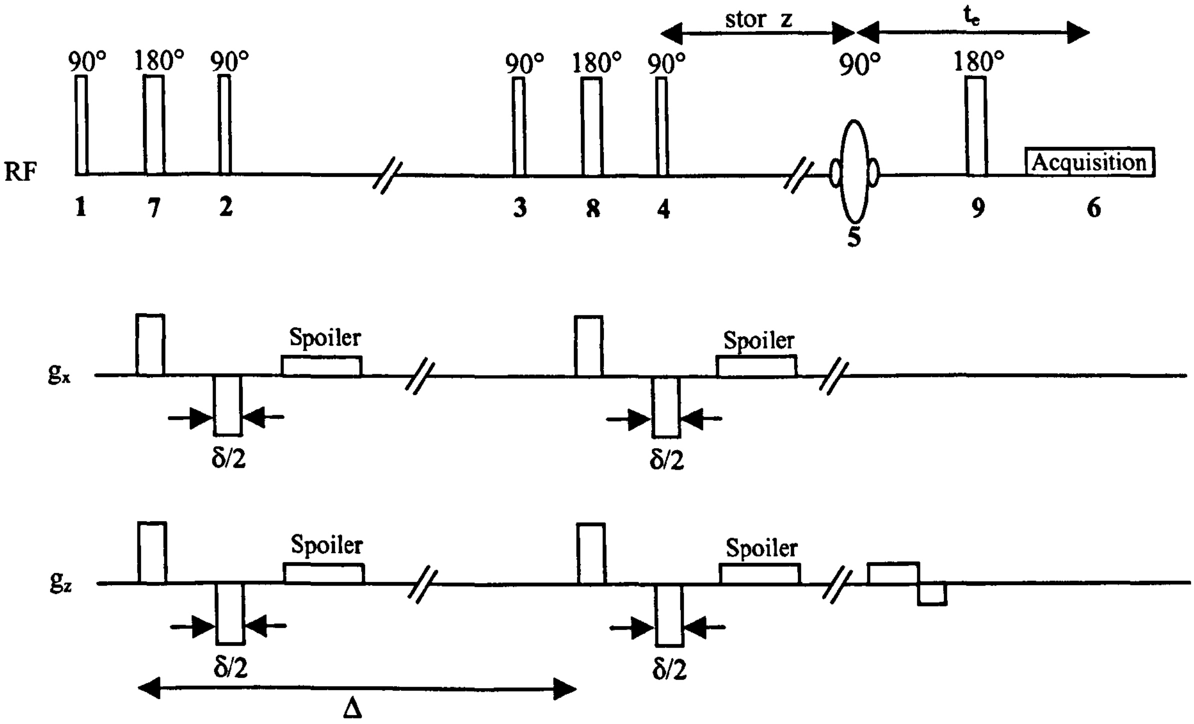

Figure 5.10 The two-dimensional Alternating Pulsed Field Gradient Stimulated Echo sequence.

5.7 References

1. Tessier J.J., Packer K.J. "Characterization of Multiphase Fluid Transport in a Porous Solid by Pulsed Field Gradient Stimulated Echo NMR". 1998. Physics of Fluids. 10. 75-85.
2. Dullien F.A.L. "Porous Media: Fluid Transport and Pore Structure". 1992. Academic Press Ltd.
3. Packer K.J. "Oil Reservoir Rocks Examined by MRI". Encyclopaedia of NMR. 3376-3378.
4. Bear J. "Dynamics of Fluids in Porous Media". 1972. American Elsevier. New York.
5. Marshall A.G., Verdun F.R. "Fourier Transforms in NMR, Optical and Mass Spectrometry". 1990. Elevier. Amsterdam.
6. Tanner J.E. "Use of the Stimulated Echo in NMR Diffusion Studies". 1970. Journal of Chemical Physics. 52. 2523-2526.
7. Hurlimann M.D. "Effective Gradients in Porous Media Due to Susceptibility Differences". 1998. Journal of Magnetic Resonance. 131. 232-240.
8. Packer K.J., Rees C., Tomlinson D.J. 1970. Molecular Physics. 18. 421.
9. Williams W.D., Seymour E.F.W., Cotts R.M. " A Pulsed-Gradient Multiple-Spin_Echo NMR Technique for Measuring Diffusion in the Presence of Background Magnetic Field Gradients". 1978. Journal of Magnetic Resonance. 31. 271-282.
10. Latour L.L., Li L., Sotak C.H. "Improved PFG Stimulated Echo Method For The Measurement of Diffusion in Inhomogeneous Fields". 1992. Journal of Magnetic Resonance B. 101. 72-77.
11. Cotts R.M., Hoch M.J.R., Sun T., Marker J.T. "Pulsed Field Gradient Stimulated Echo Methods for Improved NMR Diffusion Measurements in Heterogeneous Systems". 1989. 83. 252-266.
12. Karlicek R.F., Lowe I.J. "A Modified Pulsed Gradient Technique for Measuring Diffusion in the Presence of Large Background Gradients". 1979. Journal of Magnetic Resonance. 37. 75-91.
13. Lucas A.J., Gibbs S.J., Jones E.W.G., Peyron M., Derbyshire J.A., Hall L.D. "Diffusion Imaging in the Presence of Static Magnetic Field Gradients". 1993. Journal of Magnetic Resonance A. 104. 273-82.
14. Gibbs S.J., Johnson C.S. "A PFG NMR Experiment for Accurate Diffusion and Flow Studies in the Presence of Eddy Currents". 1991. Journal of Magnetic Resonance. 93 .395-402.
15. Fordham E.J., Gibbs S.J., Hall L.D. "Partially Restricted Diffusion in a Permeable Sandstone: Observations by Stimulated Echo PFG NMR". 1994. Magnetic Resonance Imaging. 12. 279-284.
16. Stapf S., Packer K.J., Graham R.G., Thovert J.F., Adler P.M. "Spatial Correlations and Dispersion for Fluid Transport through Packed Glass Beads Studied by Pulsed Field-Gradient NMR". 1998. Physical Review E. 58. 6206-6201.
17. Stapf S., Packer K.J. "Two-Dimensional Propagators and Spatio-Temperal Correlations for Flow in Porous Media: A comparative Study". 1998. Applied Magnetic Resonance. 15. 303-322.

Chapter 6

Relaxation Study of Fontainebleau Sandstone

Contents

6.1 INTRODUCTION 98

6.2 LONGITUDINAL RELAXATION 98

6.2.1 EFFECT OF WATER SATURATION ON LONGITUDINAL RELAXATION 98
6.2.2 EFFECT OF FLOW RATE ON LONGITUDINAL RELAXATION 103

6.3 TRANSVERSE RELAXATION 104

6.3.1 EFFECT OF FLOW RATE AND TAU VALUE ON T_2 OF OIL PHASE 104
6.3.2 EFFECT OF WATER SATURATION ON TRANSVERSE RELAXATION 105

6.4 REFERENCES 109

6.1 Introduction

This chapter is concerned with the relaxation properties of the aqueous and oil phases contained within the Fontainebleau sandstone sample. The effects of water saturation and flow on transverse and longitudinal relaxation times, of both the oil and water phases, are described. This study provided background information for other experiments performed on the Fontainebleau sample, see chapters 7, 8 and 10. The variation in the T_1 of the water phase with water saturation is particularly interesting and is discussed in more detail in chapter 9.

All relaxation curves were fitted using a discrete multiple exponential method, using a non-linear least squares regression program called XFIT. This program was written by BP research.

6.2 Longitudinal Relaxation

The inversion recovery method was used to measure longitudinal relaxation [1]. This method was previously described in section 2.5.3 and 5.5.1. The 180° pulse inverts the bulk magnetization along the z-axis. The recovery of the magnetisation to its equilibrium value can be monitored by applying a 90° pulse a time τ later. The signal as a function of τ takes the form:

$$S(\tau) = S(0)\left[1 - 2\alpha \exp\left\{-\frac{\tau}{T_1}\right\}\right] \qquad (6.1)$$

where the factor α corrects for imperfections in the 180° pulse.

6.2.1 Effect of Water Saturation on Longitudinal Relaxation

The Fontainebleau sample was saturated with an aqueous phase of 3% NaCl brine made with H_2O and an oil phase of dodecane. In this case the ^1H NMR signal arises from both aqueous and oil phases. As the chemical shift spectrum of the two phases can be resolved, it is possible to measure the longitudinal relaxation of both phases simultaneously {see section 5.5.1}.

The inversion-recovery sequence was used to measure the longitudinal relaxation of both phases, with the Fontainebleau sample at different water saturations. Different water saturation states were prepared using the primary drainage/secondary imbibition process outlined in section 5.3.4. The water saturation S_w was measured from the chemical shift spectrum, using method 1 described in section 5.3.5. The inversion-recovery sequence was used to measure 32 data points, using τ values logarithmically spaced from 0.02s to 10s. A recycle delay of 10s was used to allow full recovery of M_z to M_0 between pulse sequence repetitions. Between 16 and 128 signal averages were taken to achieve a good signal-to-noise ratio {see section 2.8.10}. Measurements were performed with both phases stationary. The observed relaxation curves of both the oil and water phases were mono-exponential at all saturation states, see figure 6.1.

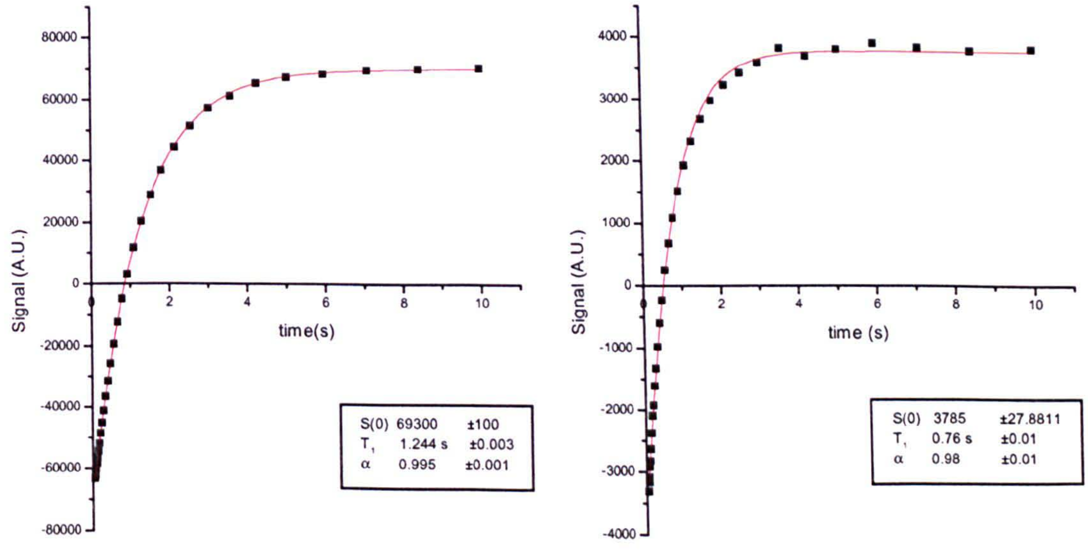

Figure 6.1 An example of longitudinal relaxation, measured using the inversion-recovery sequence, for oil (left) and water phases (right) contained within Fontainebleau sandstone at S_{wi}=0.06. The red lines show single exponential fits to the experimental data.

Figure 6.2 shows that the T_1 of the oil phase remains approximately constant, over the water saturation range studied, at around the T_1 value of bulk dodecane (1.2s). The same observation has been made by other authors [2,3,4], and these experiments were reviewed in section 4.2.1. The explanation for this lies in the strongly water-wet nature of the Fontainebleau sample. Over the range of water saturations investigated, the water phase forms a continuous film covering all the grain surfaces of the rock. This provides a barrier separating the oil phase from surface relaxation effects {section 2.6.1} which are dictated by couplings operating over atomic distances. In experiments performed by Latour [3] and discussed by Kleinberg [4], it was demonstrated that even a mono-layer of water reduces the longitudinal surface relaxivity of the oil phase by between 17 and 31 times.

By contrast, the T_1 of the water phase reduces from 2.58s for bulk water, to 1.46s when the water is contained within the Fontainebleau sample at S_w=1. Figure 6.3 shows that the T_1 of the water phase reduces further as the water saturation of the sample is reduced. This reduction in T_1 is caused by surface relaxation {see section 2.6.1}. This comparatively small decrease is consistent with the fact that Fontainebleau sandstone is a clean outcrop sandstone made up almost entirely of clean quartz, which is unlikely to be a very strong source of surface relaxation. In addition, the pore scale and large porosity gives the sample a modest surface-to-volume ratio.

It is generally assumed that at S_w=1 the water contained within a rock sample is in the fast diffusion (weak killing limit) regime of the Brownstein and Tarr surface relaxation model {see section 2.6.1}. In this regime, the rate-limiting step is relaxation

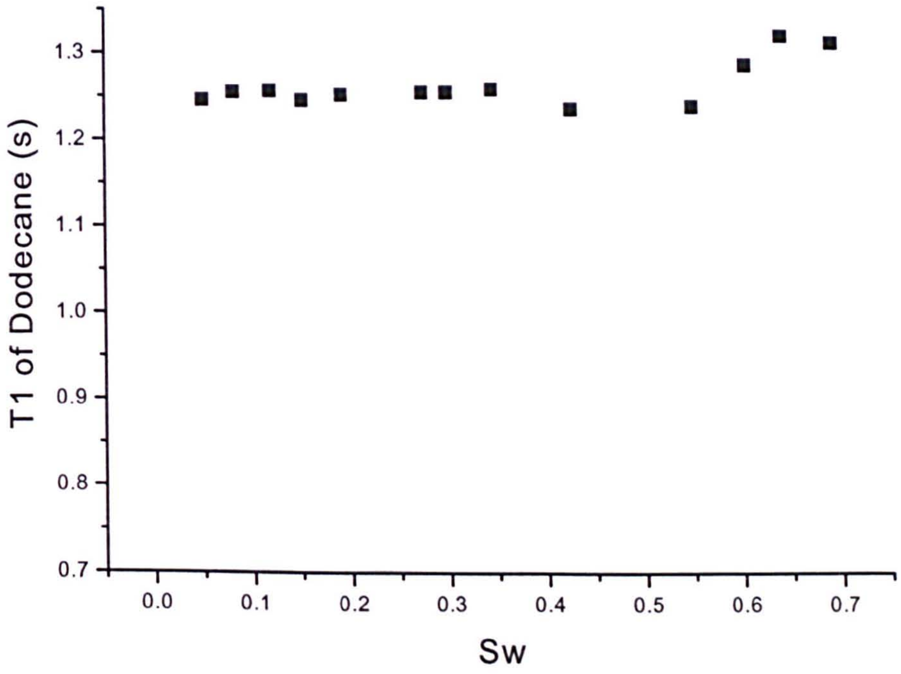

Figure 6.2 T_1 dependence of the oil phase as a function of the water saturation, S_w. The oil phase used was dodecane.

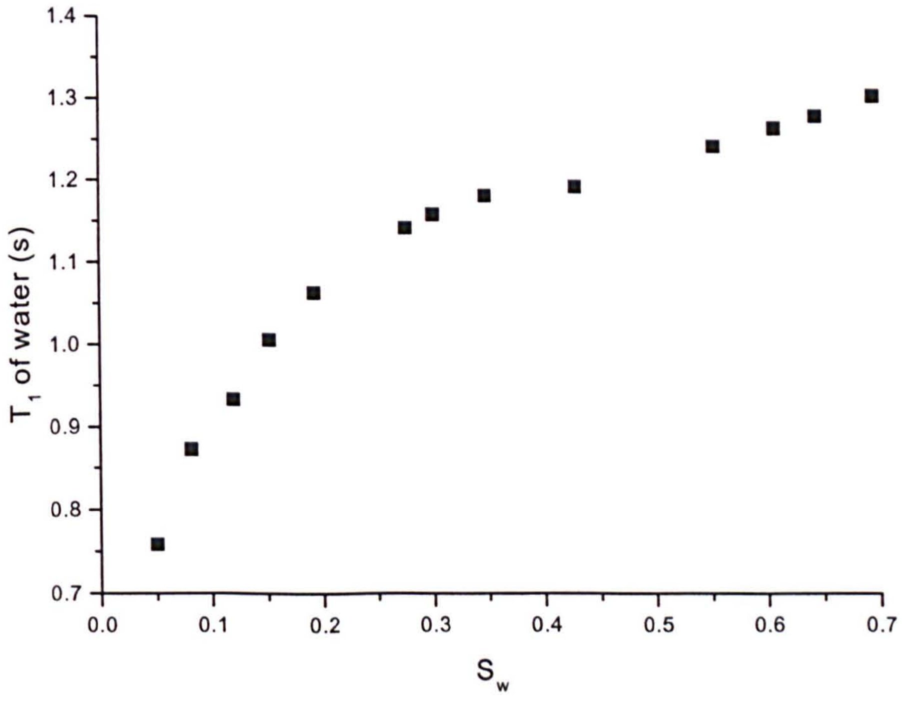

Figure 6.3 T_1 dependence of the water phase as a function of water saturation.

at the surface. Evidence for this was given by Latour et al [3], who showed that relaxation time distributions of water saturated sandstones were independent of temperature and hence, independent of the diffusion coefficient.

In the fast diffusion limit, the rate of magnetisation decay in an individual pore is mono-exponential and is dependent on the surface-to-volume ratio of the pore but is independent of the pore shape:

$$\frac{1}{T_1} = \frac{1}{T_{bulk}} + \rho_1 \left(\frac{S}{V} \right)_{pore} \tag{6.2}$$

where S is the surface area and V the volume of the pore, ρ_1 is the longitudinal surface relaxativity.

As most rocks have a large distribution of pore sizes, they exhibit multi-exponential decay. Such relaxation curves are normally fitted to a distribution of relaxation times [5]. There are two reasons for the water phase contained within Fontainebleau sandstone having mono-exponential longitudinal relaxation,

- The homogeneous Fontainebleau sample has a relatively narrow pore size distribution. This can be seen in the micrograph of Fontainebleau sandstone shown in figure 3.1.
- The weak surface relaxivity, modest S/V ratio and high permeability of Fontainebleau sandstone allows molecules to diffuse a long distance during the inversion recovery experiment. The rms displacement at S_w=1 during an observation time $T_1(S_w=1)$ is given approximately by:

$$\begin{aligned}\sqrt{\langle R^2 \rangle} &= 6D^* T_1 \\ &= 6 \times 1.1 \times 10^{-9} \times 1.46 \\ &\approx 100\mu m \approx 2 \text{ poresizes}\end{aligned}$$

  where D^* is the effective diffusion coefficient at S_w=1 {see section 8.13 for measurement of D^*}. If micro geometric heterogeneities occur over length scales small compared to this distance, then the quantity $\rho_1(S/V)$ is averaged over the volume explored by diffusing molecules. This concept of a length scale over which $\rho(S/V)$ is averaged is discussed by Borgia et al [6].

If the quantity $\rho_1(S/V)$ is averaged, then the relaxation rate should be dependant upon the surface-to-volume ratio of the whole sample:

$$R_1 = \frac{1}{T_1} = \frac{1}{T_{bulk}} + \rho_1 \left(\frac{S_0}{V_0} \right) \tag{6.3}$$

where S_0 and V_0 are the specific surface area and volume of the whole sample, respectively.

As Fontainebleau sandstone is strongly water-wet, the water phase forms a continuous film over all the grain surfaces. This film is present at all water saturations studied. Consequently, the specific surface area of the water phase is constant at all water saturations. Changes in the water saturation will only affect the specific volume of the water present in the sample. Therefore, for a strongly water-wet sample, the T_1 of the wetting phase in the fast diffusion limit, as a function of water saturation, is given by:

$$R_1 = \frac{1}{T_1} = \frac{1}{T_{bulk}} + \rho_1\left(\frac{S_0}{V_0}\right)\left(\frac{1}{S_w}\right) = \frac{1}{T_{bulk}} + C\left(\frac{1}{S_W}\right) \tag{6.4}$$

The result of plotting of $(T_1)^{-1}$ verse $(S_w)^{-1}$ for the water phase contained within Fontainebleau sandstone, is shown in figure 6.4. It can be seen that equation 6.4 holds for water saturations above $S_w=0.5$, fitting saturations above $S_w=0.5$ to equation 6.4 gives $\rho_1(S_0/V_0) = 0.20\pm0.02\ s^{-1}$. The reason for the break down of equation 6.4 at $S_w<0.5$ is that the water phase is no longer in the fast diffusion limit. This result is discussed in more detail in chapter 9, when it is compared to measurements made on an idealized porous solid.

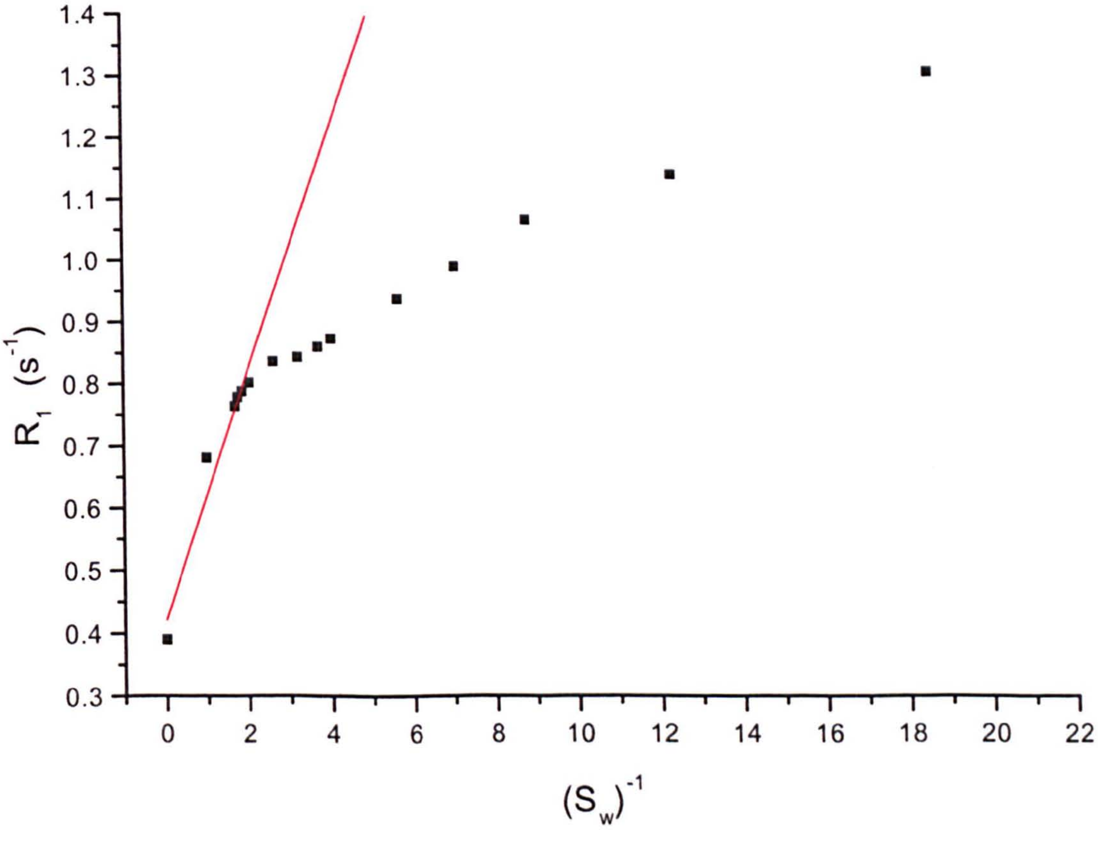

Figure 6.4 Plot of R_1 against $(S_w)^{-1}$. Line shows linear fit to equation 6.4 for $S_w>0.5$.

6.2.2 Effect of Flow Rate on Longitudinal Relaxation

In chapter 7 experiments are presented in which the oil phase is flowed through the Fontainebleau sample. It was therefore necessary to assess the effect of flow on the longitudinal relaxation of the oil phase.

The longitudinal relaxation of the oil phase was measured with the oil phase flowing through the Fontainebleau sample at different constant volume flow rates. The sample was saturated with two phases, an aqueous phase of 3% NaCl brine made with D_2O and an oil phase of either dodecane or hexane. The procedure described in section 5.3.4 was used to prepare the Fontainebleau sample in its irreducible water saturation state, $S_{wi}=0.06$. As the only ^1H NMR signal arises from the oil phase, the water saturation was determined from the magnitude of the ^1H NMR signal, compared with the ^1H NMR signal measured for the sample at $S_w=0$ {see method 2 section 5.3.5}.

The observed relaxation curves were mono-exponential at all flow rates. Figure 6.5 shows that flow has no effect on the measured T_1 value of the oil phase. Indeed, the T_1 of both oil phases was close to the measured bulk values, hexane $T_{1,bulk}=2.7$s, dodecane $T_{1,bulk}= 1.2$s.

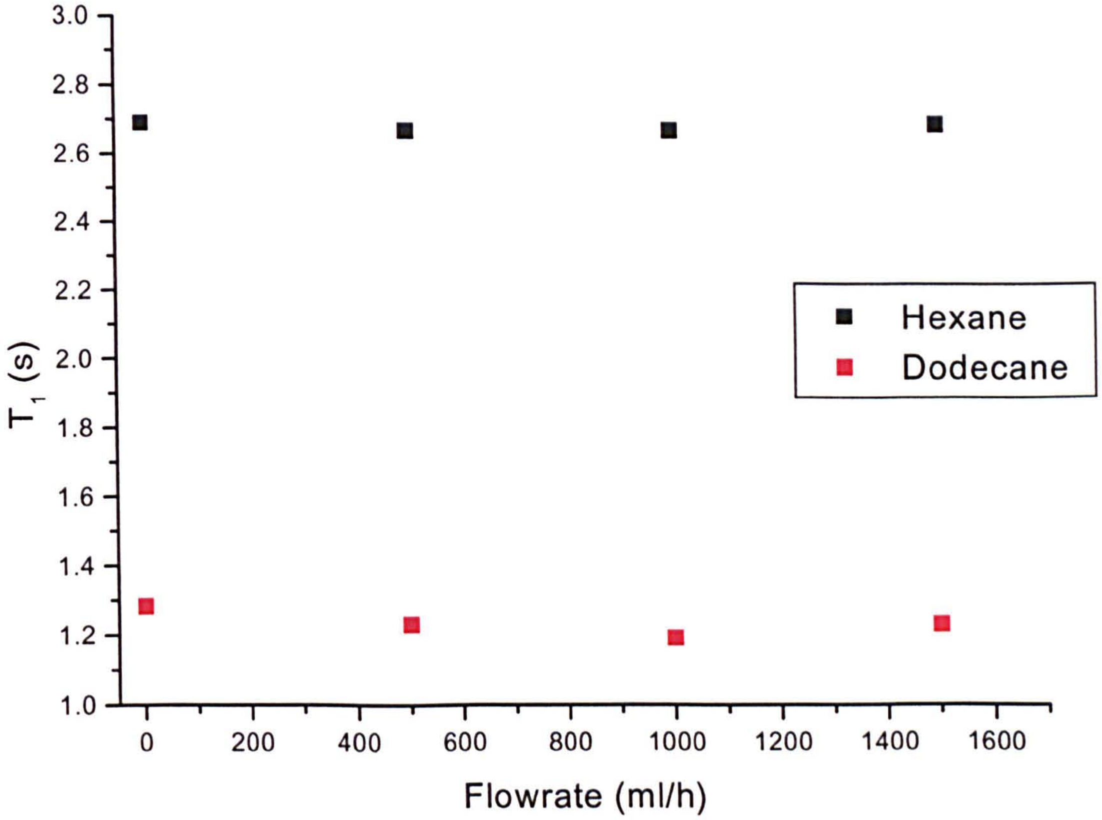

Figure 6.5 Longitudinal relaxation of the oil phase flowing through Fontainebleau sandstone, $S_{wi}=0.06$. The oil phases used were hexane and dodecane.

6.3 Transverse Relaxation

The Carr-Purcell-Meiboom-Gill (CPMG) sequence was used for measuring transverse relaxation. In this variant of the Carr Purcell sequence, the train of 180° pulses is applied along the y\` direction. This eliminates the need for perfect 180° pulses, as the echoes are always formed along the y\` axis regardless of the tip angle.

In these experiments the Fontainebleau sample was saturated with an aqueous phase of 3% NaCl brine made with D_2O and an oil phase of either dodecane or hexane. The procedure described in section 5.3.4, was used to prepare the Fontainebleau sample in different water saturation states. As the only ^1H NMR signal arises from the oil phase, the water saturation was determined from the magnitude of the ^1H NMR signal, compared with the ^1H NMR signal measured for the sample at $S_w=0$ {see method 2 section 5.3.5}.

6.3.1 Effect of Flow Rate and Tau Value on T_2 of Oil Phase

The transverse relaxation of the oil phase (both hexane and dodecane) was measured with the Fontainebleau sample at $S_{wi}=0.06$. Measurements were carried out with varying values of the spacing τ (1.2ms, 2ms ,3ms and 4ms) and with the oil phase flowing over a range of flow rates (0 to 500ml/h). The relaxation curves were well fitted by a bi-exponential function, an example fit is shown in figure 6.6.

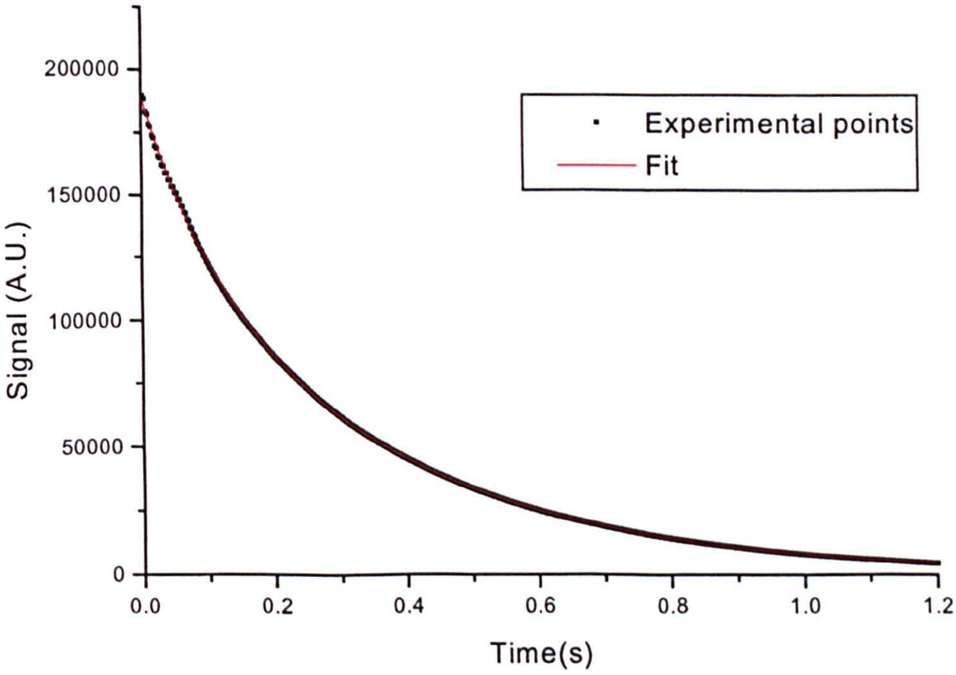

Figure 6.6 Example of a bi-exponential fit to CPMG decay curve, measured with τ =1.2ms. For Fontainebleau sandstone saturated with dodecane and D_2O at $S_{wi}=0.06$. The bi-exponential fit gives a short component of $T_2=89$ms (23.1%) and a long component of $T_2=339$ms (76.9%).

Figure 6.7 and 6.8 show how the bi-exponential fits to the CPMG decay curves, for an oil phase of hexane of dodecane, vary with τ and oil flow rate. The important features are.

- Transverse relaxation times decrease with increasing τ value, especially the long time component. The differences in magnetic susceptibilities between the porous solid and the saturating fluids results in non-uniform internal field distributions. Large τ values enable spins to explore more of the local field before being refocused, this leads to shorter transverse relaxation times.

- Transverse relaxation times decrease with increasing flow rate. This is most pronounced for the longer time component. Flow enables spins to explore more of the local field before being refocused, this leads to shorter transverse relaxation times. Flowing spins will also explore the local field differently to diffusing spins.

- The proportions of the long time components show a maxima with increasing flow rate. The position of this maxima depends on the τ value. The author offers no explanation for this result.

6.3.2 Effect of Water Saturation on Transverse Relaxation

The transverse relaxation of the oil phase (dodecane) was measured with the Fontainebleau sample in different water saturation states S_w. The τ spacing used in these experiments was 1.2ms, this was the shortest τ value the spectrometer was capable of. Other parameters are given in table 5.5.

Figure 6.9 shows the results of bi-exponential fits to relaxation curves measured at different water saturations. There is a slight decrease in the long T_2 component, from 200 to 155ms, and the short T_2 component, from 59ms to 43ms, as the water saturation is increased from $S_w = 0.06$ to 0.7. The proportion of the longer T_2 component decreases from 67% to 57% with increasing water saturation.

It was shown in section 6.2.1, that because the water phase forms a continuous surface wetting film, the oil phase experiences very little surface relaxation. The large differences in T_2 (<200ms for dodecane) and T_1(1.2s for dodecane) relaxation times of the oil phase, indicates that the diffusion of molecules through internal magnetic field gradients is the dominant transverse relaxation mechanism {see section 2.6.2}. Due to the complex nature of the internal gradients produced within a natural rock sample, the author offers no detailed explanation of these results, although others have begun to address this problem [7].

a)

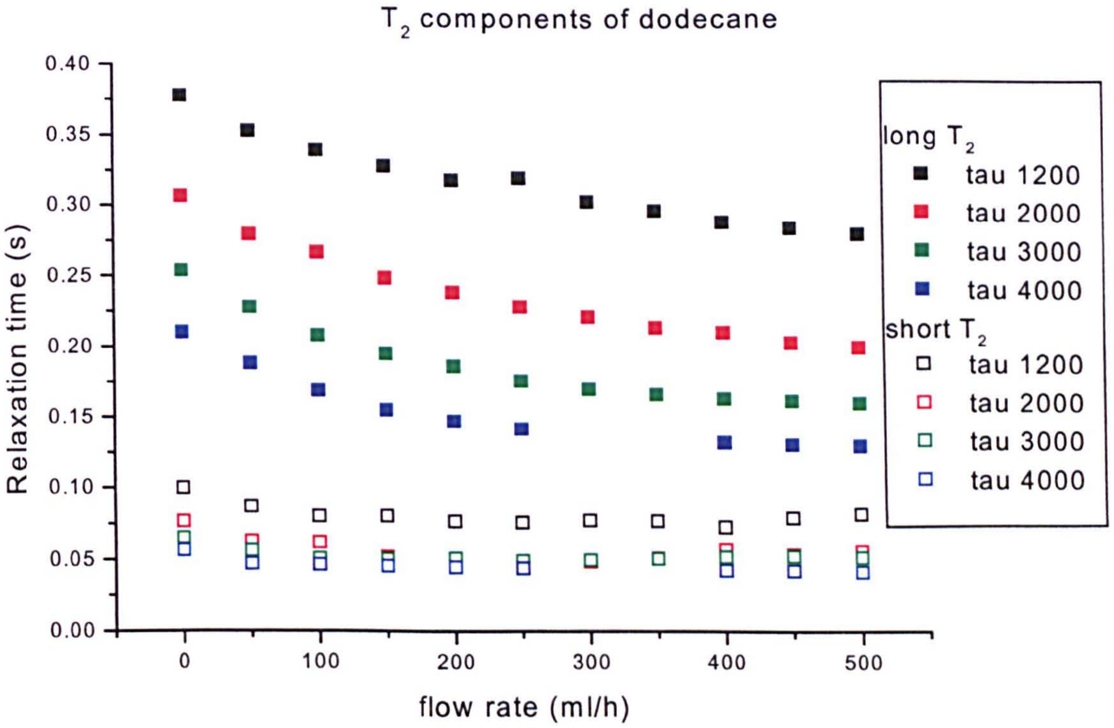

b)

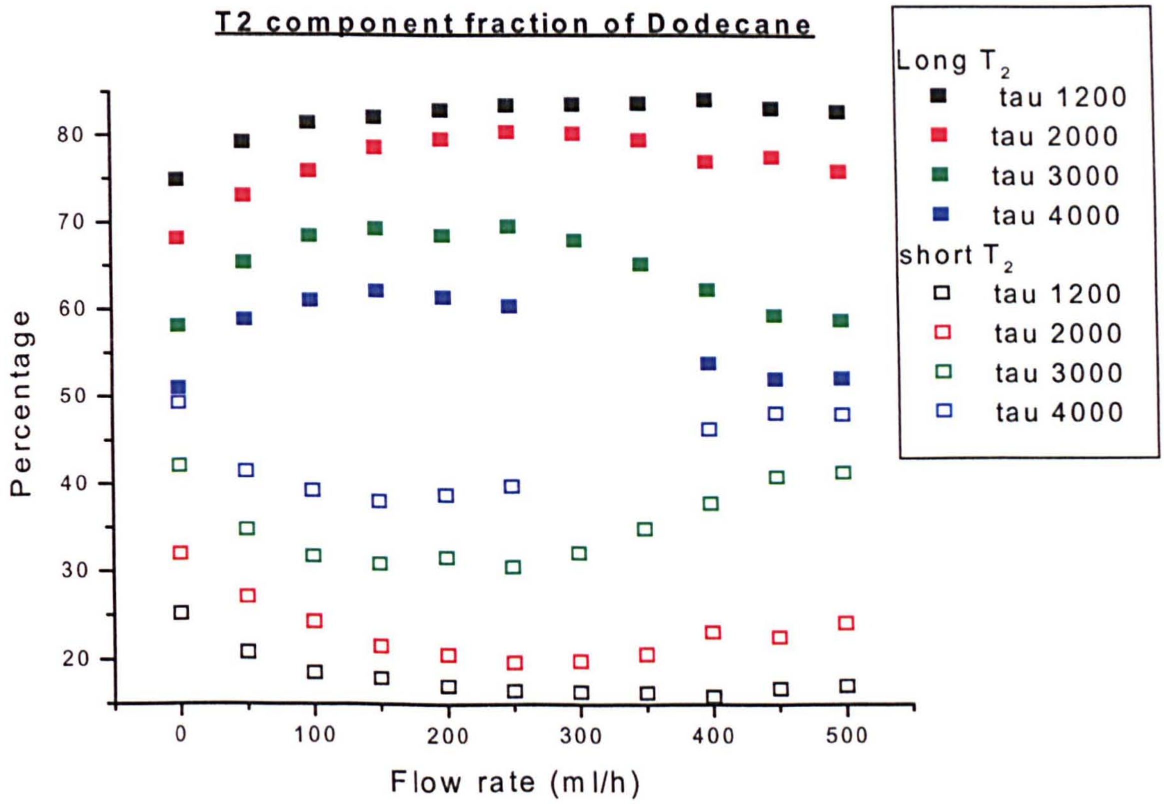

Figure 6.7 Results of fitting CPMG decay curves, for an oil phase of dodecane, to a bi-exponential function. Measurements were made at different τ spacings and for a range of oil flowrates. The sample was at its irreducible water saturation $S_{wi}=0.06$. a) Long and short T_2 components. b) Proportion of long and short T_2 components.

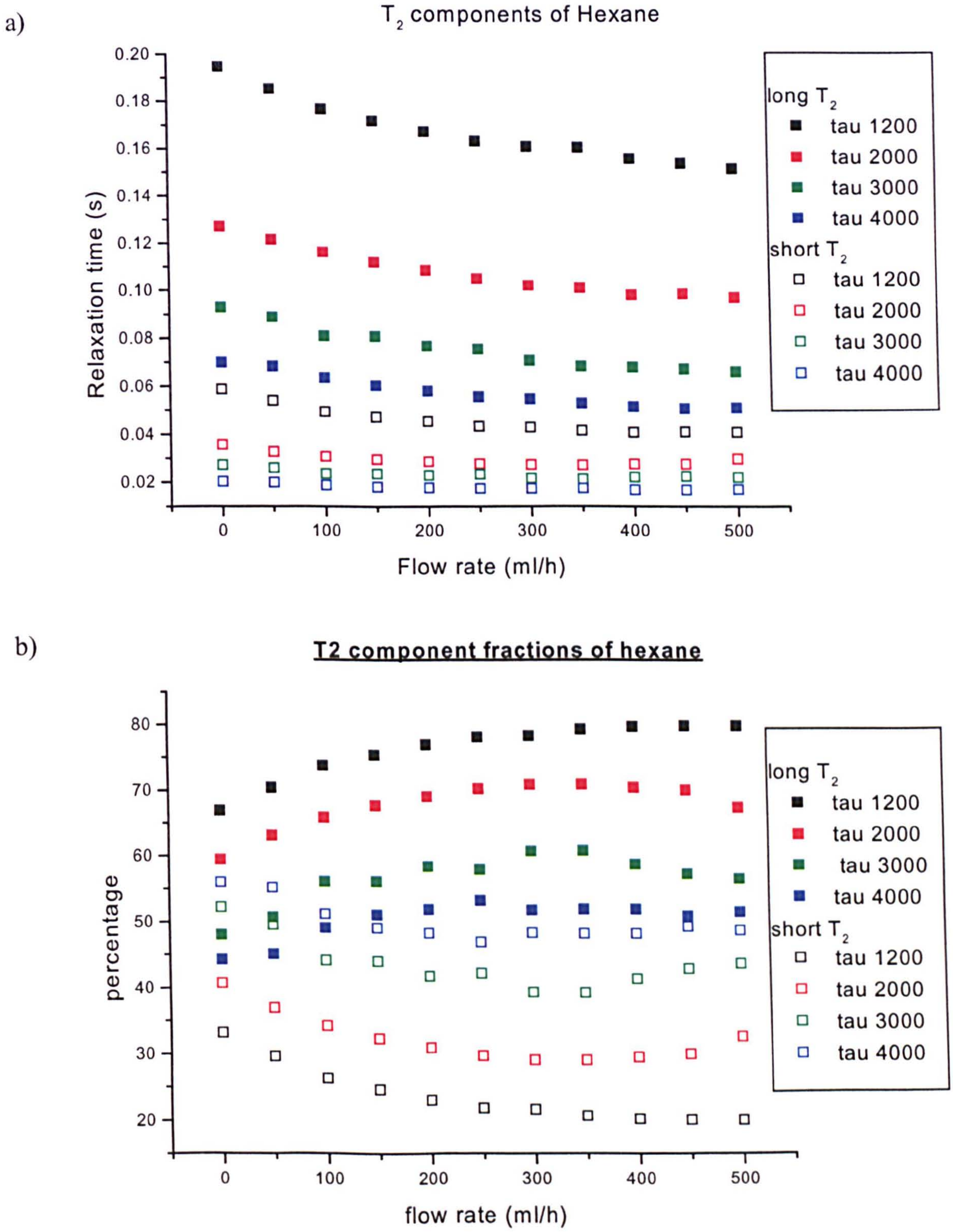

Figure 6.8 Results of fitting CPMG decay curves, for an oil phase of hexane, to a bi-exponential function. Measurements were made at different τ spacings and for a range of oil flowrates. The sample was at its irreducible water saturation S_{wi}=0.06. a) Long and short T_2 components. b) Proportion of long and short T_2 components.

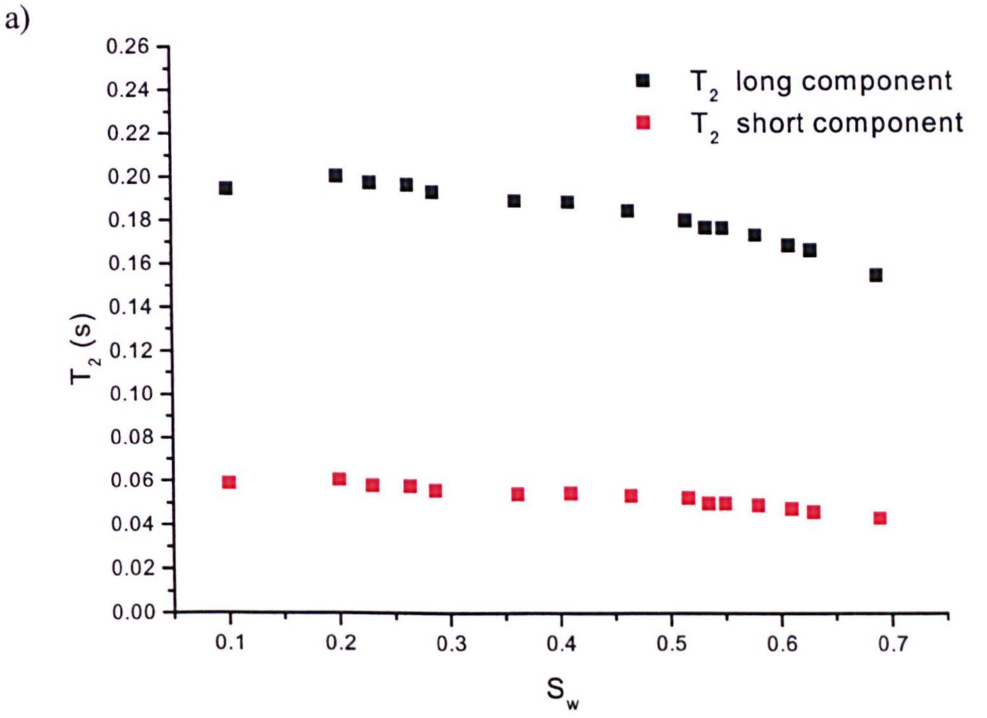

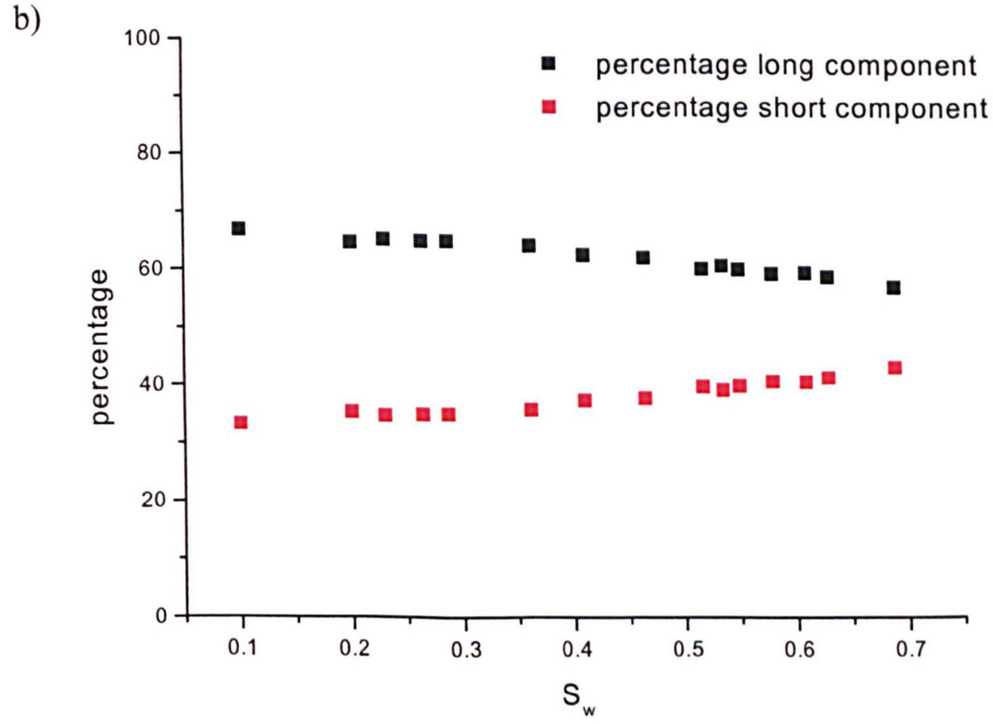

Figure 6.9 Results of fitting CPMG decay curves, measured at different water saturations, to a bi-exponential function. Using an oil phase of dodecane. a) Long and short T_2 components. b) Proportion of long and short T_2 components.

6.4 References

1. Vold R.L., Waugh J.S., Klein M.P., Phelps D.E. Journal of Chemical Physics. 1968. 48. 383.

2. Straley C., Morriss C.E., Kenyon W.E., Howard J.J. "Transactions of the SPLWLA 32nd Annual Logging Symposium". 1991.

3. Latour L.L., Kleinburg R.L. Sezginer A. "Nuclear Magnetic Resonance Properties of Rocks at Elevated Temperatures". 1992. Journal of Colloid and Interface Science. 150. 535-548.

4. Kleinberg R.L., Kenyon W.E., Mitra P.P. "Mechanism of NMR Relaxation of Fluids in Rock". 1994. Journal of Magnetic Resonance A. 108. 206-214.

5. Kenyon W.E. "Nuclear Magnetic Resonance as a Petrophysical Measurement". 1992. Nuclear Geophysics. 6. 153-171.

6. Borgia G.C., Brown R.J.S., Fantazzini P., Mesini E., Valdre G. 1992. Nuovo Cimento Soc. Ital. Fis.. 14. 745.

7. Proceedings of the Fourth International Meeting on Recent Advances in MR Applications to Porous Media. 1998. Magnetic Resonance Imaging. 14. 5-6.

Chapter 7

Stagnant Oil Produced by Secondary Imbibition

Contents

7.1 INTRODUCTION 112

7.2 PRELIMINARY INVESTIGATION 112

7.2.1 SAMPLE PREPARATION AND MEASUREMENT OF S_W 112
7.2.2 DISPLACEMENT PROPAGATORS 112
7.2.3 EXPLANATION OF INCREASING STAGNANT OIL FRACTION 117

7.3 INVESTIGATION OF THE STAGNANT OIL FRACTION 119

7.3.1 SAMPLE PREPARATION AND MEASUREMENT OF S_W 119
7.3.2 MEASURING THE ECHO ATTENUATION FUNCTION $E_\Delta(Q_Z)$ 119
7.3.3 EXPERIMENTAL RESULTS 119

7.4 PRELIMINARY SIMULATION RESULTS 124

7.5 CONCLUSIONS 126

7.6 REFERENCES 127

7.1 Introduction

In some oil wells, natural reservoir pressure causes oil and gas to flow to the surface, although most oil wells have to be pumped and eventually all have to be pumped. This constitutes the primary recovery stage. A universal method of secondary recovery from oil wells is by waterflood of the reservoir. Water is pumped into the reservoir at strategic points in an attempt to force out the oil.

For a water-wet sample like Fontainebleau sandstone, the displacement of the oil phase by water is called imbibition {see section 3.5}. During an imbibition process only a fraction of the oil phase is recovered, some of the oil phase becomes trapped in the sample. As the removal of small additional fractions of oil from large reservoirs can be extremely valuable, there is considerable interest in understanding these displacement processes [1,2].

Apart from macroscopic phenomenological observation of the relationship between fluids flowing into and out of a sample, there are very few experimental methods which can investigate these processes within the solid matrices. This chapter describes how PFG NMR was used to quantitatively differentiate between trapped and flowing oil in a sample of Fontainebleau sandstone, as the steady-state water saturation of the sample was increased in a stepwise fashion by a secondary imbibiton process.

7.2 Preliminary Investigation

A preliminary investigation was made of the effect of secondary imbibition on the transport properties of two immiscible phases flowing simultaneously through a sample of Fontainebleau sandstone. One-dimensional displacement propagators were used to monitor the transport properties of the two phases.

7.2.1 Sample Preparation and Measurement of S_w

The Fontainebleau sample was saturated with an aqueous phase of 3% NaCl solution made with H_2O and an oil phase of dodecane. Different steady-state water saturations were produced in the sample by the primary drainage/secondary imbibition process described in section 5.3.4. Figure 5.4 shows how different steady-state water saturations are produced in the Fontainebleau sample using different fractional water flowrates {see section 5.3.4}. As both phases give a ^1H NMR signal, the water saturation was determined from the ^1H NMR chemical shift spectrum {see method 1 of section 5.3.5}.

7.2.2 Displacement Propagators

A primary drainage/secondary imbibition process {see section 5.3.4} was used to produce different steady-state water saturations in the sample, with both the water and oil phases flowing simultaneously through the sample. Because it is possible to resolve the chemical shifts of the water and oil phases contained within Fontainebleau sandstone, it is possible to measure the displacement propagators of both phases simultaneously as they flow through the sample.

The one-dimensional APGSTE NMR signal was acquired as a spin echo $E_\Delta(q_z,t)$, for a central slice of the sample of thickness 36mm, where z is parallel to the flow direction. $E_\Delta(q_z,t)$ was measured for 128 equally spaced values of q_z in the range $-q_{max}$ to q_{max}. The absolute value of the two-dimensional Fourier transform of $E_\Delta(q_z,t)$ results in chemical shift resolved propagators [3]. Figure 7.1 shows an example of chemical shift resolved propagators. The one-dimensional water and oil propagators were taken from the water and oil chemical shift peaks.

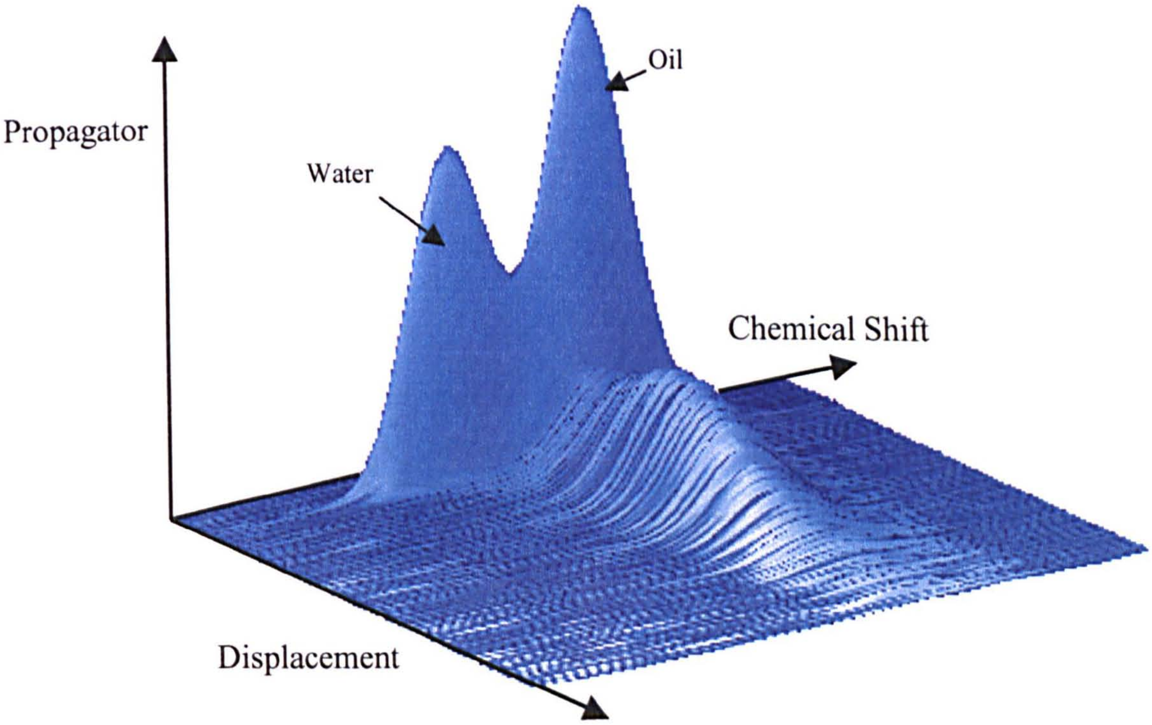

Figure 7.1 An example of chemical shift resolved propagators. Dodecane is flowing through the sample at 500ml/h, with the water phase stationary and with the sample at S_{wi}=0.06. Measurements were made for an observation time of 2s.

Figure 7.2 shows how the displacement propagators of the oil phase evolve with observation time Δ, for dodecane flowing at 500ml/h through the Fontainebleau sample at S_{wi}=0.06 (with the water phase stationary). As the observation time is increased, the oil propagator develops a bi-modal distribution. The peak centred at zero displacement represents oil molecules that have only experienced diffusive motion i.e. the stagnant oil fraction. Oil molecules that have experienced flow are moved to larger displacements, i.e. the flowing oil fraction. As the observation time is increased the flowing oil fraction has a larger mean displacement and the propagator spreads out due to dispersion [1,2], eventually forming a Gaussian-like distribution.

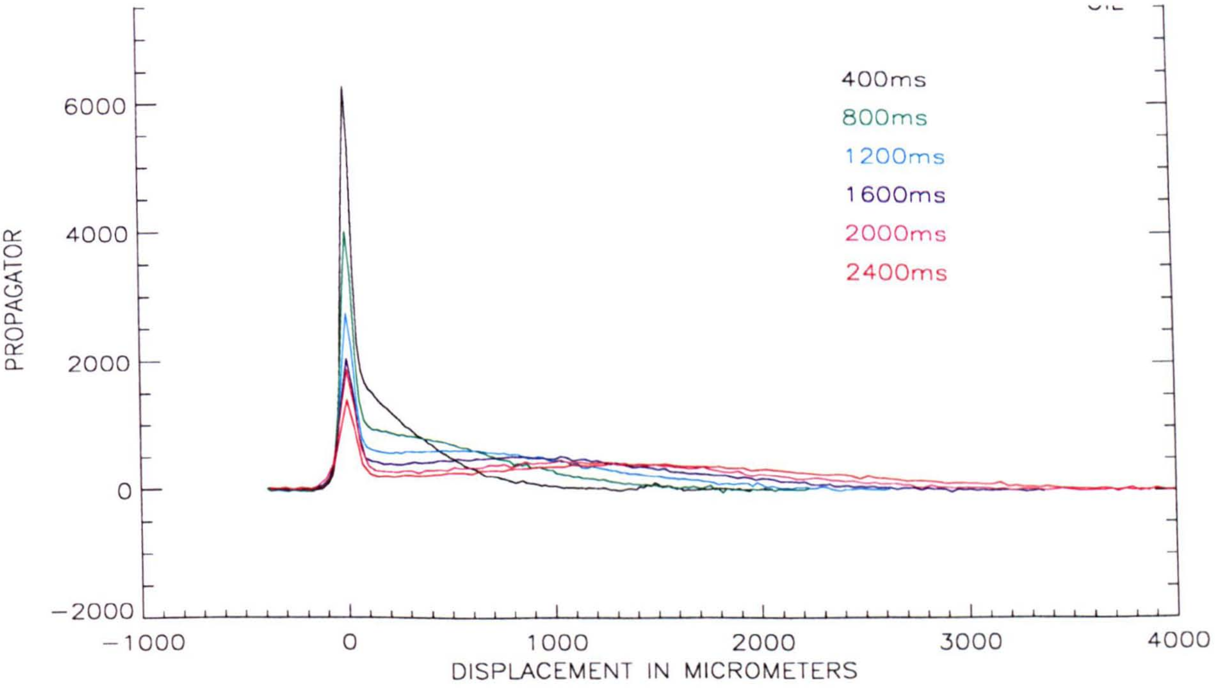

Figure 7.2 The evolution of the oil propagator with observation time, for dodecane flowing at 500ml/h through the Fontainebleau sample at $S_{wi} = 0.06$. The water phase is stationary.

To investigate the effect of secondary imbibition on transport, oil and water propagators were measured simultaneously at increasing steady-state water saturations, for an observation time of 2s. The increases in water saturation were produced by keeping the oil flow rate constant at 500ml/h and successively increasing the water flow rate from 0 to 70ml/h. After each increase in the water flow rate, time was allowed for the sample to reach a new steady-state water saturation, the oil and water propagators were then measured.

Figure 7.3 shows the effect of increasing the water flow rate, and hence the water saturation, on the water propagator. As the water flow rate is increased the water propagator spreads to larger displacements.

Figure 7.4 shows that increasing the water saturation has a greater impact on the oil propagators. The oil propagators have a bi-modal distribution and as the water saturation is increased the oil propagators become more peaked around zero-displacement. This means a larger fraction of the oil phase is stagnant (i.e. only experiencing diffusion) and a smaller fraction is carrying the flow. To carry the same oil flow rate (500ml/h) the flowing oil fraction has to flow faster i.e. the flowing part of the propagator spreads out over larger displacements.

The oil and water propagators can be qualitatively understood in terms of the wettability characteristics of the system. Fontainebleau sandstone is a strongly water-wet porous solid, as a result the water phase forms a thin continuous film over all the grain surfaces. For low capillary numbers, as the water saturation increases the thin surface film swells, blocking pore throats and filling the smaller oil occupied pores with water {see section 3.5.2} [1,4]. Therefore, as the water saturation increases, the non-wetting oil phase becomes increasingly isolated by the water network. The number of channels which can carry the oil flow thus decreases and more and more oil becomes trapped. This effect is clearly seen in the oil propagators shown in figure 7.4. The presence of the continuous surface film ensures that the water phase is entirely connected and most of the water can experience flow, this is seen in the water propagators in figure 7.3.

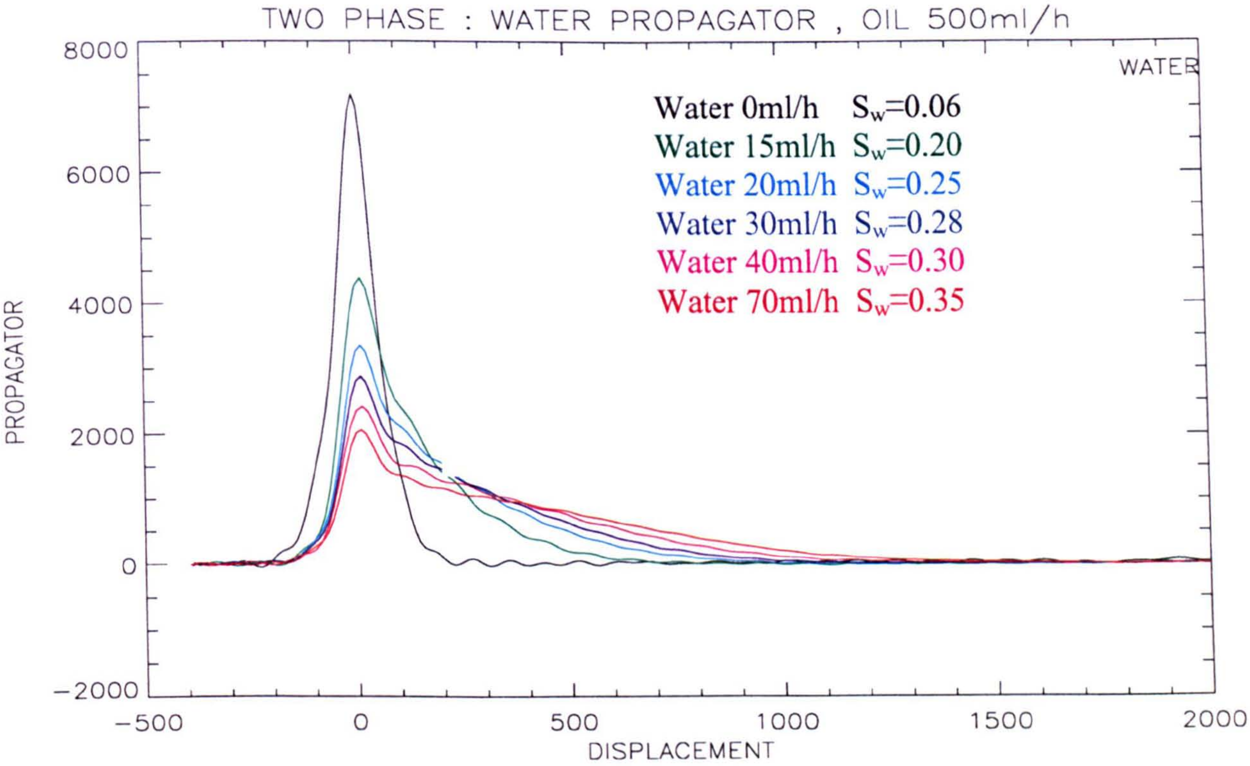

Figure 7.3 Water propagators at increasing steady-state water saturation. Observation time 2s.

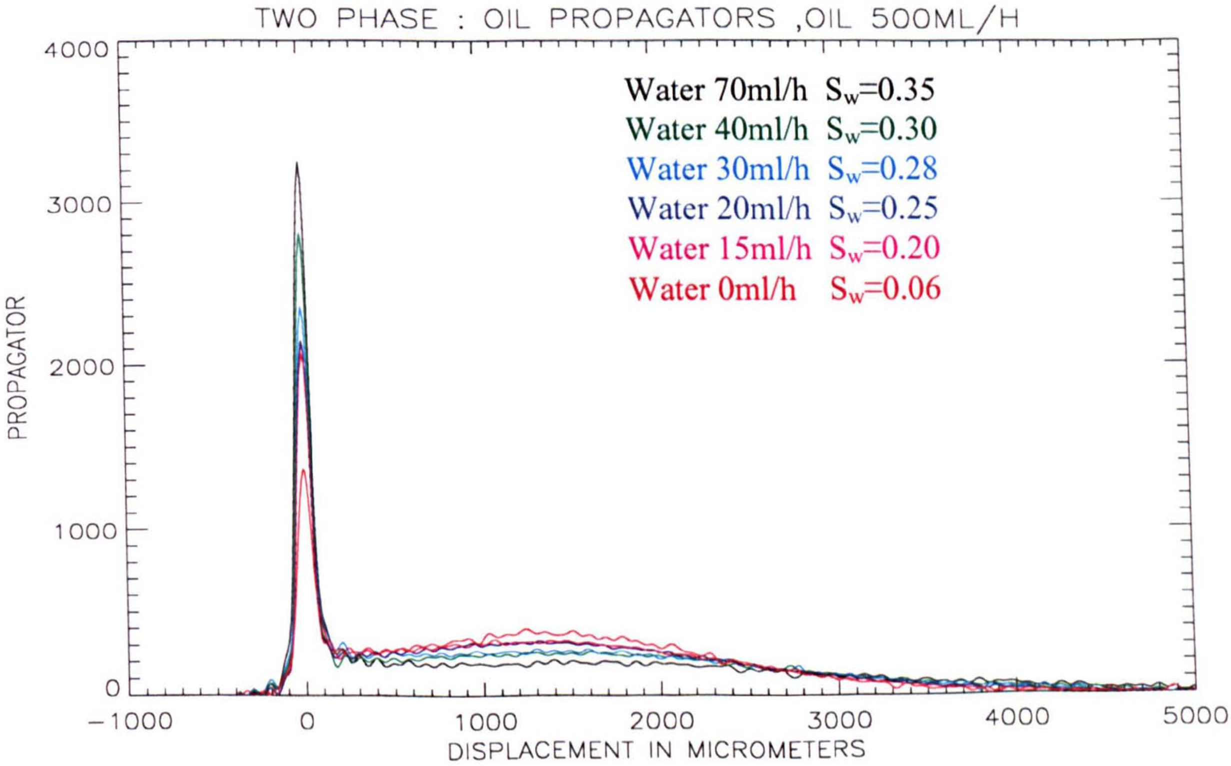

Figure 7.4 Oil propagators at increasing steady-state water saturation. Observation time 2s.

7.2.3 Explanation of increasing stagnant oil fraction

To understand the increase in the stagnant oil fraction as the water saturation is increased, it is illustrative to consider the following simple example. Consider a porous solid that is represented by a two-dimensional grid of connected pore elements, figure 7.5. Each pore element is cylindrical with a randomly assigned radius between 1and 5. The pore elements are strongly water-wet and the matrix is initially saturated with oil.

Oil and water are injected at the inlet at pressures P_{oil} and P_{water} respectively, giving an applied capillary pressure $P_c = P_{oil} - P_{water}$ {see section 3.3.4}. Starting from a very high value of capillary pressure, the water phase initially forms a thin continuous film over all the pore surfaces. Slowly decreasing the capillary pressure, allows the water to displace the oil from the narrowest cylindrical pore elements {section 3.5}, when $P_c < P_{entry}$. Because of the continuous water film, water can displace oil from any cylinder in the system, whether or not it is directly connected to the inlet. As the capillary pressure is reduced further, the water gradually displaces the oil from progressively wider cylinders, but the oil can only be displaced if it is directly connected to the outlet by oil filled cylinders.

It can be seen in figure 7.5 that as the cylinders fill with water the oil phase becomes more disconnected. The pores filled with oil can be categorised into three groups:

1. Spanning backbone i.e. those pores which form a continuous pathway connecting the inlet and outlet. Oil in these pores can experience flow from the inlet to the outlet.
2 Isolated pores. Oil in these pores is completely trapped and can only experience diffusion.
3 Dead-end pores. Oil in these pores can also only experience diffusion. Although, molecules within a distance $L \sim (6D\Delta)^{1/2}$ of the spanning backbone, may diffuse into the backbone and hence experience flow.

From this simple example it can be seen how the stagnant oil fraction, i.e. the fraction of oil present in dead-end and isolated pores, increases as the water saturation is increased. This is clearly seen in the experimental oil propagators shown in figure 7.4.

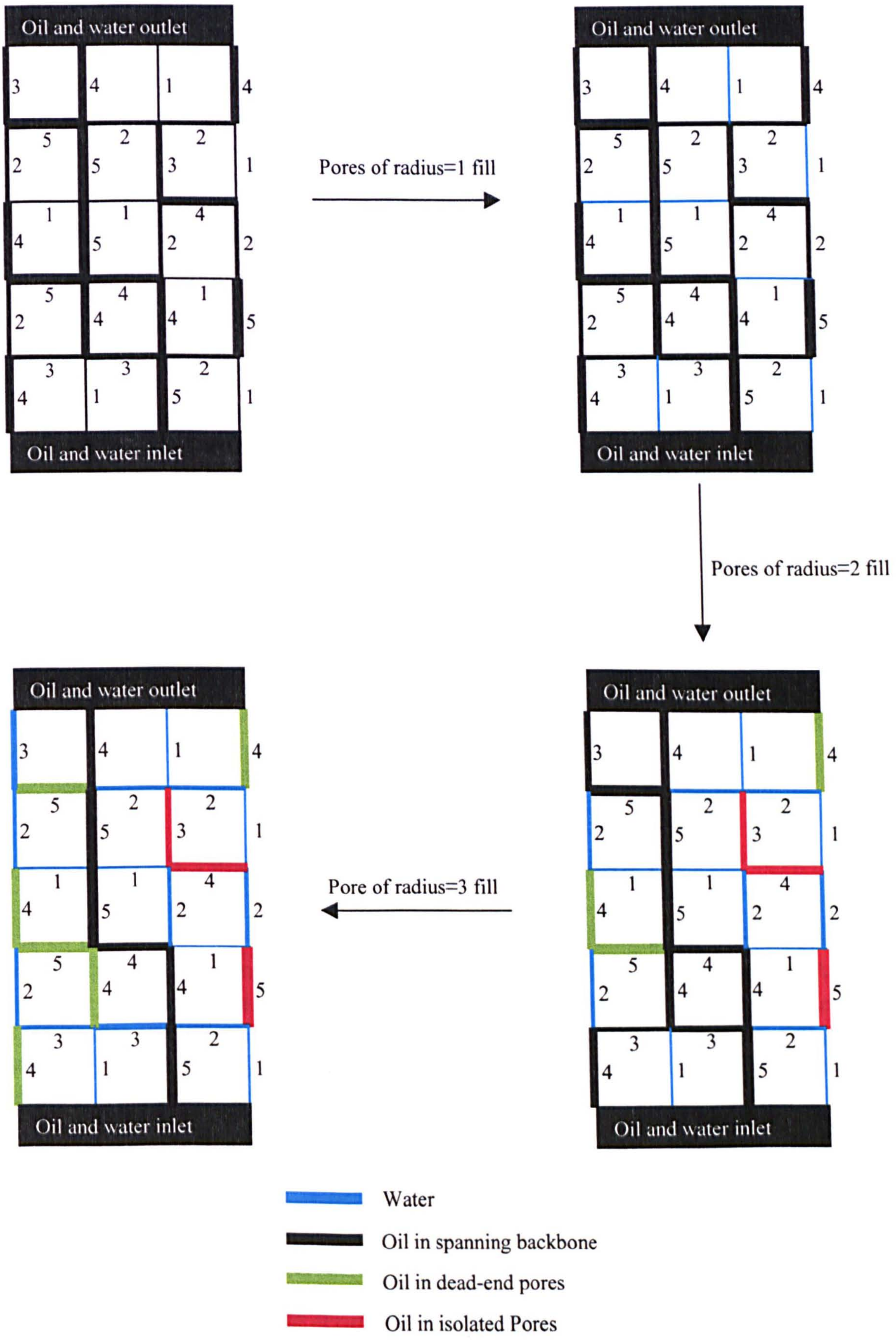

Figure 7.5 A two-dimensional network model of a water-wet porous solid, initially saturated with oil. During an imbibition process, the water displaces the oil from the smallest pore elements first. As more pore elements fill with water, an increasing amount of oil is present in dead-end and isolated pores.

7.3 Investigation of the stagnant oil fraction

In the previous section, displacement propagators were used to investigate the effect of a secondary imbibition process on the transport of the oil and water phases through the Fontainebleau sample. It was shown that with increasing observation time the oil propagator developed a distinctly bi-modal distribution i.e. a stagnant and flowing oil fraction. It was also shown that increasing the water saturation of the sample by a secondary imbibition process, increased the fraction of the oil phase that appeared stagnant.

It was decided to make quantitative measurements of the stagnant oil fraction produced by a secondary imbibition process, both as a function of water saturation and observation time. In these measurements only the oil phase was of interest, therefore it was decided to use an aqueous phase made with D_2O, so that the only ^1H NMR signal came from the oil phase. The stagnant oil fraction was determined from the echo attenuation function $E_\Delta(q)$.

7.3.1 Sample Preparation and Measurement of S_w

The Fontainebleau sample was saturated with an aqueous phase of 3% w/v NaCl brine made with D_2O, and an oil phase of either hexane or dodecane. The use of D_2O allowed for a more accurate measure of the water saturation by measuring the magnitude of the ^1H NMR signal of the oil phase {see method 2, described in section 5.3.5}. Different steady-state water saturations were produced in the sample by the primary drainage/secondary imbibition process described in section 5.3.4.

7.3.2 Measuring the Echo Attenuation Function $E_\Delta(q_z)$

The sample was prepared in a steady-state saturation, as described above, with both phases flowing simultaneously through the sample. The one-dimensional APGSTE sequence was used to measure $E_\Delta(q_z)$, for the oil phase, for the central 36mm slice of the Fontainebleau sample. The z-direction being parallel to the direction of flow. $E_\Delta(q_z)$ was measured for 16 equally spaced values of q_z in the range 0 to q_{max}. The value of q_{max} used was $8600m^{-1}$ for an oil phase of dodecane, and $5160m^{-1}$ for an oil phase of hexane. Measurements of $E_\Delta(q_z)$ were made with the Fontainebleau sample prepared in different water saturation states, for a range of observation times (200ms to 2s).

7.3.3 Experimental Results

An example of the experimental echo attenuation data $E_\Delta(q_z)$ is shown in figure 7.6. In this case dodecane (250ml/h) and D_2O (15ml/h) were flowing simultaneously through the Fontainebleau sample, with the Fontainebleau sample in a steady-state water saturation of $S_w = 0.34$. It can be seen that as the observation time is increased, $E_\Delta(q_z)$ develops a distinctly bi-modal distribution, with the flowing oil fraction attenuating more rapidly than the stagnant oil fraction with increasing q_z.

The echo attenuation function $E_\Delta(q_z)$ of the oil phase has a component from the stagnant oil fraction and a component from the flowing oil fraction, thus

$$E_\Delta(q_z) = F^s E^s_\Delta(q_z) + F^f E^f_\Delta(q_z) \tag{7.1}$$

where F^s and F^f are the respective volume fractions of the stagnant and flowing oil, $E^s_\Delta(q)$ and $E^f_\Delta(q)$ are the echo attenuation functions of the stagnant and flowing oil fractions. There is no exact form of $E^s_\Delta(q)$ and $E^f_\Delta(q)$, which could be used to fit the experimental echo attenuation function $E_\Delta(q)$, and thus find F^s and F^f.

As the stagnant oil fraction is undergoing partially restricted diffusion within the Fontainebleau sandstone, the echo attenuation $E^s_\Delta(q)$ in the low q limit is given by [5]:

$$\lim_{q\to 0} \frac{\partial \log_e\left[E^s_\Delta(q_z)\right]}{\partial q_z^2} = -4\pi^2 q_z^2 D_{\text{eff}} (\Delta - \delta/3) \tag{7.2}$$

where D_{eff} is the effective diffusion coefficient. Therefore, a logarithmic plot of the echo attenuation function $E^s_\Delta(q_z)$ against q_z^2, is linear at low q_z values. This can be seen in the experimental data shown figure 7.6.

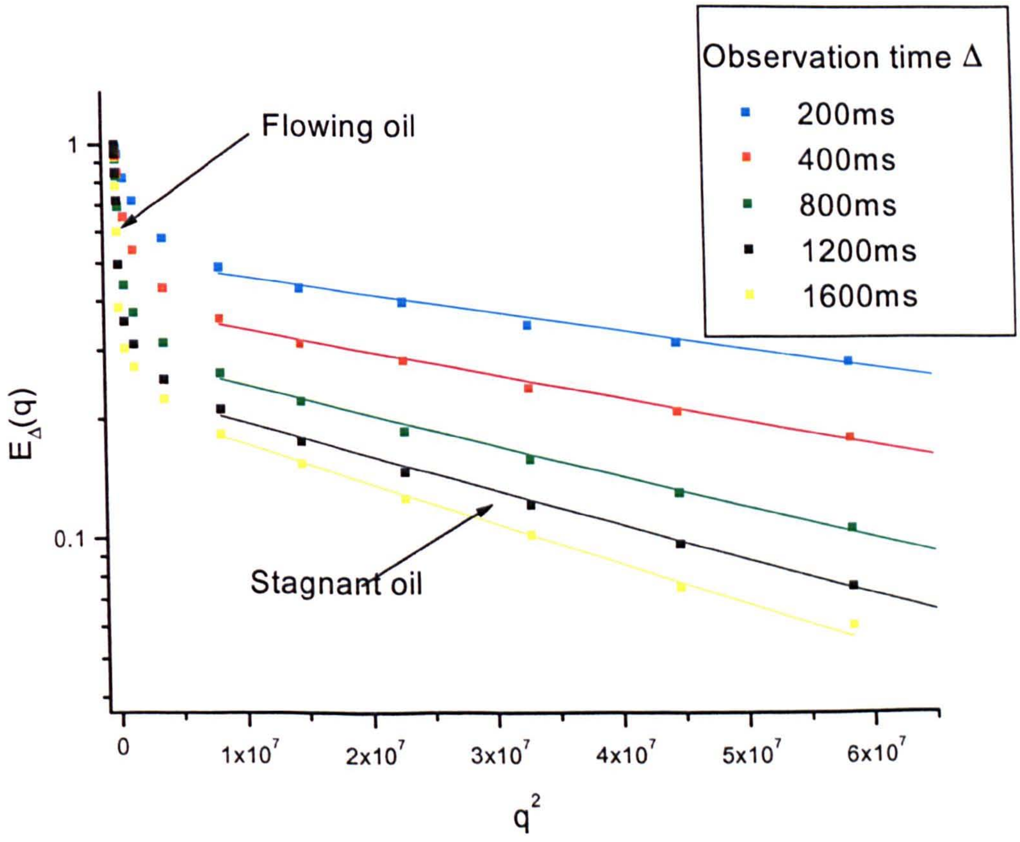

Figure 7.6 Echo attenuation plot for dodecane flowing at 250ml/h and D_20 flowing at 15 ml/h with the sample at a steady-state water saturation of $S_w = 0.34$. The solid lines are fits to the linear portion of the stagnant oil. The intercept of these fits on the y-axis gives the stagnant oil fraction.

At long observation times, when the flowing oil fraction has experienced a significantly greater mean displacement than the stagnant oil fraction (i.e. diffusing oil), $E_{\Delta}^{s}(q_z)$ and $E_{\Delta}^{f}(q_z)$ are well separated in q space, this can be clearly seen in figure 7.6. The stagnant oil fraction F^s can be found by extrapolating the linear portion of the $E_{\Delta}^{s}(q_z)$ back to $q_z = 0$, the intercept gives the stagnant oil fraction F^s. This was done by fitting the experimental data between $q_z = 2866$ and $q_z = 7644$ for an oil phase of dodecane and $q_z = 1720$ and $q_z = 4586$ for an oil phase of hexane, to a linear function. This method only gives an accurate measure of the stagnant oil fraction when $E_{\Delta}^{f}(q_z)$ does not overlap the above regions in q space, i.e. at long observation times. At short observation times there is overlap of $E_{\Delta}^{f}(q_z)$ with these regions, and this produces an overestimation of the stagnant oil fraction.

Figure 7.7 shows the stagnant oil fractions measured, as a function of observation time for various steady-state water saturations, using the method described above. The overestimation of the stagnant oil fraction at short times, i.e. below 0.8s, can be seen at all water saturations. It can also be seen that the stagnant oil fraction remains approximately constant, between 1.2s and 2s and that this constant value increases with increasing water saturation.

In section 7.2.3 it was shown that the stagnant oil produced by an imibition process is present in dead-end and isolated pores. The oil present in isolated pores is completely trapped, and only experiences diffusion. The oil present in dead-end pores also only experiences diffusion. However, oil molecules present in a dead-end pore, which is directly connected to a spanning backbone pore, may diffuse into the spanning backbone pore and then experience flow. Therefore, the stagnant oil present in dead-end pores has some time dependence.

Any time dependence in the stagnant oil fraction would be most evident for measurements made using hexane ($D = 4.2\times10^{-9}$ m^2 s^{-1}) as the oil phase, because its bulk diffusion coefficient is nearly five times greater than that of dodecane ($D = 0.89\times10^{-9}$ m^2 s^{-1}). The fact that the stagnant oil fraction, shown in figure 7.7, remains approximately constant between 1.2s and 2s, for both hexane and dodecane, indicates that the time dependence of the stagnant oil fraction is weak. This weak time dependence suggests that only a small fraction of the stagnant oil is present in dead-end pores that are within diffusing distance of the spanning backbone, in the time range 1.2s to 2s.

As the time dependence of the stagnant oil fraction is weak, then the approximately constant level of the stagnant oil fraction between 1.2s and 2s (taken as the average of the 1.2, 1.6 and 2s values), is taken as representing the fraction of the oil phase that has been trapped in dead-end and isolated pores by the secondary imbibition process. Figure 7.8a shows how the fraction of the oil phase that has been trapped in dead-end and isolated pores varies with increasing steady-state water saturations. It can be seen that a steadily increasing fraction of the oil phase becomes trapped, as the water saturation of the Fontainebleau sample is increased. It can also be seen that similar results are obtained using either hexane or dodecane as the oil phase.

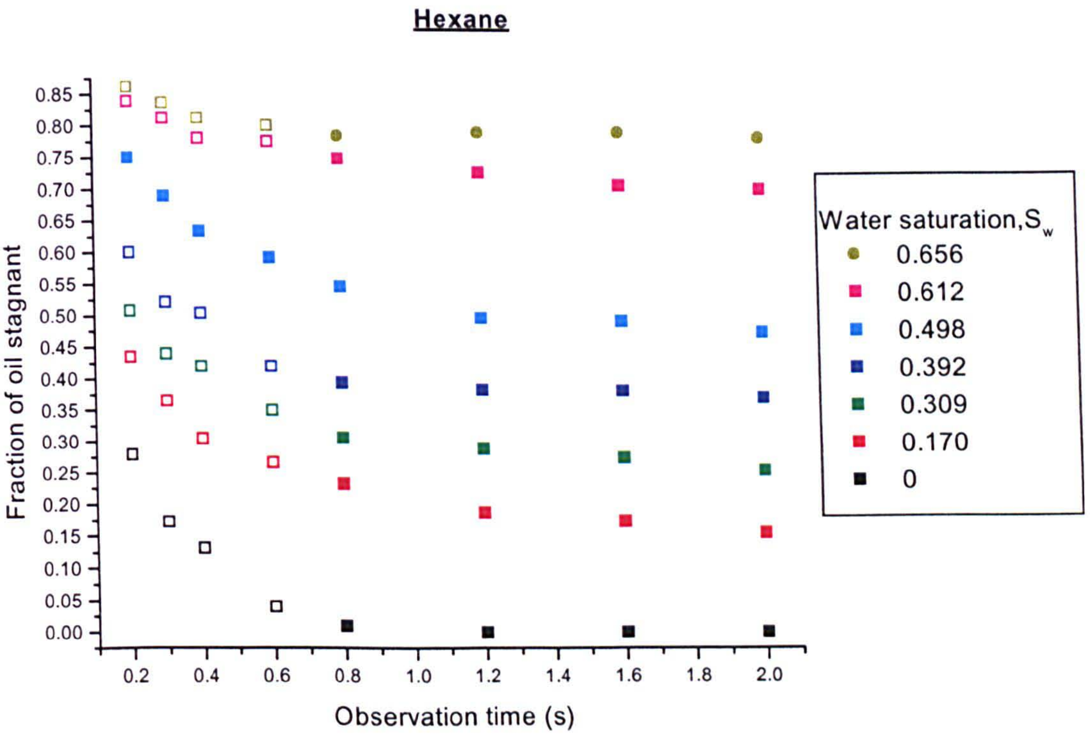

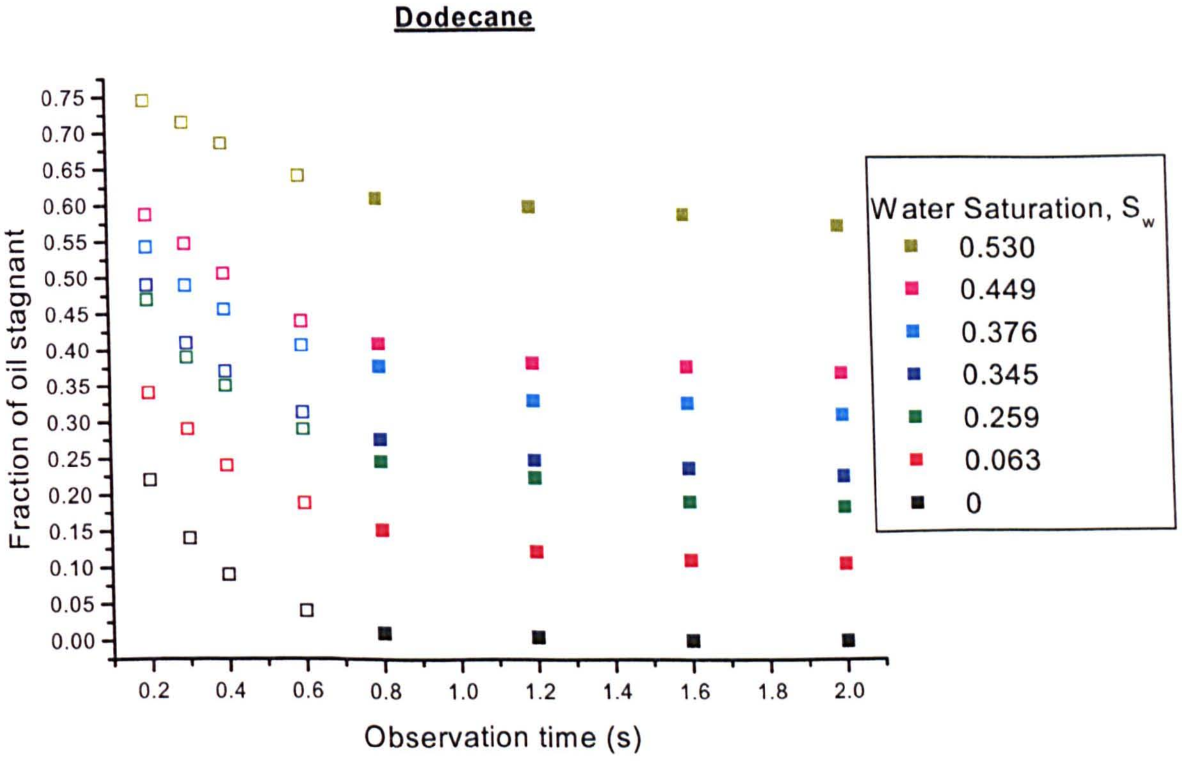

Figure 7.7 Plots of the fraction of the oil phase that is stagnant as a function of observation time. The different water saturation states being produced by a secondary imbibition process.

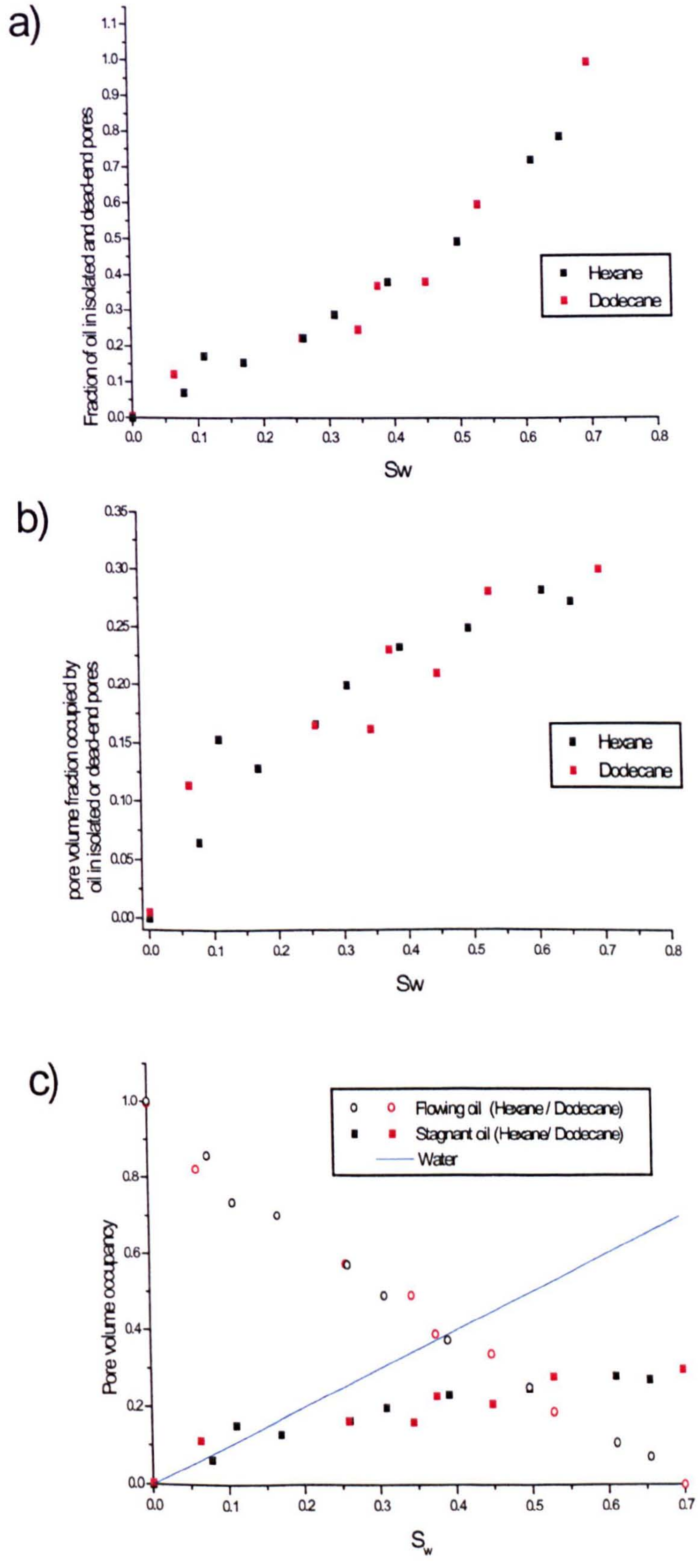

Figure 7.8 a) The fraction of the oil phase trapped in dead-end and isolated pores as a function of increasing water saturation. b) The fraction of the total pore volume occupied by oil trapped in dead-end and isolated pores as a function of S_w. c) The fraction of the total pore volume occupied by water, oil in the spanning backbone (i.e. flowing oil), and oil in dead-end and isolated pores (i.e. stagnant oil) as a function of S_w.

Figure 7.8a shows how the fraction of the oil phase that has been trapped in dead-end and isolated pores varies with increasing steady-state water saturations. As the oil phase itself only occupies a fraction of the total pore volume ($1- S_w$) the data shown in figure 7.8a can be re-plotted in terms of the total pore volume. Figure 7.8b shows how the fraction of the total pore volume of the Fontainebleau sample, that is occupied by oil in dead-end and isolated pores, varies as a function of increasing water saturation.

The occupancy of the total pore volume of the Fontainebleau sample, can be divided into three catagories, the volume occupied by the water phase, the volume occupied by the spanning oil backbone (i.e. flowing oil) and the volume occupied by oil in dead-end and isolated pores (i.e. stagnant oil). Figure 7.8c shows how the occupation of the total pore volume between these three categories changes as the water saturation of the Fontainebleau sample is increased.

7.4 Preliminary Simulation Results

In section 7.3 a secondary imbibition process was used to increase the steady-state water saturation of the Fontainebleau sandstone. At each saturation state measurements were made of the fraction of the oil phase that was stagnant. The stagnant oil fraction was assumed to be the fraction of the oil phase present in dead-end and isolated pores {see section 7.2.3}.

To help understand these results Graham[6] developed a simple site-percolation model with trapping. The computer code was based on algorithms described in Stauffer [7] and the references therein. The model used a (100×100 ×100) cubic lattice (without boundary conditions), with each site connected to six other sites. At the beginning of the simulation all the sites were filled with oil. At each step of the simulation a randomly chosen site was filled with water, but only if the oil in that site was still connected to the outlet i.e. the oil in that site had an escape route. At the end of each step the remaining oil filled sites were categorised as being spanning backbone sites (B), isolated sites (I) or dead-end sites (D) {see section 7.2.3}. The stagnant oil fraction F^s was then given by:

$$F_s = \frac{I+D}{I+D+B} \tag{7.3}$$

Figure 7.9 shows how F^s changes as sites fill with water. At the beginning of the simulation all of the sites are filled with oil, and all these sites are classed as spanning backbone sites (i.e. can carry oil flow from inlet to outlet). It is not until about 25% of the sites are filled with water that the connectiveness of the oil is affected and isolated and dead-end oil sites appear. As more sites are filled with water, the fraction of oil filled sites that are dead-end or isolated sites increases rapidly.When 69% of the sites are filled with water, then the oil phase no longer spans the lattice and the oil is only present in isolated sites (i.e. residual oil saturation).

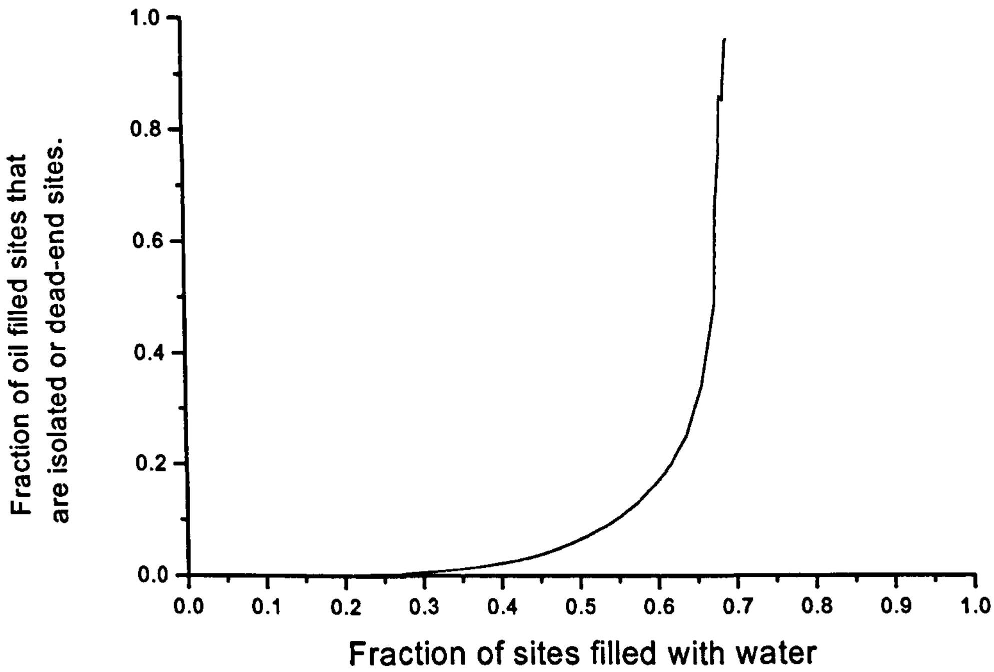

Figure 7.9 The results of a site percolation model of imbibition, which includes trapping.

It is difficult to compare the results of this preliminary simulation, see figure 7.9, with the corresponding experimental measurements, see figure 7.8a. This is because in the site percolation model all the sites are identical (i.e. same volume), and sites are filled randomly with water. Whereas in Fontainebleau sandstone the pores have a distribution of sizes, with the imbibing water phase preferentially filling the smallest pores first {see section 3.5}[1,4]. What the simulation does clearly show is that as the water saturation is increased (i.e. sites are filled with water), the oil filled sites become increasingly disconnected, producing an increase in the fraction of oil filled sites that are dead-end or isolated sites. The same behaviour is qualitatively seen in the experimental results, figure 7.8a.

7.5 Conclusions

In this chapter a secondary imbibition process was used to increase the steady-state water saturation of a strongly water-wet sample of Fontainebleau sandstone. One-dimensional displacement propagators were used to investigate how increases in the steady-state water saturation affected the transport of the oil and water phases flowing through the sample. It was found that increasing the water saturation produced an increasing amount of stagnant oil in the sample. This was qualitatively explained in terms of the wettability of the Fontainebleau sandstone and illustrated using a simple example.

A method was described for measuring the stagnant oil fraction from the echo attenuation function $E_\Delta(q)$. Measurements of the stagnant oil fraction were made for a range of observation times, with the Fontainebeleau sample prepared in increasing steady-state water saturations. Measurements were made using either hexane or dodecane as the oil phase. It was found, for both hexane and dodecane, that the stagnant oil fraction was approximately constant between 1.2s and 2s. It was also found, for both hexane and dodecane, that the stagnant oil fraction increased steadily with increasing steady-state water saturations. The stagnant oil fraction was assumed to represent the fraction of the oil phase that had become trapped in dead-end and isolated pores by the imbibing water.

A simple site percolation model was presented for imbibition with trapping. The model was based on a $100\times100\times100$ cubic lattice, with each site connected to six other sites. The model was used to investigate how randomly filling sites with water changed the fraction of oil filled sites that were dead-end or isolated sites. It was shown that as the sites are filled with water the fraction of the oil present in dead-end or isolated sites increases rapidly. This behaviour could be qualitatively seen in the experimental data.

More sophisticated pore-scale simulations have been developed to investigate imbibition and drainage displacement processes [2,8,9]. These simulations have been complimented by experiments in idealized two-dimensional porous solids, where different pore-scale displacement mechanisms can be seen [1]. These simulations are mostly used to interpret macroscopic flow parameter e.g. relative permeability, wettability. It has been demonstrated in this chapter that PFG NMR can be used to quantitatively measure the trapping of the oil phase caused by imbibition. It would be very interesting to use pore-scale modelling in association with PFG NMR measurements to understand imbibition and drainage processes in porous solids. A recent attempt at this has been undertaken by Damion et al [10].

A study by Tallarek et al [11,12,13] has many parallels to the work presented in this chapter, although using a completely different system. They used PFG NMR to study the transport, of a single phase, through packed chromatographic columns, the columns being made from totally porous particles. Measurements were made of the mass transfer between the stagnant fluid contained within the porous beads and the mobile phase flowing through the column. This is analogous to the mass transfer of stagnant oil present in dead-end pores into the spanning oil backbone (i.e. flowing oil).

7.6 References

1. Dullien F.A.L. "Porous Media: Fluid Transport and Pore Structure". 1992. Academic Press Ltd. London.
2. Sahimi M. "Flow and Transport in Porous Media and Fractured Rock". 1995. VCH. Weinheim.
3. Tessier J.J., Packer K.J. "Characterization of Multiphase Fluid Transport in a Porous Solid by Pulsed Field Gradient Stimulated Echo NMR". 1998. Physios of Fluids. 10. 75-85.
4. McDougall S.R. "The Application of Network Modelling Techniques to Steady- and Unsteady-State Multiphase Flow in Porous Media". 1994. Thesis. Heriot-Watt University.
5. Fordam E.J., Gibbs S.J., Hall L.D. "Partially Restricted Diffusion in a Permeable Sandstone: Observations by Stimulated Echo PFG NMR". 1994. 12. 279-284.
6. Graham R.G. 2000. Private Communication.
7. Strauffer D., Aharony A. "Introduction to Percolation Theory". 1992. Taylor and Francis. London.
8. Hughes R.G., Blunt M.J. "Pore Scale Modelling of Rate Effects in Imbibition". 2000. Transport in Porous Media. 40. 295-322.
9. McDougall S.R., Sorbie K.S. "The Application of Network Modelling Techniques to Multi-phase Flow in Porous Media". 1997. Petroleum Geoscience. 3.161-169.
10. Damion R.A., Packer K.J., Sorbie K.S., McDougall S.R. "Pore-scale Network Modelling of Flow Propagators Derived From Pulsed Magnetic Field Gradient Spin Echo NMR Measurements in Porous Media". 2000. Chemical Engineering Science. 55. 5981-5998.
11. Tallarek U., Dusschoten D., Van As H., Guiochon G., Bayer E. "Direct Observation of Fluid Mass Transfer Resistance in Porous Media by NMR Spectroscopy". 1998. Angew. Chem. Int.. 37. 1882-1885.
12. Tallarek U., Dusschoten D., Van As H., Guiochon G., Bayer E. "Study of Transport Phenomena in Chromatographic Columns by PFG NMR". 1998. Journal of Physical Chemistry B. 102. 3486-3497.
13. Tallarek U., Bayer E., Guiochon G. "Study of Dispersion in Packed Chromatographic Columns by Pulsed Field Gradient NMR". 1998. Journal of the American Chemical Society. 120. 1494-1505.

Chapter 8

Diffusion in Thin Films

Contents

8.1 INTRODUCTION **130**

8.2 EXPERIMENTAL **130**

8.2.1 SAMPLE PREPARATION AND MEASUREMENT OF S_W 130
8.2.2 DETERMINATION OF DIFFUSION PROPAGATORS FOR THE AQUEOUS PHASE 130
8.2.3 DIFFUSIVE PROPAGATORS OF THE WETTING PHASE. 132
8.2.4 SECOND MOMENTS OF DISPLACEMENT PROPAGATORS 133

8.3 ISOTROPIC INFINITE PLANES MODEL FOR DIFFUSION IN SURFACE WETTING FILMS **135**

8.3.1 EFFECT OF CURVATURE 139

8.4 CONCLUSIONS **143**

8.5 REFERENCES **144**

8.1 Introduction

The distribution of two immiscible fluids within a porous solid is governed by the interfacial tensions between the fluids and between each fluid and the solid. For a strongly water-wet porous solid like Fontainebleau sandstone, saturation with a mixture of aqueous and hydrocarbon phases is expected to result in a physically continuous water phase, always in contact with the solid surface, for all achievable relative saturations [1]. The local thickness and geometry of the aqueous layer will depend upon the detailed spatial variation of the curvature of the solid surface, the interfacial tensions and upon S_w. The transport of water through such films is of importance, for example, in imbibition processes [2]. Except in optically transparent materials, the availability of experimental techniques for the characterisation of surface wetting films is limited.

In this chapter PFG NMR is used to investigate diffusion within the wetting phase of a strongly water-wet sample of Fontainebleau sandstone, saturated with aqueous and hydrocarbon phases in varying proportions. The experimental results are compared with a simple theoretical model in which diffusion is restricted to the surfaces of an isotropic array of unconnected infinite planes.

8.2 Experimental

8.2.1 Sample Preparation and Measurement of S_w

The sample of Fontainebleau sandstone was saturated with an aqueous phase of 3% NaCl brine solution made with H_2O and an oil phase of dodecane. Different saturation states were produced in the sample by the primary drainage/secondary imbibition process described in section 5.3.4. As both phases give a ^1H NMR signal, the water saturation was determined from the ^1H NMR chemical shift spectrum {see method 1 of section 5.3.5}.

8.2.2 Determination of Diffusion Propagators for the Aqueous Phase

One-dimensional diffusive propagators were determined in the manner outlined in section 5.6.2. The one-dimensional APGSTE NMR signal was acquired as a spin echo $E_\Delta(q_x,t)$, for a central slice of the sample of thickness 36mm. $E_\Delta(q_x,t)$ was measured for 32 equally spaced values of q_z in the range $-q_{max}$ to q_{max}, where q_{max}= 40000m^{-1}. The absolute value of the two-dimensional Fourier transform of $E_\Delta(q_x,t)$ results in chemical shift resolved propagators [3]. The water and oil propagators were taken from the water and oil chemical shift peaks.

At low values of S_w {see figure 5.6 for a chemical shift spectrum measured at low S_w}, the question arises as to how well the chemical shift resolved separation of the oil and water propagators works, given the somewhat overlapping nature of the peaks arising from the two phases. In order to demonstrate that there was no contribution to the water propagator from the oil signal under conditions of low S_w, the following experiment was performed.

Dodecane was pumped through the Fontainebleau sample at 400ml/h, with the water phase stationary, and with the sample at a water saturation of $S_w = 0.1$. Using an observation time of 1.6s, $E_\Delta(q_z,t)$ was measured for 128 values of q_z in the range $-q_{max}$ to q_{max}, where q_{max}= 16000m^{-1}. Where the z-direction is parallel to the direction of flow. The average propagators $P_\Delta(Z)$ for each phase are shown in Figure 8.1. It can be seen that the oil propagator shows the presence of both flowing and non-flowing oil {see chapter 7}. The fraction which is flowing gives rises to a large Gaussian-like peak with a significant mean displacement (~1000μm). If the separation of the oil and water signals was not complete, it would be expected that the water propagator would also show such a feature, particularly as the oil signal is some nine times more intense than the water signal under these conditions (S_w=0.1). However, as can be seen from figure 8.1, the diffusive water propagator is symmetrical around zero-displacement and shows no detectable contribution, which could arise from the overlap of the oil signal with that from the water.

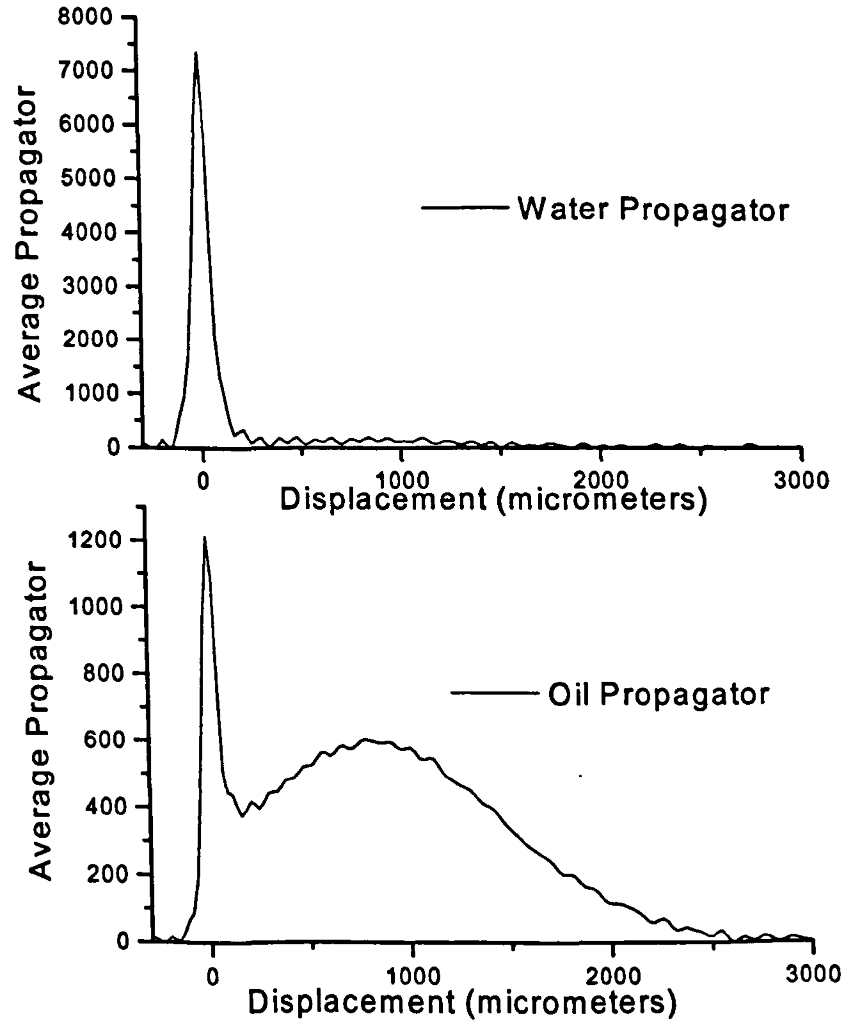

Figure 8.1 Average propagator of the oil and water phases measured with the oil phase flowing at 400ml/h and the with the water phase stationary. The sample was in a steady-state water saturation of S_w=0.1.

8.2.3 Diffusive Propagators of the Wetting Phase.

Displacement propagators were measured for the diffusion of the water phase i.e. the wetting phase, with the Fontainebleau sandstone prepared in different water saturation states. Measurements were made for observation times in the range 0.1-1.6s. For measurements made at low water saturations and long observation times the signal-to-noise ratio was improved by increasing the number of signal averages, to a maximum of 256.

Figure 8.2 shows water propagators measured for an observation time of 1.2s, with the Fontainebleau sample at different S_w. For $S_w = 1$, the water propagator is approximately Gaussian in form, having a characteristically rounded appearance around zero-displacement. This indicates that the diffusive process, although hindered, has essentially three dimensional character. As the water saturation is decreased the shape of the propagator gradually changes. It develops a cusp-like form near zero displacement and decays much more rapidly than for S_w=1 with increasing displacement. These qualitative differences indicate that the constraints on the diffusive transport, at least in the range of observation times considered here, change markedly with water saturation. Figure 8.3 shows the water propagators measured at $S_w = 0.2$, it can be seen that the cusp-like shape is retained with increasing observation time.

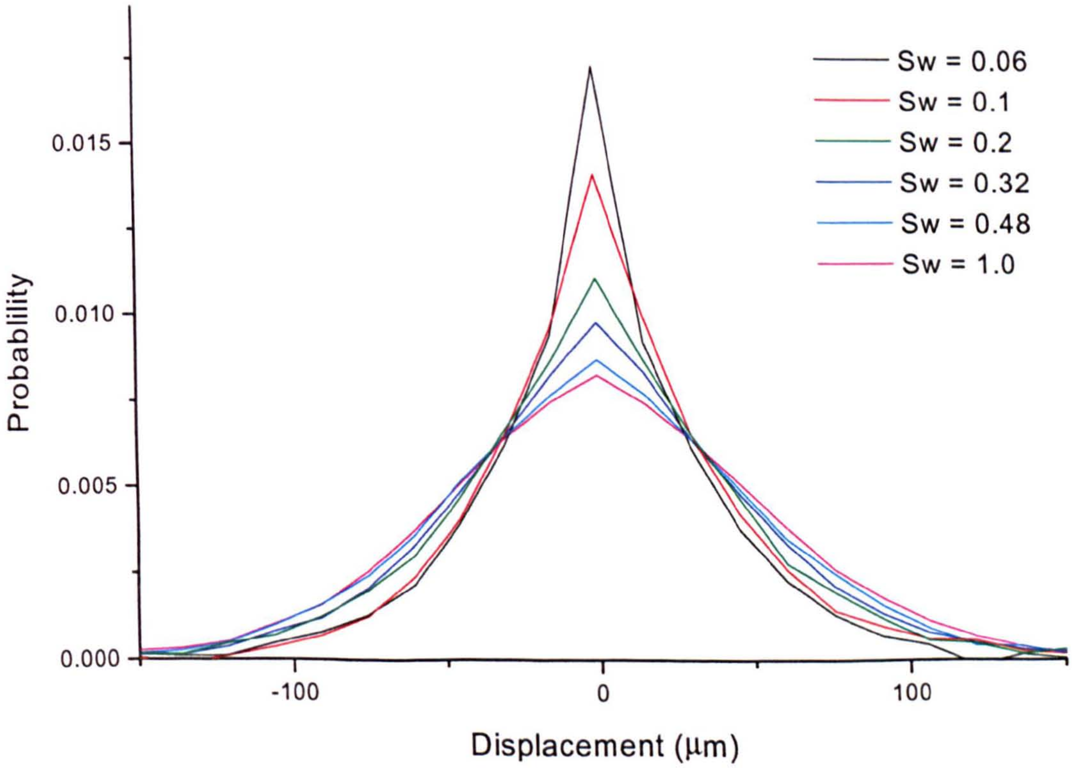

Figure 8.2 Average propagators for the diffusion of water within the Fontainebleau sample, measured at various water saturations, for an observation time of 1.2s. The lines join the experimental points and are only to guide the eye.

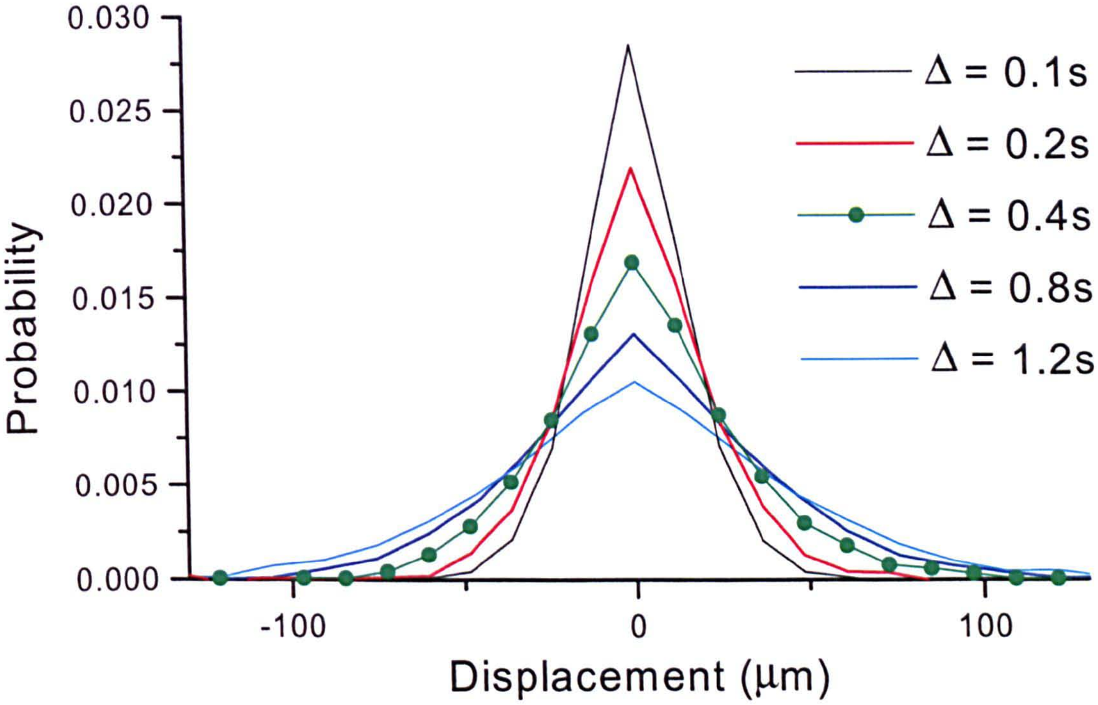

Figure 8.3 Displacement propagators for the diffusion of water contained within the Fontainebleau sample at $S_w = 0.2$, for a range of observation times. The lines join experimental points, shown for Δ=0.4, and are only to guide the eye.

8.2.4 Second Moments of Displacement Propagators

To give a simple quantitative description of the displacement propagators, measured for various observation times Δ and saturation states S_w, their second moments have been calculated. Where the second moment (mean squared displacement) of the displacement propagator $P_\Delta(X)$ is given by:

$$M_2 = \int_{-\infty}^{\infty} X^2 \, P_\Delta(X) \, dX \tag{8.1}$$

Figure 8.4 shows the time dependence of the second moments for different water saturation states. It is possible to derive the effective diffusion coefficient D^* at long times from the seconds moments:

$$D^* = \lim_{\Delta \to \infty} \frac{\langle X^2(\Delta) \rangle}{2\Delta} \tag{8.2}$$

The effective diffusion coefficient D^* was calculated from the slope of the time dependence of the second moments, between 0.8s and 1.2s (for the data available). Figure 8.5 shows how D^* varies when the sample is in different water saturation states. It can be seen that D^* decreases with decreasing water saturation. The decrease is steepest for $S_w<0.4$. This result is discussed in more detail later {see section 9.5.2}, when it is compared to the results of similar experiments performed on an idealized porous solid.

At 1.2s the rms displacement in three-dimensions, given by $(6D^{*}\Delta)^{1/2}$, ranges from 65 to 100μm (approximately ~1 to 2 pore sizes), for S_w=0.06 and S_w=1. Although the diffusing water molecules have not experienced a statistically large region of the Fontainebleau sample, the calculated values of D^{*} are still valuable in showing how decreasing the water saturation of the sample affects the diffusive transport of the water phase. It should also be noted that at lower water saturations the important length scale is less than a pore size.

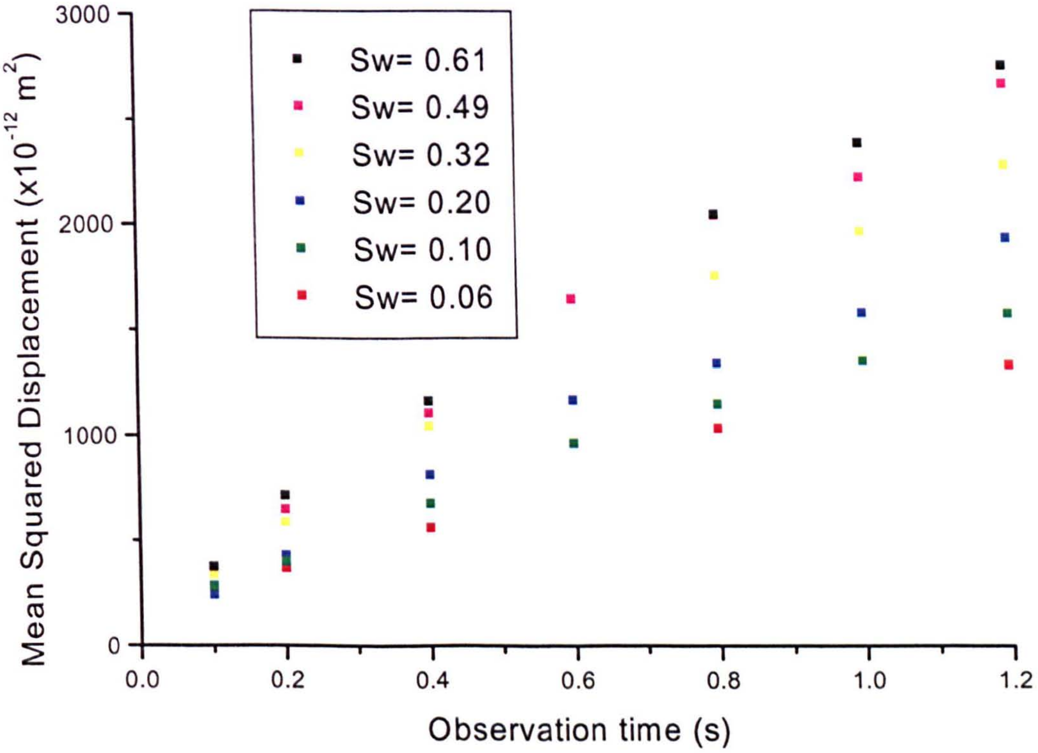

Figure 8.4 The time dependence of the second moment, for the diffusion of the water phase in Fontainebleau sandstone, at different water saturations.

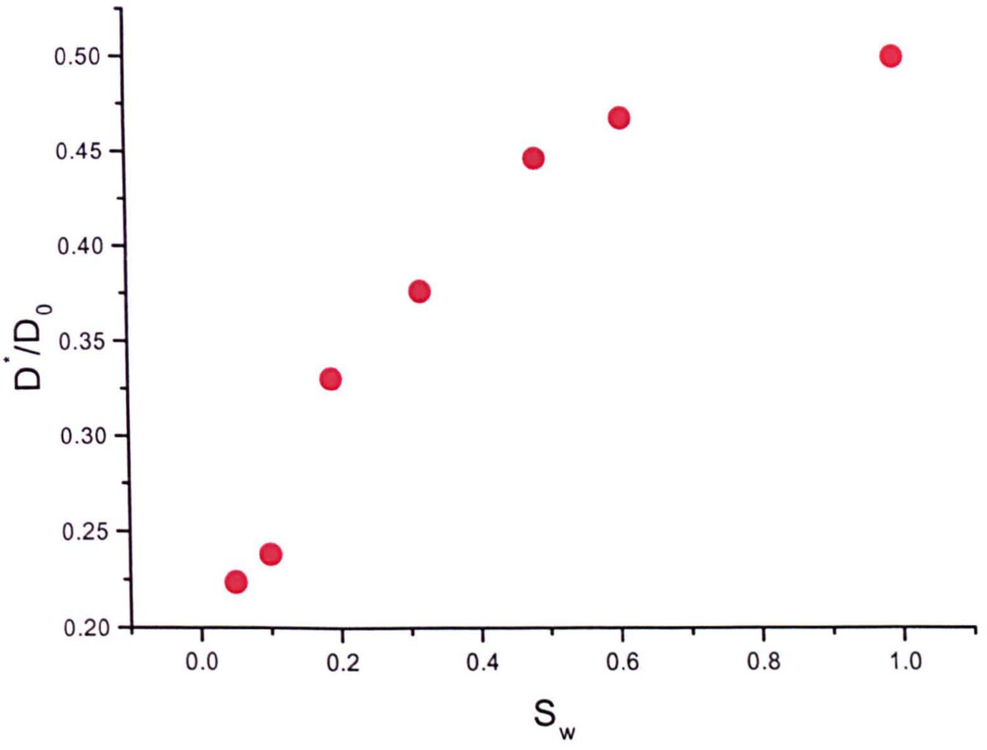

Figure 8.5 Effective diffusion coefficient of the water phase.

8.3 Isotropic Infinite planes Model for Diffusion in Surface Wetting Films

Because Fontainebleau sandstone is strongly water-wet, at low water saturations the water phase forms a physically continuous surface wetting film. At these low water saturations it is likely, therefore, that the local diffusive process within these films becomes closer to two-dimensional in character than three-dimensional. Hence, the overall propagator arises from the powder average of locally two-dimensional propagators which describe the diffusion of water in thin films. To help understand the experimental data a simple model has been proposed by Graham [4], in which the aqueous phase is distributed in thin, uniform films on an isotropically oriented array of unconnected planes. Assuming that the film thickness is small, compared to the rms displacements in the regime of observation time with which we are concerned, the effects of diffusion across the thickness of the film maybe neglected.

The solution of the diffusion equation for unrestricted diffusion was described in section 2.72 and is given by equation 2.52. For anisotropic diffusion, the diffusion equation takes the form:

$$\frac{\partial P}{\partial t} = \nabla \cdot \mathbf{D} \cdot \nabla P \qquad (8.3)$$

where **D** is the Diffusion Cartesian tensor, and P the displacement propagator. The solution to equation 8.3, for the case of two-dimensional diffusion i.e. diffusion within a thin film on an infinite plane, is given by:

$$P_\Delta(\xi,\zeta)=\frac{1}{4\pi D_2\Delta}\exp\left(-\frac{\xi^2+\zeta^2}{4D_2\Delta}\right) \tag{8.4}$$

Where ξ and ζ represent displacements along orthogonal Cartesian axes within the plane, see figure 8.6, and D_2 is the diffusion coefficient on the plane and Δ is the observation time.

The average propagator $P_\Delta(X)$ for an ensemble of particles undergoing two-dimensional diffusion on the surface of a randomly oriented array of unconnected planes, is given by projecting equation 8.4 onto the x-axis and averaging over all orientations [4], giving:

$$P_\Delta(X)=\sqrt{\frac{\pi}{4D_2\Delta}}\,\mathrm{erfc}\left(\sqrt{\frac{X^2}{4D_2\Delta}}\right) \tag{8.5}$$

where erfc is the complementary error function. This equation will be referred to as the Isotropic Infinite Planes model.

Initially, average propagators $P_\Delta(X)$ were generated from equation 8.5 using the bulk diffusion coefficient for water $2.2\times10^{-9}\mathrm{m}^2\mathrm{s}^{-1}$. These model propagators did not quantitatively match the experimental water propagators measured at low S_w. However, they did reproduce the general form of the propagator well, despite the simplicity of the model. In particular, the model propagators showed the cusp-like shape near X=0, this suggests that this feature in the experimental data probably arises from locally two-dimensional diffusion.

It was decided to fit the isotropic infinite planes model, equation 8.5, to the experimental data, using the diffusion coefficient $D_2(\Delta)$ as the fitting parameter, i.e. not forcing it to be the bulk diffusion coefficient and allowing it to vary with observation time. Figure 8.7 shows the result of least-squares fits of equation 8.5 to the experimental data for the shortest and longest observation times experimentally accessible. Figure 8.8 shows the least squares estimates of $D_2(\Delta)$ for values of Δ and S_w.

If the model were able to account quantitatively for the observed statistics, then the parameter $D_2(\Delta)$ would be independent of Δ and S_w and equal to the self diffusion coefficient of bulk water. It is evident from figure 8.8 that this is not the case. Firstly, at a given S_w, $D_2(\Delta)$ decreases, rapidly at first then less strongly, with increasing observation time Δ. Secondly, D_2 increases with increasing S_w, the extent of this increase being nearly independent of Δ. Thirdly, at higher S_w and shorter Δ the value of $D_2(\Delta)$ is actually greater than the bulk diffusion coefficient of water ($2.2\times10^{-9}\mathrm{m}^2\mathrm{s}^{-1}$).

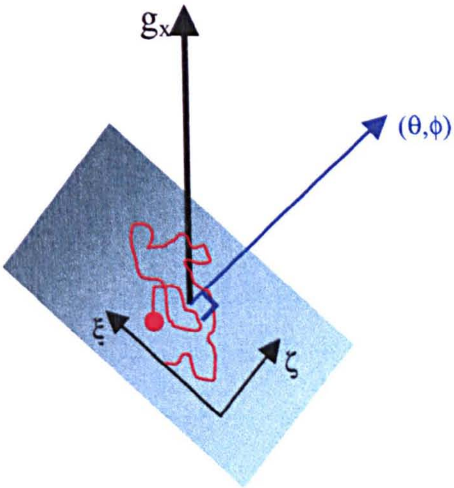

Figure 8.6 This diagram represents a particle undergoing diffusion on a plane. The normal to the plane is oriented at (θ,ϕ) to the gradient direction g_x. Where ξ and ζ are orthogonal Cartesian axes in the plane.

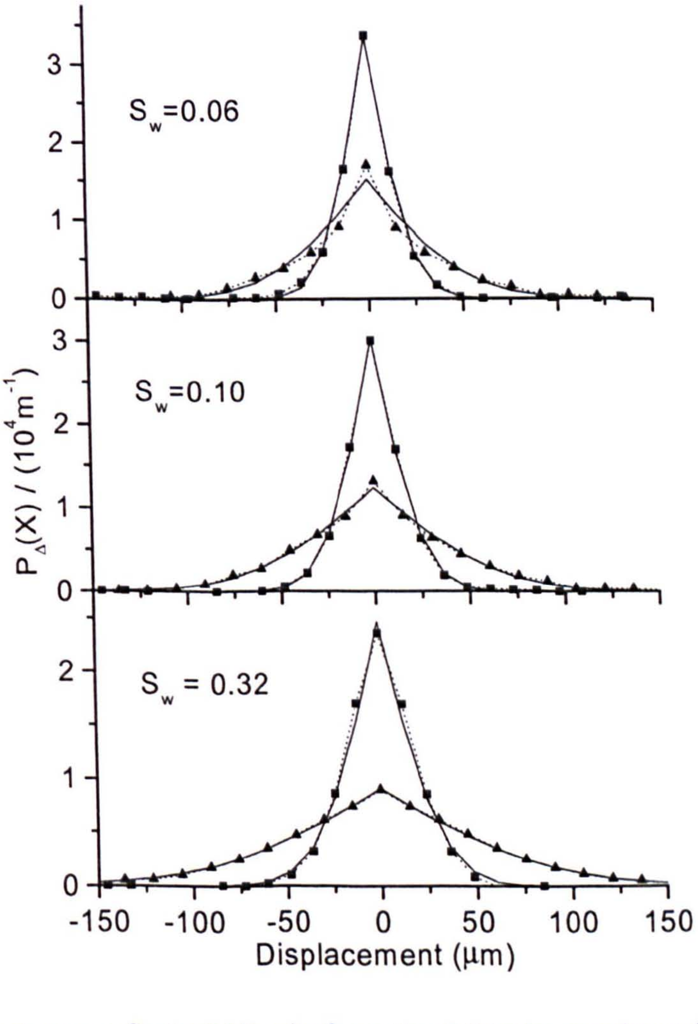

Figure 8.7 Least-squares fits (solid lines) of equation 8.5 to the experimental propagators measured at S_w= 0.06, 0.10 and 0.32. For observation times Δ=0.1s (squares) and 1.6s (triangles). The broken lines connect adjacent data points to aid comparison.

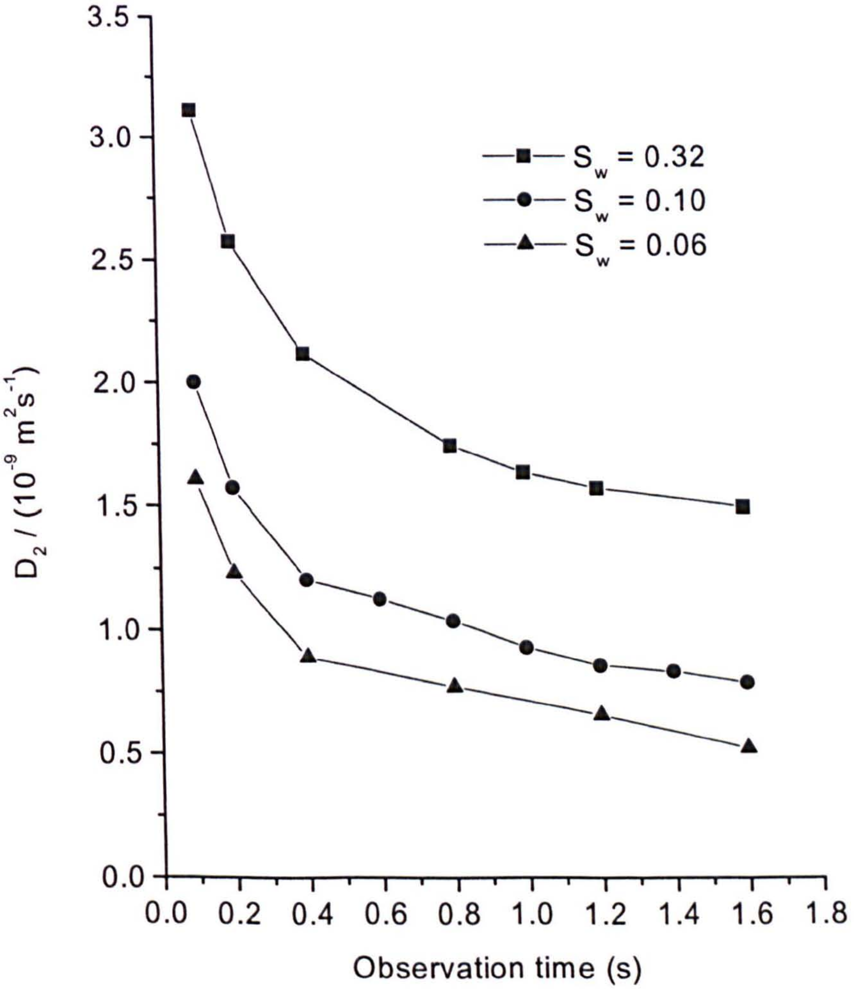

Figure 8.8 Dependence of the least-squares estimates of $D_2(\Delta)$ on Δ obtained by fitting equation 8.5 to propagators measured at S_w= 0.06, 0.1 and 0.32. The solid lines joining data points are intended only as a guide to the eye.

8.3.1 Effect of Curvature

It is possible that the dependence of $D_2(\Delta)$ upon Δ is due to the presence of local curvature in the aqueous surface wetting films. Figure 8.9 illustrates in a very simple way the idea that diffusion on a curved surface, described by a constant diffusion coefficient D_c, when projected onto the x-axis can be described by a time dependent diffusion coefficient $D_x(\Delta)$. In figure 8.9 a group of particles is initially placed on the top of the curve at $\Delta=0$. This group of particles then spread out over the curve by one-dimensional diffusion, the rms displacement of the particles is an arc of length $(2D_c\Delta)^{1/2}$. If the displacement of the particles were mapped onto the x-axis, then the spreading of the particles along the x-axis, at increasing time, can not be described by a constant diffusion coefficient, but can be described by a time dependent diffusion coefficient $D_x(\Delta)$. At very short times the particles experience very little curvature and $D_x(\Delta) \approx D_c$. At longer times the particles experience more curvature and $D_x(\Delta)$ decreases. It is also obvious that the smaller the radius of curvature the faster the decrease in $D_x(\Delta)$.

The general question of how curvature affects the form of the displacement propagator is complex, and will not be addressed here. Instead, in order to gain some general insight, the short time statistics of particles diffusing on the surface of an isolated sphere, for which the analytical result is known [5], are compared to the isotropic infinite planes model. At long times, of course, such a comparison becomes meaningless, as the bounded nature of an isolated sphere then dominates the form of the propagator. I would like to acknowledge Graham [4] for this analysis and T. De Sweit for bringing reference [5] to our attention.

For an isolated sphere of radius R the diffusion equation takes the form:

$$\frac{\partial P^s_\Delta}{\partial t} = D_s \nabla^2_s P^s_\Delta \tag{8.6}$$

Where ∇_s^2 is the Laplacian operator on the surface of a sphere. D_s is the diffusion coefficient and P_s is the displacement propagator describing diffusion on the sphere. The solution of equation 8.6, is given by [5]:

$$P^s_\Delta(\theta_0,\phi_0,\theta,\phi) = \sum_{i,j} Y^*_{i,j}(\theta_0,\phi_0) Y_{i,j}(\theta,\phi) \exp(-\Delta/\tau_i) \tag{8.7}$$

$$\tau_i = \frac{R^2}{i(i+1)D_s}$$

Where (θ_0,ϕ_0) and (θ,ϕ) are, respectively, the spherical polar coordinates of molecules at $t=0$ and $t=\Delta$, the Y_{ij} are spherical harmonics. Taking the gradient direction to define the polar axis, integration of equation 8.7 over ϕ_0 and ϕ gives:

$$P^s_\Delta(X) = \frac{1}{4R^2} \int \sum_i (2i+1)\, L\left(\frac{x_0}{R}\right) L_i \left(\frac{X+x_0}{R}\right) \exp(-\Delta/\tau_i)\, dx_0 \tag{8.8}$$

where L_i is the Legendre polynomial of the i^{th} degree.

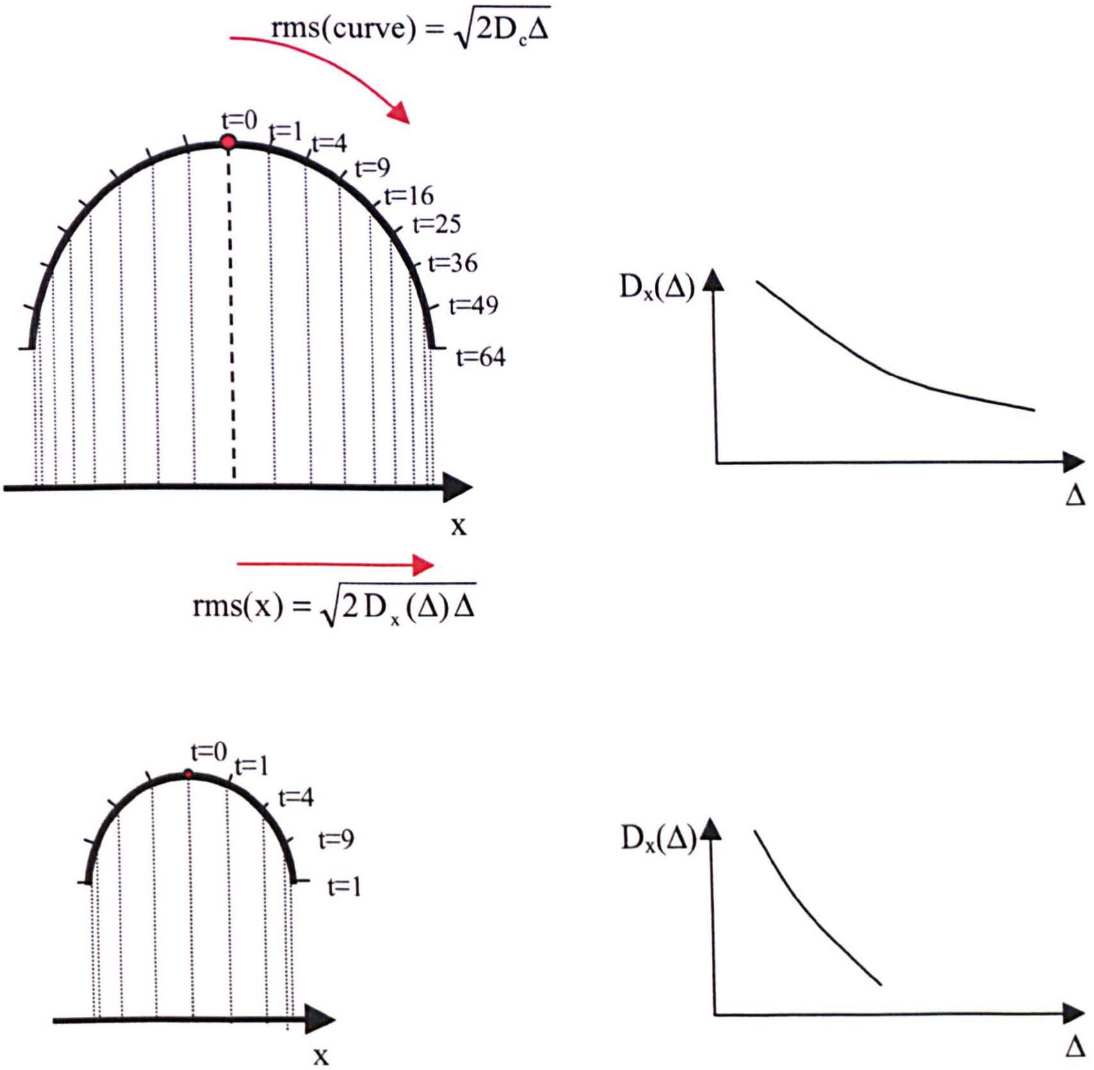

Figure 8.9 Starting at the top of the curve an ensemble of particles undergoes one-dimensional diffusion on the curve, the diffusion coefficient on the curve is D_c, which is constant. The marks on the curve represent equal increases in rms displacement, at increasing time, of the particles as they spread out on the curve. The dashed lines are the projection of these uniform increases in rms displacement on the curve, onto the x-axis.

Propagators were generated from Equation 8.8 for a sphere of radius 75μm with $D_s = 2.2\times10^{-9}$ m^2s^{-1} and Δ= 0.1, 0.8, 1.6s. These propagators were then fitted to the infinite planes model, equation 8.5, with $D_2(\Delta)$ as the fitting parameter, following the same procedure used for the experimental data. Examples of these fits are shown in figure 8.10. It is evident that for short to intermediate times, when the bounded nature of the isolated sphere model is insignificant, the infinite planes model is capable of reproducing the one dimensional statistics of diffusion on a sphere with near-quantitative accuracy, if $D_2(\Delta)$ is regarded as an observation time dependant quantity. Calculations for a variety of sphere radii and observation times indicate that, for $D_s\Delta/R^2 \leq 0.2$, the dependence of $D_2(\Delta)$ on observation time and sphere radius is well represented by:

$$D_2(\Delta,R)=D_s(1-(D_s\Delta/R^2)) \qquad (8.9)$$

This result suggests a possible relationship between the diffusion coefficient $D_2(\Delta)$ and the curvature of the space. The rapid decrease of $D_2(\Delta)$ with increasing Δ in Figure 8.8, could reflect the relatively tight curvatures of small scale irregularities which dominate the statistics at short times. As the particles explore larger regions of the pore surface, the effect of small-scale irregularities will tend to average out, resulting in a larger effective radius of curvature.

Furthermore, the dependence of $D_2(\Delta)$ on Δ has a similar form for all S_w, see figure 8.8. There is also a systematic trend towards higher values of $D_2(\Delta)$ as S_w increases. In particular, at small Δ, for $S_w = 0.32$ the value of $D_2(\Delta)$ exceeds the bulk self-diffusion coefficient of water (~2.2×10^{-9} m^2s^{-1}). This behaviour cannot be interpreted in terms of the curvature of the aqueous film, instead it is believed to arise from a non-negligible contribution to the displacements from diffusion normal to the film surface, which were assumed negligible in the calculation.

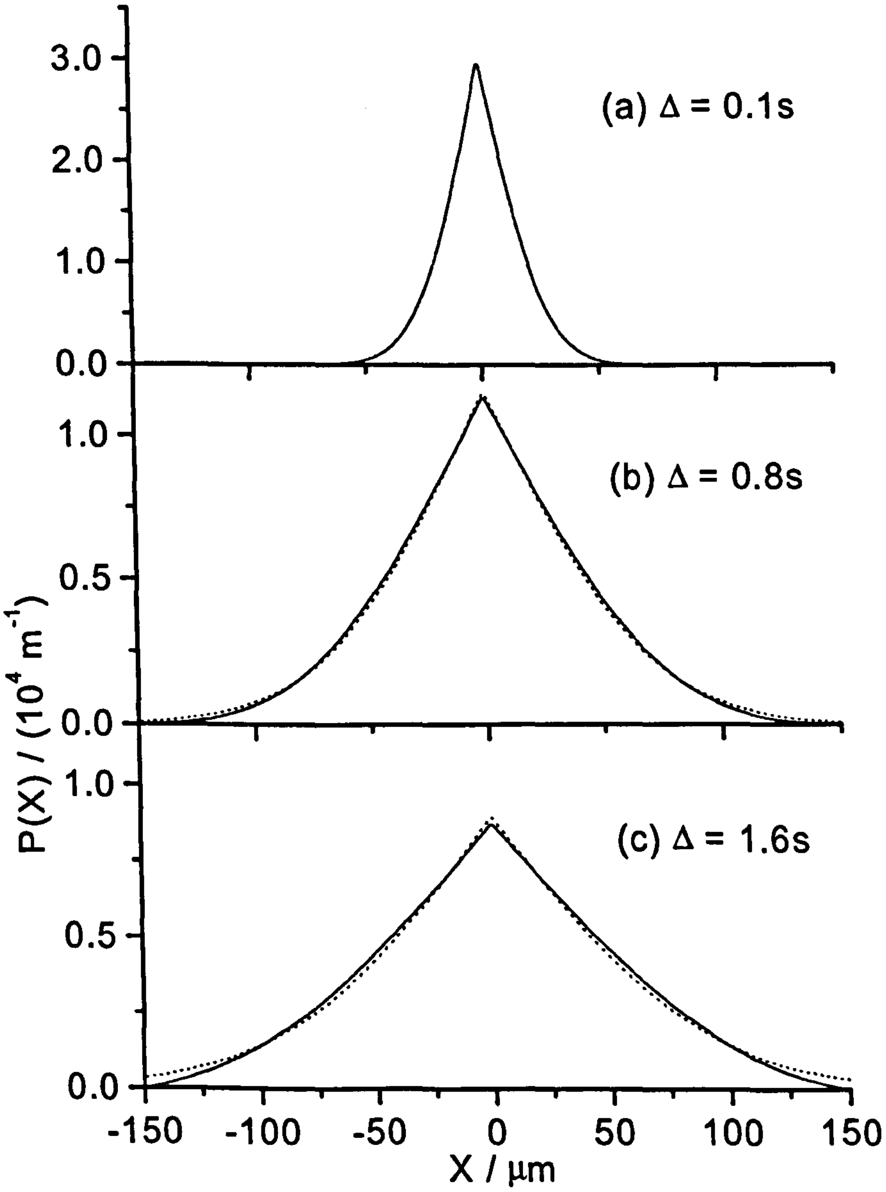

Figure 8.10 Fit of the infinite planes model (broken lines) to the propagators calculated for diffusion on a sphere of radius 75μm at Δ=0.1, 0.8 and 1.6s (solid lines). At Δ=0.1 s the two curves are indistinguishable at the resolution of the figure.

8.4 Conclusions

PGSE NMR measurements have been used to determine the displacement propagators for the diffusion of the wetting phase within a strongly water-wet sample of Fontainebleau sandstone. The sample being saturated with 3% NaCl solution and dodecane in various proportions. Displacement propagators were measured for a range of observation times, with the Fontainebleau sample in different saturation states. A primary drainage/secondary imbibition process was used to prepare the Fontainebleau sample in different saturation states.

The shape of the water propagator depends strongly on the water saturation of the sample. At high water saturations the shape of the water propagator is Gaussian-like, but at low water saturations a cusp-like shape develops around zero-displacement. The effective diffusion coefficient of the water phase, calculated from the second moments of the displacement propagators, shows a strong decrease as the water saturation is reduced. This clearly shows that as the water saturation of the sample is decreased the diffusion of the water phase, i.e. the wetting phase, is becoming increasingly constrained.

To model the diffusion of water within the wetting phase a simple model has been proposed, which is based on two-dimensional diffusion on the surface of an unconnected array of isotropically oriented infinite planes. The measured propagator shapes are remarkably well fitted by this simple model, if the diffusion coefficient $D_2(\Delta)$ is allowed to vary with the observation time. The comparison of the model with diffusion on the surface of an isolated sphere, suggests that the variation of the diffusion coefficient $D_2(\Delta)$ with time, may arise in part, from the local curvature of the pore space.

In order to gain a deeper insight into diffusive displacements of the wetting phase at low water saturations, further experiment were carried out on an idealized porous solid [6,7]. These results are discussed in the next chapter.

8.5 References

1. Bears J. “Dynamics of Fluids in Porous Media”. 1972. Elsevier. New York.
2. Dullien F.A.L. “Porous Media: Fluid Transport and Pore Structure”. 1992. Academic Press Ltd.
3. Tessier J.J., Packer K.J. “The Characterization of Multiphase Fluid Transport in a Porous Solid by Pulsed Field Gradient Stimulated Echo Nuclear Magnetic Resonance.”. 1998. Physics of Fluids. 10. 75-85.
4. Holmes W.M., Graham R.G., Packer K.J. “Diffusion in Surface-Wetting Films in a Two-Phase Saturated Porous Solid Characterized by Pulsed Magnetic Field Gradient NMR”. 2000. Chemical Engineering Journal. 3647. 1.
5. Abragam A. “Principle of Nuclear Magnetism”. 1961. University press Oxford. p.298.
6. Holmes W.M., De Panfilis C., Packer K.J. “Diffusion in Thin Films on the Surface of a Porous Solid”. 2000. Magnetic Resonance Imaging. In Press.
7. Holmes W.M., Packer K.J. In Preparation.

Chapter 9

Diffusion in Thin Films 2

Contents

9.1 INTRODUCTION 147

9.2 EXPERIMENTAL 147

- 9.2.1 SAMPLE PREPARATION AND MEASUREMENT OF S_W 147
- 9.2.2 DETERMINATION OF DIFFUSIVE PROPAGATORS 147
- 9.2.3 SECOND MOMENTS OF DISPLACEMENT PROPAGATORS 149
- 9.2.4 LONGITUDINAL RELAXATION. 152

9.3 COMPUTER SIMULATIONS 154

- 9.3.1 RANDOM WALK DIFFUSION ON A ISOLATED SPHERE 154
- 9.3.2 RANDOM WALK DIFFUSION ON CONNECTED SPHERES 157

9.4 FINAL SIMULATION 159

- 9.4.1 STRUCTURE OF THE SPHERE PACK 160
- 9.4.2 DIFFUSION WITHIN THE SURFACE FILM 162
- 9.4.3 DIFFUSION WITHIN PENDULAR RINGS 162
- 9.4.4 COMBINING DIFFUSION IN THE SURFACE FILM WITH DIFFUSION IN PENDULAR RINGS 164
- 9.4.5 SURFACE RELAXATION. 166
- 9.4.6 RUNNING THE SIMULATION 166

9.5 RESULTS AND DISCUSSION 169

- 9.5.1 CRITICAL WATER SATURATION 169
- 9.5.2 THE EFFECTIVE DIFFUSION COEFFICIENT 171
- 9.5.3 AVERAGE PROPAGATORS 172
- 9.5.4 RELAXATION 176

9.6 CONCLUSION 179

9.7 REFERENCES 180

9.1 Introduction

In chapter 8 PGSE NMR was used to study the diffusion of water molecules contained within the wetting phase of a natural water-wet porous solid [1] (Fontainebleau sandstone), that was saturated with two immiscible phases. For a strongly water-wet porous solid, saturation with two immiscible phases results in the wetting phase forming a continuous surface wetting film. At lower water saturations, these surface wetting films dominate the diffusion statistics of the wetting phase. PGSE NMR was used to determine the one-dimensional displacement probability distributions (average propagators) of the wetting phase. Interpretation of these results is made onerous on account of the complex pore structure of Fontainebleau sandstone. Therefore, these results were analysed with a simple theoretical model in which the water was distributed in thin uniform films on an isotropic array of infinite and unconnected planes.

In order to investigate this problem in a more defined and controllable system, similar measurements were performed on an idealized porous solid, comprising of water-wet, mono disperse, glass beads saturated with two phases [2 ,3]. This chapter presents the experimentally determined average propagators for the diffusion of the wetting phase at various water saturations in such a system. These results are then interpreted using a random walk simulation of diffusion in a suitable model structure. Experimental measurements were also made of the longitudinal relaxation properties of the wetting phase at various water saturations and these results are also interpreted using the random walk simulation model.

9.2 Experimental

9.2.1 Sample Preparation and Measurement of S_w

The sample used in this study was a bead pack made of 100μm diameter, water-wet, mono disperse, glass beads, saturated with two phases. The wetting phase was distilled water and the non-wetting phase was tetrachloroethylene (C_2Cl_4 , 99% Aldrich), ensuring that the ^1H NMR signal arises solely from the wetting phase. Different water saturation states were produced in the sample by the methods described in section 5.4.2. As the only ^1H NMR signal arises from the water phase, the water saturation was determined from the magnitude of the ^1H NMR signal, compared with the ^1H NMR signal with the sample at $S_w=1$ {see method 2 section 5.3.5}.

9.2.2 Determination of Diffusive Propagators

One dimensional diffusive propagators were determined in the manner outlined in detail in section 5.6.2. The one-dimensional APGSTE NMR signal $E_\Delta(q_x)$ was acquired for a central slice (40mm) of the sample. $E_\Delta(q_x)$ was measured for 32 equally spaced values of q_x in the range $-q_{max}$ to q_{max}, where $q_{max}= 36120m^{-1}$. The average propagator was then obtained by Fourier transformation of $E_\Delta(q_x)$ with respect to q_x, see equation 2.48.

Average propagators were acquired for a range of water saturation states S_w and for a range of observation times Δ. To improve the signal-to-noise ratio of measurements made at lower water saturations and longer observation times, progressively more signals were accumulated and averaged, to a maximum of 96 {see section 2.8.10}. Figure 9.1 shows how the displacement propagators $P_\Delta(X)$ for the diffusion of the wetting phase change as a function of water saturation. For $S_w = 1$ the propagator is approximately Gaussian in form. As the water saturation of the sample is decreased the propagator develops a cusp-like appearance around zero-displacement and decays more rapidly with increasing X. It can be seen from figure 9.2 that, for a constant and low value of S_w, the cusp-like shape persists at larger observation times.

I would like to acknowledge C. De Panfilis for making the experimental measurements some of the water propagators presented in this chapter. C. De Panfilis measured water propagators for the higher water saturations ($S_w > 0.2$).

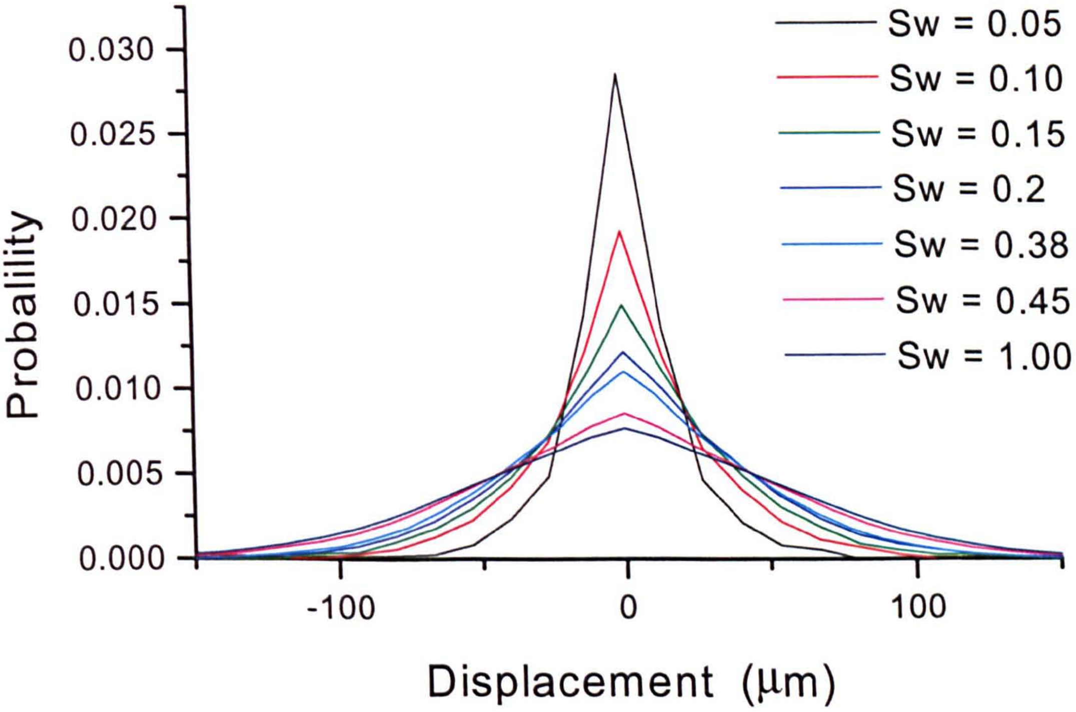

Figure 9.1 Water propators measured at various water Saturations,S_w, for an observation time of 1.2s. The lines connect data points and are only a guide for the eye.

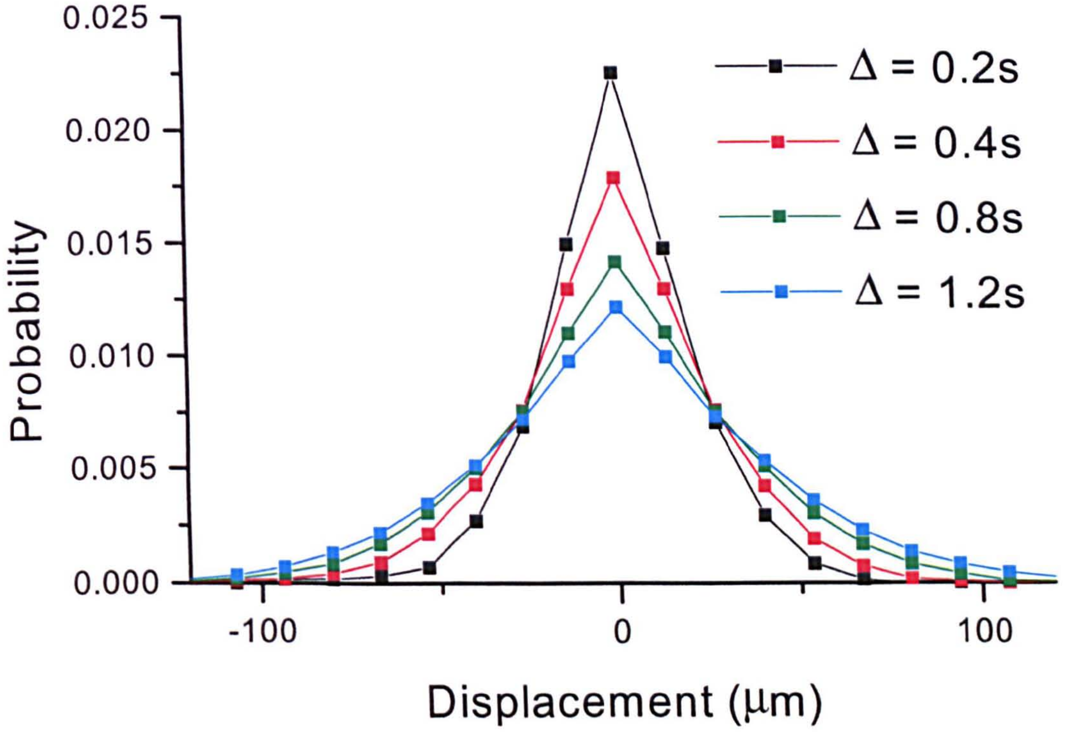

Figure 9.2 Water propagators measured at various observation time Δ, with the sample at a water saturation $S_w = 0.2$. The lines connect data points and are only a guide for the eye.

9.2.3 Second Moments of Displacement Propagators

In section 9.2.2 displacement propagators, measured for various water saturations and observation times, were presented. To give a simple quantitative description of these propagators their second moments have been calculated, where the second moment (mean squared displacement) of the propagator $P_\Delta(X)$ is given by:

$$M_2 = \int_{-\infty}^{\infty} X^2 \, P_\Delta(X) \, dX \tag{9.1}$$

Figure 9.3 shows the time dependence of the second moments for different water saturations states. It can be seen that for $S_w > 0.38$ the second moments do not vary much with increasing S_w. In contrast, for $S_w<0.38$ there is a steady and marked decrease in the second moments with decreasing S_w.

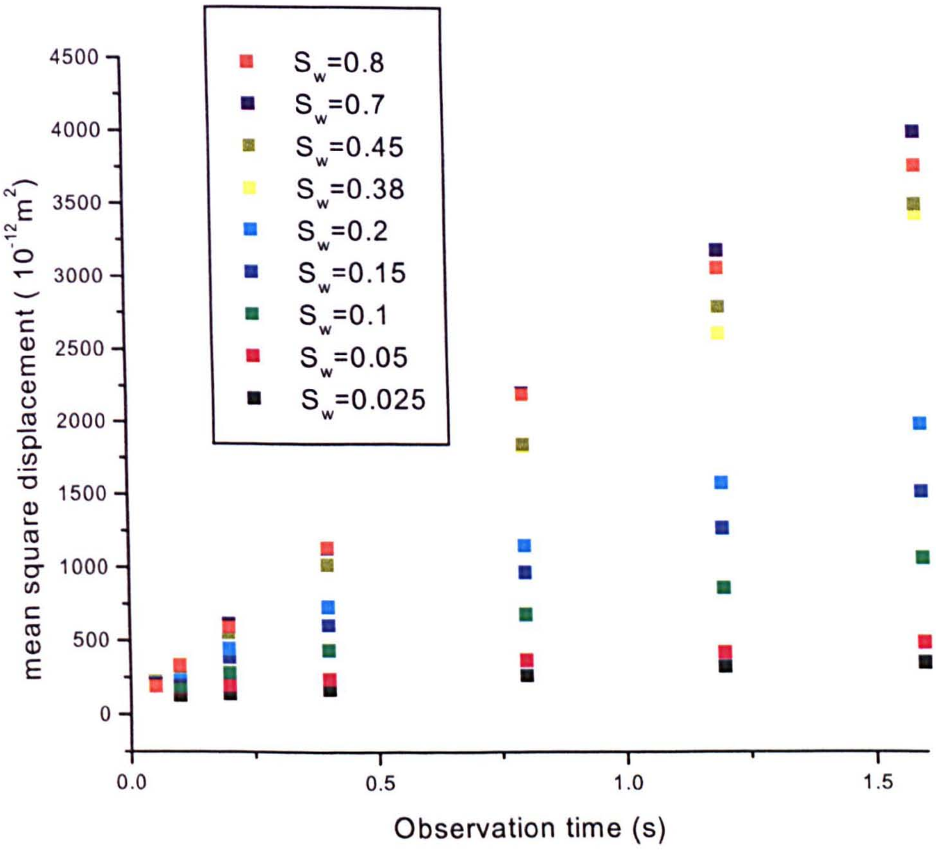

Figure 9.3 The time dependence of the mean squared displacement.

It is possible to calculate an effective diffusion coefficient D^* at long times from the seconds moments:

$$D^* = \lim_{\Delta\to\infty} \frac{\langle X^2(\Delta) \rangle}{2\Delta} \tag{9.2}$$

The effective diffusion coefficient D^* was calculated from the slope of data shown in figure 9.3 between 0.8s and 1.6s. Figure 9.4 shows how the effective diffusion coefficient depends on the water saturation of the glass bead pack. An explanation of this result is given later.

The root mean squared (rms) displacement in three-dimensions of the water molecules is given by $(6D^*\Delta)^{1/2}$. At S_W=1, for an observation time of 1.6s, the rms displacement is 112µm, which is just over a sphere diameter (100µm).Therefore, the water molecules are experiencing the structure of the glass beads, but D^* has probably not reached it infinite time limit.

At S_W= 0.05, for an observation time of 1.6s, the rms displacement is just 32µm, which in considerably less than a sphere diameter (100µm). At first sight it appears that the water molecules do not experience enough of the structure of the glass beads, to be able to give a reasonable long time effective diffusion coefficient. In fact, at lower water saturations the distribution of the water phase in the sample and the nature of the restrictions experienced by diffusing water molecules changes considerably. It is shown in section 9.5.3 that the values of D^* measured at low water saturations are a good approximation of the long time effective diffusion coefficient.

Even though at high water saturations the calculated D^* may not be at its infinite time limit, it is still valuable in showing how decreasing the water saturation of the sample affects the diffusive transport of the water phase.

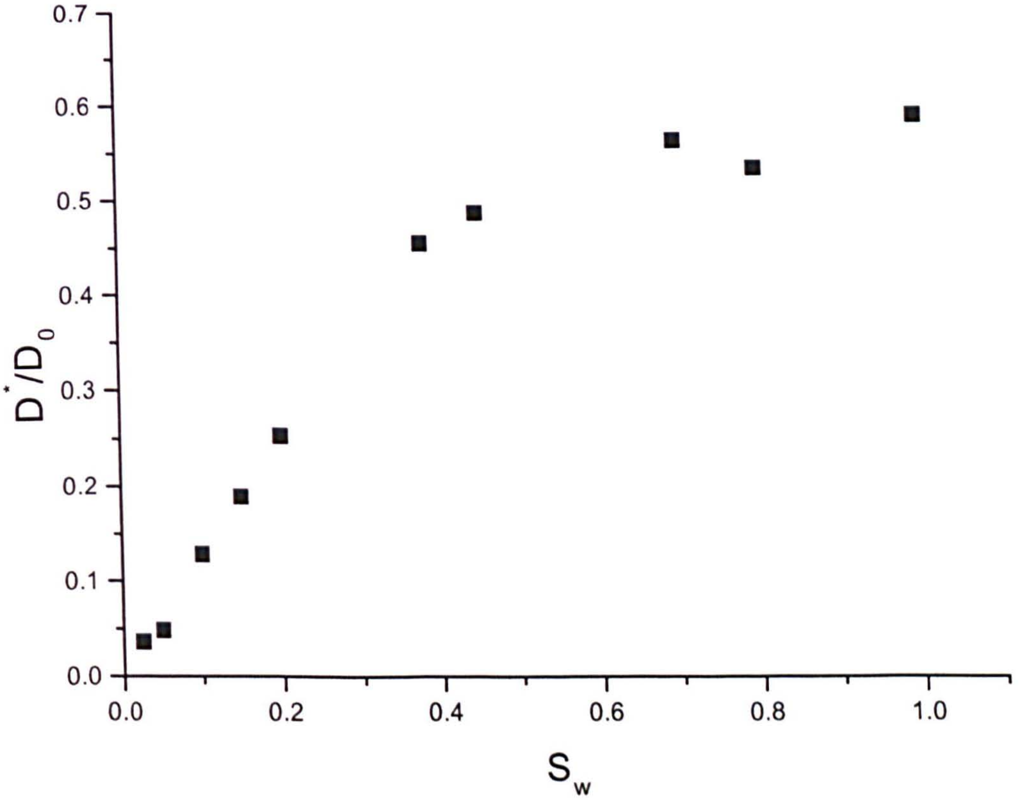

Figure 9.4 Effective diffusion coefficients of the water phase in glass bead packs at different water saturations.

9.2.4 Longitudinal Relaxation.

The inversion recovery sequence {see section 5.5.1} was used to measure the longitudinal relaxation of the water phase, with the sample in different saturation states. In these measurements 32 data points were taken, using τ values logarithmically spaced from 0.005s to 15s. A Recycle delay of 15s was used to allow full T_1 relaxation. Between 16 and 128 averages were used to achieve a good signal to noise ratio. The relaxation curves were fitted using a discrete multiple exponential method using a non-linear least squares regression program called XFIT. This program was written by BP research.

The observed longitudinal relaxation curves for the water phase were mono-exponential at all water saturation states. The reason for this is discussed in section 6.2.1. The variation of T_1 with S_w is shown in figure 9.5.

As discussed in section 3.4, for a strongly water-wet porous solid, the water phase forms a continuous film over all the bead surfaces. Therefore, the specific surface area of the water phase is constant at all saturations and changes in the water saturation S_w only change the specific volume of the water present in the sample. In the fast diffusion limit, i.e. the rate limiting step is surface relaxation, the longitudinal relaxation rate is given by:

$$R_1 = \frac{1}{T_1} = \frac{1}{T_{bulk}} + \rho_1\left(\frac{S_0}{V_0}\right)\left(\frac{1}{S_w}\right) = \frac{1}{T_{bulk}} + C\left(\frac{1}{S_W}\right) \tag{9.3}$$

where S_0 and V_0 are respectively the specific surface area and volume of the whole pore space. C is a constant. It can be seen in figure 9.6 that there is a linear relationship between $(T_1)^{-1}$ verse $(S_w)^{-1}$, for $(S_w)^{-1} < 3.7$, giving $\rho_1(S_0/V_0)=0.08\pm0.01s^{-1}$. At higher values of $(S_w)^{-1}$ there is a deviation from the fast diffusion model. This is discuss in detail in section 9.5.4.

For a pack of spheres the surface-to-volume ratio is given by:

$$\frac{S_0}{V_0} = \frac{3(1-\phi)}{\phi r} \tag{9.4}$$

where ϕ is the porosity of the bead pack and r is the bead radius. Using $\phi = 0.44$ [4,5], the surface relaxtivity of the glass beads was calculated as $\rho_1 = 11\times10^{-7}$ m s^{-1}. Hills et al have calculated the surface relaxivity of water saturated glass beads as 8.9×10^{-7} m s^{-1} [6] and 7.3×10^{-7}m s^{-1} [7].

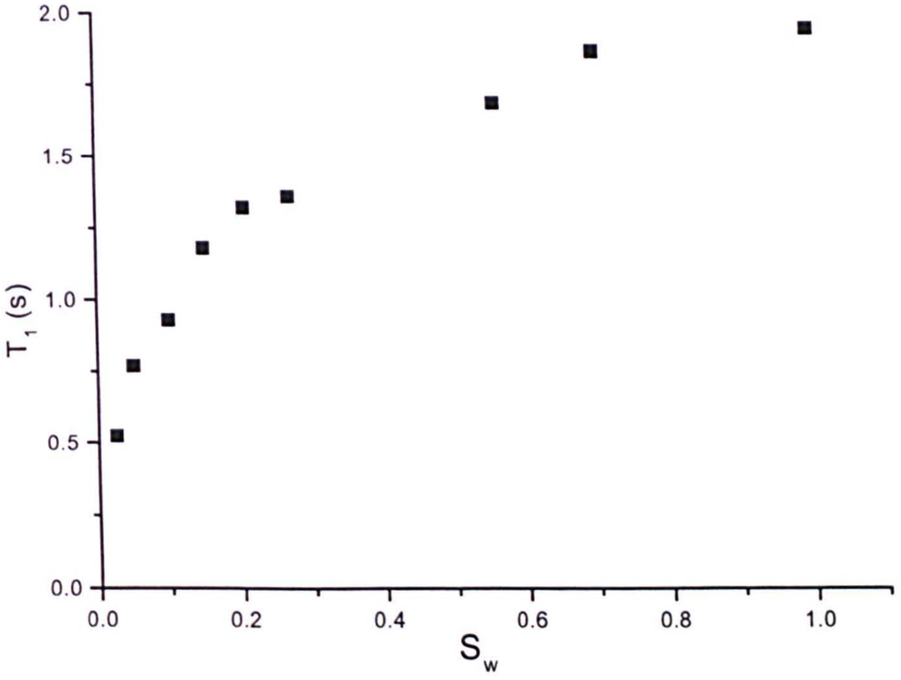

Figure 9.5 T_1 of the water phase as a function of S_w.

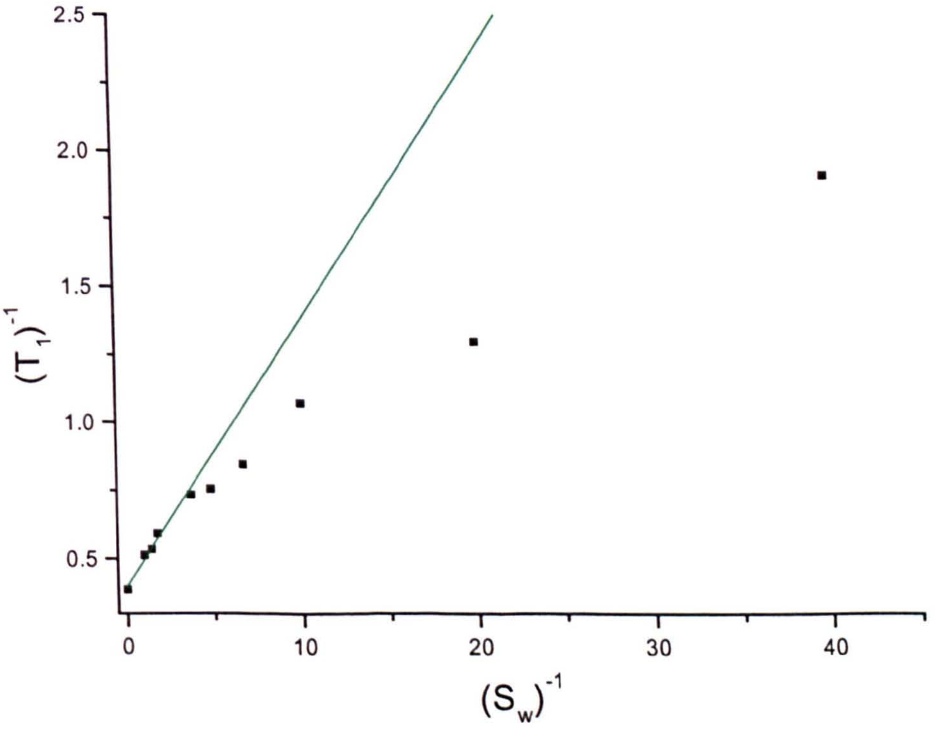

Figure 9.6 $(T_1)^{-1}$ plotted against $(S_w)^{-1}$. The line shows a linear fit to the initial slope.

9.3 Computer simulations

The simple theoretical model used in chapter 8 is clearly limited in helping understand the changes seen in the experimental data at lower water saturations i.e. the shape of the displacement propagators, the behaviour of the effective diffusion coefficient and the longitudinal relaxation data. Therefore, a more realistic random walk simulation was developed specifically to understand these phenomena at low water saturations. In order to comprehend the final version of this simulation the various stages in its development are explained in detail.

9.3.1 Random walk diffusion on a isolated sphere

Initially a random walk simulation was developed for the diffusion of water molecules on the surface on an isolated sphere. This problem has the advantage that the results of the simulation can be compared to an analytical solution, equation 8.8, to provide a check on the random walk calculation. As with all random walk simulations time is incremented in small discrete steps τ. During each time step, each particle moves a fixed distance in a random direction. The fixed distance is the rms displacement that an ensemble of particles would move during the same timestep.

A particle performing a quasi two-dimensional random walk on the surface of a sphere must move a fixed distance L along the arc of the sphere, in a random direction, in a timestep τ :

$$L = \sqrt{4D\tau} \tag{9.5}$$

where D is the bulk diffusion coefficient of water and τ is the timestep of the simulation.

It was quickly realised that the manner of performing these random steps was not trivial. It was not possible to use polar coordinates and simply have random increments of θ and ϕ because they are not independent variables. Therefore, to move a particle an arc length L, in a random direction, over the surface of the sphere, a sequence of six individual rotations were used, giving a resultant rotation matrix M:

$$\left(R_z(-\theta)R_y(-\phi)\right)\left(R_z(\alpha)R_y(\gamma)\right)\left(R_y(\phi)R_z(\theta)\right) = M \tag{9.6}$$

where θ and ϕ are the initial polar coordinates of the particle, R_Z and R_Y are rotation matrices which perform rotations about the Z and Y axis respectively. The angle γ is the angle swept out by an arc of length L (γ = L/radius). The angle α is randomly generated between 0 and 2π, it provides the random direction of each step. The sequence of rotations used to perform each random walk step on the surface of the sphere is illustrated in figure 9.7.The new position of a particle after moving a fixed arc length L in a random direction is given by:

$$M\,P_i = P_f \tag{9.7}$$

where P_i and P_f are the Cartesian coordinate vectors of the initial position of the particle and its position after one time step.

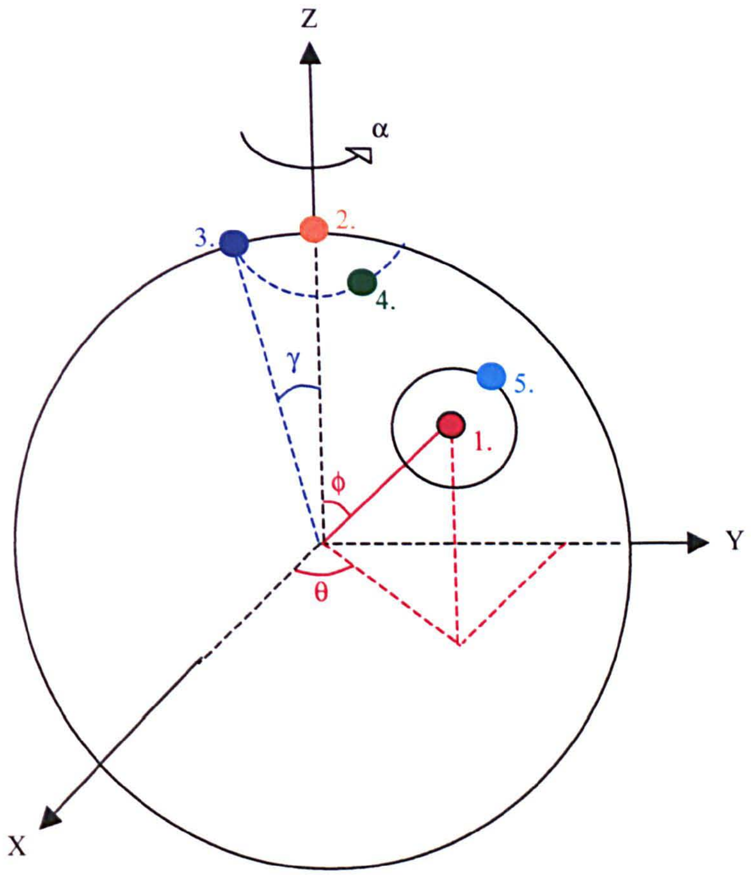

Figure 9.7 The sequence of rotations used to a perform random walk step on the surface of a sphere.

a) The particle starts at position 1 with polar coordinates θ and ϕ.

b) The particle is moved to the position 2 (the North pole) by $R_y(\phi)R_z(\theta)$.

c) The particle is then rotated about the y axis by the angle γ to position 3. The angle γ is the stepangle, whose arc length is the mean displacement of a water molecule in the time step τ.

d) The particle is then rotated about the z axis by a random angle α to position 4. This gives the random direction moved in this step.

e) Finally the reverse of the initial rotation to the North pole is applied by $R_z(-\theta)R_y(-\phi)$. Moving the particle to position 5.

To test the simulation 500,000 particles were randomly positioned on the surface of an isolated sphere of diameter 100μm. The particles were moved randomly over the surface, using the method described above, for observation times of 0.4s, 0.8s and 2s. The timestep used was 0.002s, corresponding to 200,400 and 1000 steps respectively. The diffusion coefficient was taken as $2.2\times10^{-9}m^2s^{-1}$.

The accuracy of the simulation was tested in two ways. The first test of the simulation uses the fact that the projection of the density of a spherical shell along any axis is rectangular. Therefore, a histogram of the positions of the particles along any axis, at any point during the simulation, should also be rectangular. Figure 9.8 shows this is true for the initial and final positions of the particles in the simulation. This demonstrates the simulation exhibits no bias for a particular direction.

The second test of the simulation was to compare simulated displacement propagators with the analytical propagators calculated from equation 8.8. The simulated displacement propagators $P_\Delta(X)$ were produced by making a histogram of the individual displacements of each particle along the x-axis. It can be seen in figure 9.9, that the analytical and simulated propagators are indistinguishable, apart from the noise of the simulated propagators. These results show the random walk simulation accurately describes the diffusion of particles on an isolated sphere. This simulation could now be used confidently as the basis of more complex simulations, for which no analytical result is available.

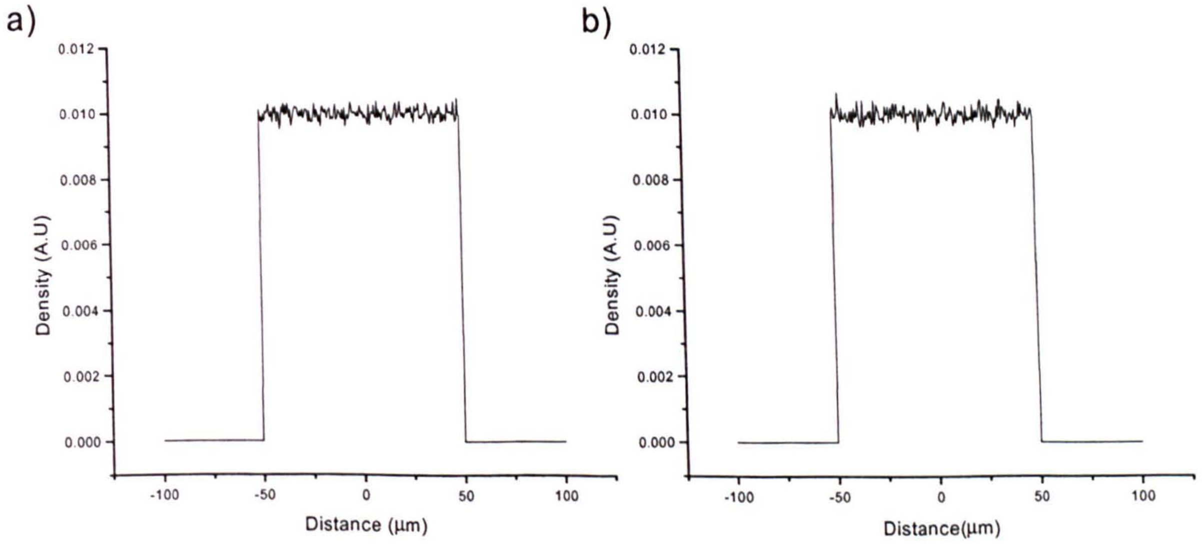

Figure 9.8 Density profiles projected along the x-axis. a) start of simulation b) end of simulation.

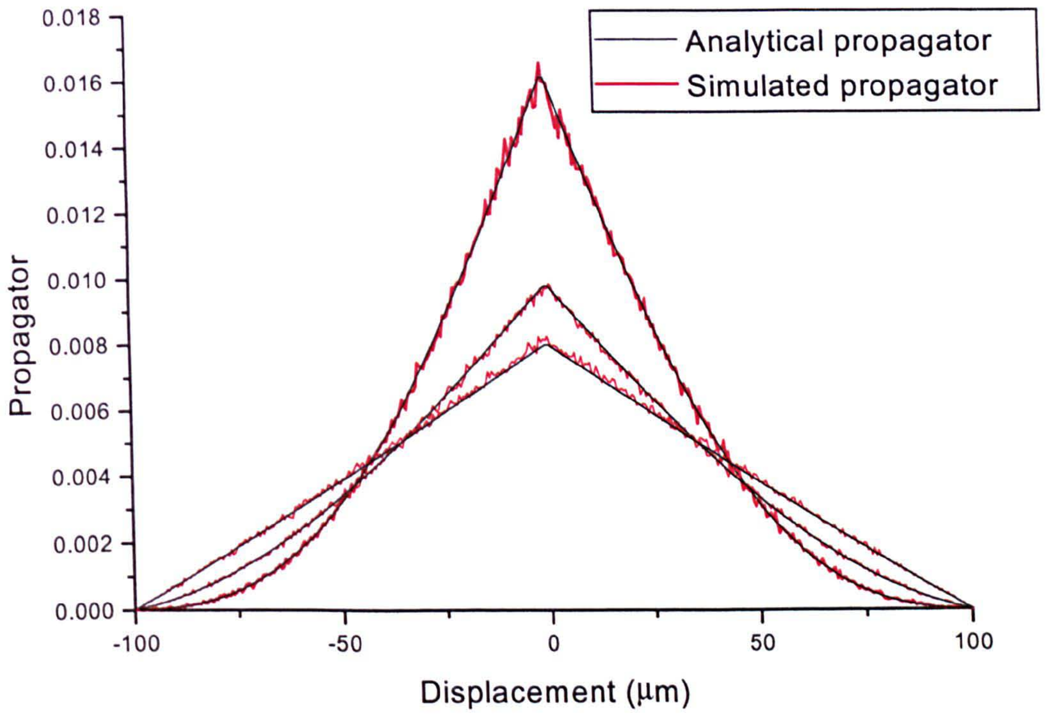

Figure 9.9 Simulated and analytical propagators for diffusion on the surface of an isolated sphere of 100μm diameter, for observation times of 0.4, 0.8 and 2s. The simulation used 500,000 particles, each moving 80, 160and 400 steps of 0.005s respectively. Diffusion coefficient of water used was $2.2\times10^{-9}m^2s^{-1}$.

9.3.2 Random Walk Diffusion on Connected Spheres

The simulation described above accurately recreates diffusion on the surface of an isolated sphere. The next step was to allow particles diffusing on the surface of one sphere to move to the surface of a connected sphere. This requires some kind of structure for the connected spheres, which ideally would be a random packing of spheres to reproduce the experimental situation.

In the experimental water propagators, figure 9.1, it can be seen that no particles have a displacement greater than 1.7 sphere diameters (170μm). Therefore, it was considered unnecessary to use a computer generated random sphere pack structure, as individual particles would 'experience' very little of this structure. Instead, a simple though abstract structure was used. In this structure each particle was allowed to diffuse on the surface of spheres arranged in a simple cubic lattice. However, to make the structure more random, the simple cubic lattice was given a random orientation for each particle.

In this simulation particles diffusing on the surface of one sphere were allowed to move to an adjacent sphere when they came within a distance d of the contact point of two spheres, see figure 9.10.

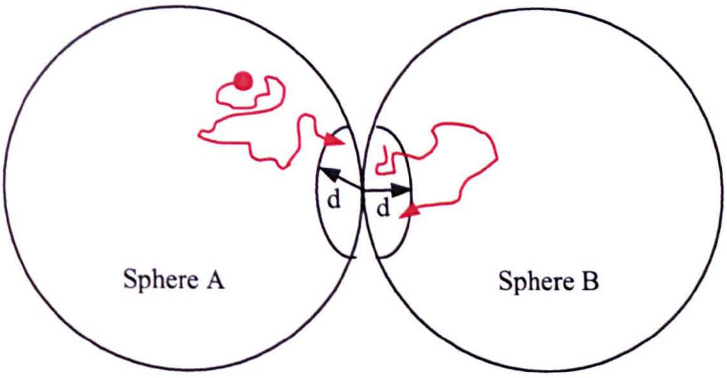

Figure 9.10 A particle diffusing on the surface of sphere A, is moved onto a mirror image position on sphere B, if it moves within a distance d of the contact point between sphere A and sphere B. Once on sphere B the particle is not allowed to return to sphere A until it has moved outside a distance d from the contact point.

Simulations were run with 500,000 particles diffusing on the connected surface of 100μm diameter spheres, for an observation time of 2.8s and a time step $\tau = 0.005$s. Figure 9.11 shows propagators simulated for values of d between 0 and 6μm . For d=0, i.e. no connections, the simulated propagator is triangular, which is expected for an isolated sphere in the long time limit. Increasing the value of d increases the connectivity of the spheres, and the propagators spread over a larger displacement range. The shape of the simulated propagators fails to reproduce the cusp-like shape of the experimental propagators. Therefore, diffusion on the surface of connected spheres is not a successful model for this system.

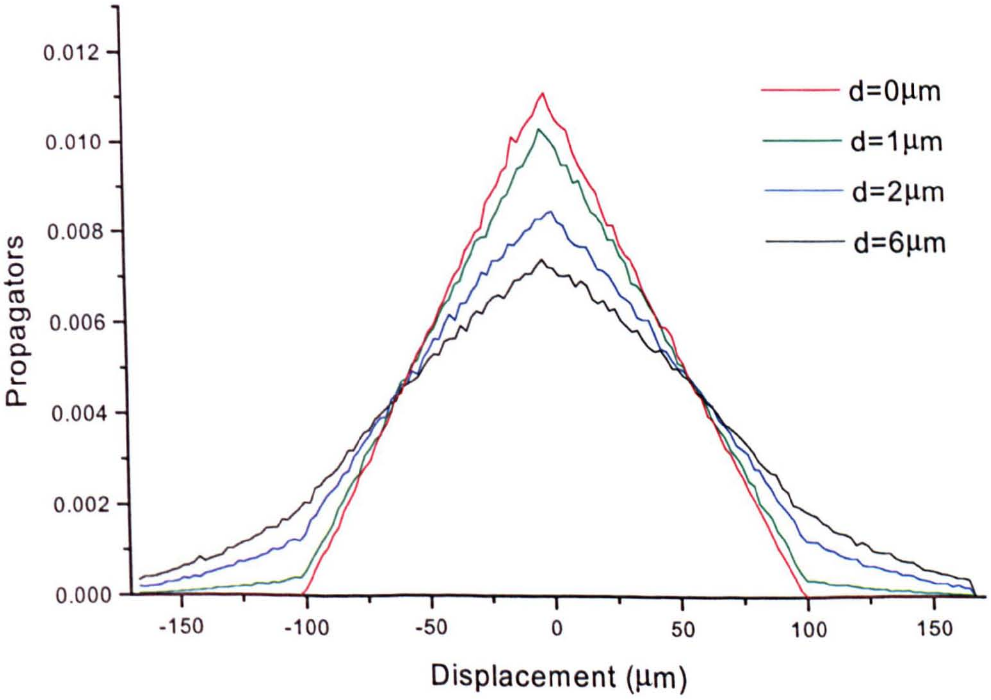

Figure 9.11 Simulated propagators for diffusion on the surface of connected spheres, of 100μm. Using an observation time of 2.8s and a diffusion coefficient of $2.2\times10^{-9}m^2s^{-1}$.

9.4 Final simulation

To improve the simulation a more realistic account was taken of the distribution of the water phase within the sample. At low water saturations this distribution is governed by the interfacial tensions between the two fluids and between each fluid and the solid surface of the spheres. At low water saturations, it is known that the water phase does not form a uniform film over the sphere surfaces. To minimize the Gibbs free energy [8] of the system the water phase is present in discrete masses, each mass is a ring of water wrapped around the contact point of an adjacent pair of spheres [9], as shown in figure 9.13. These single rings of water were called 'pendular' rings by Versluys [10]. The water phase is also present as a thin continuous film covering the remaining surface of each sphere. This thin surface film provides a connection between pendular rings at low water saturations.

A random walk simulation for the diffusion of water molecules confined within such a system of pendular rings connected by thin surface films, would ideally be performed by having random walkers moving in three-dimensions around the confined system. Unfortunately, this method of performing the random walk simulation proved to be impractical for this system, because the thickness of the surface film was expected to be only of the order ~10nm [11].

The impracticality of a three-dimensional random walk in a film ~10nm thick, can be understood by considering this would require a step length of less than 10nm, for example 2nm. Figure 9.12 shows a diagram of diffusion within a surface film of water on a sphere of diameter 100μm. For water molecules, a step length of 2nm corresponds to a timestep τ for the simulation of 3×10^{-10}s. Using this time step to simulate an observation time of 1.6s would require each particle to perform ~5 billion tiny steps. Performing this for 300,000 particles would require inordinate computing time.

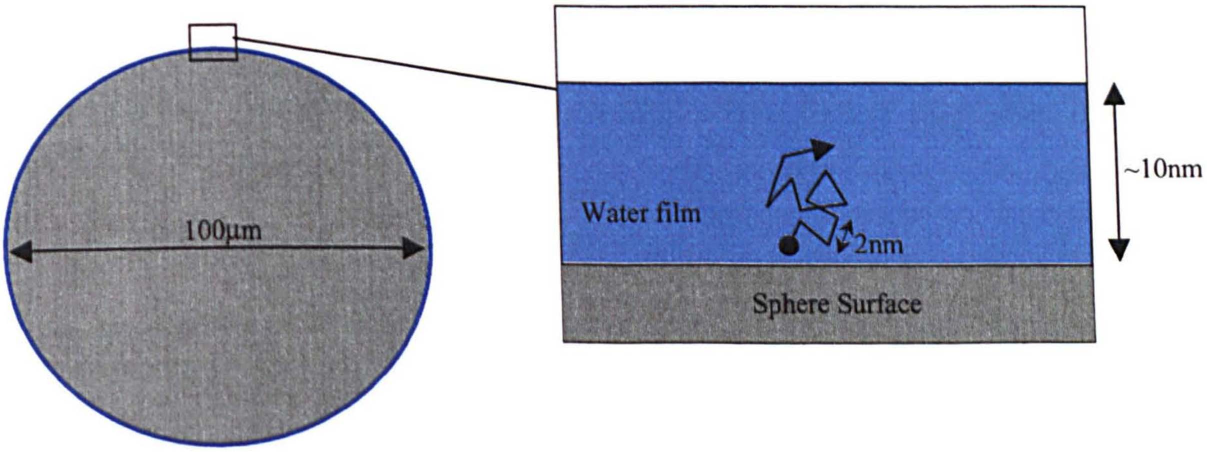

Figure 9.12 Diagram showing the thin surface film covering a sphere of diameter 100μm. A section of the film is enlarged.

The solution to this problem was to break the simulation into two sections. Particles present in the thin surface film would undergo quasi 2-d diffusion on the surface of the sphere, whereas particles present in pendular rings would undergo a typical three-dimensional random walk

9.4.1 Structure of the Sphere Pack

The final simulation uses the same abstract structure, described in section 9.3.2, to approximate the random packing of spheres. A simple cubic lattice of spheres is used for the local structure. Figure 9.14 shows the unit cell of a simple cubic lattice and how the water phase is distributed at low water saturations, i.e. as a thin surface wetting film connecting pendular rings which form at the contact point of two spheres. To make the overall structure more isotropic, for each particle the cubic lattice is given a random orientation with respect to the laboratory axis system.

The unit cell contains 1 complete sphere and 3 complete pendular rings. The volume of water in the surface film V_s ,per unit cell, is given by:

$$V_s = 4\pi r(r-3m)t \tag{9.8}$$

where r is the sphere radius, m is the half width of the pendular rings and t is the thickness of surface film. The volume of water present in pendular rings V_p, per unit cell, is given by:

$$V_P = 3(2\pi rm^2 - \tfrac{4}{3}\pi m^3) \tag{9.9}$$

The water saturation is then given by:

$$S_w = \frac{V_p + V_s}{V_{void}} = \frac{(6\pi rm^2 - 4\pi m^3) + 4\pi r(r-3m)t}{8r^3 - \tfrac{4}{3}\pi r^3} \tag{9.10}$$

Assuming the volume of water present in the surface film is negligible, the water saturation is given by :

$$S_w \cong \frac{(6\pi rm^2 - 4\pi m^3)}{8r^3 - \tfrac{4}{3}\pi r^3} \tag{9.11}$$

From equation 9.11 the half-width m of the pendular rings can be calculated for different water saturations S_w.

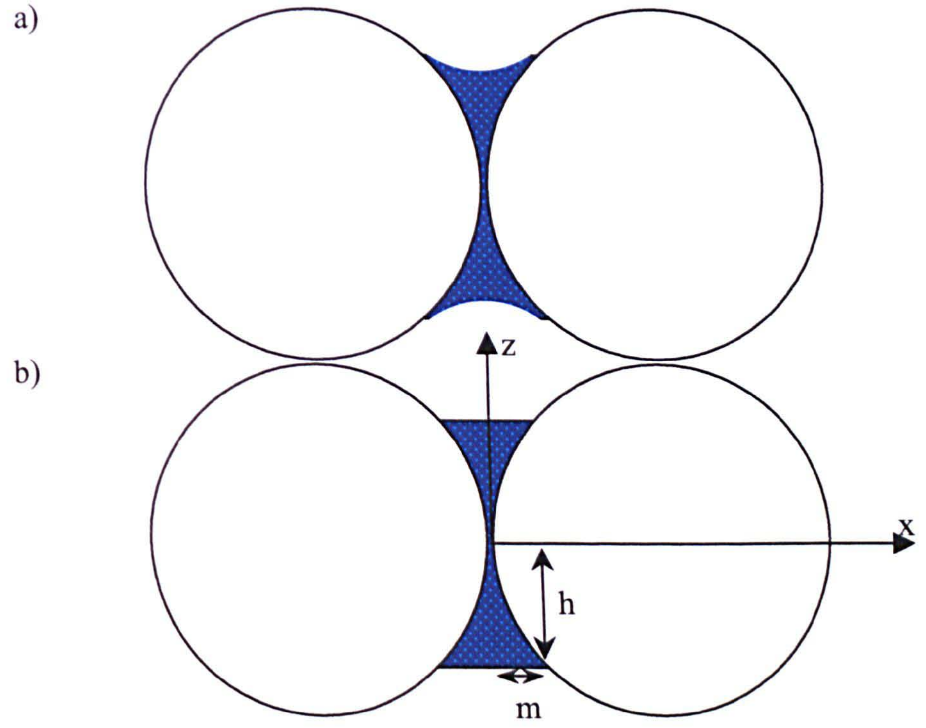

Figure 9.13 a) The cross section of a pendular ring of water which forms at the point of contact between two spheres. b) The cross section of the simplified pendular ring shape used in the simulations, the curved meniscus is replaced by a straight line. The half width of the pendular ring m and the half height of the pendular ring h are labelled.

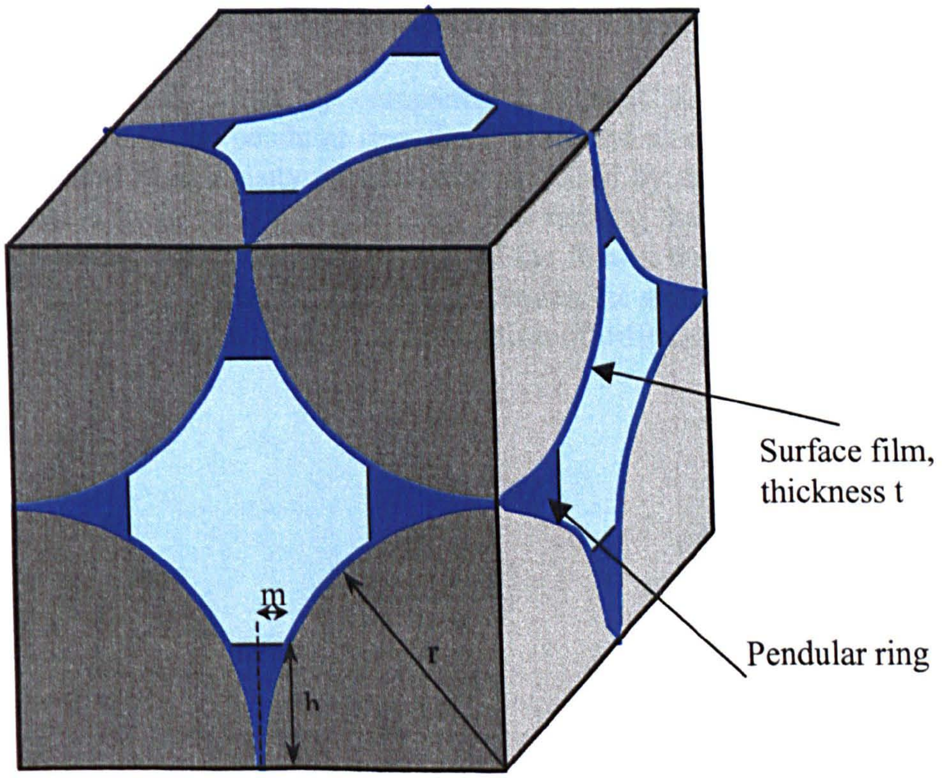

Figure 9.14 Unit cell of a simple cubic lattice of spheres. The water phase is present as pendular rings and a thin surface film

9.4.2 Diffusion within the surface film

In the final simulation particles present in the surface film perform a quasi two-dimensional random walk on the surface of the spheres. The random walk is performed using the same method described in section 9.3.1, for diffusion on an isolated sphere. This means that in the final simulation the surface film has no actual thickness. The thickness of the surface film t is instead related to the fraction of the total number of particles used in the simulation, that are present in the surface film F_s:

$$F_s = \frac{n_s}{n_s + n_p} = \frac{V_s}{V_p + V_s} = \frac{4\pi r(r-3m)t}{(6\pi r m^2 - 4\pi m^3) + 4\pi r(r-3m)t} \tag{9.12}$$

Where n_s and n_p are the number of particles within the surface film and pendular rings respectively.

9.4.3 Diffusion within Pendular Rings

A subprogram was written for the three dimensional random walk of particles confined within a pendular ring. To simplify the program a slightly less complicated shape was used for the pendular ring, see figure 9.13, by using a straight line to replace the curved meniscus. Any particles hitting the walls of the confining shape were reflected back, the reflection being treated like an elastic collision.

This subprogram was tested by comparing simulated density profiles with calculated density profiles of the pendular ring shape projected along the x and z-axes, see figure 9.13. The simulated density profiles were acquired by randomly positioning 500,000 particles inside an isolated pendular ring, then running the simulation for 2s (400 steps of 0.005s each). Histograms were made of the final x and z positions of the 500,000 particles. Figure 9.15 shows a good match between the simulated and calculated density profiles. This shows the random walk simulation of diffusion within an isolated pendular ring is free of bias.

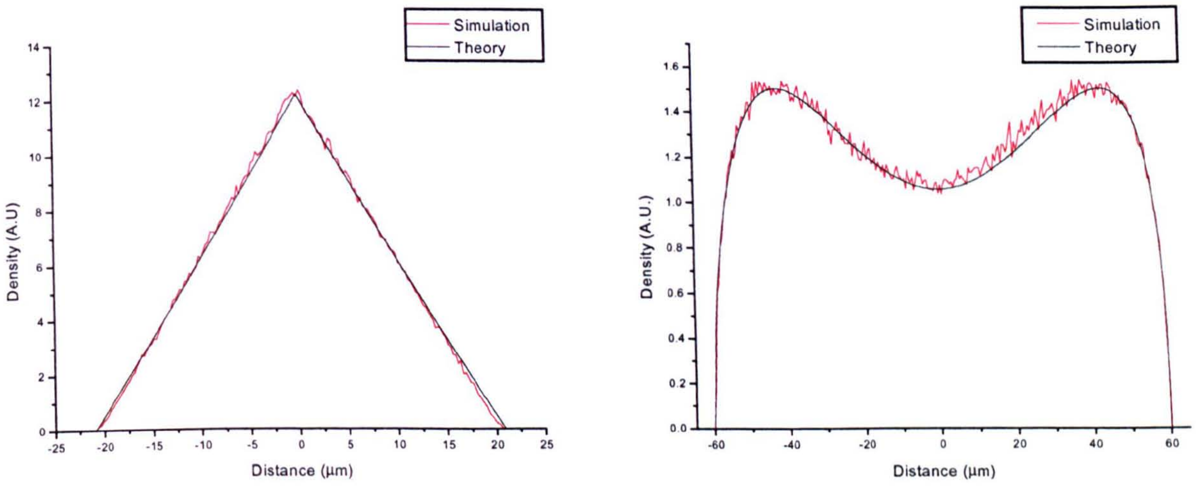

Figure 9.15 Density profiles of an isolated pendular ring, of half width m=10µm and half height h=30µm. a) along the x axis (see figure 9.13). b) along the z axis.

9.4.4 Combining Diffusion in the Surface Film with Diffusion in Pendular Rings

In the final simulation particles within the surface film undergo a random walk as described in section 9.3.1, and particles present in pendular rings undergo a random walk as described in section 9.4.3. To combine these two separate sections successfully, particles have to be able to move from one to the other in a realistic and self-consistent manner.

Surface film to pendular ring

A particle diffusing in the surface film is transferred into a pendular ring when it moves into an area of the sphere's surface which is in contact with a pendular ring, see figure 9.16. The particle then continues its random walk inside the pendular ring. The rate at which particles leave the surface film and move into pendular rings is governed by the area of the sphere's surface that is in contact with pendular rings and the thickness of the surface film.

Pendular rings to surface film

Particles diffusing inside a pendular ring can move into the surface film as follows. Figure 9.17 shows the cross section through a pendular ring. From the coordinates of the particle in the pendular ring three distances are calculated d_1, d_2 and d_3. These distances are used to decide what happens to the particle after each random walk step.

If $d_1 < r$ the particle is reflected back into the pendular ring from the surface of sphere A.

If $d_2 < r$ the particle is reflected back into the pendular ring from the surface of sphere B.

If $d_1 > r + P$ and $d_2 > r + P$ and $d_3 > h$ the particle is reflected back into the pendular ring from the top surface of the pendular ring.

If $d_1 > r$ and $d_1 < r + P$ and $d_3 > h$ the particle moves into the surface film of sphere A.

If $d_2 > r$ and $d_2 < r + P$ and $d_3 > h$ the particle moves into the surface film of sphere B.

The rate at which particles move from the pendular rings into the surface film is controlled by the parameter P. It should be noted that P is not the film thickness. The value of P is adjusted so that the rate at which particles leave the surface film is balanced by the rate at which particles leave the pendular rings.

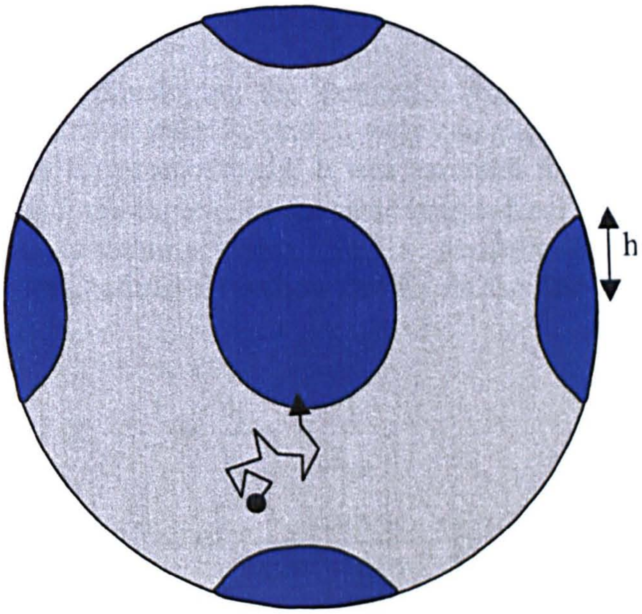

Figure 9.16 Top view of sphere. Blue areas shows where pendular rings contact the sphere surface for the simple cubic lattice structure. The grey area is the thin surface film covering the surface of each sphere. When a particle diffusing on the surface moves into an area of the surface that is in contact with a pendular ring (blue area) the particle moves into that pendular ring.

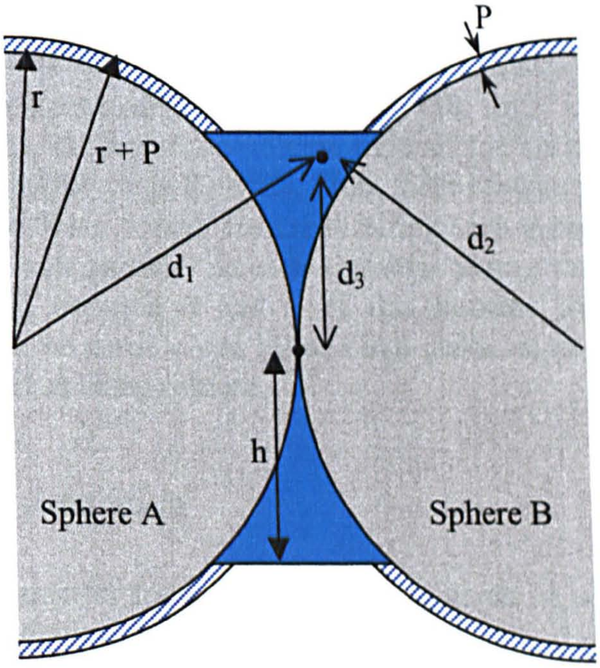

Figure 9.17 Shows a cross section through a pendular ring. From the coordinates of the random walker in the pendular ring three distances are calculated d_1, d_2 and d_3. These distances are used to decide what happens to the random walker after each step.

9.4.5 Surface Relaxation.

The final stage in developing the simulation was to take account of surface relaxation. Separate relaxation rates R_p and R_s were calculated for particles in pendular rings and in the surface film respectively. It was assumed that particles in the surface film and in the pendular rings experience the same longitudinal surface relaxivity ρ_l , but have different surface-to-volume ratios. For a pendular ring of half width m {see figure 9.13} the longitudinal relaxation rate R_P, in the fast diffusion limit, is given by:

$$\begin{aligned} R_p &= \frac{1}{T_p} = \frac{S_p}{V_p}\rho_l + \frac{1}{T_{bulk}} \\ &= \left(\frac{4\pi rm}{2\pi rm^2 - \frac{4}{3}\pi m^3}\right)\rho_l + \frac{1}{T_{bulk}} \end{aligned} \tag{9.13}$$

Where S_p and V_p are the surface area and volume of a pendular ring. For a surface film of thickness t the longitudinal relaxation rate R_s in the fast diffusion limit, is given by:

$$\begin{aligned} R_s &= \frac{1}{T_s} = \frac{S_s}{V_s}\rho_l + \frac{1}{T_{bulk}} \\ &= \frac{\rho_l}{t} + \frac{1}{T_{bulk}} \end{aligned} \tag{9.14}$$

where S_s and V_s are the surface area and volume of the surface film.

In section 9.2.4 an experimental value of the longitudinal surface relaxivity was calculated for water in a pack of glass beads ($\rho_l = 11\times10^{-7}$ m s^{-1}). This value was used to calculate R_s and R_p. As the surface-to-volume ratio of the surface film is considerably greater than for the pendular rings $R_s \gg R_P$. From these relaxation rates the probabilities K_s and K_p, of a particle being 'killed' (relaxed) during each timestep τ of the simulation, were calculated. For each particle, at each timestep during the simulation, a random number was generated between 0 and 1. If this number was less than K_p or K_s (depending on whether the particle was located in a pendular ring or in the surface film) the particle was labelled as being relaxed.

9.4.6 Running the simulation

Typical input parameters for the simulation are given in table 9.1. The simulation was run in the following way

1. Using the selected water saturation S_w, equation 9.11 is solved numerically to give the half width m of the pendular rings that form in a simple cubic lattice at this water saturation.
2. Using this value of m and the chosen value of film thickness t, equation 9.12 gives the fraction of water particles present in the surface film F_s at this water saturation.

3. The number of particles starting the simulation in the surface film is, nF_S, where n is the total number of particles. The number of particles starting the simulation in pendular rings is $(1\text{-}n)F_S$.

4. (nF_s) particles are randomly positioned in the surface film and $(1\text{-}F_s)n$ particles are randomly positioned inside pendular rings. The simulation runs for each particle in turn, each particle undergoing a random walk, with a timestep τ, for an observation time Δ (Δ/τ steps). The particles move between the surface film and pendular rings as described earlier.

5. After each timestep τ each particle has a probability K_s or K_p (see section 9.4.5) of being relaxed, depending on whether the particle is in the surface film or in a pendular ring.

6. The simulation is run a number of times with adjustments being made to parameter P, so that the number of particles in the surface film remains constant during the simulation.

7. At the end of the simulation, the initial and final position of each particle, and whether or not the particle has been relaxed, is given as output.

At the end of the simulation the displacement of each particle along the x-axis is calculated, and a histogram is then made of these displacements, see figure 9.18. The ‘binsize’ used for the histogram being the same as the resolution of data points (ΔX=13.84) in the experimental propagators, see figure 9.18. This allows experimental and simulated propagators to be compared directly.

Total number of Particles, n	Typically 300,000
Diffusion coefficient of water	$2.2\times10^{-9}m^2s^{-1}$
Sphere diameter	100μm
Water saturation, S_w	0.05, 0.1, 0.15, 0.2
Parameter P (see section 9.4.4)	Adjusted for each S_w
Observation time, Δ	Between 0.1 and 1.2s
Surface film thickness	Between 1-100 nm
Random walk time step, τ	0.00025s
Experiment surface relaxivity, ρ (see section 9.2.4)	11×10^{-7} m s^{-1}

Table 9.1 Typical parameters used in the final random walk simulation.

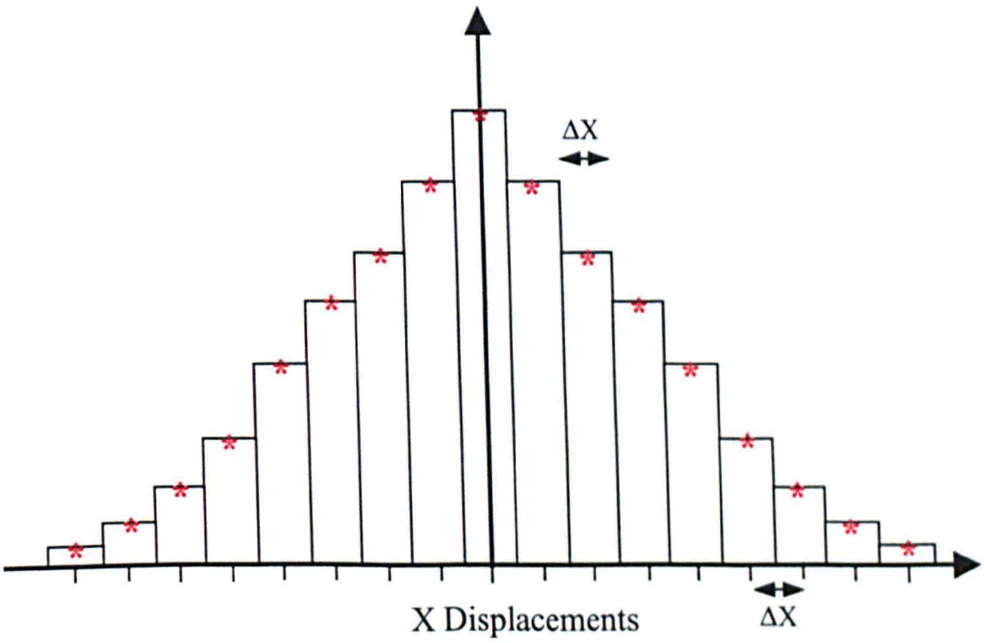

Figure 9.18 A histogram of the X-displacement of each particle, using a binsize=ΔX, where ΔX is the resolution of the experimental propagators. The data points of the simulated propagator are shown in red and also have a resolution ΔX.

9.5 Results and Discussion

Earlier in this chapter experimental results were presented for measurements made on glass bead packs saturated with water and tetrachloroethylene. These measurements included the determination of diffusive propagators, longitudinal relaxation times and effective diffusion coefficients of the water phase, at different water saturations. In Chapter 8 results were presented for similar measurements made on the wetting phase of Fontainebleau sandstone.

In this section the results from glass beads and Fontainebleau sandstone will be compared and discussed in connection with the random walk simulation described in section 9.4. Particular attention will be paid to the effect of the thin surface films that are present at low water saturations.

9.5.1 Critical water saturation

In the computer simulation described in section 9.4 the spheres representing the glass beads were given a simple cubic lattice structure. Figure 9.19 shows the unit cell of a simple cubic lattice and illustrates the distribution of the water phase at different water saturations. At high water saturations the pendular rings interpenetrate, and the water phase is well connected. At lower water saturations the pendular rings become separated and are only weakly connected by the thin surface wetting film.

For a simple cubic lattice structure there is a critical water saturation at which the pendular rings just touch. This is shown in figure 9.19b. The half width m of the pendular rings at this saturation is given by:

$$r^2 = (r-m)^2 + (r-m)^2 = 2(r-m)^2$$

this gives:

$$m = \left(1 - 1/\sqrt{2}\right)r = 0.2929r \qquad (9.15)$$

From equation 9.11 this corresponds to a water saturation of S_w=0.34.

For an irregular structure like Fontainebleau sandstone there is unlikely to be a critical saturation at which pendular rings become separated. Instead, the separation of pendular rings, as the water saturation is decreased, will occur over a some range of saturations. Nevertheless, it is likely that it will occur around S_w=0.34. For a random packing of mono-disperse beads it maybe expected that the separation of pendular rings will occur over a narrow range of saturations, close to the value S_w=0.34 calculated for a cubic lattice.

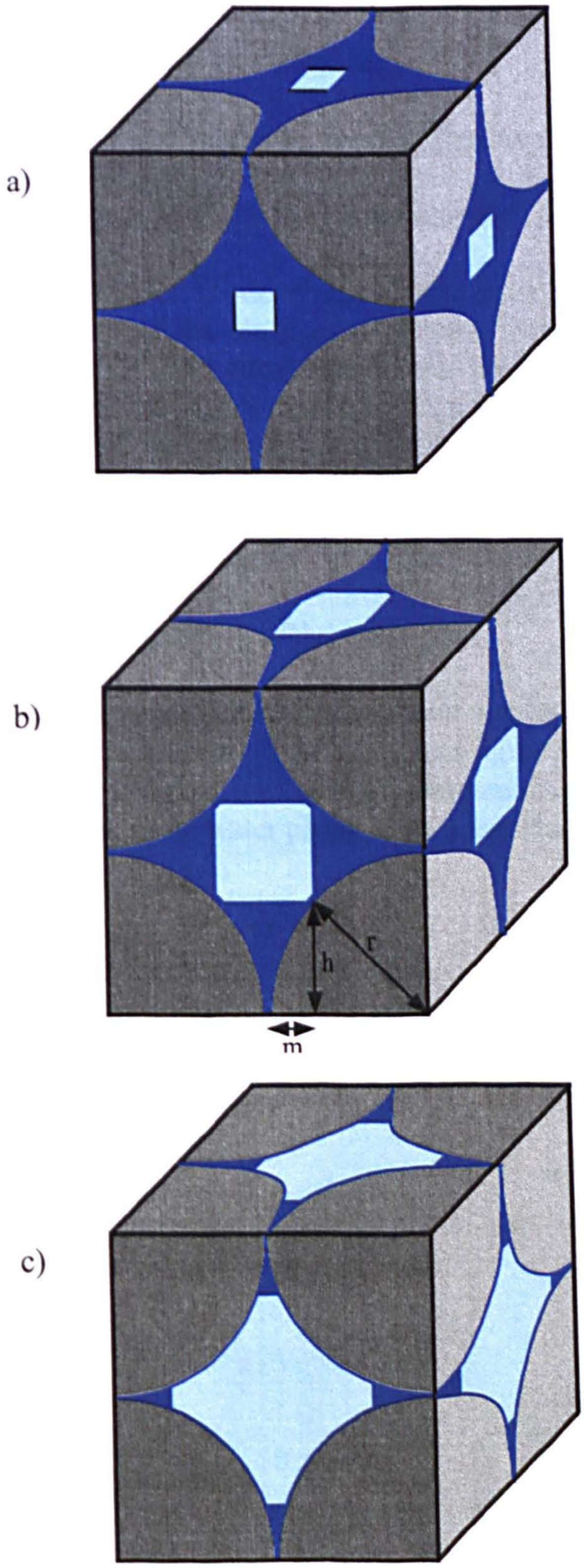

Figure 9.19 The distribution of the water phase in a simple cubic lattice of spheres, with pendular rings represent as in figure 9.13.

a) S_w >0.34 pendular rings are interconnected.
b) S_w=0.34 pendular rings just touch.
c) S_w <0.34 pendular rings are separated and only connected by the thin surface film.

9.5.2 The Effective Diffusion coefficient

Earlier the effect of water saturation on the effective diffusion coefficient D^* was determined for glass beads {section 9.2.3} and Fontainebleau Sandstone {section 8.1.3}. This data is re-plotted in figure 9.20 and the water saturation S_w=0.34 is marked.

In the case of glass beads D^* decreases slowly from S_w=1 to S_w ~0.34. At these high water saturations the pendular rings interpenetrate, hence the water phase is well connected, giving a large D^*. At water saturations below S_w~0.34 there is a rapid decrease in D^*, caused by the pendular rings becoming separated and only weakly connected by the thin surface film. The lower the water saturation the more separated the pendular rings become and the further water molecule have to travel through the thin surface film to get to another pendular ring, hence the lower the effective diffusion coefficient. Simulation results presented later {section 9.5.3}, also indicate that the thickness of the surface wetting film decreases as the water saturation is decreased, which further reduces the connectivity of the water phase.

The same behaviour is seen for Fontainebleau sandstone, but below S_w~0.34 the decrease in D^* is less marked than for glass beads, see figure 9.20. A probable reason for this is the more irregular structure and surface roughness of Fontainebleau sandstone {see figure 3.1}, which makes the water phase more connected than in glass beads at low water saturations.

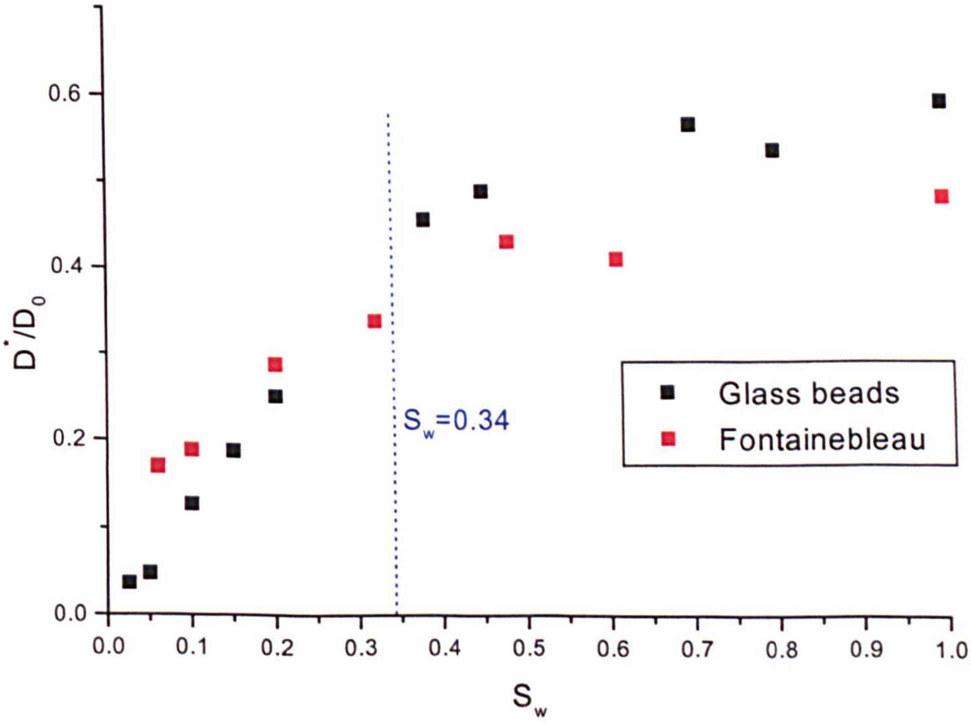

Figure 9.20 Effective diffusion coefficients of the water phase in glass bead packs and Fontainebleau sandstone at different water saturations.

9.5.3 Average Propagators

Earlier the average water propagators measured at different water saturations were presented for both glass beads {figure 9.1} and Fontainebleau sandstone {figure 8.2}. In both cases, the shape of the water propagators becomes more cusp-like at lower water saturations. In order to understand this a random walk computer simulation was developed, see section 9.4.

The random walk simulation was used to investigate the effect of surface film thickness on the shape of the water propagators. Figure 9.21 shows simulated water propagators calculated for various values of surface film thickness t, for an observation time of 1.2s and a water saturation of S_w=0.2. It can be seen that the shape of the simulated water propagator is strongly sensitive to the thickness of the surface film. With a film thickness of 6nm the connection between pendular rings is weak. Few molecules can diffuse across the surface film to another pendular ring, hence the shape propagator resembles that of restricted diffusion in an isolated pendular ring. Whereas for a film thickness of 79nm there is a much stronger connection between pendular rings, this gives the propagator a more Gaussian appearance.

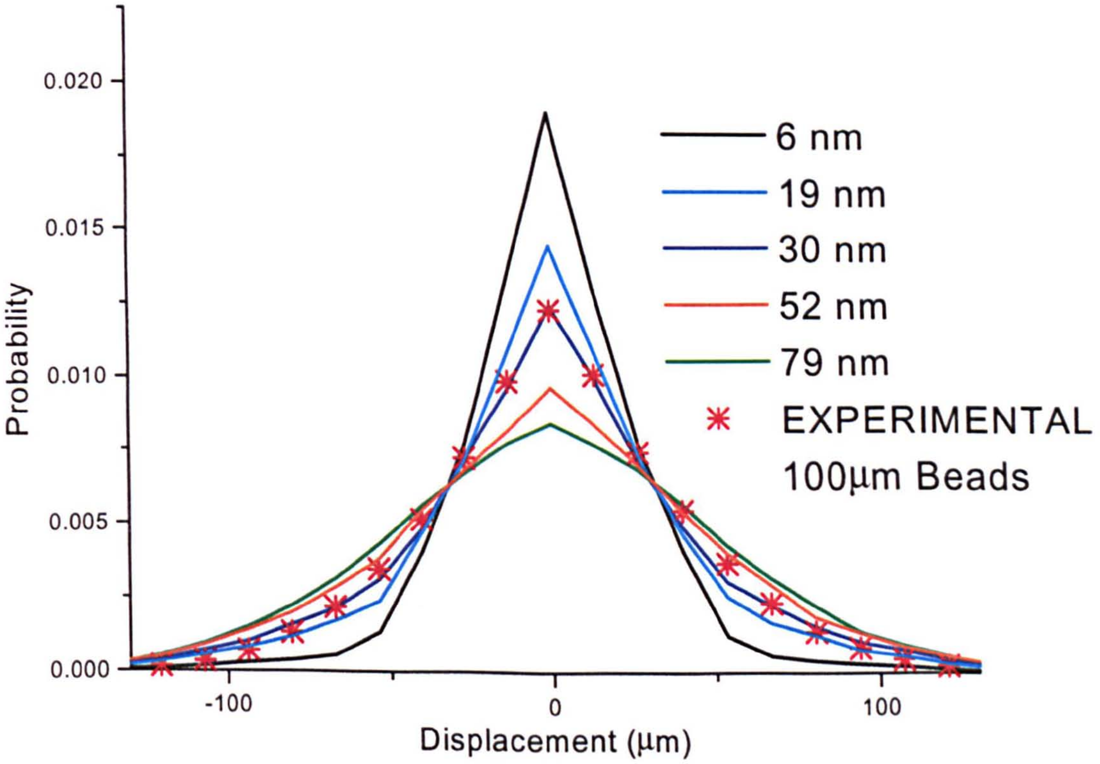

Figure 9.21 Simulated water propagators calculated for various values of surface film thickness, for an observation time of 1.2s and a water saturation of S_w=0.2.

It is clear from the simulated propagators in figure 9.21, that the cusp-like shape of water propagators at low water saturations is caused by the hindered diffusion of water molecules within separated pendular rings, that are weakly connected by a thin surface wetting film.

The water propagator measured experimentally for glass beads at S_w= 0.2 and for an observation time of 1.2s {see section 9.2.2}, is also plotted in figure 9.21. The experimental water propagator is well matched by the simulated water propagator calculated for a film thickness of 30nm.

Simulated water propagators were fitted to the experimental water propagators measured for glass beads at S_w= 0.05, 0.1, 0.15 and 0.2 and for an observation time 1.2s. This fitting process involved simulating propagators for each S_w and adjusting the surface film thickness t to minimise the least-squares fit to the experimental propagator. Figure 9.22 shows the variation of the surface film thickness t with water saturation, given by fitting the simulated propagators to the experimental propagators. The surface film thickness increases from 5 to 30 nm as the water saturation is increased from 0.05 to 0.2.

It is very interesting to note that the volume fraction of water present in the surface film F_s, for the simulated propagators, stays roughly constant with water saturation at around 0.006, see figure 9.23. That is only 0.6% of the water phase is present in the surface wetting film and 99.4% is present in the pendular rings.

The computer simulation used to simulate the water propagators incorporated relaxation {see section 9.4.5}. It was considered important to incorporate relaxation into the computer simulation because of the effect relaxation might have on experimental displacement propagators, measured at low water saturation. At low water saturations, for a particle to have a large displacement it has to move from one pendular ring to another via the thin surface film, and relaxation in the surface film is considerably greater than in pendular rings {see section}. Therefore, it was thought that the experimental displacement propagator would be weighted against particles having the largest displacements.

Figure 9.24 shows simulated propagators for S_w=0.05 and 0.2, simulated with and without relaxation. These propagators were simulated using the value of t that best fitted the experimental propagators at each saturation, see above. It can be seen that for S_w=0.2 the presence of relaxation makes very little difference to the simulated propagator. At S_w=0.05 relaxation has a more noticeable effect on the simulated propagator, the probability of larger displacement being less for the propagator simulated with relaxation. It can be seen that at the water saturations studied, relaxation only has a small effect on the displacement propagators.

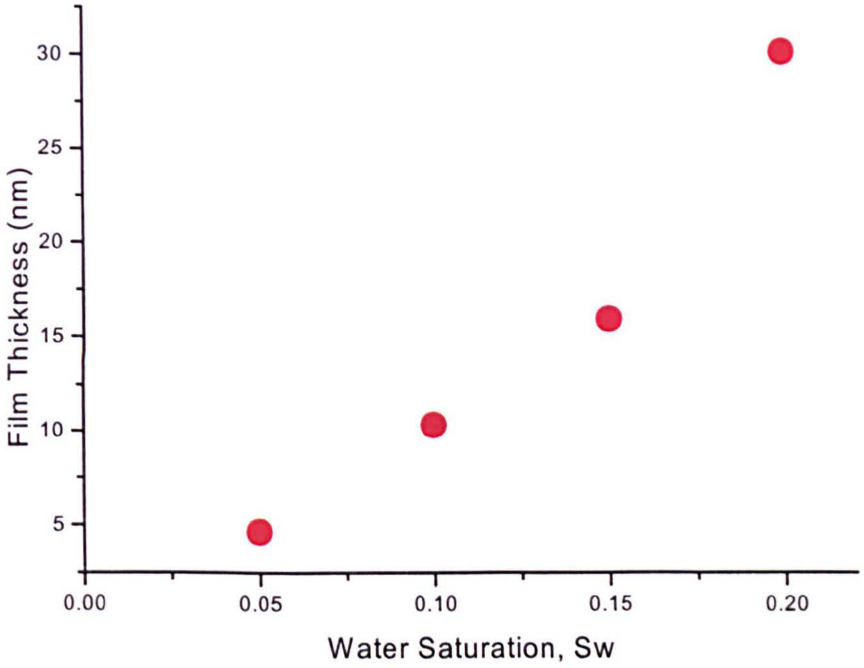

Figure 9.22 Variation in the surface film thickness with water saturation.

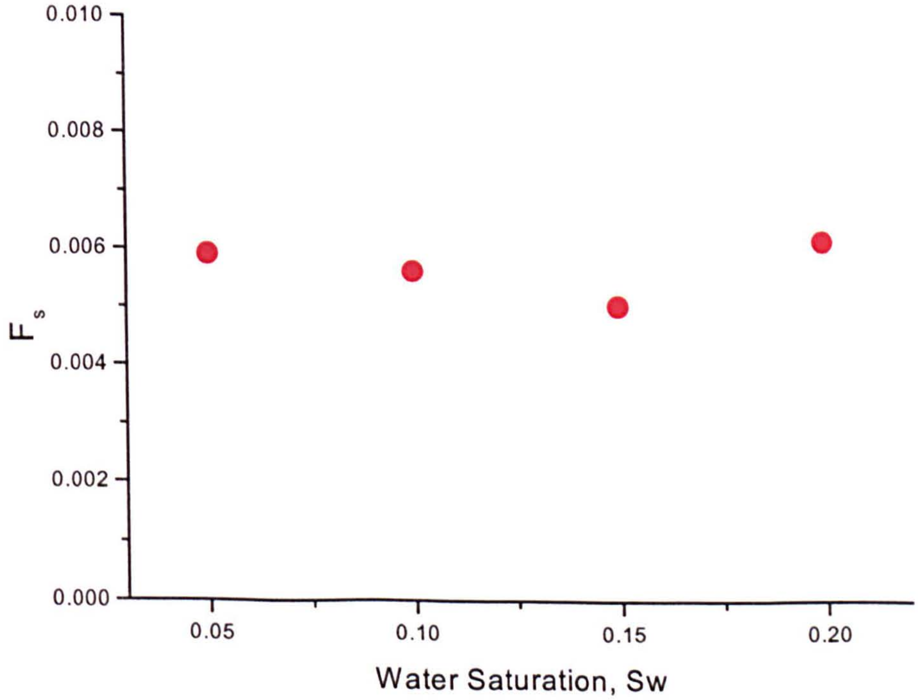

Figure 9.23 Variation in the fraction of particles present in the surface film F_s with water saturation.

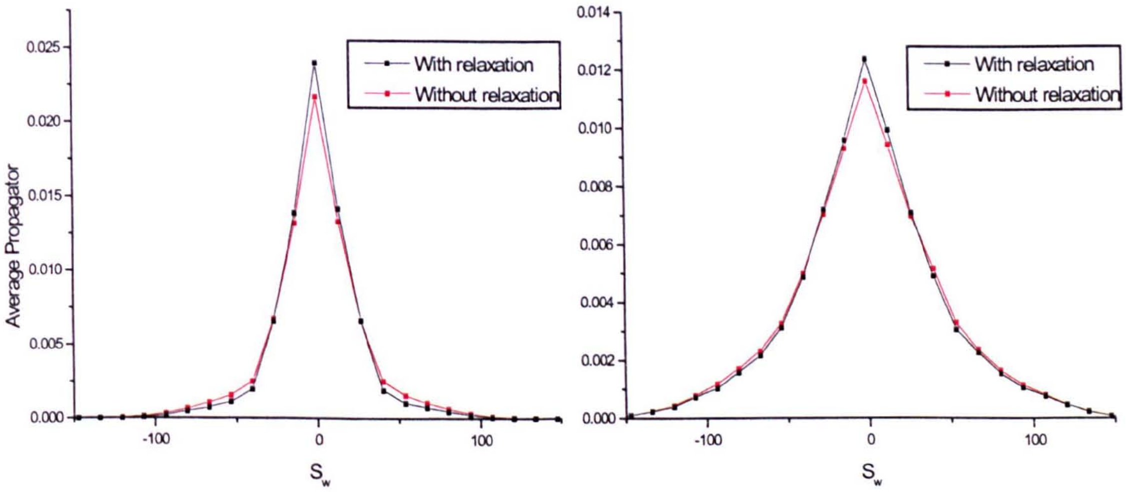

Figure 9.24 Propagators simulated with and without relaxation, for an observation time of 1.2s. a) S_w=0.05. b) S_w=0.2

9.5.4 Relaxation

Earlier, experimental measurements of longitudinal relaxation were presented, for both glass beads {see section 9.2.4} and Fontainebleau sandstone {see section 6.2.1}, as a function of water saturation. In both cases, the observed relaxation curves were mono-exponential at all water saturation states. Furthermore, in both cases, the longitudinal relaxation times measured at low water saturations showed a marked deviation from the predictions of the fast diffusion model. These results are re-plotted in figure 9.25.

As discussed in section 6.2.1, for a strongly water-wet solid, the water phase forms a continuous film over all the grain surfaces, hence the specific surface area of the water phase is constant at all water saturations. Therefore, in the fast diffusion limit the rate of longitudinal relaxation is given by:

$$R_{1,\text{fast}} = \frac{1}{T_{1,\text{fast}}} = \frac{1}{T_{\text{bulk}}} + \rho_1\left(\frac{S_0}{V_0}\right)\left(\frac{1}{S_w}\right) = \frac{1}{T_{\text{bulk}}} + C\left(\frac{1}{S_W}\right) \qquad (9.16)$$

where S_0 and V_0 are respectively the specific surface area and volume of the whole pore space. C is a constant.

The quantity $\rho_1(S_0/V_0)$ was determined, from the initial slope of the data in figure 9.25, as 0.08±0.01 s^{-1} for glass beads and 0.20±0.02 s^{-1} for Fontainebleau sandstone. It can be seen that the longitudinal relaxation deviates from the fast diffusion model at around $S_w \sim 0.27$ for glass beads and $S_w \sim 0.5$ for Fontainebleau sandstone. In both cases this is close to the critical water saturation for a simple cubic lattice $S_w = 0.34$,discussed in section 9.5.1. The deviation from the fast diffusion model means that the water phase is no longer in fast exchange, i.e. the water molecules in pendular rings are not in fast exchange with water molecules in the surface film.

At low water saturations, when there is no longer fast diffusive exchange between water molecules in pendular rings and the surface film, it would be expected that the longitudinal relaxation be multi-exponential, but experimental measurements are mono-exponential. The reason for this can readily be understood by considering the results of the computer simulation presented in section 9.5.3, where simulated propagators were fitted to the experimental water propagators for water diffusing in glass beads. It was shown that only ~0.6% of the water phase is present in surface films (with a very short relaxation time T_s ~15ms) and ~99.4% is present in pendular rings (with a longer relaxation time T_p ~1s). This makes it difficult to detect experimentally the true multi-exponential nature of the longitudinal relaxation at low water saturations

Longitudinal relaxation was incorporated into the random walk computer simulation, described in section 9.4.5. Water molecules in the surface film experienced a relaxation time T_s and water molecules in pendular rings experienced a relaxation time T_p.The overall relaxation time being dependent on the rate of exchange of water molecules between the surface film and the pendular rings. The rate of exchange being governed by the size of the pendular rings (and hence S_w), and the thickness of the surface film t (see section 9.5.3).

The overall relaxation time of the simulation was found by measuring the total magnetisation (number of alive spins) at 32 time points logarithmically spaced between 0.005s and 15s (same as for experimental measurements). The resulting decay curves were then fitted using the Xfit program. As with the experimental data, all the simulated decay curves were well fitted by a mono-exponential function.

Figure 9.26 shows how the overall relaxation time given by the simulation varies with S_w and t. The relaxation time in the fast diffusion limit $T_{1,fast}$ is plotted as a solid line for each water saturation. Decreasing S_w and t, decreases the rate of exchange of water molecules between the surface film and pendular rings, as a result the overall relaxation time deviates more from the fast diffusion limit. As t approaches zero, ie no exchange, the overall relaxation time approaches T_p (i.e. the relaxation time of pendular rings)

Hills et al [7] have studied the longitudinal relaxation of water in glass bead packs saturated with water and air. They also found the longitudinal relaxation of the water phase to be single exponential, for all glass bead sizes and all degrees of water saturation. They did not however observe any deviation from the fast diffusion model at lower water saturations. This maybe because they did not take measurements at very low saturations. It may also have to do with the fact that Hills et al used air as the non-wetting phase in their experiments, and it is possible for water molecules to be transported as water vapour in pores at low water saturations [12,13], thus bypassing the restriction of the surface film.

From the measurements of longitudinal relaxation presented in this thesis it appears that at low water saturations the water phase is no longer in the fast diffusion limit. Investigating the temperature dependence of the longitudinal relaxation could test this hypothesis. If the water phase is not in the fast diffusion limit then longitudinal relaxation will be dependent on the diffusion coefficient of the water phase, which is very temperature dependent. At present the only investigation of the temperature dependence of T_1 and T_2 has been by Latour et al [14] who only investigated fully water saturated rocks (S_w=1) {see section 4.2.1}. At S_w=1 he found T_1 and T_2 were independent of temperature, i.e. in the fast diffusion limit.

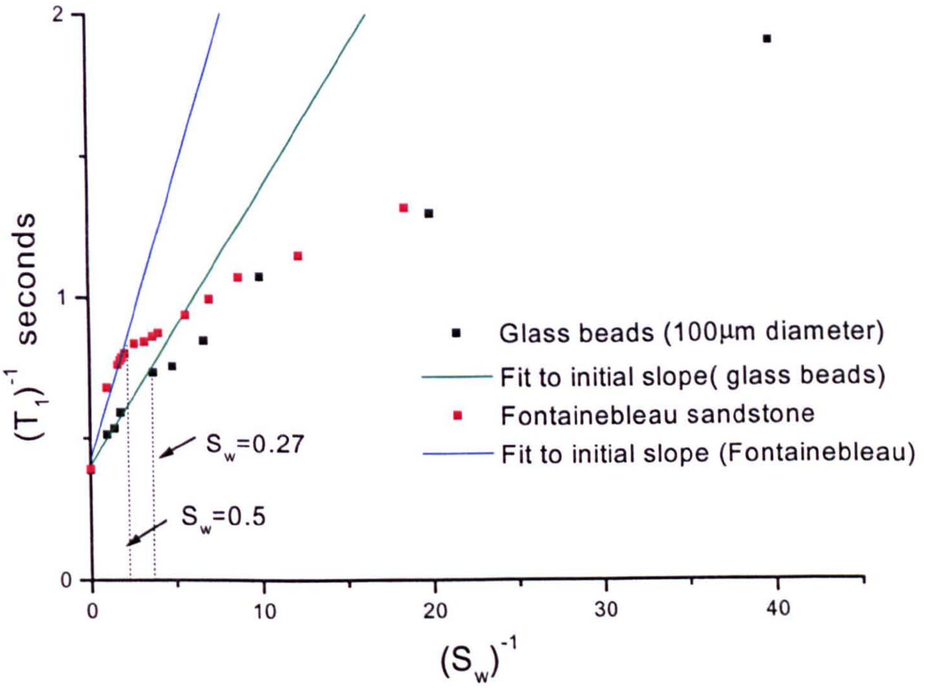

Figure 9.25 A plot of $(T_1)^{-1}$ versus $(S_w)^{-1}$ for glass beads and Fontainebleau sandstone. The green and blue lines are fits to the initial slope, and were used to calculate the surface relaxivity of glass beads and Fontainebleau sandstone respectively {see section 6.2.1 and 9.2.4}.

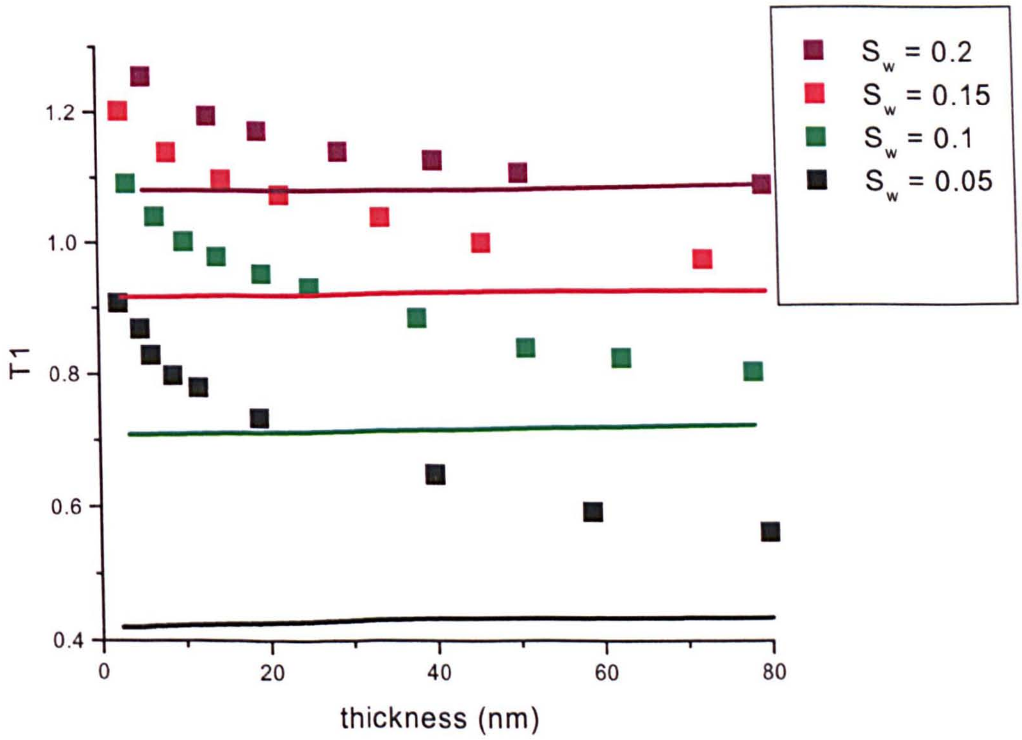

Figure 9.26 Simulated values of T_1 as a function of water saturation and surface film thickness. The solid line is the relaxation time in the fast diffusion limit $T_{1,fast.}$

9.6 Conclusion

In this chapter results were presented for experiments performed on packs of water-wet glass beads (100μm diameter) saturated with water and tetrachloroethylene in various proportions. Average propagators were determined for the diffusion of the water phase, for a range of observation times and water saturations. At decreasing water saturation the shape of the water propagator changes from being approximately Gaussian, to developing a narrow cusp-like appearance. There was a corresponding decrease in the effective diffusion coefficient of the water phase at lower water saturations. Longitudinal relaxation times of the water phase were also determined for various water saturations. At lower water saturations, it was found that the longitudinal relaxation times deviated from the fast diffusion model.

To understand the changes seen in the experimental results at lower water saturations, a random walk computer simulation was developed. The simulation was based on a simple cubic lattice of spheres. The water phase being distributed in pendular rings, which form where two spheres touch, and as a thin surface wetting film. The simulation was used to show how the shape of the water propagator depends strongly on the thickness of the surface film. The thickness of the surface film was determined by fitting simulated propagators to the experimental propagators. In this way it is found that the surface film thickness increases form 5 to 30nm as the water saturation increases from S_w= 0.05 to 0.2. From these fits its was also determined that only ~0.6% of the water phase is present in the surface film and 99.4% is present in pendular rings. The simulation was also used to show how the water saturation and surface film thickness affect the rate of longitudinal relaxation of the water phase. Finally some comparisons were made with similar experimental results obtained for the wetting phase of Fontainebleau sandstone, which were presented in chapter 8.

9.7 References

1. Holmes W.M., Graham R.G., Packer K.J. "Diffusion in Surface-Wetting Films in a Two-Phase Saturated Porous Solid Characterized by Pulsed Magnetic Field Gradient NMR". 2000. Chemical Engineering Journal. 3647. 1.

2. Holmes W.M., De Panfilis C., Packer *K.J. "Diffusion* in Thin Films on the Surface of a Porous Solid". 2000. Magnetic Resonance Imaging. In Press.

3. Holmes W.M., Packer K.J. In preparation

4. Stapf S., Packer K.J., Graham R.G., Thovert J.F., Adler P.M. " Spatial Correlations and Dispersion for Fluid Transport Through Packed Glass Beads Studied by Pulsed Field-Gradient NMR". 1998. Physical Review E. 58. 6206-6221.

5. De Panfilis C., Packer K.J. "Characterization of Porous Media by NMR Imaging and Flow Diffraction". 1999. European Physical Journal Applied Physics. 8. 77-86.

6. Hills B.P., Snaar J.E.M. 1995. Molecular Physics. 84. 141.

7. Hills B.P., Snaar J.E.M. "Water Proton Relaxation Studies of Air-Water Distributions in Beds of Randomly Packed Mono-disperse Glass Microspheres". 1995. Molecular Physics. 86. 1137-1156.

8. Atkins P.W. "Physical Chemistry". 1991. Oxford University Press.

9. Dullien F.A.L. "Porous Media: Fluid Transport and Pore Structure". 1992. Academic Press Ltd. London.

10. Versluys J. 1917. Int. Mitt. Bodenk. 7. 117.

11. De Gennes P.G. "Wetting: Statistics and Dynamics". 1985. Reviews of Modern Physics. 57. 827.

12. Dorazio F., Bhattachatja S., Halperin W.P., Gerhardt R. "Enhanced Self-Diffusion of Water in Restricted Geometry". 1989. Physical Review Letters. 63. 43-46.

13. Dorazio F., Bhattachatja S., Halperin W.P., Eguchi K.., Mizusaki T. "Molecular-Diffusion and NMR Relaxation of Water in Unsaturated Porous Silica Glass". 1990. Physical Review B. 42. 9810-9818. Part A.
14. Latour L.L., Kleinburg R.L. Sezginer A. "Nuclear Magnetic Resonance Properties of Rocks at Elevated Temperatures". 1992. Journal of Colloid and Interface Science. 150.

Chapter 10

Two-dimensional Propagators

Contents

10.1 INTRODUCTION **184**

10.2 THE TWO-DIMENSIONAL APGSTE SEQUENCE **184**

10.2.1 FONTAINEBLEAU SANDSTONE AT S_{WI}. 185
10.2.2 FONTAINEBLEAU SANDSTONE AT S_{OR}. 186
10.2.3 RANDOMLY PACKED GLASS BEADS, S_W =0.25 186
10.2.4 POLY DISPERSE EMULSION 189

10.3 HANKEL TRANSFORM **189**

10.3.1 MONO-DISPERSE EMULSION. 191

10.4 CORRELATION BETWEEN DISPLACEMENTS IN X AND Z **193**

10.4.1 CORRELATION DISTRIBUTION $C_\Delta(X,Z)$ 193

10.5 THEORETICALLY DERIVED $C_\Delta(X,Z)$ **194**

10.6 EXPERIMENTALLY DERIVED $C_\Delta(X,Y)$ **197**

10.6.1 FONTAINEBLEAU SANDSTONE S_{WI} 197
10.6.2 FONTAINEBLEAU SANDSTONE S_{OR} 197
10.6.3 RANDOM WALK SIMULATIONS OF DIFFUSION IN FONTAINEBLEAU 197
10.6.4 GLASS BEADS, S_W=0.25 202
10.6.5 MONO-DISPERSE EMULSION 203
10.6.6 10.4.6. POLY-DISPERSE EMULSION 203

10.7 CONCLUSION **206**

10.8 REFERENCES **207**

10.1 Introduction

In chapter 7, one-dimensional propagators $P_\Delta(Z)$ were presented for the flow of oil through Fontainebleau sandstone, where the z-axis was parallel to the flow direction. Similarly, other authors have used one-dimensional propagators, measured either perpendicular or parallel to the flow direction, to study flow through porous solids [1]. It should be remembered *that* $P_\Delta(Z)$ *is just* the projection of the three-dimensional propagator $P_\Delta(\mathbf{R})$ onto the z-axis. Therefore, any inform*ation about the angular* distribution of fluid displacements is lost.

Recently Stapf et al [2,3] employed a two-dimensional PGSE NMR experiment, which measured the joint probability density $P_\Delta(X,Z)$. This describes the probability of a spin-bearing particle simultaneously having displacements X and Z during a given observation time Δ. This experiment has been used to study flow through glass beads, Fontainebleau sandstone (single- and two-phase flow) and various fibrous systems (orientated and non oriented) [4].

In this chapter two methods are described for measuring two-dimensional propagators $P_\Delta(X,Z)$ for diffusive transport. The first method is the two-dimensional APGSTE sequence {see section 5.6.3} developed by Stapf et al [2,3,4]. The second method involves the Hankel transform of the echo attenuation function $E_\Delta(q)$, $E_\Delta(q)$ being measured using the one-dimensional APGSTE sequence {see section 5.6.2}. These two methods were used to measure two-dimensional propagators $P_\Delta(X,Z)$, for the diffusion of a liquid phase confined within various structures.

Stapf et al [2,3] introduced the correlation distribution $C_\Delta(X,Z)$, derived from the two-dimensional propagator $[C_\Delta(X,Z)=P_\Delta(X,Z) - P_\Delta(X)P_\Delta(Z)]$, to analyse correlations between X and Z displacements, for fluids flowing through porous solids. In this chapter the correlation distribution $C_\Delta(X,Z)$, is derived from experimental two-dimensional propagators, for diffusion confined within various structures. These results are then compared to theoretically derived $C_\Delta(X,Z)$ for diffusion within isotropically orientated ellipsoidal containers of different aspect ratio, in the long time limit.

10.2 The Two-dimensional APGSTE sequence

The pulse sequence for the two-dimensional APGSTE NMR experiment is described in section 5.6.3, and typical experimental parameters are given in table 5.6. The echo attenuation $E_\Delta(\mathbf{q})$ of this sequence is given by equation 2.48. Where $\mathbf{q}$ consists of two orthogonal components q_x and q_z thus:

$$\mathbf{q} = q_x\mathbf{i} + q_z\mathbf{k} \qquad (10.1)$$

where **i** and **k** are unit vectors along the x- and z-axes, respectively. A 16×16 matrix of $E_\Delta(\mathbf{q})$ was acquired by stepwise variation of q_x and q_z, using 14 positive and 2 negative evenly spaced values of q_x and q_z. The two negative q values serve to determine the zero-q phase shift, which enables the reconstruction of the full 28×28 matrix of $E_\Delta(\mathbf{q})$. The maximum q value used is q_{max}, which determines the resolution in displacement space. The two-dimensional propagator $P_\Delta(X,Z)$, for displacements X and Z, is calculated by successively Fourier transforming the matrix in both directions.

To verify that this process correctly generates the two-dimensional propagator, the marginals of the two-dimensional propagator were compared to the one-dimension propagator. The marginals $P_\Delta(X)$ and $P_\Delta(Z)$ of the propagator $P_\Delta(X,Z)$, are defined as:

$$\begin{aligned} P_\Delta(X) &= \int P_\Delta(X,Z)\,dZ \\ P_\Delta(Z) &= \int P_\Delta(X,Z)\,dX \end{aligned} \tag{10.2}$$

The one-dimensional propagators were measured, under identical conditions to the two-dimensional propagators, by measuring $E_\Delta(q_x)$ for 32 equally spaced values of q_x in the range $-q_{max}$ to q_{max} and then Fourier transforming with respect to q_x {see section 5.6.2}. In this study the marginals of the two-dimensional propagators matched the one dimensional propagators satisfactorily in all cases.

Two-dimensional propagators were measured, using the above method, for the diffusion of a liquid phase in a number of different confining structures. These included the diffusion of the non-wetting phase within two-phase saturated Fontainebleau sandstone at S_{wi} and S_{or}, diffusion of the wetting phase within a randomly packed glass bead system and diffusion within the droplets of oil-in-water emulsions. These measurements are described below.

Contour plots are used to display the two-dimensional propagator $P_\Delta(X,Z)$. Because contour plots of two-dimensional diffusive propagators appear very similar, only $P_\Delta(X,Z)$ measured for the diffusion of the non-wetting phase within Fontainebleau sandstone at S_{wi} and S_{or} are presented here.

10.2.1 Fontainebleau Sandstone at S_{wi}.

The Fontainebleau sample was saturated with an aqueous phase of 3% w/v NaCl in D_2O and an oil phase of hexane. An irreducible water saturation of $S_{wi}=0.06$ was produced by flowing hexane through the sample at 1500ml/h until no more water was displaced. The saturation state was measured using method 2 of section 5.3.5. With both phases stationary, one- and two-dimensional displacement propagators were determined for the diffusing oil phase. Measurements were made for observation times of 0.6, 1.2 and 1.8s, using a q_{max} of 36000, 24000 and 21600m^{-1} respectively. The T_1 of hexane was measured as 2.7s {see section 6.2}, therefore a recycle delay of 13.5s (i.e. $5\times T_1$) was used.

Figure 10.1 shows contour plots of the two-dimensional propagators measured for the three observation times. The maximum intensity of $P_\Delta(X,Z)$ is normalised to unity. Contour intervals are 0.1 in the range ± 1 to ± 0.1 and have values ± (0.01,0.02,0.03 and 0.05) in the range 0.1 to -0.1. As expected for diffusion in an overall isotropic sample, the lines of equal probability are completely symmetric in all directions. It can also be seen that the propagators spread to larger displacements at longer observation times.

10.2.2 Fontainebleau Sandstone at S_{or}

A residual oil saturation S_{or}=0.3 (i.e. S_w=0.7) was produced in the Fontainebleau sample using the primary drainage/secondary imbibition process described in section 5.3.4. With both phases stationary, one- and two-dimensional propagators of the diffusing oil phase were measured, for observation times of 0.6, 1.2 and 2s. Using q_{max}= 32000m^{-1} and a recycle delay of 13.5s.

Figure 10.2 shows contour plots of the two-dimensional propagators, for the three observation times. The maximum intensity of $P_\Delta(X,Z)$ is normalised to unity. Contour intervals are 0.1 in the range ± 1 to ± 0.1 and have values ± (0.01,0.02,0.03 and 0.05) in the range 0.1 to –0.1. Again, as expected for diffusion in an overall isotropic sample, the lines of equal probability are completely symmetric in all directions. Unlike the propagators measured at S_{wi} the propagators measured at S_{or} show a limit of displacement with increasing time. This limit is the result of the oil phase being located in isolated droplets {see section 3.5.2}, which restricts the displacement range of the oil molecules.

10.2.3 Randomly Packed Glass Beads, S_w =0.25

Two-dimensional propagators were measured by De Panfilis [6] for the diffusion of the water phase in a pack of glass beads saturated with both water and tetrachloroethylene. This is the same system that was studied in detail in chapter 9. A bead pack made with strongly water-wet glass beads (100µm diameter) was saturated with water. Tetrachloroethylene was then pumped through the sample at 600ml/h displacing some of the water phase. This reduced the water saturation to S_w = 0.25. {The water saturation was measured as described in section 5.4.2}. The remaining water phase is expected to form pendular rings where the glass beads touch and a thin continuous film covering the remaining surface of the glass beads [7]. The value of q_{max} used was 40800m-1 and the recycle delay was 8s.

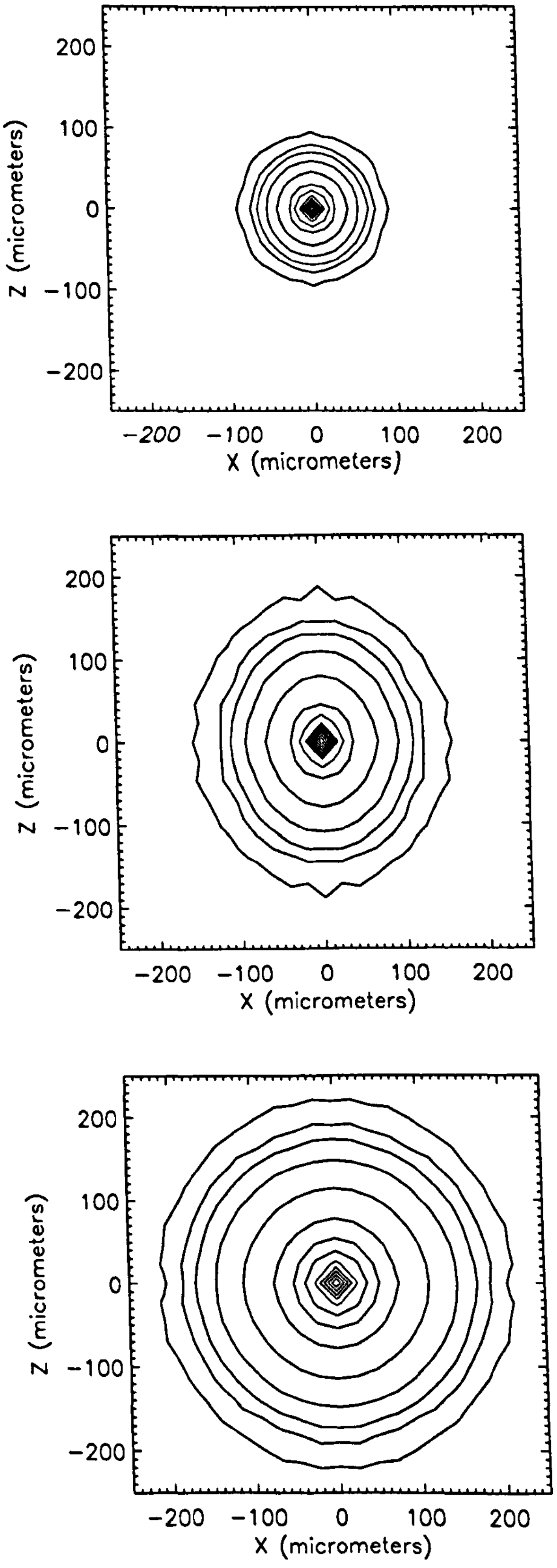

Figure 10.1 Two-dimensional propagators for the diffusion of hexane contained with Fontainebleau sandstone at S_w=0.06. Measured for observation times of 0.6s (top), 1.2s (middle) and 1.8s (bottom).

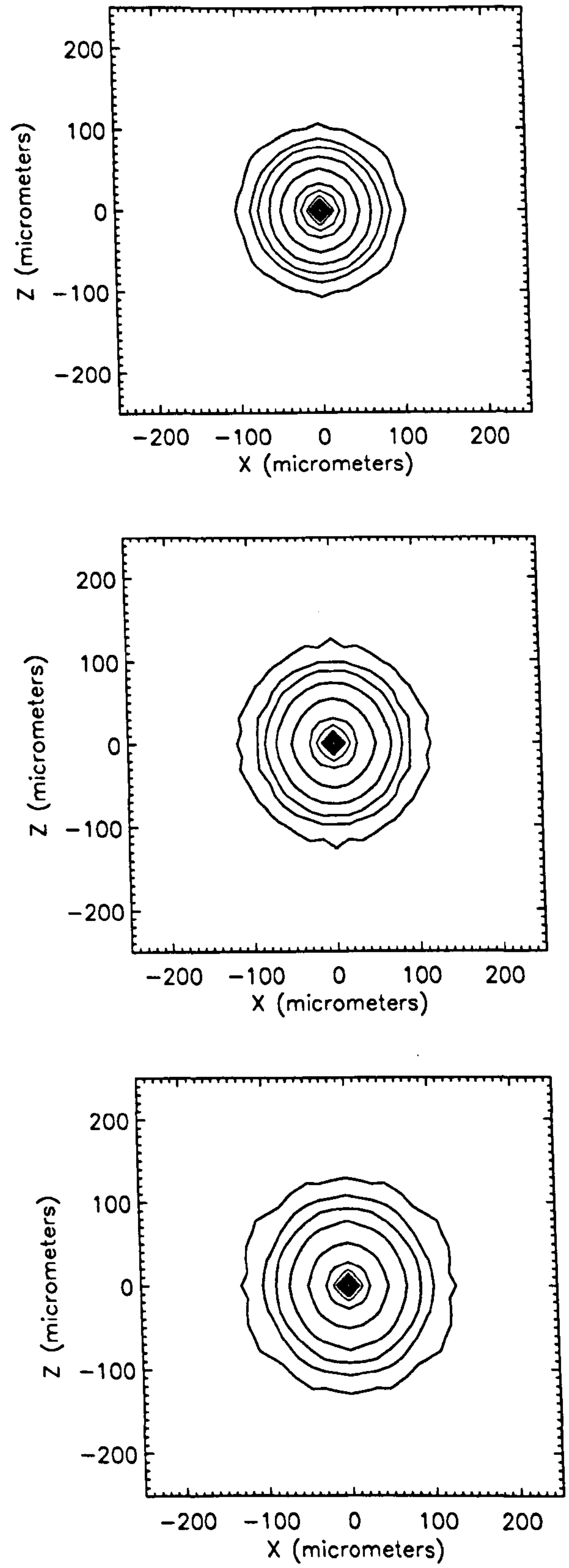

Figure 10.2 Two-dimensional propagators for the diffusion of hexane contained with Fontainebleau sandstone at $S_{or}=0.3$ (i.e. $S_w=0.7$). Measured for observation times of 0.6s (top), 1.2s (*middle) and 2s* (bottom).

10.2.4 Poly Disperse Emulsion

A poly-disperse oil-in-water emulsion was produced using the emulsifying agent Tween 40 (HLB=15.6). First, 2g of tween 40 was dissolved in 50cm^2 of D_2O (99.1%, Aldrich). Then 30cm^3 of hexane was then added to this solution in 5cm^3 steps. After each addition, the mixture was shaken by hand for approximately 2 minutes. This produced a coarse poly-disperse oil-in-water emulsion which quickly 'creamed' [8,9], i.e. the droplets of hexane rise to the top of the container and concentrate there. An optical micrograph of this creamed emulsion phase is shown in figure 10.3. There is a wide range of droplet sizes, the maximum droplet size being approximately 90μm.

The 'cream' of the emulsion was placed in a cylindrical glass container, 24mm in diameter and 20mm in length. Two-dimensional and one-dimensional propagators were measured for the diffusion of hexane confined within the spherical droplets. Measurements were made using the actively shielded 26mm diameter gradient coils that generate gradients up to 2.5T/m {see section 5.2}, using an observation time of 1s and a q_{max}= 156000m^{-1} and a recycle delay of 13.5s

10.3 Hankel Transform

The major problem with the two-dimensional APGSTE experiment is the length of time needed for each experiment. The acquisition of a 16×16 grid of $E_\Delta(\mathbf{q})$ values, using a 16 scan phase cycle and a recycle delay of 13.5s takes approximately 15hours. Higher resolutions e.g. a 32×32 grid of $E_\Delta(\mathbf{q})$, take a prohibitively long time (~61 hours).

For an isotropic diffusion process $E_\Delta(\mathbf{q})$ depends only upon the magnitude of $\mathbf{q}$ and not upon its direction. Using this fact it has been proposed by Graham [10] that the two-dimensional propagator can be generated from any one-dimensional dataset of $E_\Delta(\mathbf{q})$, using the Hankel transform of $E_\Delta(\mathbf{q})$ with respect to q, defined as:

$$P_\Delta(X,Z) = 2\pi \int_{-\infty}^{\infty} E_\Delta(q)\, J_0\left(2\pi q (X^2+Z^2)^{1/2}\right) q\ dq \qquad (10.3)$$

where J_0 is the zero-order Bessel function of the first kind. The derivation of equation 10.3 is given in Appendix 1.

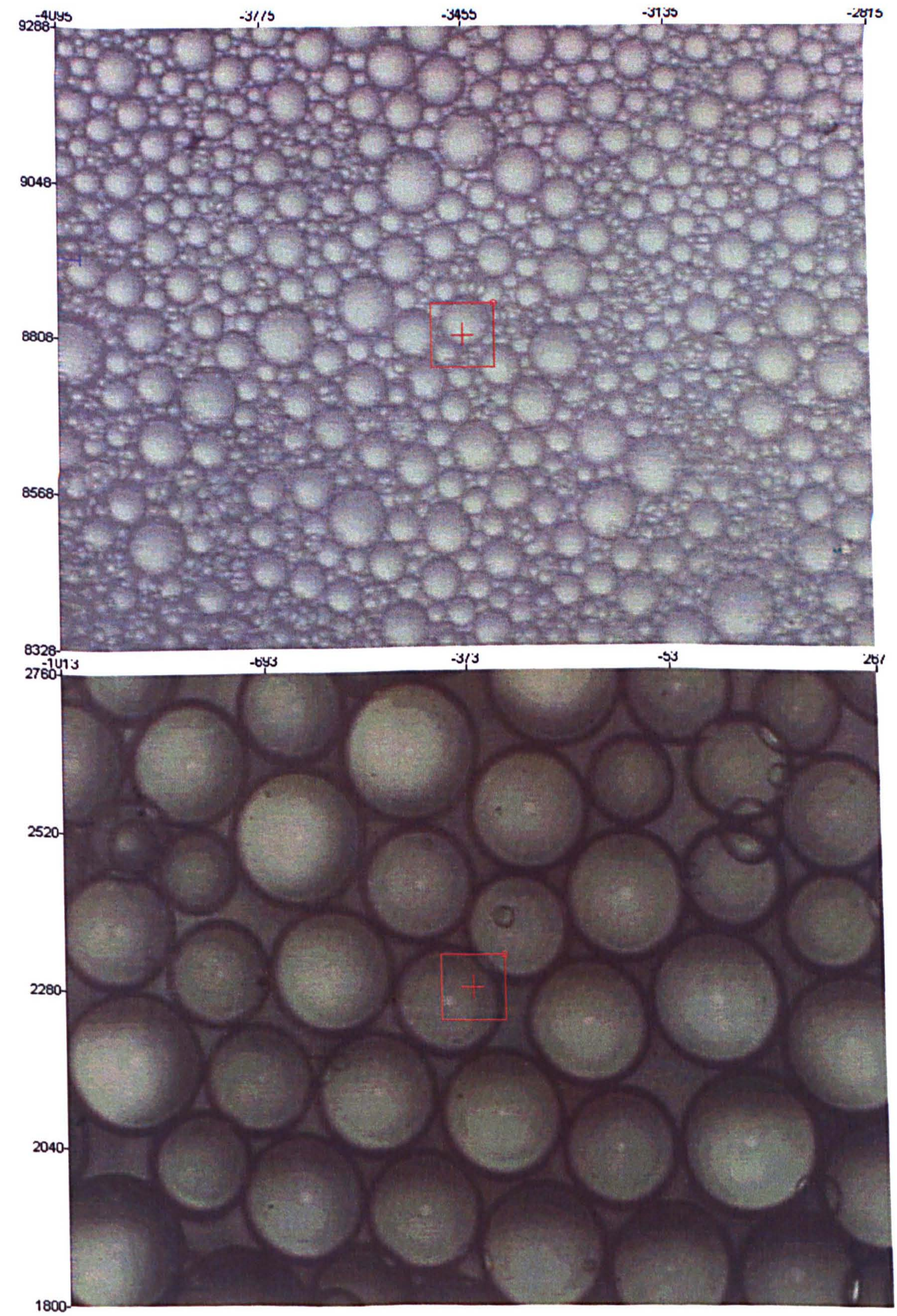

Figure 10.3. Optical micrograph of the poly-disperse hexane-in-D_2O emulsion (top) and the almost mono-disperse hexane-in-D_2O emulsion (bottom). The red square has a length of 100μm.

10.3.1 Mono-disperse Emulsion.

For reasons that will become apparent later, it was desirable to produce a mono-disperse version of the hexane-in-D_2O emulsion described in section 10.2.4. The preparation of an approximately mono-disperse emulsion is not a trivial task and a number of methods were tried.

Initially, an attempt was made to separate the differently sized droplets of hexane in the poly-disperse emulsion used in section 10.2.4. The basis for this separation was the fact that large droplets of hexane rise faster than small droplets when suspended in D_2O. The poly-disperse emulsion was injected into the bottom of a 1m high column of D_2O, the hexane droplets then rise due to buoyancy. At the top of the column, fractions were collected at different time intervals. This method had only limited success in separating the hexane droplets according to droplet size.

After much experimental endeavour, the following method of preparing an approximately mono-disperse emulsion was devised. A 1mm diameter glass capillary was heated and drawn out, producing a very fine capillary (~100μm). This was then attached to a constant flow rate HPLC pump {see section 5.3.2}. The tip of the capillary was angled into a beaker containing 75cm^3 of a 4% w/v solution of tween in D_2O. Hexane was then pumped at a constant volume flow rate through the fine capillary into the aqueous phase. The apparatus is shown in figure 10.4. A layer of hexane was placed on top of the aqueous phase to prevent the D_2O exchanging with the atmosphere.

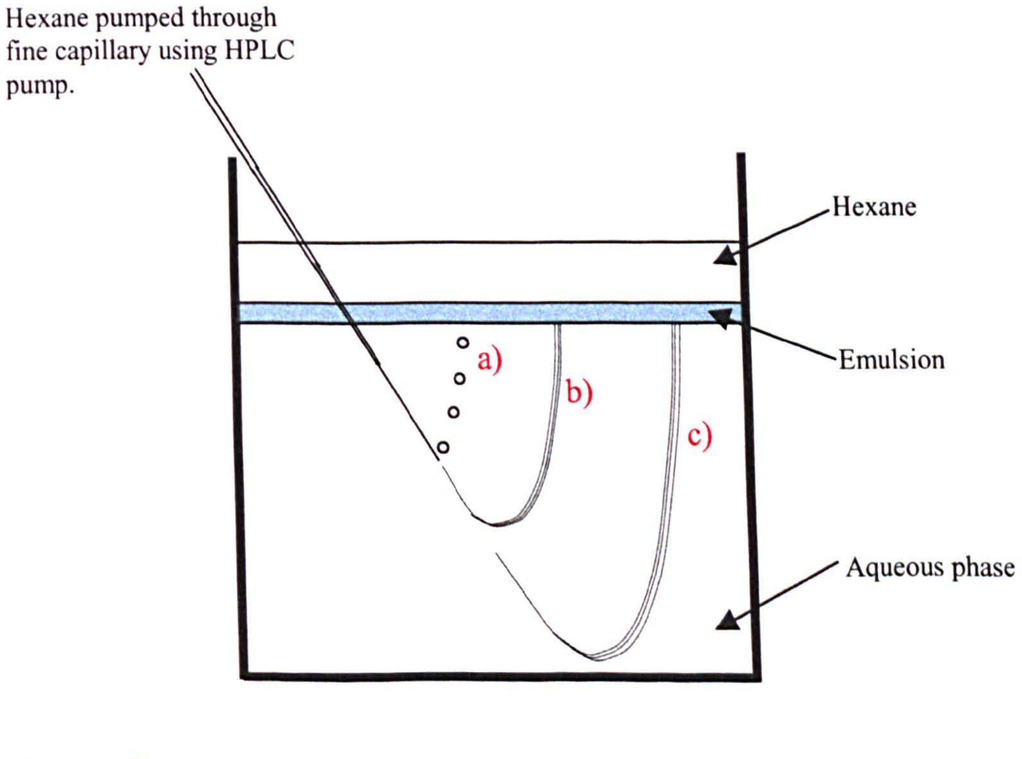

Figure 10.4 The apparatus used to produce an approximately mono-disperse emulsion. Hexane is pumped through the fine capillary into the aqueous phase, hexane droplets then form and rise to the top of the aqueous phase. Using a hexane flowrate of a) <20ml/h , b) 20ml/h , c) >20ml/h.

It was found for this system that if the flow rate of hexane through the capillary (diameter ~100μm) was below 20ml/h then large hexane droplets (~1mm) grew on the tip of the capillary before breaking away and rising to the surface of the aqueous phase, see figure 10.4. At a flow rate of 20ml/h the hexane, however, leaves the capillary in a very fine jet, which breaks up into fine droplets of hexane, which rise to the surface forming the emulsion. At flow rates above 20ml/h the fine jet of hexane persists for longer before breaking up and rising to the surface. It was observed qualitatively that the higher the flow rate of hexane through the capillary the finer the droplets of hexane produced, but also the broader the distribution of droplet sizes.

To produce the most mono-disperse emulsion, the hexane was flowed through the capillary at 20ml/h. A micrograph of the emulsion produced is shown in figure 10.3. The droplets of hexane have a diameter of 180 ± 20μm. The emulsion was placed in a cylindrical glass container 24mm in diameter and 20mm in length. The diffusion of hexane molecules confined within the spherical droplets of the emulsion was examined using the one-dimensional APGSTE sequence {see section 5.6.1}. Measurements were made using the actively shielded 26mm diameter gradient coils, that generate gradients up to 2.5T/m {see section 5.2}. $E_\Delta(q)$ was measured for 64 evenly spaced values of q, 62 positive and 2 negative, with $q_{max}= 15000m^{-1}$. An observation time of 1.2s and a recycle delay of 13.5s were used. The two negative values served to determine the zero-q phase shift, which was used to phase the dataset. The Hankel transform of $E_\Delta(q)$, using equation 10.3, gives the two-dimensional propagator $P_\Delta(X,Z)$.

The one-dimensional dataset of $E_\Delta(q)$ was also Fourier transformed to give the one-dimensional propagator $P_\Delta(Z)$. To verify that the Hankel transform process works, this one-dimensional propagator was compared to the marginal of the two-dimensional propagator $P_\Delta(X,Z)$, it gave a very good match.

The rms displacement of bulk hexane in 1.2s is ~170μm. Therefore, the diffusion of hexane confined within droplets of 180±20μm diameter will be close to the long time limiting case. The analytical echo attenuation of restricted diffusion within a spherical geometry, in the long time limit, is given by [11]:

$$E(q,\infty) = \left| \frac{3[2\pi qr\cos(2\pi qr) - \sin(2\pi qr)]}{(2\pi qr)^3} \right|^2 \qquad (10.4)$$

Figure 10.5 shows a plot of the experimental one-dimensional propagator for the diffusion of hexane within the mono-disperse emulsion and a plot of the analytical propagator for a sphere with diameter 180μm. The agreement is good considering that there is a finite distribution of droplet sizes in the mono-disperse emulsion, albeit small.

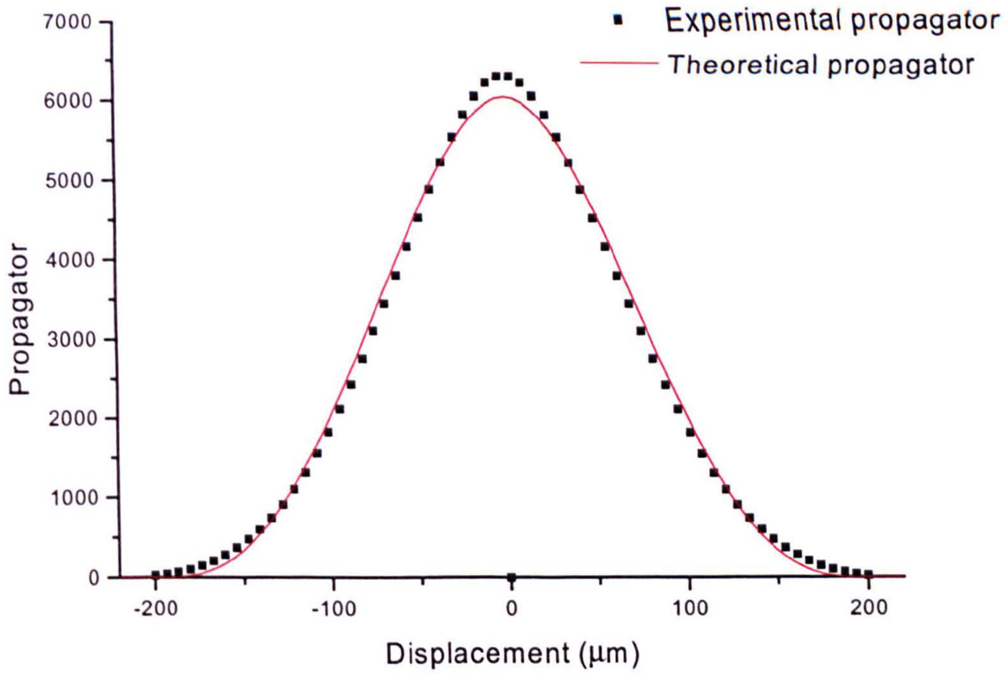

Figure 10.5 A plot of the average one-dimensional propagator for diffusion within the hexane droplets of the mono-disperse emulsion (droplet diameter of 180 ±20 μm), for an observation time of 1.2s. Also plotted is the theoretical propagator for restricted diffusion in a sphere of diameter 180μm, in the long time limit.

10.4 Correlation between Displacements in X and Z

In the previous sections two-dimensional propagators $P_\Delta(X,Z)$ were measured, using two different approaches, for the diffusion of molecules in various constrained environments. The two-dimensional propagator represents the joint probability of X and Z displacements in time Δ. As expected $P_\Delta(X,Z)$ was circularly symmetric reflecting the isotropy of the samples and the diffusive process overall. The aim of this section is to show that information about the correlation between X and Z displacements can be obtained from these two-dimensional propagators.

10.4.1 Correlation distribution $C_\Delta(X,Z)$

In the discussion of two-dimensional propagators measured for flow through porous solids, Stapf et al [3] introduced the displacement correlation distribution $C_\Delta(X,Y)$, defined as :

$$C_\Delta(X,Z)= P_\Delta(X,Z) - P_\Delta(X)P_\Delta(Z) \qquad (10.5)$$

where $P_\Delta(X)$ and $P_\Delta(Z)$ are the so called marginals of $P_\Delta(X,Z)$ {equation 10.2}. To understand the mathematical meaning of the displacement correlation distribution $C_\Delta(X,Y)$, it is necessary to consider the correlation coefficient. The mathematical definition of the correlation coefficient between the two quantities A and B, ρ_{AB}, is given by:

$$\rho_{AB} = \frac{\mathrm{cov}(A,B)}{\sqrt{\mathrm{var}(A)}\sqrt{\mathrm{var}(B)}} \tag{10.6}$$

where the covariance and the variance are defined as:

$$\mathrm{cov}(A,B) = \langle AB\rangle - \langle A\rangle\langle B\rangle \tag{10.7}$$

$$\mathrm{var}(A) = \sigma_A^2 = \langle A^2\rangle - \langle A\rangle^2 \tag{10.8}$$

and $\langle A\rangle$ is:

$$\langle A\rangle = \int_{-\infty}^{+\infty}\int_{-\infty}^{+\infty} P(A,B)A \; dA\, dB \tag{10.9}$$

From equations 10.5 and 10.6 it follows that the correlation coefficient which relates X and Z is given by:

$$\rho_{XZ} = \frac{1}{\sigma_X\sigma_Z}\int_{-\infty}^{+\infty}\int_{-\infty}^{+\infty} C_\Delta(X,Z)XZ\, dX\, dZ \tag{10.10}$$

The correlation matrix $C_\Delta(X,Z)$ is therefore interpreted as representing a 'spatially' resolved view of the correlation between *X* and *Z*. The correlation matrix $C_\Delta(X,Z)$ contains only zero elements if displacements in *X* and *Z* are completely statistically independent. This case is realized for Brownian motion where:

$$P(X,Z) = \frac{1}{2\pi\sigma_X\sigma_Z}\exp\left[-(X-X_0)^2/(2\sigma_X^2)\right]\times\exp\left[-(Z-Z_0)^2/(2\sigma_Z^2)\right] \tag{10.11}$$

However, if the displacements X and Z are correlated, a plot of $P_\Delta(X,Z) - P_\Delta(X)P_\Delta(Z)$ renders the correlation distribution $C_\Delta(X,Z)$ directly.

10.5 Theoretically derived $C_\Delta(X,Z)$

Theoretical displacement correlation distributions $C_\Delta(X,Z)$, *have been* calculated by Graham [10] for completely trapped diffusion in an isotropic distribution of prolate ellipsoidal containers of varying aspect ratio, in the long time limit ($\Delta \rightarrow \infty$). The calculation proceeds by determining the individual 3-D infinite time propagators for an isotropic array of ellipsoids using the relationship between the average propagator and the density autocorrelation function [11]:

$$P_{\Delta\to\infty}(\mathbf{R}) = \int \rho(\mathbf{r}+\mathbf{R})\rho(\mathbf{r})\, d\mathbf{r} \tag{10.12}$$

where $\rho(\mathbf{r})$ is the molecular spin density. The three-dimensional propagator is then generated by a powder-averaging over the array. Finally, the two-dimensional propagator is obtained by projection onto the XZ plane. $C_\Delta(X,Z)$ is then calculated from the two-dimensional propagator using equation 10.5.

Figure 10.6 shows the calculated $C_\Delta(X,Z)$ for ellipsoids of different aspect ratios. It can be seen that the form of $C_\Delta(X,Z)$ is very sensitive to the aspect ratio. $C_\Delta(X,Z)$ is plotted as a contour plot with the maximum intensity normalised to unity. Contour intervals are 0.1 in the range ± 1 to ± 0.1 and have values ± (0.01,0.02,0.03 and 0.05) in the range 0.1 to –0.1. Regions of positive correlation are plotted as solid lines and negative correlation as dashed lines.

For a sphere, aspect ratio 1, positive maxima are found along the axes, which are defined, of course, by the direction of the gradients used. For a spherical restricting surface this is intuitively correct, because for a particle to have the maximum displacement in the x direction, it has to also have zero-displacement in the z-direction. Hence , large X displacements are correlated with small Z displacements and vice versa. At higher aspect ratios the maxima of $C_\Delta(X,Z)$ are found along the diagonals, this indicates the strongest correlations exists for equal values of X and Z.

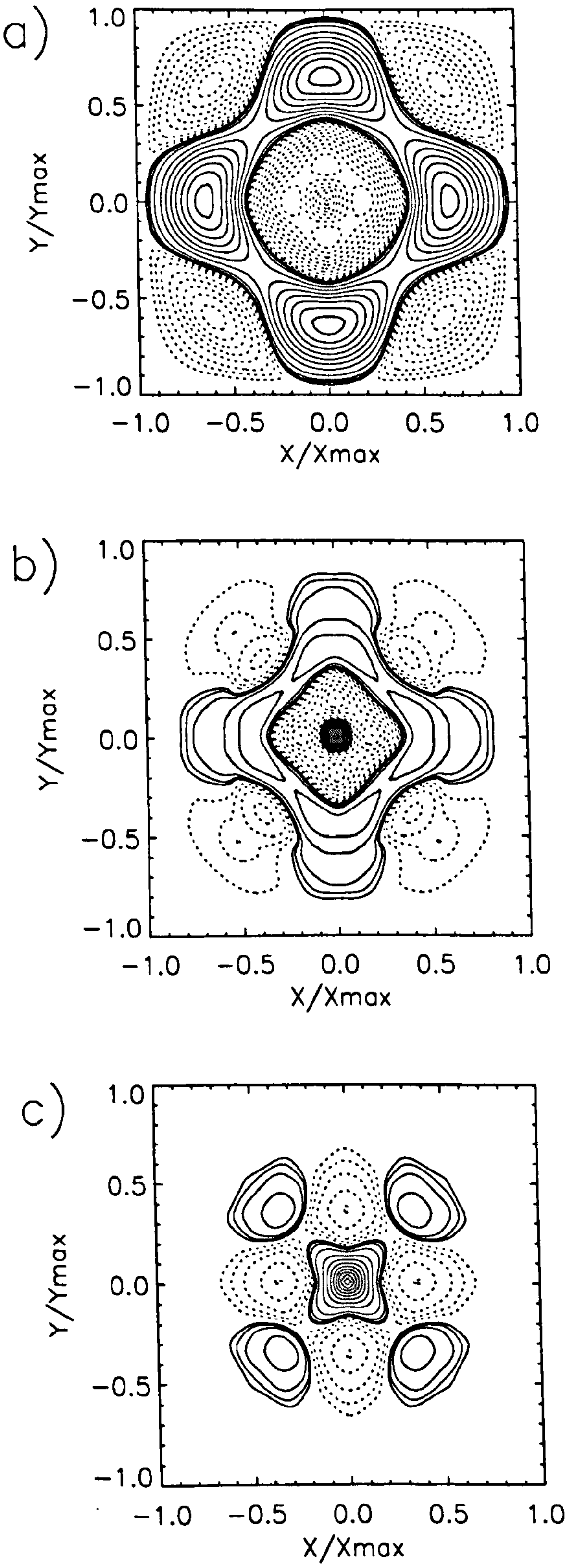

Figure 10.6 Theoretical $C_{\Delta}(X,Z)$ for the infinite time limit of restricted diffusion in prolate ellipsoids of varying aspect ratios a) 1.0 (sphere) b) 1.67 and c) 2.5. $X_{max}(=Y_{max})$ is the dimension of the long axis of the prolate ellipsoid and represents the maximum possible displacement magnitude for this completely restricted diffusion. Regions of positive correlation are represented by solid lines and negative correlation by dashed lines.

10.6 Experimentally derived $C_\Delta(X,Y)$

Earlier in this chapter experimental two-dimensional propagators were presented for diffusion within various confining structures. In this section these two-dimensional propagators are used to calculate the displacement correlation distributions $C_\Delta(X,Z)$, using:

$$C_\Delta(X,Z) = P_\Delta(X,Z) - P_\Delta(X)P_\Delta(Z) \tag{10.13}$$

All contour plots of $C_\Delta(X,Z)$ are based on the maximum intensity being normalised to unity. Contour intervals are 0.1 in the range ± 1 to ± 0.1 and have values ± (0.01,0.02,0.03 and 0.05) in the range 0.1 to –0.1.

10.6.1 Fontainebleau sandstone S_{wi}

Figure 10.7 shows the experimental $C_\Delta(X,Z)$ for the diffusion of hexane contained within Fontainebleau sandstone at $S_{wi}=0.06$ {see section 10.2.1}. Positive correlation is found along the diagonals and negative correlation along the axes. $C_\Delta(X,Z)$ spreads to larger and larger displacements as the observation time is increased, because of the substantially connected nature of the oil phase at S_{wi}.

10.6.2 Fontainebleau sandstone S_{or}

Figure 10.8 shows the experimental $C_\Delta(X,Z)$ for the diffusion of hexane trapped within Fontainebleau sandstone at S_{or} {see section 10.2.2}. Positive correlation is again found along the diagonals and negative correlation along the axes. The size and form of $C_\Delta(X,Z)$ does not vary with observation time, because at S_{or} the oil phase is trapped in isolated droplets at the centre of pores. The diffusive rms displacements thus being bounded.

10.6.3 Random walk simulations of diffusion in Fontainebleau

J. Dunsmuir (Exxon, USA)[12] has used X-ray micro-tomography to provided a pore structure for a Fontainebleau sandstone sample of porosity 22% (the porosity of the Fontainebleau sandstone used in this study was 25%). The synchrotron intensity was measured for 512^3 voxels, each voxel representing a volume of $(5.72\mu m)^3$, the total sample size being approximately 3mm in each direction. From this dataset five sub-datasets, of 100×100×100 voxels, were selected, the average porosity of these sub-volumes being 20.4%. Figure 10.9 shows an example of the pore space of five successive 2-D cross sections.

Seungoh Ryu (SDR,USA)[13] has used this structure to perform numerical simulations of diffusion within Fontainebleau sandstone. The statistics of diffusional displacements were simulated by randomly positioning a random walker in each voxel of the structure. For example, a structure of 100x100x100 voxels of porosity 20% uses 0.2

million random walkers. The random walkers were then allowed to move randomly through the structure. Figure 10.10 shows $P_\Delta(X,Z)$ and $C_\Delta(X,Z)$, obtained from the simulation, for Δ=700ms. As with the experimentally derived $C_\Delta(X,Z)$ for Fontainebleau sandstone at S_{wi} {figure 10.7}, the simulated $C_\Delta(X,Z)$ shows positive correlation along the diagonals and negative correlation along the axes.

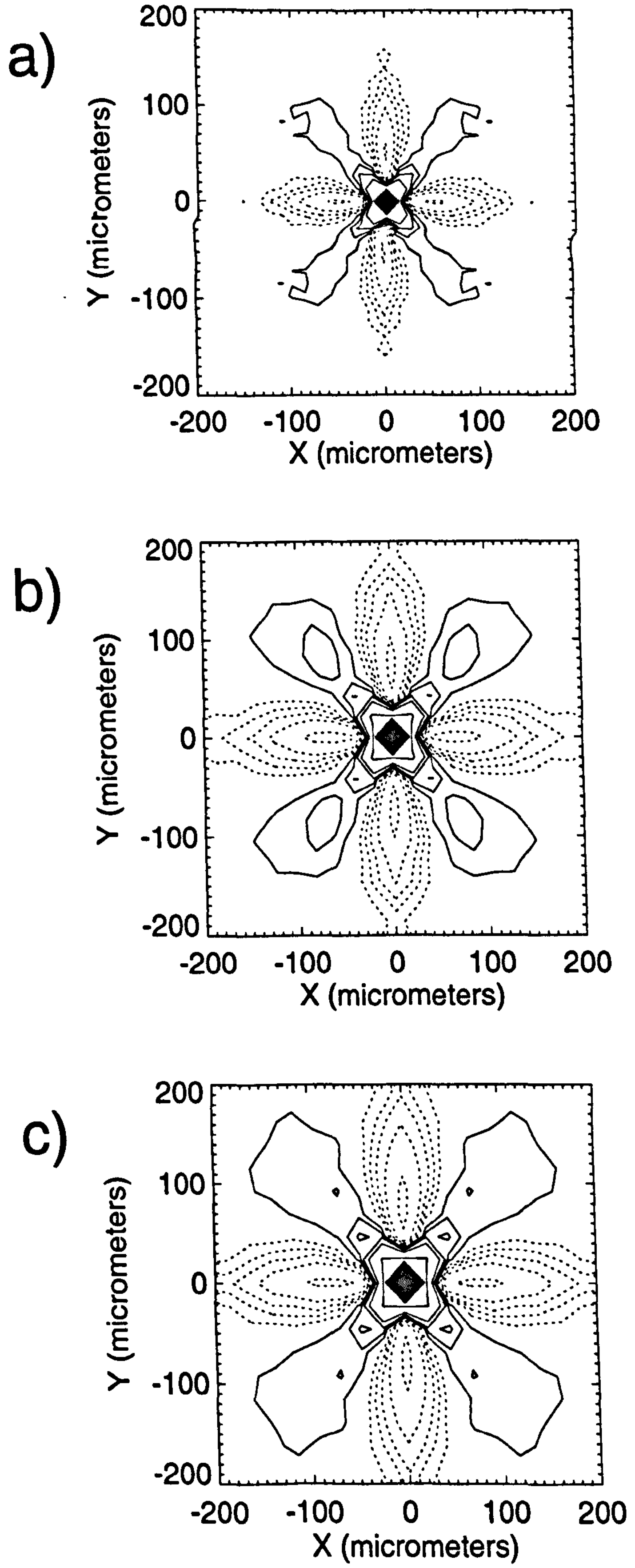

Figure 10.7 Plots of $C_\Delta(X,Z)$ for the diffusion of hexane within Fontainebleau sandstone at S_{wi}. Observation times of a) $\Delta=0.6s$ b) $\Delta=1.2s$ c) $\Delta=1.8s$.

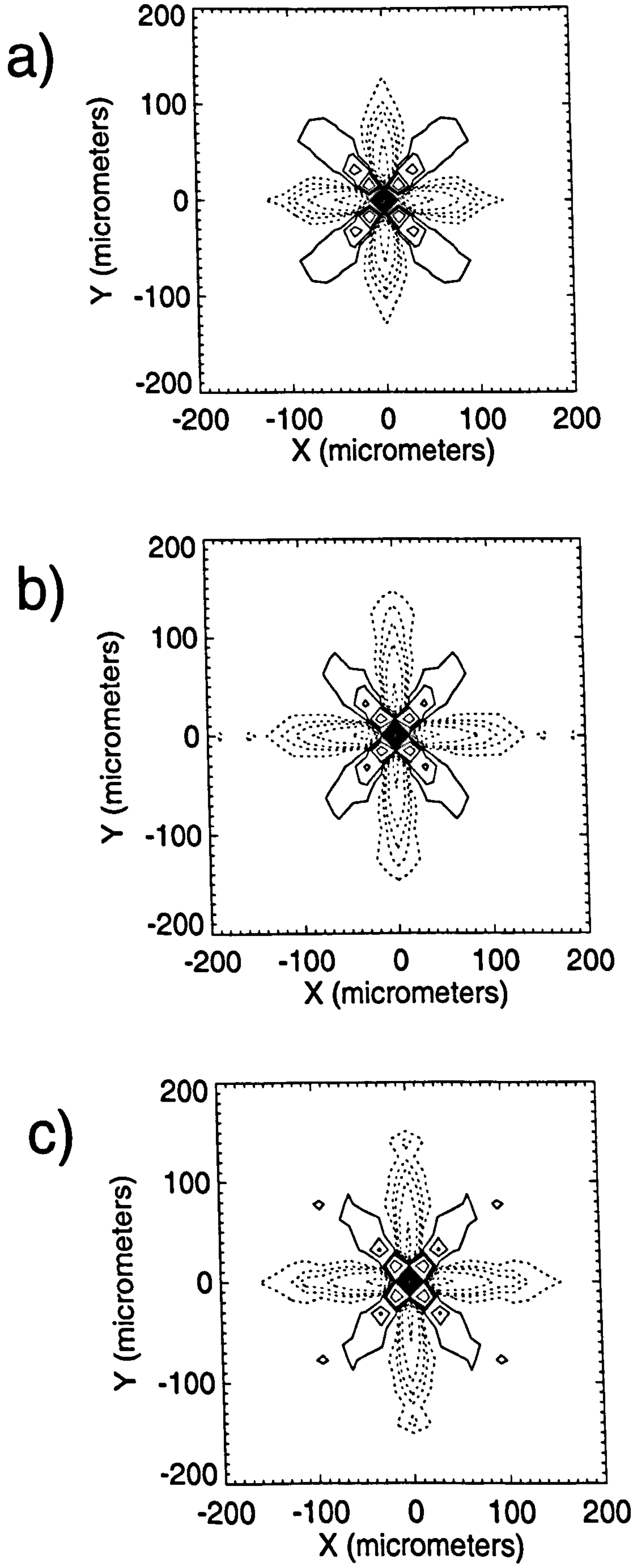

Figure 10.8 Plots of $C_{\Delta}(X,Z)$ for the diffusion of hexane within Fontainebleau sandstone at S_{or}. Observation times of a) Δ=0.6s b) Δ=1.2s c) Δ=2.0s .

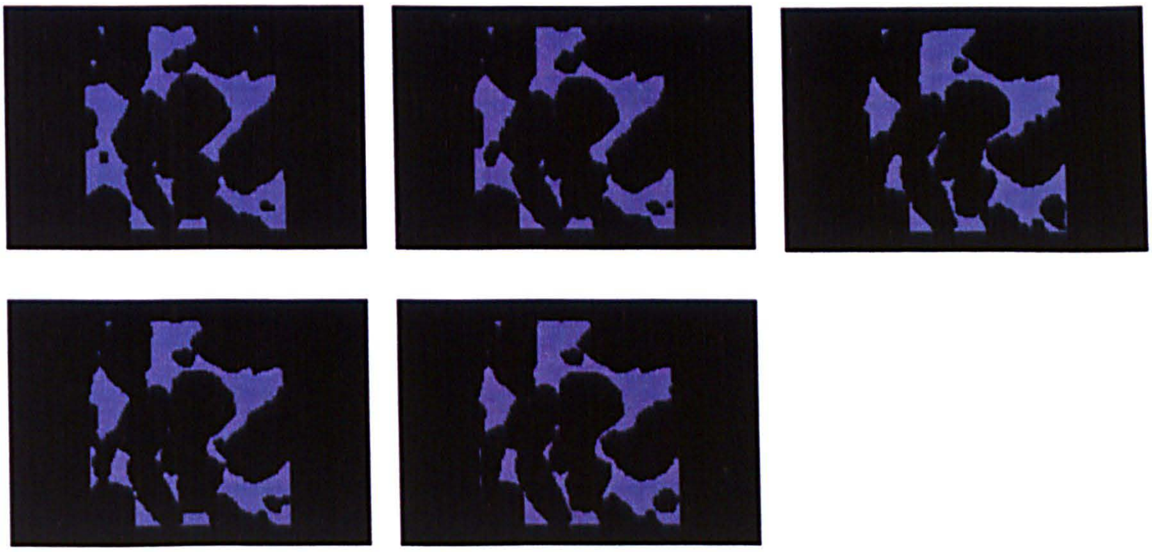

Figure 10.9 A sample of five successive 2D cross-sections from micro-tomography. Each layer is 5.72μm thick. The distance between the left edge and right edge of the blue (pore) area is 572μm.

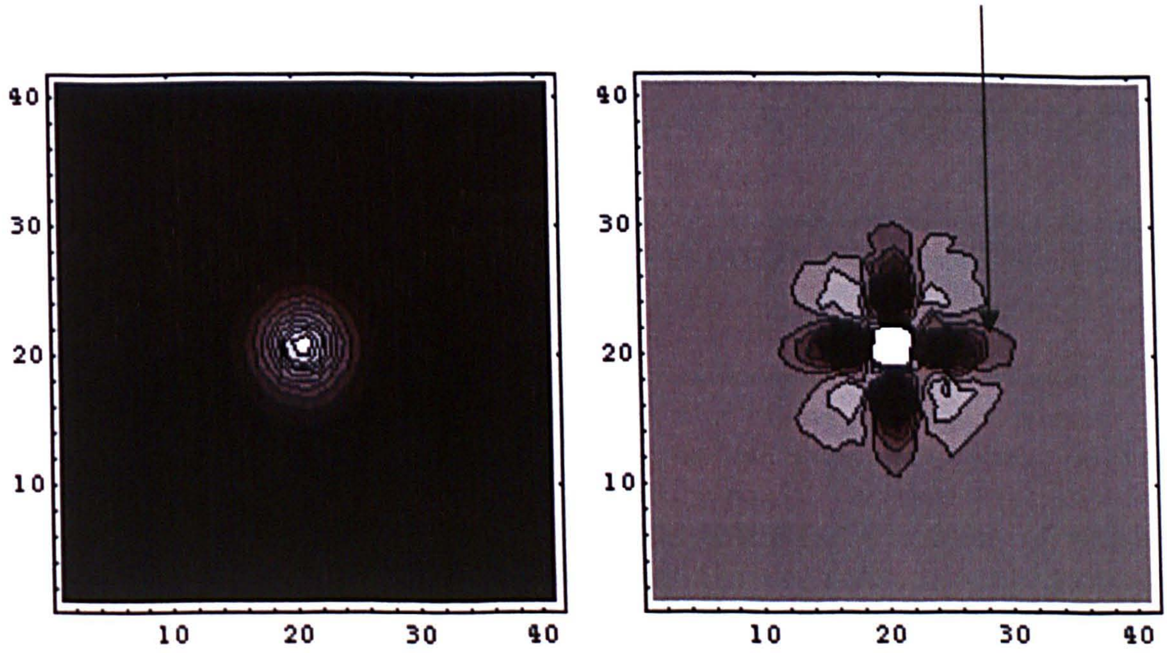

Figure 10.10 Simulated $P_\Delta(X,Z)$ and $C_\Delta(X,Z)$ for an observation time of 0.7s. The length scale factor is 2.53659 μm per unit in x- and y-axes.

10.6.4 Glass Beads, S_w=0.25

Figure 10.11 shows experimentally derived $C_\Delta(X,Z)$ for the diffusion of the water phase in a pack of glass beads (100μm diameter) saturated with both water and tetrachloroethylene, S_w=0.25 {section 10.2.3}. The water phase is expected to form pendular rings where the glass beads touch, and a thin continuous film covering the surface of the glass beads. It is estimated that at this water saturation the pendular rings have an height-to-width ratio of 2.8 {using equation 9.11}. $C_\Delta(X,Z)$ for this system can be seen to have a similar form to that calculated for an ellipsoid of aspect ratio 2.5 { figure 10.6c }, i.e. positive correlation along the diagonals and negative correlation along the axes.

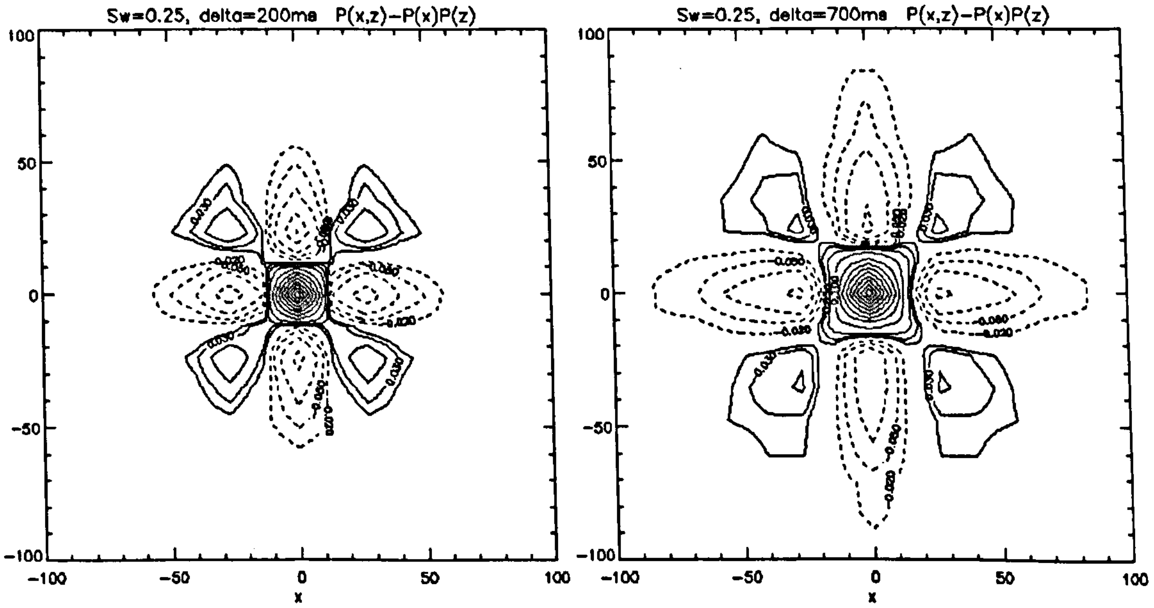

Figure10.11 $C_\Delta(X,Z)$ for diffusion of the wetting phase in a glass bead pack (beads 100μm diameter) at a water saturation S_w=0.25. Measured for observation times of 0.2 and 0.7s.

In chapter 9 a random walk simulation was described for the diffusion of the water phase in such a system [14,15]. The simulation allows for surface relaxation as well as the transport by diffusion of water molecules both within the pendular rings and between them, via thin films on the surface of the beads. The local structure of the random bead pack is approximated by a cubic lattice, the orientation of which is distributed isotropically in the overall calculation. The simulation was used to acquire $P_\Delta(X,Z)$ {see section 9.4} for the random walk of 3×10^5 particles. The simulation used, as input, a height to width ratio for the pendular rings of 2.8 and a film thickness of 29.1nm.

Figure 10.12 shows the results of the simulation in the form $C_\Delta(X,Z)$ for Δ= 200, 700 and 1200ms. There is good agreement between the simulated $C_\Delta(X,Z)$ for Δ= 200ms and the experimental $C_\Delta(X,Z)$ for Δ= 200ms, shown in figure 10.11.

In both the experimental and simulated plots of $C_\Delta(X,Z)$ there is a central 'cross' shape, of positive correlation, which has a diameter of ~80μm. This probably represents the correlation distribution of the strongly hindered diffusion inside the pendular rings. At longer observation times, the simulation shows further, weaker, positive correlation appearing at larger displacements on the diagonals. Particles that have larger displacements have moved from one pendular ring to another via the thin surface film. Therefore, these weaker correlations are associated with particles moving between pendular rings. The reason why these weaker correlations, at larger displacements, are seen in the simulated $C_\Delta(X,Z)$ and not in the experimental $C_\Delta(X,Z)$ may be attributable to the simple cubic lattice structure used in the simulation to approximate the local structure of a random bead-pack. These correlations maybe present in the experimental data, but are not seen due to experimental noise.

In a confining structure that is anisotropic on a local scale but isotropic on a larger scale, it is expected that as particles experience more of the structure any correlations between X and Z displacements will become weaker, and eventually become zero.

10.6.5 Mono-disperse Emulsion

Figure 10.13 shows $C_\Delta(X,Z)$ determined experimentally for the diffusion of hexane confined within the spherical droplets of an approximately mono-disperse emulsion (diameter 180 ± 20 µm, see section 10.3.1}. It can be seen that $C_\Delta(X,Z)$ shows positive correlations along the axes and negative correlations along the diagonals. This is to be expected for diffusion confined by a spherical restricting surface, as large X displacements have to be strongly correlated with small Z displacements and vice versa.

It can be seen that figure 10.13 differs from the theoretical plot of $C_\Delta(X,Z)$ calculated for diffusion in an isolated sphere in the long time limit, see figure10.6a. This deviation from the theoretical $C_\Delta(X,Z)$ is caused by the distribution in sizes of the hexane droplets. The effect of a size distribution on $C_\Delta(X,Z)$ becomes more apparent when a poly-disperse emulsion is considered in the next section.

10.6.6 10.4.6. Poly-Disperse Emulsion

Figure 10.14 shows the experimental $C_\Delta(X,Z)$ for the diffusion of hexane contained within the spherical drops of a poly-disperse emulsion {see section 10.2.4}. Even through all the droplets in the emulsion are spherical, the form of $C_\Delta(X,Z)$ resembles the theoretical $C_\Delta(X,Z)$ of an ellipsoid with an aspect ratio of 2.5 {figure 10.6c} not a sphere {figure 10.6a}. Obviously, the broad distribution of drop sizes is affecting the displacement correlation distribution accessible by these methods.

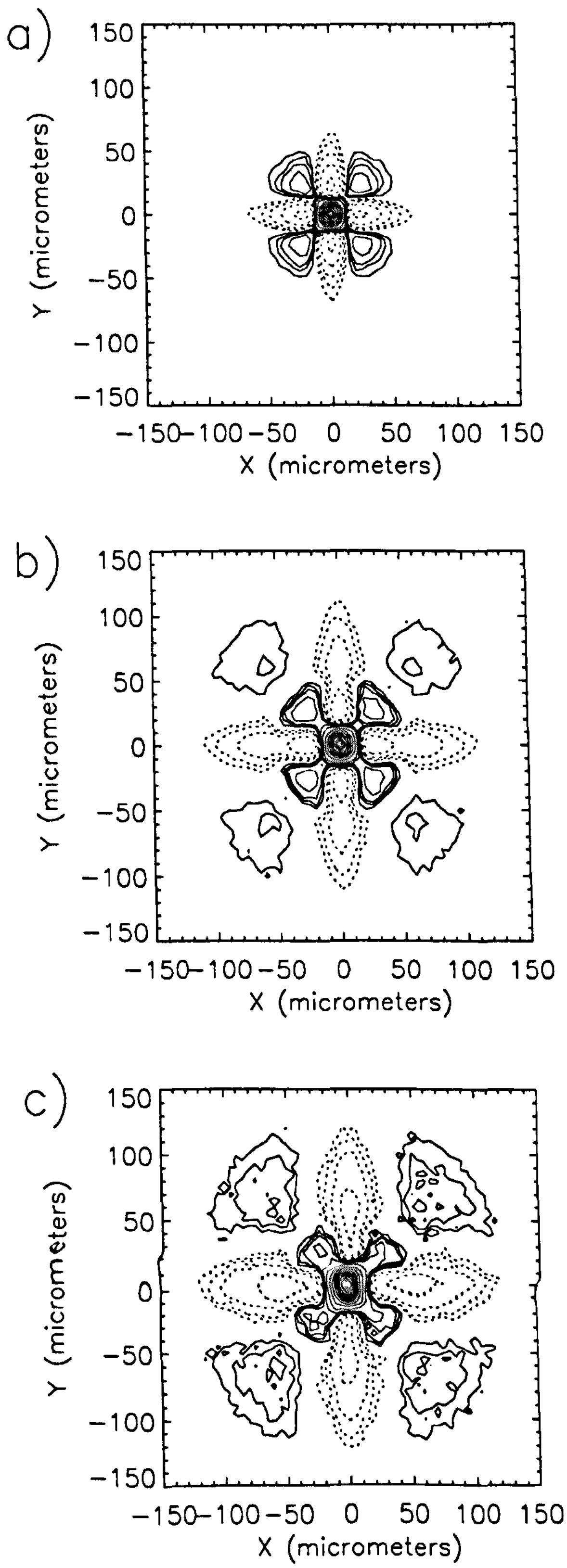

Figure 10.12 Simulated $C_\Delta(X,Z)$ for the diffusion of the wetting phase in a glass beads $S_w=0.25$, for observation times a) 200ms b) 700ms and c) 1200ms.

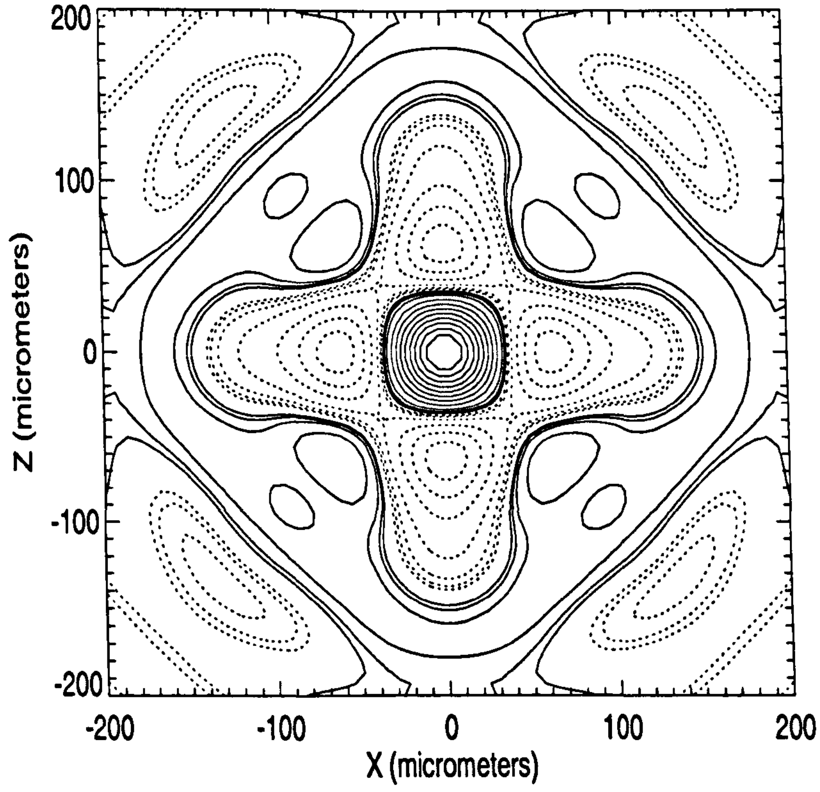

Figure 10.3 Experimental $C_\Delta(X,Z)$ for the diffusion of hexane confined within the spherical droplets of the mono-disperse emulsion (diameter 180±20μm.).

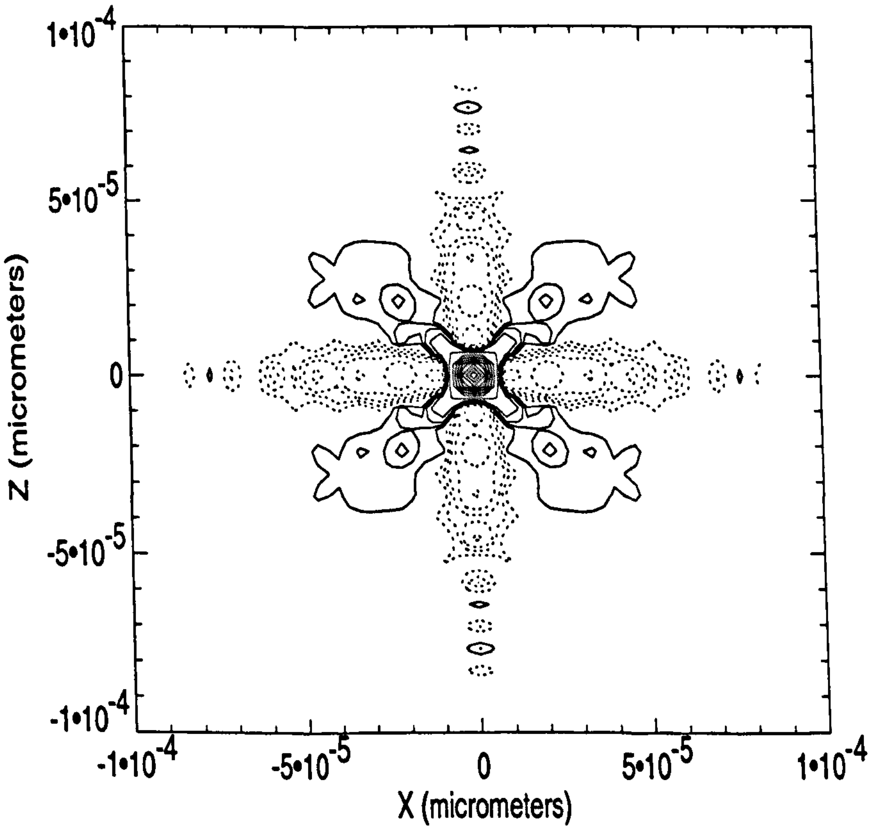

Figure 10.14 Experimental $C_\Delta(X,Z)$ for the diffusion of hexane contained within the spherical drops of a poly-disperse emulsion.

10.7 Conclusion

In this chapter two methods of measuring two-dimensional propagators for diffusion have been described, the two-dimensional APGSTE sequence and the one-dimensional APGSTE sequence followed by use of the Hankel transform. Using these two methods, experimental two-dimensional propagators have been presented for various confining systems.

The displacement correlation distribution $C_\Delta(X,Z)$ was introduced. Theoretical examples of $C_\Delta(X,Z)$ were presented for diffusion within an isotropic distribution ellipsoidal containers of different aspect ratios. These theoretical results were then compared to the $C_\Delta(X,Z)$ derived from the various experimental two-dimensional propagators. The results of two different computer simulation of $C_\Delta(X,Z)$ were also presented.

The form of $C_\Delta(X,Z)$ for a spherical restricting structure can qualitatively be understood. For example in a spherical restricting structure, maximum displacement in the x-direction has to be strongly correlated with zero displacement in the z-direction. This is seen in $C_\Delta(X,Z)$ as positive intensity along the x and z axes. The form of $C_\Delta(X,Z)$ produced for ellipsoids with large aspect ratios is less clearly understood and is still being investigated.

The displacement correlation distribution $C_\Delta(X,Z)$ was measured experimentally for a mono-disperse and poly-disperse hexane-in-D_2O emulsion. The $C_\Delta(X,Z)$ obtained for the mono-disperse emulsion gave a result similar to the $C_\Delta(X,Z)$ obtained theoretically for an isolated sphere i.e. positive correlation on the axes and negative correlation on the diagonals. In the case of the poly-disperse emulsion, the form of $C_\Delta(X,Z)$ was similar to the theoretical result obtained for a ellipsoid of aspect ratio 2.5, i.e. negative correlation on the axes and positive correlation on the diagonals. This clearly indicates that a size distribution in the confining structure can have a large effect on the form of $C_\Delta(X,Z)$. Work is still in progress on understanding the effect of size distributions on $C_\Delta(X,Z)$.

All the contour plots of $C_\Delta(X,Z)$ presented in this chapter were plotted with the maximum value of $C_\Delta(X,Z)$ made equal to unity. This was done for convenience as initially only the form of $C_\Delta(X,Z)$ was of interest. Though, in doing this information about the absolute displacement correlation values is lost. Work is still in progress on the absolute values of $C_\Delta(X,Z)$, and the information this may contain. There are indications that the absolute displacement correlation values found in the case of spherical geometry are considerably lower than in the case of ellipsoids with large aspect ratios

NMR experiments of fluids in porous solids have been used to determine the pore size distributions, the pore interconnections, the surface-to-volume ratios and typical length scales of the confining structure. Recently, there has been interest in quantifying the eccentricities and symmetries of the confining cavities, even when the cavities have an isotropic distribution [5]. In this chapter the correlation distribution $C_\Delta(X,Z)$ is measured experimentally for diffusion within various confining structures.

10.8 References

1. Proceedings of the Fourth International Meeting on Recent Advances in MR Applications to Porous Media. 1998. Magnetic Resonance Imaging. 14:4-5.
2. Packer K.J., Stapf S., Tessier J.J., Damion R.A. "The Characterisation of Fluid Transport in Porous Soilds by means of Pulsed Magnetic Field Gradient NMR". 1998. Magnetic Resonance Imaging. 16. 463-469.
3. Stapf S., Packer K.J., Graham R.G., Thovert J.F.,Adler P.M. "Spatial Correlations and Dispersion for Fluid Transport through Packed Glass Beads Studied by Pulsed Field-Gradient NMR". 1998. Physical Review E. 58. 6206-6201.
4. Stapf S., Packer K.J. "Two-Dimensional Propagators and Spatio-Temperal Correlations for Flow in Porous Media: A comparative Study". 1998. Applied Magnetic Resonance. 15. 303-322.
5. Cheng Y., Cory D.G. "Multiple Scattering by NMR". 1999. Journal of the American Chemical Society. 121. 7935-7936.
6. De Panfilis C. Phd Thesis. 2000. Nottingham University.
7. Dullien F.A.L. "Porous Media: Fluid Transport and Pore Structure". 1992. Academic Press Ltd. London.
8. Hey M.J. Personal Communication. 2000. Nottingham University.
9. Hey M.J., Al-Sagheer F. "Interphase Transfer Rates in Emulsions Studied by NMR Spectroscopy". 1994. Langmuir. 10. No. 5. 1370-1376.
10. Graham R.G., Holmes W.M., De Panfilis C., Packer K.J. "Characterisation of Locally Anisotropic Structures within Isotropic Porous Solids using 2-D PFG NMR". Dec 2000. Chemical Physics Letters. 332. 319-323.
11. Callaghan P.T. "Principle of Nuclear Magnetic Resonance Microscopy". 1991. Oxford University Press.
12. Dunsmuir J. Personnel Communication. Nov 2000. Exxon.
13. Seungoh Ryu. Personal Communication. Nov 2000. Schlumberger Doll Research.
14. Holmes W.M., De Panfilis C., Packer K.J. "Diffusion in Thin Films on the Surface of a Porous Solid". 2001. Magnetic Resonance Imaging. In Press.
15. Holmes W.M., Packer K.J. In preparation.

Appendix 1

Reconstruction of Axially-symmetric 2-D Densities from their 1-D projections.

Let us suppose that we have a two-dimensional q-space response function S(**q**) which we know depends only upon the magnitude q of **q** and not upon its direction. We wish to obtain from this the two-dimensional probability density P(X,Y), which we know is the two-dimensional inverse Fourier transform of S(**q**) with respect to q_x, q_y:

$$P(X,Y) = \int_{-\infty}^{\infty}\int_{-\infty}^{\infty} S(q) e^{-i2\pi X q_x} e^{-i2\pi Y q_y} dq_x dq_y \qquad (1)$$

It will be convenient to define:

$$\begin{aligned} q &= \sqrt{q_x^2 + q_y^2} \\ r &= \sqrt{X^2 + Y^2} \end{aligned} \qquad (2)$$

and

$$\begin{aligned} q_x + iq_y &= q\,e^{i\phi} \\ X + iY &= r\,e^{i\theta} \end{aligned} \qquad (3)$$

It follows from equations 2 and 3 that:

$$\begin{aligned} q_x &= q\cos\phi \\ q_y &= q\sin\phi \end{aligned} \qquad (4)$$

and

$$\begin{aligned} X &= r\cos\theta \\ Y &= r\sin\theta \end{aligned} \qquad (5)$$

Substituting for X,Y, q_x, q_y into equation 1 we find:

$$P(X,Y) = P'(r) = \int_0^{\infty}\int_0^{2\pi} S(q) \exp(-i2\pi qr(\cos\theta\cos\phi + \sin\theta\sin\phi))\, q\, dq\, d\phi \qquad (6)$$

Since cosAcosB+sinAsinB = cos(A-B), equation 6 can be written:

$$P(X,Y) = P'(r) = \int_0^{\infty}\int_0^{2\pi} S(q) \exp(-i2\pi qr \cos(\theta - \phi))\, q\, dq\, d\phi \qquad (7)$$

Making the change of variable $\xi = \theta - \phi$, equation 7 becomes:

$$P(X,Y) = P'(r) = \int_0^{\infty}\int_0^{2\pi} S(q)\,\exp(-i2\pi qr\cos\xi)\,q\,dq\,d\xi \tag{8}$$

In integral form the zero-order Bessel function of the first kind, $J_0(z)$, is defined as:

$$J_0(z) = \frac{1}{2\pi}\int_0^{2\pi} e^{-iz\cos\theta}\,d\theta \tag{9}$$

Comparison with equation 8 gives us finally :

$$P'(r) = 2\pi\int_0^{\infty} S(q)\,J_0(2\pi qr)\,q\,dq \tag{10}$$

The right hand side of equation 10 is, by definition, the Hankel transform of S(q).